University of Alberta

Laboratory Study of Freeze-Thaw Dewatering of Albian Mature Fine Tailings (MFT)

by

Ying Zhang

A thesis submitted to the Faculty of Graduate Studies and Research in partial fulfillment of the requirements for the degree of

Master of Science

In

Geotechnical Engineering

Civil and Environmental Engineering

©Ying Zhang
Spring 2012
Edmonton, Alberta

Permission is hereby granted to the University of Alberta Libraries to reproduce single copies of this thesis and to lend or sell such copies for private, scholarly or scientific research purposes only. Where the thesis is converted to, or otherwise made available in digital form, the University of Alberta will advise potential users of the thesis of these terms.

The author reserves all other publication and other rights in association with the copyright in the thesis and, except as herein before provided, neither the thesis nor any substantial portion thereof may be printed or otherwise reproduced in any material form whatsoever without the author's prior written permission.

Abstract

Tailing ponds in Northern Alberta has covered an area of 170 km^2. Directive 074 issued in 2009 set stringent criteria for tailings reclamation. Freeze-thaw dewatering is one of the most promising approaches for dewatering MFT as one cycle of freeze-thaw can release up to 50% pore water. In this research, freezing tests were conducted with different temperature boundaries. A lower freezing rate induced higher solids content and higher undrained shear strength. In addition, finite strain consolidation tests were performed on both as-received and frozen/thawed MFT. Freeze-thaw decreased the compressibility to about half that of as-received MFT and increased the permeability to 6 times that of as-received MFT with the same void ratio. Both compressibility and permeability curves converged at higher effective stress (σ'=100 kPa). The coefficient of consolidation of frozen/thawed MFT was larger at lower effective stress and smaller at higher effective stress, comparing with that of as-received MFT. These results can be used to predict the field behaviors of Albian MFT and optimize the application of freeze-thaw dewatering.

Acknowledgement

I would like to thank my supervisor Dr. Dave Sego for his insightful guidance, great patience and continuous encouragement during my M.Sc. study at the University of Alberta.

I would like to express my gratitude to Mrs. Christine Hereygers for her great help on preparing the test setups and working out the problems during the experiments. Thank you also to Mr. Steve Gamble for the technical support on my experiments.

I would like to thank the financial support from the Oil Sands Tailings Research Facility (OSTRF).

I would also like to thank my friend Sorta Amarebh for his advices on my experiments and results discussion. I would like to express my gratitude to Saidul Alam for his advices at the beginning of my research. I appreciate the encouragements from friends who are/were in the Geotechnical center at the University of Alberta: Sorta Amarebh, Mohan Acharya, Daniel Meles, Dr. Silawat Jeeravipoolvarn, Chenxi Zhang and Renato Macciotta. Thank you to Dr. Del Fredlund for recommending me to the University of Alberta and his continuous concern during my study in Canada. Thank you to Dr. David Y.F. Ho for his care on me.

I would like to express my gratitude to my grandparents, parents, two sisters and brother for their love and support in life. Finally, specially thanks to my girlfriend Yuan Li for her encouragement, support and love.

Table of Contents

LIST OF TABLES

LIST OF FIGURES

LIST OF SYMBOLS

MFT	Mature Fine Tailings
LVDT	Linear Variable Differential Transducer
SAGD	Steam-Assisted Gravity Drainage
CHWE	Clark Hot Water Extraction Process
%	Percentage
D	Diameter
ERCB	Alberta Energy Resources Conservation Board
NST	Non-Segregating Tailings
G_s	Specific gravity
SEM	Scanning Electron Microscopy
P_o	Initial effective stress
e_o	Initial void ratio
e_B	Void ratio at frozen state
e_c	Void ratio after thawing
X	Depth of thawing front
a	Proportionality coefficient
k_u	Thermal conductivity of unfrozen soil
k_f	Thermal conductivity of frozen soil
c_u	Volumetric heat capacity of unfrozen soil
c_f	Volumetric heat capacity of frozen soil
T_g	Initial ground temperature
T_s	Applied constant surface temperature
L	Volumetric latent heat of water
Ste	Stefan's number
D_f	Freezing depth
P_f	Freezing Time
T_f	Freezing point temperature

$\overline{T}_{af}$	Average ambient temperature during freezing
ρ_f	Density of frozen sludge
$\bar{h}_c$	Convection coefficient
ε	Thickness of the frozen sludge layer
K_{fs}	Conductivity coefficient of frozen sludge
OCR	Over-consolidation ratio
RPM	Rotation per minute
i	Hydraulic gradient
T	Time factor
U	Degree of consolidation
δ	Deformation
γ_w	unite weight of water
Δh	Height difference between water in glass tube and water surface in consolidometer
c_v	Coefficient of consolidation
k	Permeability
m_v	Coefficient of volume compressibility
δ_r	Relative deformation rate
δ_p	Magnitude of primary consolidation
C_c	Compression index
H_0	Initial specimen height
U_e	Excess pore pressure
ω	Water content
LL	Liquid limit
PL	Plastic limit
S_u	Undrained shear strength
I_p	Plastic index
σ'_v	Vertical effective stress
I_L	Liquidity index

CHAPTER 1

1. INTRODUCTION

1.1 Oil sand overview

Although renewable energies contribute more than ever to the total energy consumption worldwide, fossil fuels account for up to 86% of the consumed energy, for which petroleum derivates account for 42.7% (International Energy Agency 2007). Along with the depletion of conventional petroleum and the advance of technology, unconventional bitumen extraction (i.e., oil sands exploitation) has become an essential part of petroleum production. Tremendous reserves occur in several countries: Canada, Venezuela, the United States and Russia. The oil sands in Alberta have been proven to reserve 169.9 billion barrels crude oil, and it can meet Canada's current oil demand for 400 years. It currently produces 1.5 million barrels crude oil per day, and equals to half of all Canadian crude oil production (Government of Alberta 2011a).

Oil sands are a mixture of sand, clay, silt and a type of heavy oil named bitumen. Bitumen behaves like cold molasses at room temperature and acts as viscous liquid upon warming. It can either be extracted on site or in the processing plant, depending on the extraction methods. The selection of extraction methods is based on the proximity of the resource to the ground surface. About 20% of the oil sands are located less than 75 m deep and are extractable by open-pit surface mining with shovels and trucks. The deeper oil sands are accessible by in-situ methods, such as steam-assisted gravity drainage (SAGD) (Government of Alberta 2011b).

1.2 Tailings management

Unlike the in-situ extraction method, bitumen can only be recovered in the processing plant for the surface mining. Various modified Clark Hot Water Extraction Processes (CHWE) are available to separate the bitumen from soils by mixing the crushed ores with hot water in separation vessels. During the extraction process, the left-over sand, silt, clay, residual bitumen and chemical additives form tailings slurry. One barrel of crude oil production induces 3 m^3 tailings by-product (Qiu 2000). Traditionally, tailings are discharged in either above ground tailings ponds or in-pit retaining structures.

Upon the deposition of tailings, the sand component settles down immediately and captures about half of the fine particles to form a beach in the upstream of the pond dyke. The tailings' solids content reduces from an original 55% to 8%. The finer tailings flow into the central part of the pond and the particles settle to form a quasi-stable material referred as mature fine tailings (MFT) after a few years. Figure 1.1 shows the cross-section profile of tailings pond. The solids content of MFT is in the range of 30 to 35%, and over 95% of the solids are fine particles (D≤44 μm) and 30 to 50% are clay particles (D≤2 μm) (Sobkowicz and Morgenstern 2009). Combining with the effects of the residual bitumen and chemical additives, the dispersed flatten clay particles form an edge to face cardhouse fabric (Mikula et al. 1993). The fabric is responsible for high water retention capacity. In term of the geotechnical behaviors, it makes MFT a material with high compressibility, low permeability, low shear strength and low consolidation rate (Proskin 1998). Suthaker (1995) argued that up to hundreds of years are required to reduce half of the volume of MFT under self-weight consolidation. As a result, the accumulated volume of MFT is estimated more than 700 Mm^3 (Mihiretu et al. 2008).

Due to the accumulation of tailings and difficulties in implementation of reclamation, the area of tailings ponds has reached 170 km^2 (Government of

Alberta 2011c). In order to stem the growth of environmental footprint, Alberta Energy Resources Conservation Board (ERCB) released Directive 074: Tailings Performance Criteria and Requirements for Oil Sands Mining Schemes on February 2009. It set stringent criteria that the oil sands industry must significantly reduce the amount of tailings and provide reclamation schemes.

Extensive research has been conducted to eliminate the volume of the MFT and increase its shear strength. Efforts are mainly focused on the prevention of tailings segregation and tailings dewatering. Sobkowicz and Morgenstern (2009) presented a technology roadmap for reclamation of the oil sands tailings. The prevailing method to produce non-segregating tailings (NST) is that mixing MFT with coarse materials (e.g., hydrocyclone underflow) and chemical additives (e.g., gypsum) in specific proportions. NST products possess higher specific gravity (G_s) and higher permeability compared to MFT. Both properties can accelerate the consolidation rate and enhance the strength in a much shorter period. However, it requires stringent proportion of particles and water chemistry to generate NST, which is a challenge since variations in the ores and extraction processes occur.

Dewatering is an approach to decrease the volume and increase the strength of MFT, achievable by mechanical treatment, environmental treatment, chemical treatment and electrical treatment. Centrifuge technology is presently a widely used mechanical method to increase tailings' solids content in plant. The output tailings do not have very high solids content, due to the limitation of technology and consideration of financial cost. Therefore, centrifuges are mostly used in preparing coarse materials (e.g., hydrocyclone underflow) for making NST and shortening the time to form MFT (e.g., thickener underflow). Other mechanical methods like in-line filtration are still in the research stage (Zhang et al. 2009). Chemical additives like gypsum are extensively used by enhancing the tailings' ionic strength and escalating the consolidation rate. These chemicals accumulate with time and result in higher ion concentration in tailings' water. Recycle water

causes erosion to the extraction facilities and pipelines, and leakage of pond water engenders serious environment problems. Electrical methods are in the stage of research; one with promising potential is electrokinetics (Fourie 2009). Environmental approaches are attractive among other methods, as they are environmental friendly and economically. Long et al. (2010) reviewed the research on non-segregating tailings, atmospheric drying, plant dewatering and freeze-thaw dewatering. A scenario was then postulated to incorporate all these methods and maximum the dewatering of tailings. Oil sands in Canada are mostly found in Northern Alberta where the air temperature stays below zero for five months in a year (Environment Canada 2011). As known, freezing can give birth to polygonal fissures within fine grained soils, it is expected that tailings would release a large amount of water upon thawing. Johnson et al. (1993) stated that freeze-thaw can increase the solids content of tailings sludge from 30 to 50% by conducting tests on Syncrude MFT. Proskin (1998) reported that Suncor MFT can release over 50% pore water upon three cycles of freeze-thaw.

1.3 Effect of freeze-thaw on MFT

1.3.1 Effects of freezing on the fabric of MFT

To observe the fabric of MFT and its changes during freezing are prerequisites in the understanding of freeze-thaw dewatering. Mikula et al. (1993) first examined the microfabric of MFT by taking microscopic photography. They found that Syncrude and Suncor MFT have long range ordering of clay particles while OSLO MFT has random clay particle association. Proskin (1998) investigated the effect of freezing on the microfabric of Suncor MFT by Scanning Electron Microscopy (SEM). The photos taken at 100 μm and 4 μm scale in Figure 1.2 demonstrated that the cardhouse fabric was altered to a compacted, face to face aggregated fabric after freezing. The original diameter of pore void was approximate 10 μm.

The compaction of the voids accounts for the decant water upon thawing. Concerning the fabric change in macro scale, Sego and Dawson (1992) observed the homogeneous MFT changed into isolated stiff soil peds with a length of 2 mm and a width of 0.1 mm surrounded by a reticulated ice network in closed system freezing. Proskin (1998) stated that the irregular four-side soil peds are separated by reticulate ice network. The ice lenses have generally 2 or 3 sets of preferred orientations and a thickness up to 2 mm. The vertical ice veins have a width approximate 2 to 4 mm at the top and narrow down towards the bottom. The ice network provides channels for the released water to flow towards the surface upon thawing, while the soil peds settle down.

The stress induced by freezing are declared to be responsible for the fabric changes. Since the pore water at the freezing front is partially frozen at subzero temperatures, suction is generated due to the surface tension difference between the ice crystals and the pore water. The suction gradient drives adjacent pore water flow to the freezing front and forces MFT to consolidate even without adding overburden stress. Moreover, the non-planar freezing front absorbs water in both vertical and horizontal directions. Ice veins and lens occur once the stresses engendered by the ice formation go beyond the tensile strength of the MFT. Overall, a particular structure forms with soil peds surrounded by reticulate ice network (Andersland & Ladanyi 2004, Proskin 1998). The impact of freezing on fabric can also be explained in terms of pore fluid chemistry. The crystal lattice for ice is very selective because of its great regularity. Along with the formation of ice reticulate, chemistry solvent is rejected and concentrated at grain boundaries under low freezing rate (Andersland & Ladanyi 2004). The diffuse double layer theory (Mitchell & Soga 2005) states that the increase in the concentration of electrolytes decreases the absorbed water layer thickness and the repulsive force between the negative charged clay particles. On the other hand, the Val der Waals attractive force is independent with pore fluid chemistry. Consequently, the particles tend to

flocculate and re-orient themselves to accommodate the changes in repulsive forces (Mitchell & Soga 2005, Proskin 1998).

1.3.2 Effects of freeze-thaw on the geotechnical properties of MFT

The solids content of MFT is expected to increase with released water sitting on top after freeze-thaw. Figure 1.3 shows the solids content profile of Syncrude MFT after multi-layer freeze-thaw test. Obviously the decant water contains few soil particles. It is of interest to find the solids content of top part is lower than the original value, while the average solids content of thawed MFT is much higher (Sego and Dawson 1992). Figure 1.4 summarized the results of the solids content enhancement of Suncor, Syncurde, and OSLO MFT by freeze-thaw (Dawson 1994).

In order to identify the factors affecting dewatering, researchers have investigated the effects of initial solids content, freeze-thaw cycles, layer thickness, freezing rate, and chemical additives. Johnson et al. (1993) conducted small scale laboratory freeze-thaw tests on Syncrude MFT with initial solids content of 29 to 35%. Up to half of the pore water was liberated after one freeze-thaw cycle and additional cycles caused further dewatering with less efficiency. Figure 1.5 summarizes the cumulative change in percent solids in large-scale single layer freeze-thaw tests. It shows lower initial solids content experienced a more significant increase in solids content and additional cycles of freeze-thaw became less efficient compared with the first cycle. Moreover, an exponential relationship between the initial solids content and solids content after freeze-thaw was found regardless of thermal history as shown in Figure 1.6. Large scale multi-layer freeze-thaw tests were also implemented to compare with the large scale single layer tests. Results indicated multi-thin layer freeze-thaw could improve dewatering by 40% over the single layer freeze-thaw. Sego and Dawson (1992) performed both small scale single layer and large scale multi-

layer freeze-thaw tests on Syncrude MFT. The information on sample heights and temperature boundaries is described in Figure 1.7. It indicates that larger sample height and lower freezing rate result in higher post-thaw solids content. Multi-layer tests were carried out at different boundary temperatures. Incorporated with the single layer tests, it also concluded that a lower freezing rate yields higher thaw strain. Sego (1992) and Proskin (1998) conducted freeze-thaw tests on as-received and chemical-amended Suncor MFT. They found reducing pH and increasing the concentration of multi-valence cations before freezing could generate higher post-thaw solids content (Figure 1.8).

The decanted water due to freeze-thaw looked clear and had small patches of bitumen floating on the surface (Johnson et al. 1993). Proskin (1998) claimed that freeze-thaw only affected concentration of some ions, while the pH and electrical conductivity were unchanged. The released water of chemical amended MFT had lower pH and two times the electrical conductivity compared with pond water.

1.3.3 Related theoretical models

1.3.3.1 Model of Stress path in the freeze-thaw process

In the perspective of geotechnical engineering, it is of great interest to construct a stress path model for the freeze-thaw process. Once the model is established, it can explicitly describe the variation of void ratio with changes in effective stress during the freeze-thaw. Practically it can predict the solids content increase and the thawed settlement. Nixon and Morgenstern (1973) emphasized the importance of thermal history on permafrost soil. A stress path model for fine grained soil during freeze-thaw was proposed based on laboratory test results. As shown in Figure 1.9, the sample first consolidates under an effective stress of P_o along the normally consolidation curve to a void ratio of e_o at point A. Closed system freezing (no access to external water) takes place and the void

ratio increases to e_B at point B by the phase change from water to ice. External effective stress P_o stays the same, while the inner effective stress consolidates the sample along the dash line to point D. The consolidation attributes to the suction formed at the freezing front. When thawing occurs, soil peds absorb part of the thawed water (D to E) and leave the residual water for drainage. Excess pore pressure would generate if the free water cannot expel instantly. The magnitude of the excess pore pressure can reach a maximum value equal to the external overburden pressure and make the effective stress drop to zero. Since the overburden stress P_o is constant, the sample consolidates both during and after thawing. Finally, it will reach an effective stress P_o with a void ratio of e_c at point C on the recompression line. The net strain from the frozen to the fully thawed consolidated state (BC) is defined as thaw strain.

Dawson (1994) first applied the stress path model to study the consolidation due to freezing. Proskin (1998) modified the above model to correlate with fabric changes during the multi-layer freeze-thaw dewatering of MFT. As shown in Figure 1.10, as-received MFT first experiences freezing expansion from the point A to A''. Meanwhile the MFT consolidates to point A' under suction generated during freezing. Subsequent thawing and post-thaw self-weight consolidation takes MFT to point B. Then suction creates as desiccation occurs and MFT is recompressed to point B' along the recompression curve. An additional layer is deposited and some of the MFT penetrates into the cracks. The pervious MFT swells to point C corresponding to the wetting. The second cycle of freezing further consolidates the MFT to point C' and yields larger cracks.

1.3.3.2 Thermal models for predicting freezing and thawing depths

The one-dimensional Neumann problem is commonly used in the prediction of thawing depth of soil. As shown in Figure 1.11, a homogeneous soil is subjected

to a step temperature increase from T_g to T_s. The properties of soil are independent of temperature. The movement of the thawing front is given as:

$$X = \alpha\sqrt{t}$$

where X is the depth of thawing front; t is the thawing time; α is the proportionality coefficient which relies on soil thermal properties and temperatures: $\alpha = f\left(k_u, k_f, c_u, c_f, T_g, T_s, and\ L\right)$, k_u and k_f are the thermal conductivities of unfrozen and frozen soil (cal/°C·cm·s), c_u and c_f are the volumetric heat capacities of unfrozen and frozen soil (cal/°C·cm^3), T_g is the initial ground temperature (°C below freezing point), T_s is the constant surface temperature (°C) and L is the volumetric latent heat of water (cal/cm^3) (Nixon and McRoberts 1973).

Based the assumption that temperature distribution has no effect on the rate of thawing, Nixon and McRoberts (1973) postulated a semi-empirical solution to the proportionality coefficient.

$$\alpha = 2\sqrt{\frac{k_u}{c_u}}\sqrt{\frac{Ste}{2}}\left(1 - \frac{Ste}{8}\right)$$

where Ste is the Stefan's number, $Ste = c_u T_s / L$.

Nixon and McRoberts (1973) obtained the Stefan solution by further assuming linear temperature in the thawed zone and zero degree temperature in the frozen zone.

$$X = \alpha\sqrt{t} = \left(\frac{2k_u T_s}{L}\right)^{1/2}\sqrt{t}$$

On the other hand, the freezing depth of soil can also be predicted by substituting the thawing material properties with freezing material properties.

More recently, Martel (1988) proposed new mathematical models for predicting the freezing and thawing depths of municipal waste treatment sludge in terms of heat balance. The formula for freezing depth (D_f) prediction is given as below:

$$D_f = \frac{P_f\left(T_f - \overline{T}_{af}\right)}{\rho_f L\left(\frac{1}{\overline{h}_c} + \frac{\varepsilon}{2K_{fs}}\right)}$$

where P_f is the freezing time; $T_f$is the freezing point temperature; $\overline{T}_{af}$ is the average ambient temperature during freezing; ρ_f is the density of frozen sludge; L is the latent heat of fusion; $\overline{h}_c$ is the convection coefficient; ε is the thickness of the frozen sludge layer; and K_{fs} is the conductivity coefficient of frozen sludge.

In the derivation of the freezing model, it was assumed that solar radiation has a negligible effect on freezing and the freezing bed is operated in the following conditions: new thin layer sludge must be placed upon a totally frozen previous layer; temperature at the interface of sludge and bed is at the freezing point; and no snow is allowed on the bed surface (Martel 1989, 1993).

The model for predicting thawing depth (Y) of sludge was derived accounting for the removal of supernatant as thawing occurs:

$$Y = \left[\left(\frac{K_{ss}}{\theta\overline{h}_c}\right)^2 + \frac{2K_{ss}P_{th}}{\theta\beta}\right]^{1/2} - \frac{K_{ss}}{\theta\overline{h}_c}$$

where $\beta = \rho_f L/\left(\overline{T}_{at} - T_f + \alpha\tau\overline{I}/\overline{h}_c\right)$; K_{ss} is the thermal conductivity of settled sludge; θ is the fraction of settled sludge per unit depth of thawed sludge; P_{th} is the thawing time; $\overline{T}_{at}$ is the average ambient air temperature during thaw; α is the solar absorptance of the sludge; τ is the transmittance of the roof material; $\overline{I}$ is the average insulation during the thawing period.

The thawing model assumed precipitation is kept out of the bed, and 90% of solar radiation passes through the roof material (Martel 1989, 1993). The

thawing model is not applicable in the freeze-thaw dewatering of MFT as it is impossible to cover the tailings ponds with roofs.

1.3.3.3 Applicability of thermal models in thermal analysis of MFT

An appropriate thermal model is necessary to optimize the freeze-thaw dewatering of tailings. Johnson et al. (1993) checked the Stefan solution by conducting large-scale, one-dimensional, laboratory freeze-thaw test on Syncrude MFT. The freezing temperature was selected as -24°C and the proportionality coefficient was determined in the thick single layer freezing tests. It was then applied in predicting the freezing time for multi-layer MFT. The added thickness of all thin layers equaled to that of the thick single layer. Based on the Stefan solution, it was expected the time to freeze multi-layer was much shorter, while the results showed the freezing time was almost same. The Stefan solution was proved to be imprecise in thermal analysis of MFT. However, the rationality of the selected freezing temperature is questionable. Temperature profiles showed the freezing temperature was between -1 and -3°C. The newly deposited MFT released its heat to both air and the underlying MFT. The temperature of older MFT climbed to around -4°C and was still below freezing. Therefore, the time to cool the MFT to -24°C should be excluded in the freezing time and more work is required to examine the applicability of Stefan solution.

Dawson (1994) employed a modified version of Martel solution in predicting the freezing and thawing depth of multi-layer OLSO MFT in field condition at Fort McMurray. The temperature of the frozen MFT and the newly deposited MFT was assumed as zero. The downwards heat conduction to the deep earth was taken into account during thawing. Design scenarios of freeze-thaw dewatering were then evaluated for commercial implementation. However, the examination of the validity of Martel solution in the predicting the freezing and thawing depth of MFT was not presented.

Proskin (1998) pointed out the semi-empirical solution, Stefan solution and Martel solution only considered the heat transferred to air and neglected the heat conduction downwards. The Stefan solution was adopted to account for this heat flow during freeze-thaw. Besides, the thaw strain and changes in thermal properties were considered in the prediction of thawing front. In the large scale laboratory test on Suncor MFT, the predicted freezing time was found to be two to four times longer than the measured freezing time. Instead of the thermal models, test facility deficiencies (imperfect insulation and low frequency of temperature recording) were claimed as the causes to shorten the freezing time. The predicted thawing time was consistent with the measured thawing time. By comparing the three thermal models, Proskin (1998) concluded the Stefan solution is convenient and accurate in a thermal analysis of MFT. In the field tests, freezing rate parameters α were first determined based on field freezing data and freezing temperatures were then back-calculated. Finally, the frozen/thawed depths were predicted by varying freezing temperature, correlation between surface and air temperature, and thin layer thickness.

1.4 Necessity of finite strain consolidation theories

Terzaghi's one-dimensional consolidation theory has been extensively used in the analysis of compressibility and permeability of clayey soil. It is established on several assumptions including: infinitesimal strain, negligible self-weight, constant compressibility and permeability at certain load increment. The theory is not reliable when it comes to soft soils, since large deformation may occur even under small load increment. To account for large strain and changes in compressibility and permeability, Gibson et al. (1967) derived the governing equation for finite strain consolidation of homogeneous clay. Compressibility and permeability are two fundamental properties in the equation. The void ratio was found as a privileged variable, and the compressibility and permeability are functions of void ratio. In addition, the governing equation was solved for thin

layer consolidation by ignoring the self-weight. Gibson et al. (1981) considered the self-weight and further solved the governing equation for thick layer consolidation of clay. The finite strain consolidation theory was found to predict higher excess pore pressure and consolidation rate compared with Terzaghi's theory. Pollock (1988) reviewed available finite strain consolidation theories in details. All in all, the primary purpose of a consolidation test is to determine the compressibility and permeability in terms of void ratio (Znidarcic et al. 1984).

1.5 Consolidation behaviors of MFT and the effects of freeze-thaw

Unlike ordinary normally consolidated clay, the compressibility of as-received MFT at lower stress level depends on the initial solids content. Figure 1.12 shows the compressibility curves of as-received MFT with different initial solids contents. The effect of initial solids content is obvious at lower effective stress. It diminishes at higher effective stress as the compressibility curves converge. Suthaker (1995) argued that the process of aging yields various micro-structure and it accounts for the variation in compressibility of as-received MFT. Regarding the effects of freeze-thaw, the increase in solids content is obvious. As the void ratio is much decreased, the thawed MFT becomes less compressible at lower stress level and approaches the compression curve of as-received MFT at higher stress level (Figure 1.13). In other words, the compressibility of thawed MFT is more sensitive to void ratio (Proskin 1998).

Suthaker (1995) and Proskin (1998) found an identical power law relationship between permeability and void ratio of as-received MFT. Different initial void ratios did not give birth to a group of permeability curves as they did in the compression curves. Proskin (1998) investigated the effect of freeze-thaw on the permeability of MFT. Cracks formed upon freezing provided flow channels during thawing and post-thaw consolidation. At lower stress level, the thawed MFT was proved to have a permeability approximate two orders that of as-received MFT

at the same void ratio. As the overburden stress increases, the framework of thawed MFT collapses and cracks close. The permeability of thawed MFT approaches that of as-received MFT at higher stress level and it is therefore more sensitive to void ratio (Figure 1.14).

Besides compressibility and permeability, Suthaker (1995) stated that consolidation behavior is also governed by creep properties and thixotropic strength of the materials.

Creep is the time-dependent volumetric strains/shear strains at a rate controlled by the viscous resistance of the soil structure (Mitchell & Soga 2005). Suthaker (1995) declared that the creep rate of MFT increased linearly with void ratio and creep accounted for 30% of total settlement during 10 years for a 10 m MFT column deposit. The MFT deposit had very low permeability and a long drainage path. It required tremendous time to complete the primary consolidation. On the other hand, the high void ratio contributed to a high creep rate. Large creep accumulated along with the primary consolidation of the MFT deposit. Suthaker (1995) also presented other factors that might affect the creep rate: the over consolidation ratio (OCR) and the size of load increment. Higher OCR and smaller load increment reduce the magnitude of creep.

Another prominent property of MFT is that it becomes weaker upon remolding and gains back strength with time at constant water content and void ratio. This phenomenon is called thixotropy and it commonly occurs in a water-clay system. As the inter-particle bonding becomes stronger with time, the consolidation behavior may be influenced. Suthaker (1995) studied the thixotropic behavior of MFT by performing cavity expansion tests. She found that the thixotropic strength was higher for MFT with lower water content and it increased quadratically with age. The thixotropic ratio, which is usually associated with sensitivity, is defined as the ratio of strength after certain time to the remolded strength. It increased with water content when the water content of MFT was

higher than 150%; the opposite took place when the water content was lower than 150%.

Previous research has given an idea of the geotechnical properties and behaviors of MFT, the effects of freeze-thaw on most of those properties and behaviors, and the mechanisms involved in the freeze-thaw process. However, it also showed that the effectiveness of freeze-thaw dewatering on different MFT varies much. It was known that the location of oil sands mines and extraction methods give birth to particular mineralogy and chemistry component of MFT. An optimum MFT management plan requires knowledge of the specific MFT. Since no data have been published on the freeze-thaw dewatering of Albian MFT, the research program was carried out to accomplish it at a bench scale.

1.6 Objectives of the research

The main objective of this thesis was to study the effect of freeze-thaw on the consolidation behavior of Albian MFT. The specific objectives were

1) to obtain the basic geotechnical properties of Albian MFT;
2) to investigate the effect of freezing rate and post-thaw consolidation on solids content and shear strength of Albian MFT;
3) to determine the consolidation and permeability behaviors of as-received Albian MFT;
4) to investigate the effect of freeze-thaw on the consolidation and permeability behaviors of Albian MFT;
5) and to establish written procedures of the experiment and results interpretation.

1.7 Scope of the research

Characterization tests are carried out to determine the geotechnical behaviors. They include: density test, solids content test, bitumen content tests, specific gravity measurement, hydrometer tests and sieve tests, vane shear tests, and bearing capacity tests.

One dimensional freeze-thaw tests are conducted to investigate the effect of freezing rate and post-thaw consolidation on solids content and undrained shear strength of MFT. Three samples are frozen under top freezing temperatures at -5°C, -10°C, and -20°C, respectively. Then enough time is given for post-thaw consolidation before measuring the solids content and shear strength. A fourth sample is frozen with temperature of -5°C and tested right after thawing.

Slurry consolidation tests on as-received MFT are performed and analyzed to determine the compressibility, permeability, and consolidation rate. Three samples with initial solids content of 30% are tested following basically the same procedures. A fourth sample is specially used to investigate the self-weight consolidation.

Freeze-thaw and post-thaw consolidation tests are performed to examine the effects of freeze-thaw on dewatering and post-thaw consolidation behaviors. Two samples with initial solids content of 30% were tested to check the repeatability.

1.8 Organization of the thesis

Chapter 2 describes the location of sampling, the geotechnical properties of the sample, the instruments and test procedures for freezing rate investigation test, the conventional techniques for consolidation and permeability tests, and the setup and brief procedures for slurry consolidation tests. Later on, it presents

the instruments and test procedures for both types of finite strain consolidation tests involved in this study. Finally, the methods of locating the end of primary consolidation are discussed.

Chapter 3 first presents the methods of determining coefficient of consolidation, and the selection of proper hydraulic gradient. The test results and discussion of the freezing rate investigation are given afterwards. Then it shows the results of compressibility and permeability for both as-received and frozen/thawed MFT. The pore pressure data during consolidation and the post-consolidation solids content and shear strength are also reported. The effect of hydraulic gradient and the comparison between one-way and two-way drainage are also investigated. Finally, it discusses the above results and estimated the average pre-consolidation pressure and undrained shear strength.

Chapter 4 contains the summary, conclusions of this research work, and recommendations for future work.

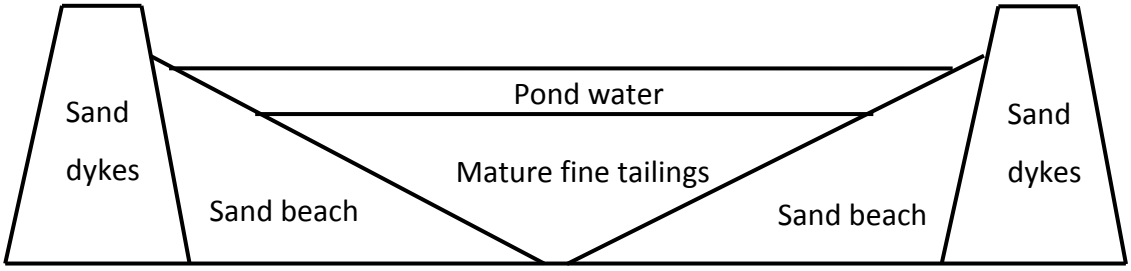

FIGURE 1.1 Profile of tailings pond (after Beier and Sego 2008)

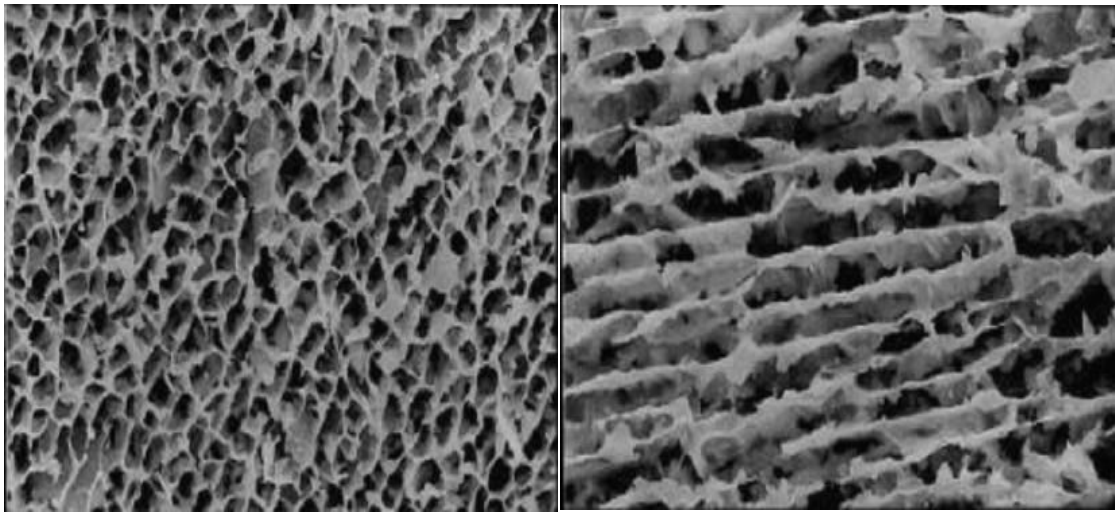

(a) As-received, never frozen Suncor MFT

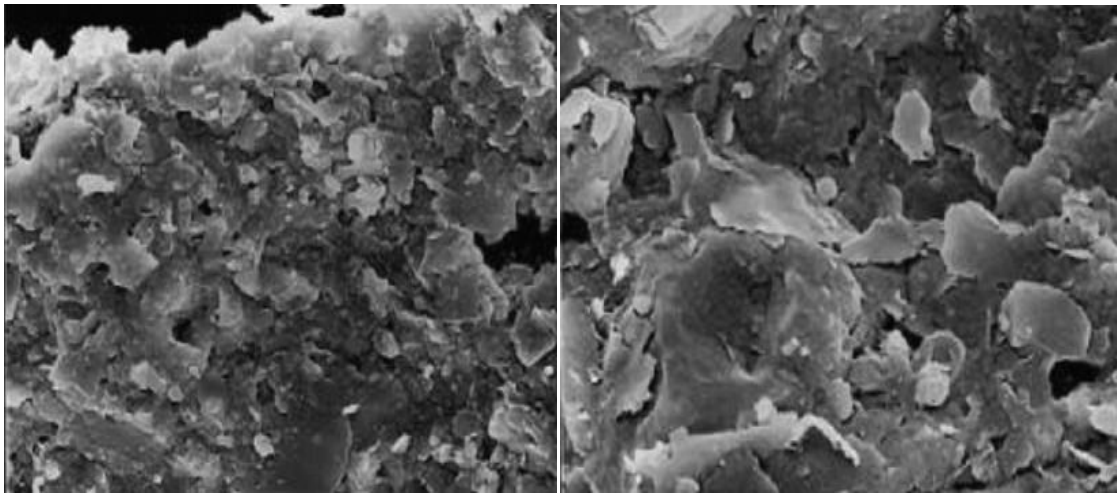

(b) As-received, frozen/thawed Suncor MFT

FIGURE 1.2 Scanning electron micrographs in scale: 100 µm (left), 4 µm (right) (after Proskin 1998)

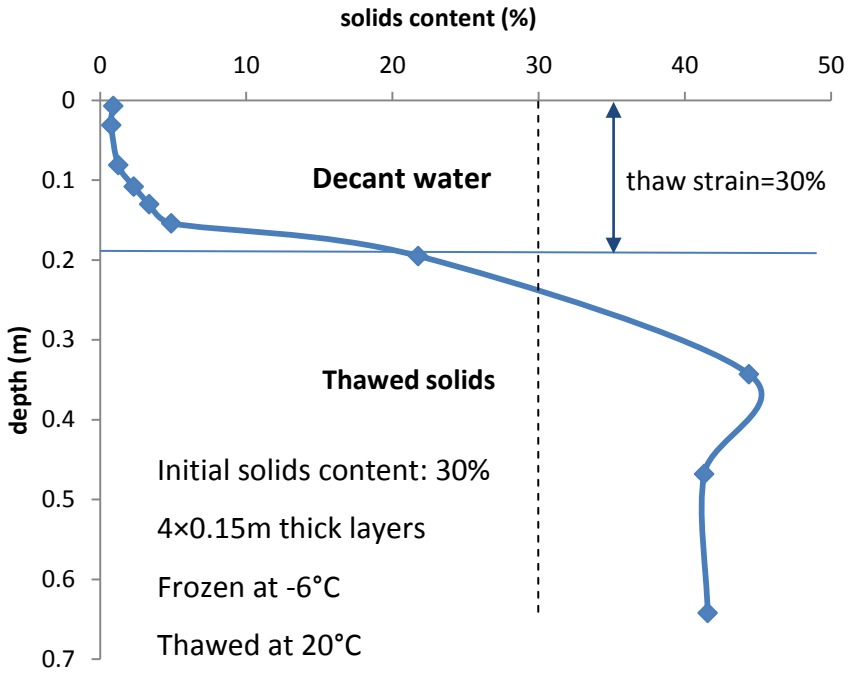

FIGURE 1.3 Solids content profile of Syncrude MFT in multi-layer freeze-thaw test (after Sego and Dawson 1992)

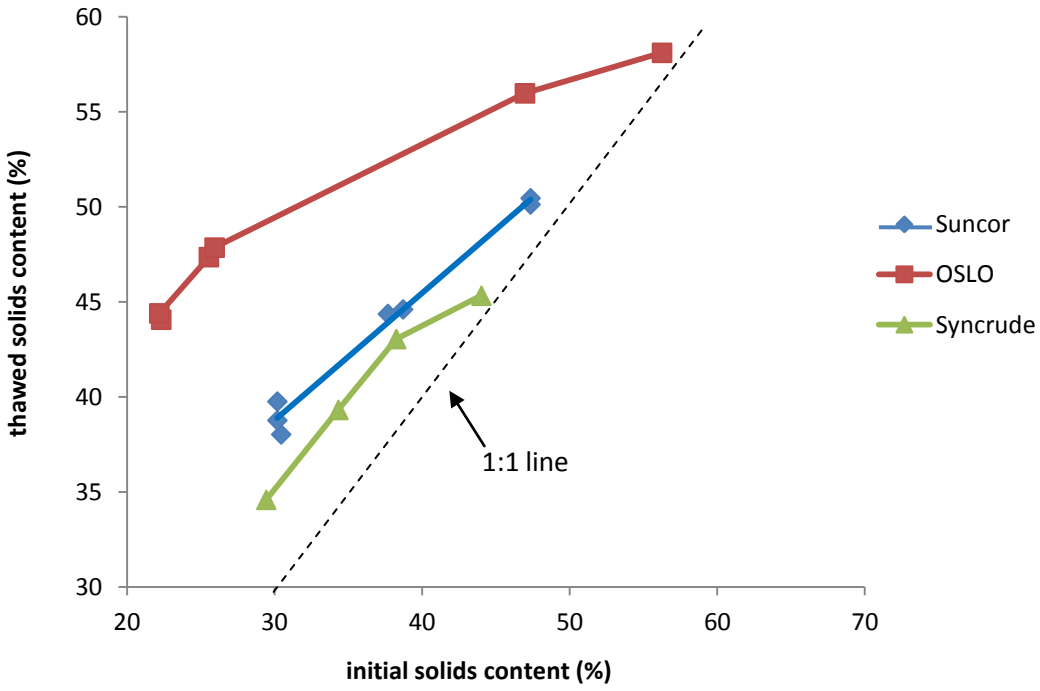

FIGURE 1.4 Thawed solids content of MFT (after Dawson 1994)

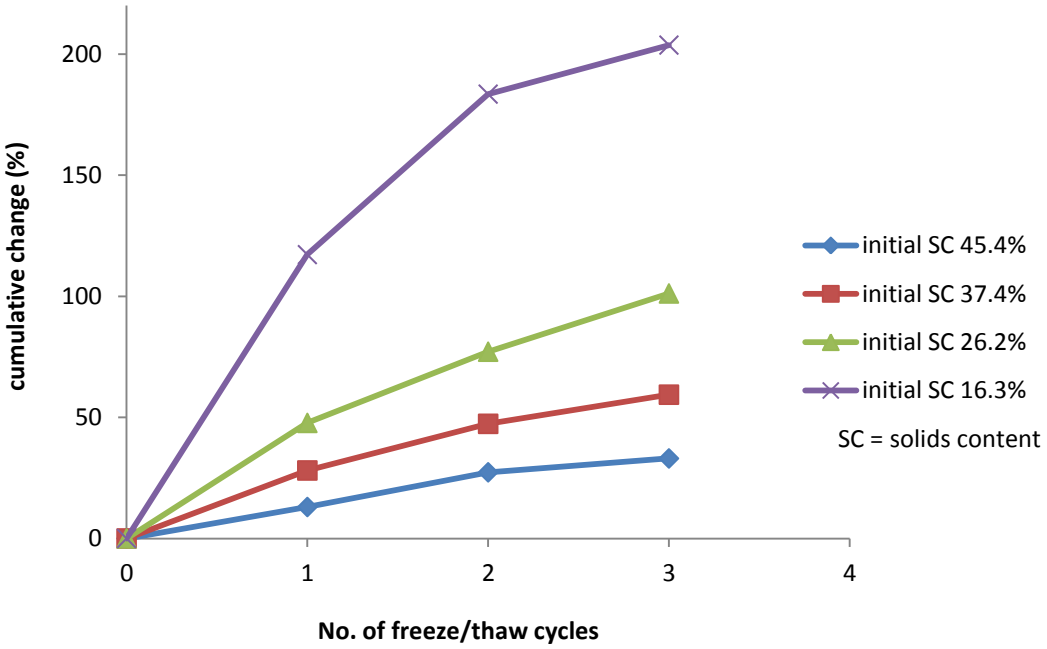

FIGURE 1.5 The cumulative increase in solid content through three freeze-thaw cycles (after Johnson et al. 1993)

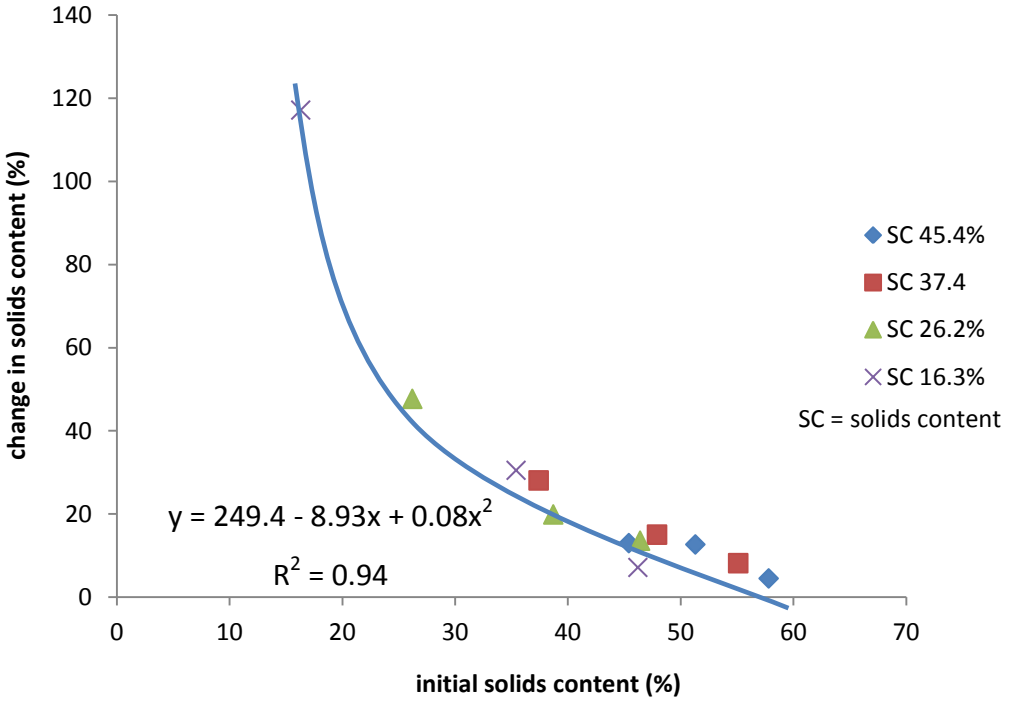

FIGURE 1.6 The change in solids content relative to initial solids content and freeze-thaw cycles (after Johnson et al. 1993)

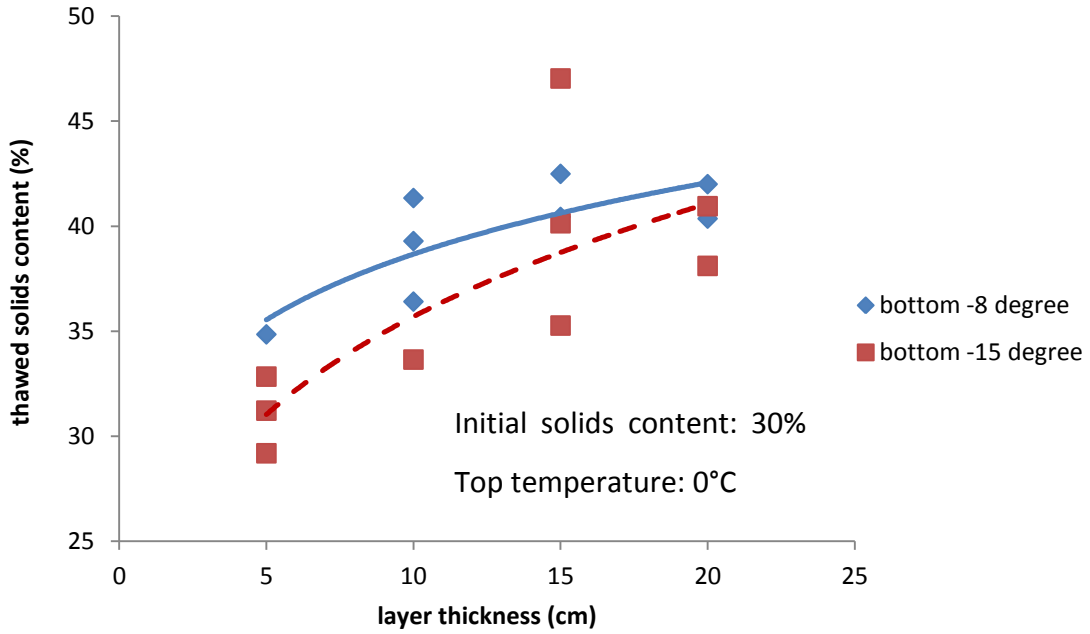

FIGURE 1.7 Thawed solids content of Syncrude MFT (after Sego and Dawson 1992)

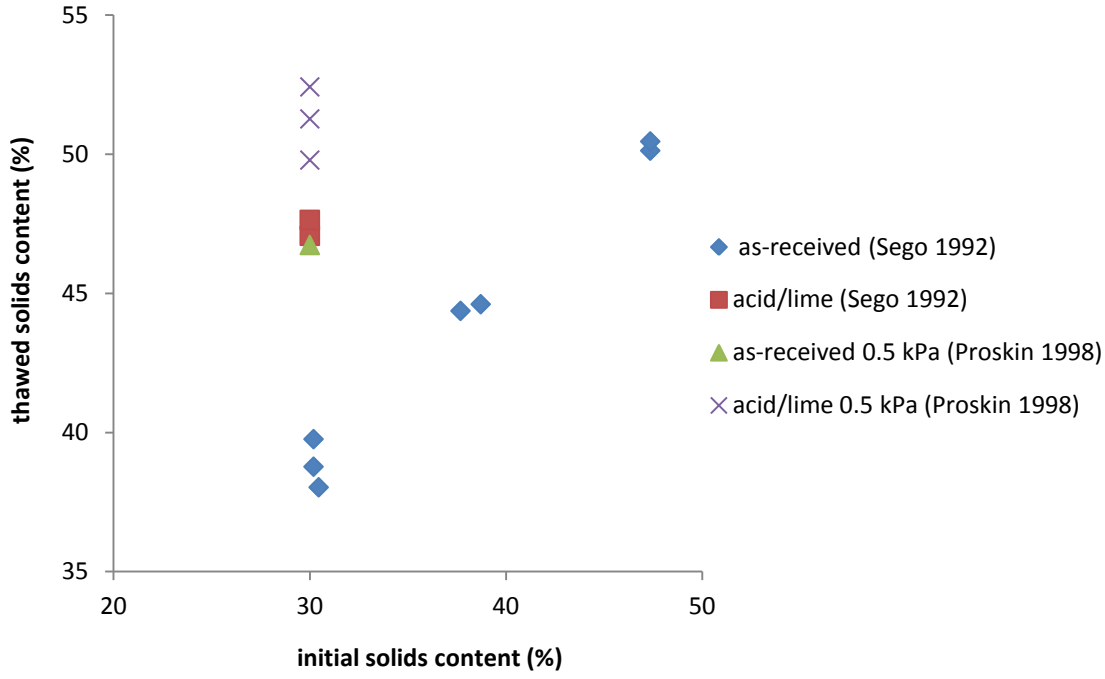

FIGURE 1.8 Effect of chemistry on thawed solids content of Suncor MFT

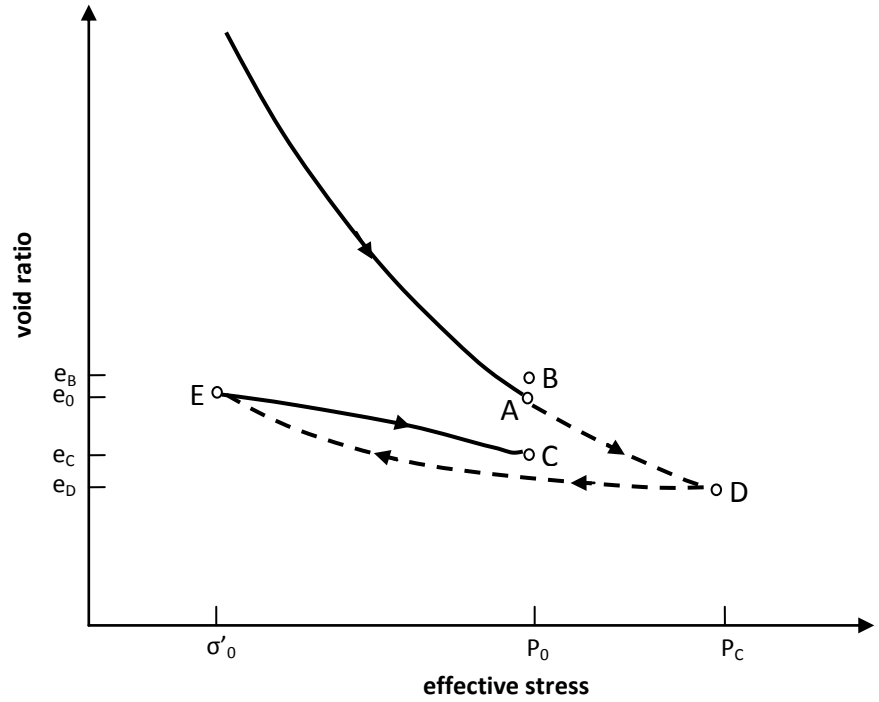

FIGURE 1.9 Stress path in a closed system freeze-thaw cycle (after Nixon and Morgenstern 1973)

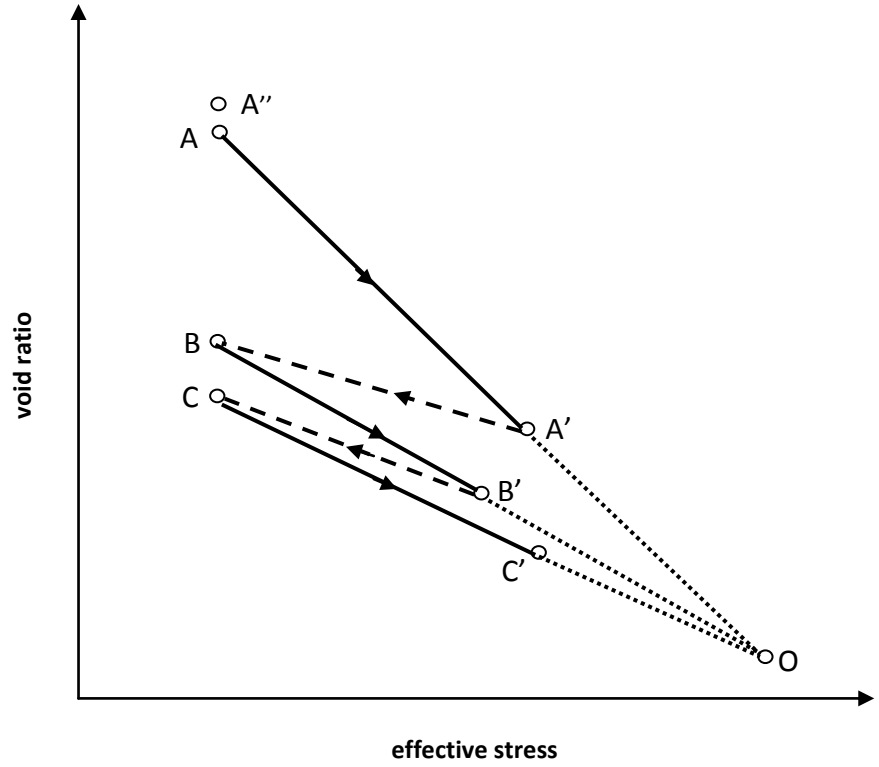

FIGURE 1.10 Stress path for multi-layer freeze-thaw (modified after Proskin 1998)

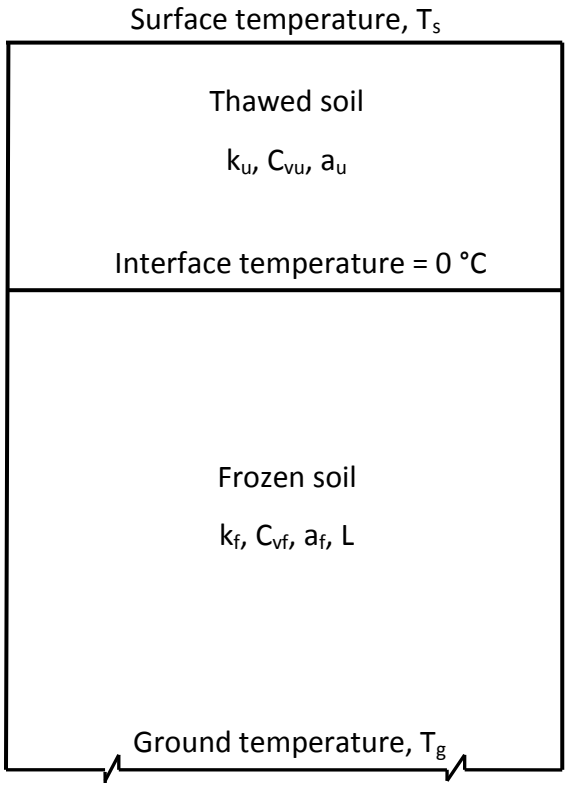

FIGURE 1.11 The Neumann problem (after Nixon and MacRoberts 1973)

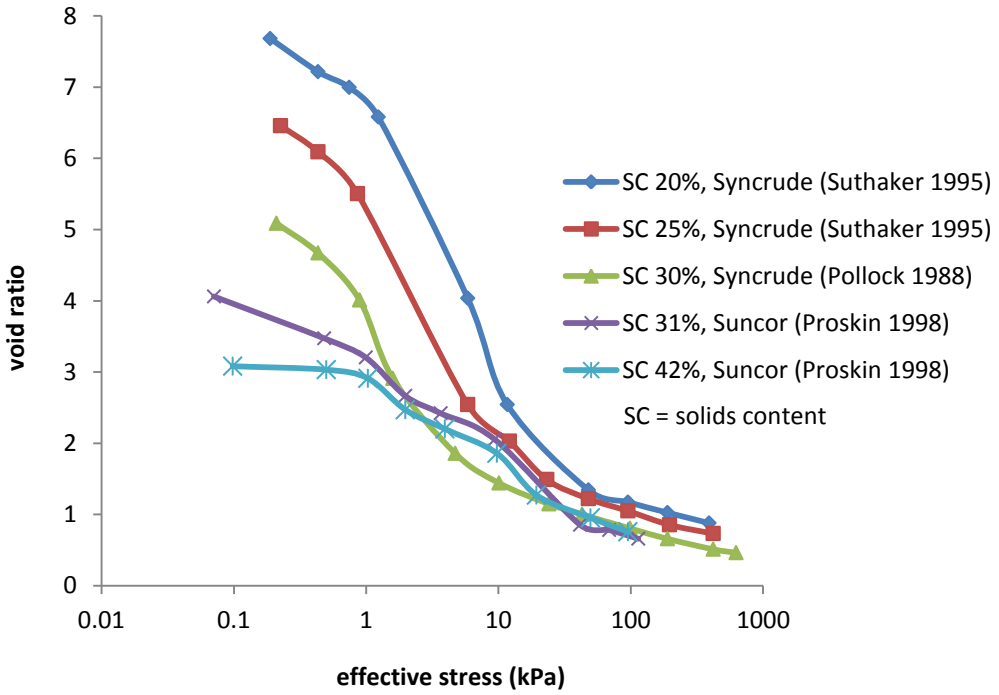

FIGURE 1.12 Compressibility curves for MFT with different initial solids content

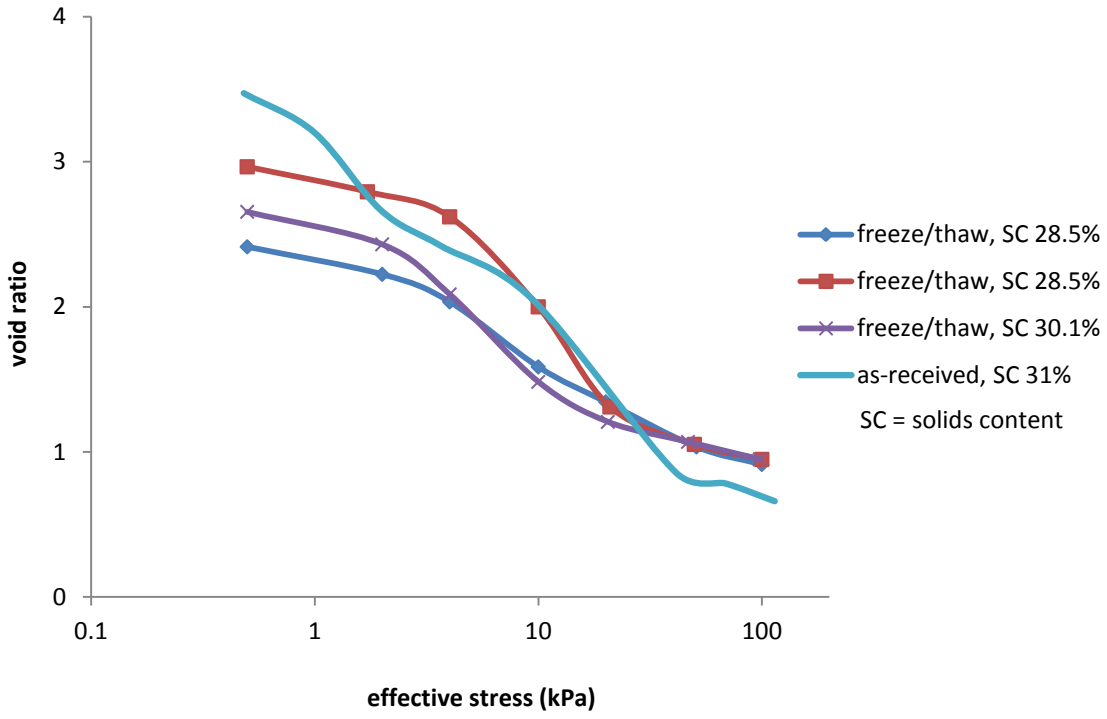

FIGURE 1.13 Compressibility curves for both as-received and frozen/thawed Suncor MFT (after Proskin 1998)

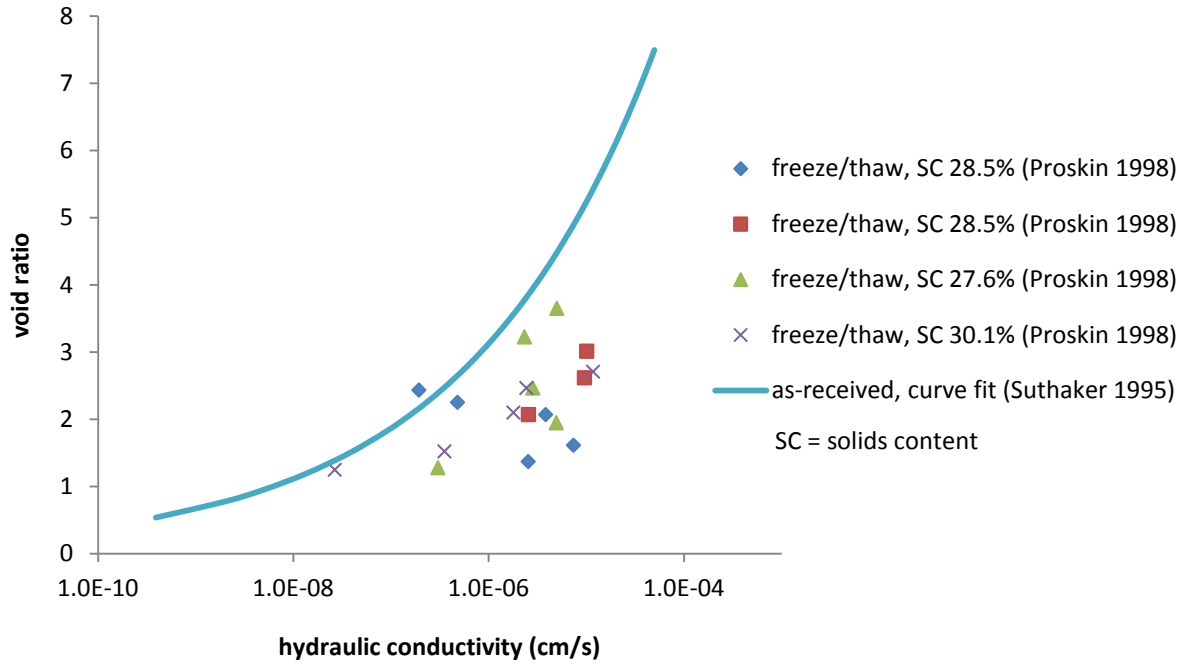

FIGURE 1.14 Effect of freeze-thaw on the permeability of MFT

CHAPTER 2

2. TEST MATERIALS AND PROCEDURES

2.1 Characterization of test materials in geotechnical perspective

Approximate 2000 liters of MFT was obtained at the depth of 7.5 m in Albain main pond by Geoforte Services Ltd., June 2008. The sampling location was Easting 465371 and Northing 6342304. On the same occasion, about 400-500 L of pond water was also collected. Part of the MFT and pond water was shipped to the University of Alberta for characterization and freeze-thaw dewatering investigation.

The basic properties of MFT, including water content, solids content, void ratio, bulk density, Atterberg limits, specific gravity, bitumen content, fines content, particle size distribution, and shear strength, were determined in accordance with ASTM standards. The brief procedures and results were described as follows. The water content was determined as 174% by oven-drying at 105°C for 24 hours (ASTM 2010a). The solids content, defined as the ratio of solids weight to total weight, was 36.6%. The void ratio was 4.35 by assuming degree of saturation is 100%. The density was determined as 1.29 Mg/m^3 by measuring the weight of MFT filled in a 1 L cylinder. The plastic limit equaled to 27%, liquid limit equaled to 54%, and liquid index was 5.4 (ASTM 2010b). The specific gravity was determined as 2.51 (ASTM 2010c). The bitumen content was defined as bitumen weight over solids weight. It was determined as 1.29% by removing the bitumen from small dry MFT lumps. Fines content was defined as the ratio of weight of solid particles passing sieve # 325 (D=45 μm) to weight of total solids. Wet sieving was used to determine the fines content as 99.8% (ASTM 2007). Hydrometer (152 H) test was adopted to determine the size distribution of dispersed MFT (Figure 2.1). Undrained shear strength of MFT was measured

using the BROOKFIELD DV-II+ programmable viscometer with spindle #73 at shear rate of 0.2 RPM (ASTM 2005). The peak undrained shear strength was 36.5 Pa and residual strength was 32.1 Pa.

2.2 Setups and procedures for the freezing tests

In order to examine the effect of freezing rate on dewatering of MFT, three samples were frozen with top boundary temperatures of -20°C, -10°C and -5°C, respectively. The top thawing temperature was set as 5°C. The bottom temperature stayed at 0°C throughout both freezing and thawing tests. Freezing lasted for 72 hours and thawing continued for 96 hours. Samples were allowed 50 days' post-thaw consolidation[1]. For the aim of examining the effect of post-thaw consolidation, one more sample with top freezing temperature of -5°C was tested without post-thaw consolidation. The solids content and shear strength profiles of all four samples were determined after freeze-thaw and post-thaw consolidation.

The freeze-thaw cells in Figure 2.2a were adopted to accommodate samples with height of 13.6 cm and diameter of 10 cm. Base plates and top caps applied boundary temperatures to the samples when connected with temperature control systems (BATHs). Cells were wrapped with insulation to ensure one dimensional thermal conduction. Plastic wrap was used to cover the caps to avoid any moisture loss. Freezing cells have no bottom drainage ports and water was only allowed to drain upwards. In order to eliminate radial thermal exchange with the environment, experiments were carried out in a walk-in freezer with temperature maintained between 0°C and 1°C.

The three samples were frozen one after another and thawed together in a series connection. Figure 2.2b shows the test setup during freezing of all three

[1] The author recommends 120 hours for self-weight consolidation. In this study, the author had to wait for 50 days to acquire the appropriate equipment for testing.

samples. Sample one was first frozen with a top temperature of -20°C. Then sample two was installed in a series connection and the temperature of top BATH was increased to -10°C. After sample two was frozen, sample three was connected and frozen with a top temperature of -5°C. Finally, all three samples were thawed with a top temperature of +5°C. The bottom temperature stayed at 0°C throughout the investigation. The freezing of each sample lasted for 72 hours to ensure the samples were thoroughly frozen. The time for thawing was chosen as 96 hours. Samples were conditioned for another 50 days for post-thaw self-weight consolidation. Sample four was tested separately with top freezing temperature of -5°C. No time was given for post-thaw consolidation.

At the end of the thawing/post-thaw consolidation, the thickness of decant water layer and underlying solids layer were measured. Surface water was removed by layer using a syringe and its solids content profile should be determined. Undrained shear strengths were measured using a programmable viscometer or manual vane shear machine (Serial 899) depending on the magnitude of shear strength. The viscometer measured shear strength smaller than 0.961 kPa by using spindle #74 (H=1.176 cm, D=0.589 cm) and spindle #75 (H=1.610 cm, D=0.803 cm) at a shear rate of 0.2 RPM. The manual vane shear machine was used to determine shear strength between 0.99 and 6.96 kPa by using spring #1 and self-designed spindle (D=19 mm, H=38 mm). Extension rods were manufactured for both machines to reach the lower part of samples. The torque induced by the stress around the spindle rod was also considered. It equaled the periphery area of rod multiplied by the residual strength along the rod. Test points distributed in a spiral style. The manual vane shear machine was used to determine the shear strength at lower part of sample two and three. The peak strength was obtained in accordance with ASTM D4648. Shear was continued for another five revolutions and then the residual strength was measured. The pointer and pointer carrier departed and stabilized to the rotating scale during this process. The deflection angle of spring for residual

strength equaled to the deflection angle of spring for peak strength minus the angle between the pointer and pointer carrier. Finally, specimens were sampled by layer to determine the solids content profile.

2.3 Investigation on consolidation behaviors of MFT

2.3.1 Conventional consolidation testing techniques

Znidarcic et al. (1984) reviewed existing consolidation testing procedures and analysis methods. According to different boundary and initial conditions, the consolidation tests included step loading (standard oedometer) test, constant rate of deformation test, controlled gradient test, constant rate of loading test, continuous loading test, relaxation test and seepage test. All tests except the seepage test employed consolidation theory and inversion process to estimate material properties. It limits their application only to soils with linear/ constant properties. The seepage test (Imai 1979) directly measures the compressibility versus void ratio and permeability versus void ratio. However, seepage forces during the test cause an effective stress difference within the slurry sample and therefore induce a non-uniform void ratio distribution. The final void ratio distribution is determined by slicing the sample. Rebound upon removing the seepage force also introduces errors in the final distribution of void ratio.

2.3.2 Conventional permeability testing techniques

As stated in the previous section, permeability can be determined by inversing consolidation theory and applying it to consolidation data. However, it is not appropriate for the permeability determination of MFT because of its non-linear behavior. The direct methods involve passing a permanent through the sample and monitor the flow rate, or hydraulic gradient induced. Pollock (1988) and Suthaker (1995) reviewed available direct permeability testing methods including constant head/ falling head test, flow pump test, restricted flow test,

and seepage test. Various drawbacks were found with specific techniques. A constant head test takes a very long time to complete on fine grained soils. The high hydraulic gradient in a falling head test could consolidate the MFT by seepage force. The pump capacity in a flow pump test is too large for the flow rate through MFT. Pore pressure transducers in restricted flow test are not precise enough to measure the small pore pressure difference. Rebound of sample during void ratio measurement makes seepage test less effective.

2.3.3 Finite strain consolidation tests and testing procedures

Slurry consolidometers (Figure 2.3) combined with a constant head permeability measuring system were used to investigate the finite strain consolidation behavior of MFT (Pollock 1988, Suthaker 1995, Proskin 1998). They accommodate much larger sample (e.g., D≥10 cm, H≥10 cm) to account for large deformation occurring during consolation. The step-loading technique directly obtains the relationship between effective stress and void ratio. In addition, the permeability test is conducted at the end of consolidation under each load increment. The constant head testing allows for application of small head difference. Upwards flow through the sample avoids seepage consolidation. The glass tube in the permeability test is sensitive to volume change as the permanent passes through the sample. Although slurry consolidometer tests can take up to one year, it is the most appropriate approach to study the consolidation behaviors of MFT.

Based on the experience of Pollock (1988) and Suthaker (1995), Proskin (1998) described his test procedures to determine the consolidation behaviors of Suncor MFT. The step loads were self-weight, 0.5, 2, 4, 10, 20, 50 and 100 kPa. The sample was first poured into the cell and consolidated under self-weight. To avoid squeezing of the sample, seepage forces were applied to consolidate the sample up to 4 kPa. Then air pressure was used to load the sample via a piston to

consolidate the sample until 100 kPa. The completion of primary consolidation was determined using the deformation curve. A constant head permeability tests were performed at the end of consolidation under each load increment.

2.3.4 Test setup and instrument calibration

The slurry consolidometer used by Proskin (1998) was modified in this study (Figure 2.4). It could measure not only deformation and permeability, but also excess pore pressure generated during consolidation. Drainage during consolidation could be either one-way or two-way. One-way drainage allows determination of excess pore pressure and two-way drainage enhances the consolidation process. The total head at the top and bottom of the specimen is identical during two-way drainage. Decant water accumulates on top of specimen as consolidation proceeds. Two layers of porous stones were attached beneath the PVC loading cap to keep the cap vertical. The top opening of consolidometer was covered with plastic wrap to avoid evaporation.

Gravity driven LVDT was used to measure real time deformation. Pore pressure transducer (5 psi) was chosen to measure pore pressure at the bottom of sample. Both were connected to data logging system together with air pressure transducer. The air pressure system was found to have a variation up to 1 kPa at pressure lower than 10 kPa. In order to ensure the precision of the loading, bellofram (12 square inches) was only used to apply higher load (≥10 kPa) on the sample. Dead weights were used for small loads (0.23 kPa to 4 kPa) and the buoyant weight of the PVC loading cap is 0.5 kPa. More specifically, a plastic porous plate with negligible buoyant weight was used as the loading cap for loads smaller than 0.5 kPa. A plastic platform was made to keep the dead weight (0.23 kPa) from interacting with the surface water (Figure 2.5). Based on the author's experience, two sets of steel discs in Figure 2.6 were designed to apply

2 and 4 kPa. These discs were added to the existing loading cap to eliminate any need to remove existing loads in the future.

The calibration of the gravity-driven LVDT was necessary for two reasons. First, the conversion factor from voltage to millimeter was required as input in the data recording software. Second, the LVDT only gave correct outputs if the induction needle stayed in certain range of the magnetic coil. This zone had to be located. To calibrate the LVDT, some small, flat objects with known thickness were prepared. The detail procedures were as follows: Fix LVDT in a stand and connect it with the data recording system. Let the needle go down to its end in the channel and mark the intersection as the starting point. Take a reading and put one object beneath the needle to change its position in the channel for another reading. Repeat the previous procedure to accumulate data. Plot the relationship between accumulated thickness (deformation) and the output readings (Figure 2.7). The linear calibration and its range were determined. The reciprocal of the slope of the linear line was input in the software. Mark the linear zone on the needle for use during testing.

Calibration sheets were supplied with the pore pressure transducers. Although conversion factors were directly used as input in the data recording system, any air bubble in the consolidometer system could introduce errors in the readings. Therefore, the saturation of the system and the effectiveness of the transducer were checked as follows. Mount transducer to consolidometer and connect transducer to the data recorder. Add pond water in the cell to get pressure readings and repeat. Plot the relationship between the applied pressure (depth of water multiply by unit weight of water) and output readings (Figure 2.8). Only if the slope of the curve is near 0.1, was the test considered reliable.

A calibrated loading ring was used to calibrate the loading system. The air pressure system and bellofram were considered as a whole. Place load ring under the loading bar of bellofram and apply load by adjusting the regulator.

Record the readings on the dial of loading ring (1 kg = 9.5 division) and from the software. Repeat to complete calibration. Convert the unit of division to kN and divide it by the cross section area of the cell to make the unit into kPa. Plot the relationship between the readings of load ring in kPa and the readings from data recording software (Figure 2.9). The slope of the line and the intercept were the conversion factors required during the test.

2.3.5 Test procedures for finite strain consolidation of as-received MFT

Saturation of the base plate and pore pressure transducer was first implemented. Assemble the base plate (Figure 2.10) and connect plastic tubes (0.5 m long). Turn off all three valves. Install the cell (main cylinder) on the base plate and fill it with pond water to one third of its height. Allow water to flow into the plastic tube by opening valve 1 and lowering plastic tube. Seal the end of tube with thumb and lift it up. Release thumb and let water flush back into cell. Repeat the flushing process until no air bubble was observed. Close valve 1 and open valve 2. Flush the air bubbles in the line. Close valve 2 and switch the cross-connector to raise the nut higher. Remove the nut and let water flow. Tap the connector to help in de-airing. Tighten the nut once no air bubbles were observed. Open valve 3 and flush air bubbles. Finally, refill the cell and repeat the whole saturation process for base plate. Before the installation of pore pressure transducer, drip pond water in the port of transducer using an eye dropper. Use a bended copper wire (no sharp tip) to stir in the port of transducer and release air-bubbles. Switch port 3 upwards and open valve 3. Mount the transducer at port 3 right after the flow appeared and close valve 3.

Boil porous stone with pond water to saturate. Cut filter paper to a diameter about two millimeters larger than that of porous stone. Siphon the water in the cell off and remove the cell. Drip water on top surface of base plate to form a water arc. Smear porous stone in from side and add more water on top. Dip the

filter paper in pond water and place it on porous stone with no air bubbles beneath it. Smear grease on base part of the cell and re-install it. The periphery of filter paper was between the cell and side of base plate. The calibration of pore pressure transducer was ready to be performed by adding pond water in cell. Once the calibration was completed, remove the water left in the cell and prepare for consolidation test.

Thoroughly mix the as-received MFT in the pail and pour it into the cell by layer using a funnel. Mix MFT with steel bar (no sharp tip) after each layer to eliminate air bubbles. When the specimen reached the height of 13 cm, place filter paper (diameter was 1 mm smaller than cell) on top. Screw LVDT needle into the plastic porous plate. Hold the needle and keep the plate a little bit above the filter paper. Fix the main body of LVDT in a stand and adjust position to ensure in effective range. Freely drop the needle and let the plate contact the specimen. Add pond water in the cell until it reached the top side port. Fill up the plastic tubes and connect one (valve 1) to the top port for two-way drainage during consolidation. Connect the other one (valve 2) with glass tube (filled with pond water) and tap both the plastic and glass tubes to drive air bubbles out. Fix the glass tube on a stand for permeability tests. The water meniscus in glass tube must be far enough to the opening end and adhesive tape was placed to partially seal the opening to reduce evaporation. Another approach was to add corn oil to prevent evaporation. Cover the top opening of cell with plastic wrap and open valve 3 to measure pore pressure. Finally, initiate the data logging system to collect data for self-weight consolidation.

One specimen was specifically prepared for investigating self-weight consolidation as the process takes months to complete. Another three specimens were prepared in one week interval to investigate consolidation under load increments from 0.5 to 100 kPa. The effect of self-weight

consolidation was considered in the interpretation of results from these three consolidation tests.

Bearing capacity of remolded MFT in consolidometer is less than 0.23 kPa. A period of one week was given for MFT to gain strength under two-way drainage. A transitional load of 0.23 kPa was added before the application of PVC loading cap (0.5 kPa). When deformation was small, valve 1 was turned off and 0.23 kPa load was removed. Negligible rebound was measured. Remove the surface water, LVDT and plastic porous plate in sequence. Change the data recording interval to 5 seconds. Fix upper portion of cell on main cylinder and hang the PVC loading cap above the filter paper. Porous stones were saturated in advance and upper portion was used to keep the loading cap from tilting (Figure 2.11). Adjust the position of LVDT to contact the loading cap and then slowly lower the cap to contact the sample. Add surface water back in cell. After pore pressure reached its peak value, open valve 1 for two-way drainage. Change the data recording interval back to 1 hour. When slope of the deformation curve approached horizontal, valve 1 was closed for excess pore pressure determination. Excess pore pressure was the difference between pore pressures measured during one-way drainage and two-way drainage. The end of consolidation was determined based on the deformation versus time curve, deformation versus log time curve, rectangular hyperbola method and value of excess pore pressure. These methods will be discussed in detailed at the end of this chapter.

A permeability test was performed at the end of consolidation. The height of water surface in the cell relative to bench surface and the thickness of sample were measured/ calculated. The height of glass tube was then determined to create a constant hydraulic gradient $i = 0.5$. The reasons for selection $i = 0.5$ are discussed in Chapter 3. A leveler was used to adjust the glass tube to horizontal. Close valve 3 and open valve 2 to start permeability measurement. The flow velocity was faster at the beginning and then stabilized with time. The

time interval for each reading was the time for water to move 5 mm in the glass tube. Three stable readings were necessary to establish an average permeability. Finally, close valve 2, open valve 3 and convert the permeability to its value at 20°C. The water level in cell may change due to the lowering of loading cap or evaporation. It should be adjusted a few days before the permeability test as the pore pressure requires time to respond. So far, the consolidation and permeability tests under 0.5 kPa were accomplished.

The next step in consolidation test was to apply overburden load of 2 kPa. First change the data recording interval to 5 seconds. Lift weight No. 1 with threaded rod and place the needle of LVDT on it by adjusting its position. Slowly lower the weight onto the specimen. When pore pressure reached its peak, remove the threaded rod. Then open valve 1 and change the time interval to 1 hour. The following steps were basically the same as those in the previous paragraphs. Similarly, conduct consolidation under 4 kPa by adding weight No.2. After measuring permeability, remove top cell and move consolidometer into the loading frame with bellofram loading system. Raise consolidometer close to the bellofram bar as the bar has only 4 cm of travel. Apply additional air pressure of 6 kPa to achieve a total of 10 kPa overburden. The rest of test was carried out following procedures mentioned above. In addition, incremental loads 20 kPa, 50 kPa and 100 kPa were also applied to investigate the compressibility and permeability. If necessary, adjust water level in the cell by lowering the attached plastic tube to lower side port to ensure water does not interact with weights.

At the end of the test, unload and siphon surface water off through side ports. If squeezing occurs, collect the MFT on porous stone and measure its dry weight and solids content to back-calculate the height. Perform manual vane shear test at the center of specimen. Solids content profile was measured by slicing the specimen.

2.3.6 Test setup and procedures for freeze-thaw and post-thaw consolidation tests

Proskin (1998) carried out freeze-thaw and post-thaw consolidation tests on Suncor MFT. Samples were first frozen in the freeze/thaw cells. Then they were removed and trimmed in the frozen state. To ensure the sample surface was level, the first load increment was 0.5 kPa instead of self-weight. The remainder of the test followed procedures as outlined for consolidation of as-received samples.

The freeze/thaw consolidometer shown in Figure 2.12 was first used to investigate the freeze/thaw strain of MFT. It can accommodate a sample with a height of 13 cm and a diameter of 10 cm. Both top and bottom plates can be maintained at constant temperatures to freeze/thaw sample in the consolidometer. The strain during freezing and thaw strain were measured. The air chamber was used to transfer air pressure onto sample. Top side port was open during consolidation to avoid any air pressure generated in the space between rolling diaphragm and sample. Stainless wire supported the LVDT needle for displacement measurement. Insulation was wrapped around the cell to minimize radial thermal conduction. Two thermal BATHs were connected to provide constant temperature boundary. Tests were performed in a walk-in freezer kept at 0 to 1°C. Consolidometers and samples were placed in the freezer for a couple of days before the tests started. A pore pressure transducer, air-pressure regulator and data logging system were also used.

Besides similar preparation work as before, tightness of air chamber was also examined. Assemble the consolidometer and connect the air pressure system. Fill the residual space in base cell with pond water and apply air pressure up to 100 kPa. Observe if any air bubble generated.

Pour and stir pre-mixed MFT by layer until 13 cm was placed. Place filter paper on top. Mount the top part on base cell and smear grease on connections where air leakage may occur. The top freezing plate (no porous stone) was held a little bit above the sample using stainless wire. Then the stainless wire was fixed by a clamp. The plate cannot fall down but it can move up under uplift pressure during freezing. Ensure the rolling diaphragm folded properly without wrinkles. Connect consolidometers to BATHs and set top BATH temperature as -15°C and bottom BATH temperature as -5°C. Install LVDT and initiate the data recording software with time interval of 5 seconds. When the top BATH decreased to -15°C, and the top plate was lowered to contact the sample. Change the time interval to one hour after a few minutes. Wait three days to freeze the sample thoroughly. Take displacement data during the freezing process.

Set the top BATH to 30°C and lift the top plate once it was possible. Turn off top BATH and take off top part of the consolidometer. Mount porous stone on the top plate with gaskets in between to create gap as a drainage channel. Re-install the consolidomter and add some surface water. Tilt the cell to exclude trapped air bubble and then add more water to the height of side drainage port. Clamp the top plate and set the top BATH to 5°C and bottom BATH to 0°C. Thaw the sample for four days and then give another 120 hours for self-weight consolidation. Finally, measure sample height to determine thaw strain.

Although the overall solids content increased, the MFT near the surface was too weak to support the top plate. The buoyant weight of top plate under test condition was determined to be 1.3 kPa. A spring was placed between the clamp and the cap of consolidometer to offset some weight. Start pore pressure and displacement recording. The spring was then released little by little every day to exert larger load to the sample. Finally, remove the spring and let the sample consolidate under 1.3 kPa. At the end of consolidation, perform permeability test under hydraulic gradient $i = 0.5$. Connect air pressure system to

consolidometer and apply additional 2.7 kPa air pressure to consolidate sample at 4 kPa. Take permeability measurement after consolidation. Repeat the same procedures for consolidation and permeability tests under overburden pressure of 10 kPa, 20 kPa, 50 kPa and 100 kPa. Unload the specimen and remove surface water and top part of consolidometer. Run vane shear test in the middle of sample and obtain the solids content profile.

2.4 Methods of determining the end of primary consolidation

Curve fitting methods are capable of determining the end of primary consolidation in conventional consolidation tests. They are based on the similarities with Terzaghi's consolidation curve, among which square root time method and log time method are the most popular ones in practice. Pollock (1988) and Suthaker (1995) used the log time method to predict the end of primary consolidation for MFT. The method was effective at higher load increments, while no definite deflection point was observed at small load steps (Figure 2.13). The consolidation was stopped before displacement leveled out, since void ratio barely changed in the 10^4 minutes log cycle. The rectangular hyperbolic method (Sridharan & Sreepada 1981, Sridharan et al. 1987) is another curve fitting method applicable for all types of compression curves. It is based on relationship between time factor T and degree of consolidation U which can be represented by a rectangular hyperbola for consolidation from 60% to 90%. Hence, the magnitude of primary consolidation can be determined base on the similarities of the theoretical T/U versus T and the experimental t/δ versus t. Furthermore, deformation rate can also indicate the end of primary consolidation. The primary consolidation is near its end when deformation rate becomes negligible.

In addition to volume reduction, primary consolidation is also known as a process of excess pore pressure dissipation. Properly measuring the pore

pressure not only gives a direct indication of the state of consolidation, but also saves time to determine the end of consolidation with MFT. It is preferred to use it together with the above mentioned methods. When the displacement curve or any of the curve fitting methods implies the completion of primary consolidation, measure the excess pore pressure by switching to one-way drainage. If the excess pore pressure determined is less than the excess pore pressure ($\gamma_w \Delta h$) applied in the permeability test, it is at the end of primary consolidation.

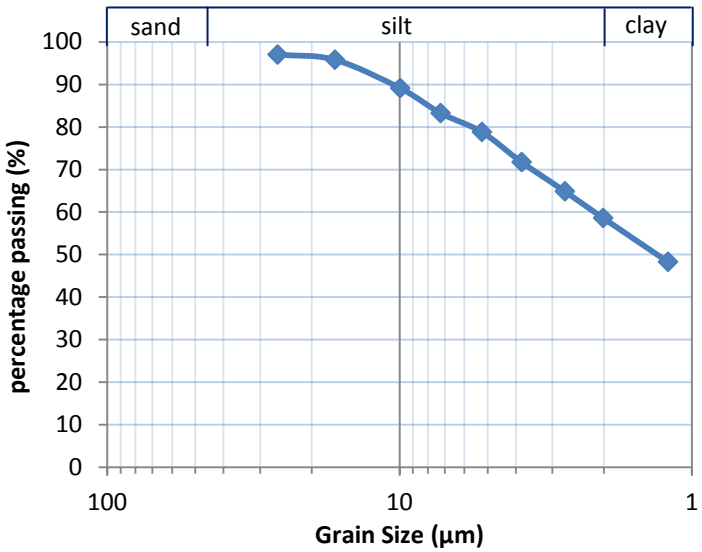

FIGURE 2.1 Size distribution of dispersed Albian MFT at 7.5 m

(a) Freeze/thaw cells

(b) Test setup during freezing of all three samples

FIGURE 2.2 Test setup of freezing tests

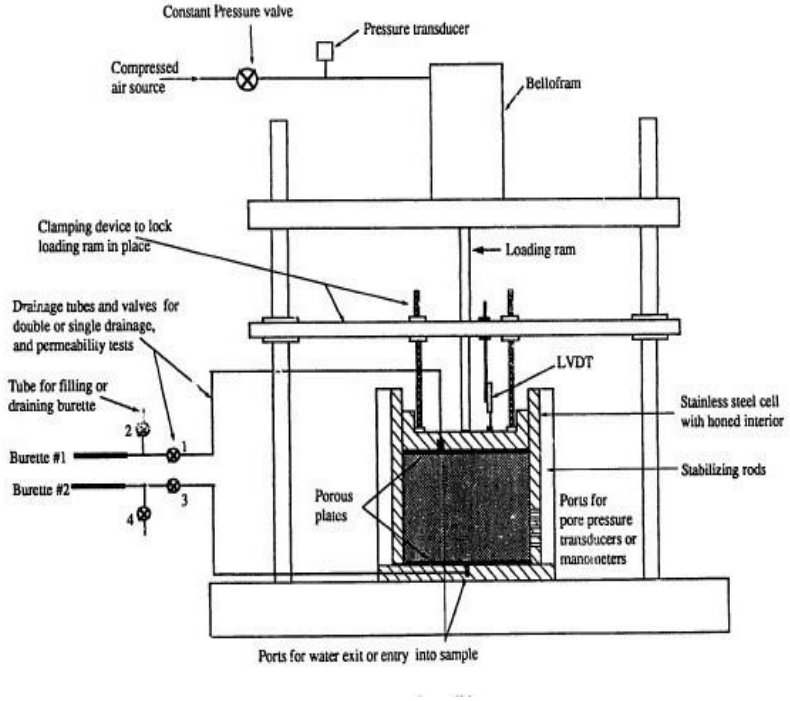

(a) Slurry consolidometer one (after Pollock 1988 and Suthaker 1995)

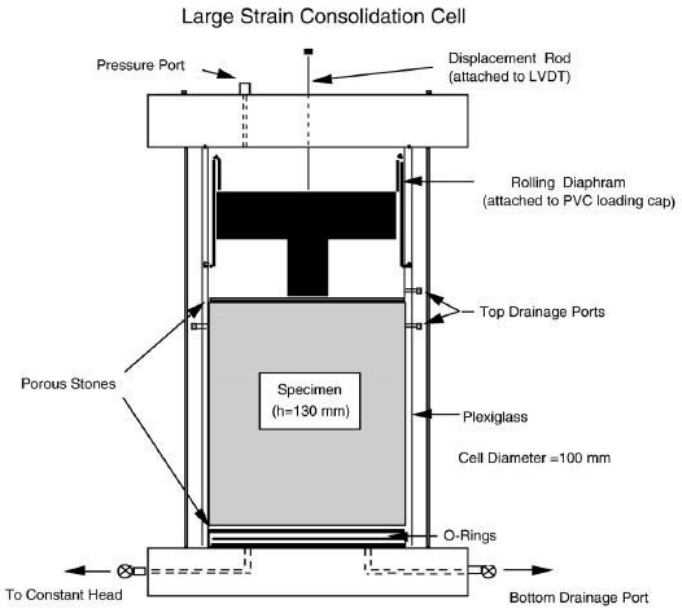

(b) Slurry consolidometer two (after Proskin 1998)

FIGURE 2.3 Slurry consolidometers used by previous researchers

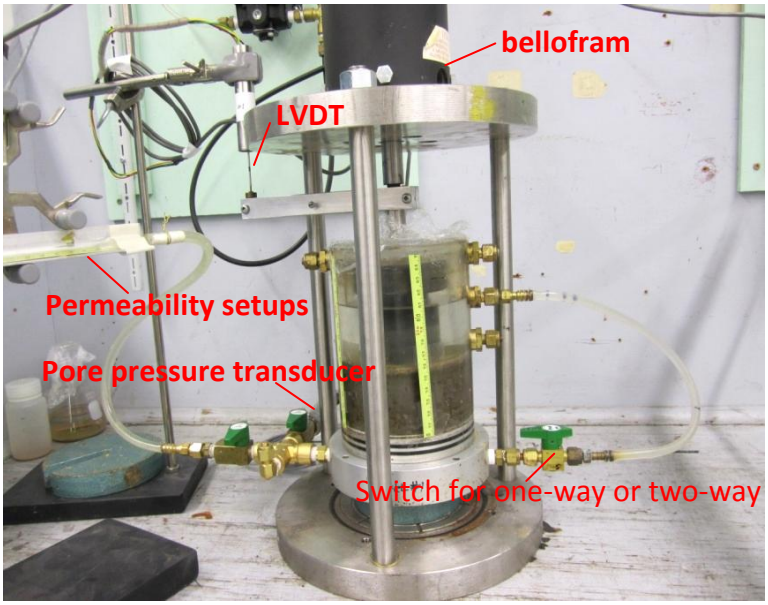

FIGURE 2.4 Modified slurry consolidometer

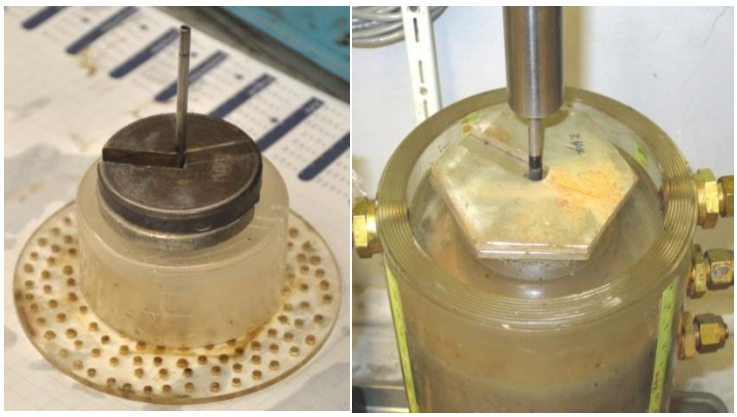

FIGURE 2.5 Apparatus to apply overburden of 0.23 kPa

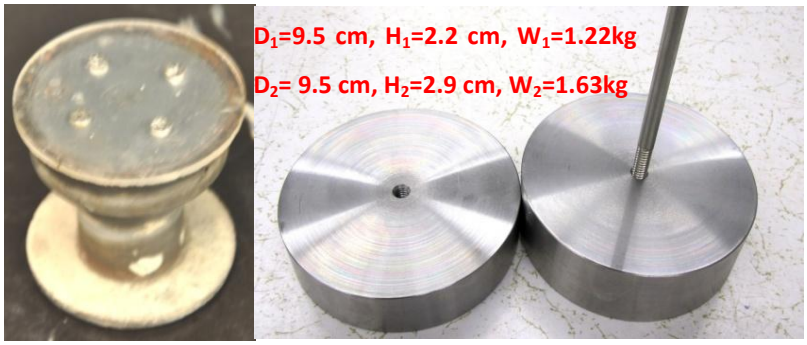

FIGURE 2.6 Weights to apply overburdens of 0.5 kPa, 2 kPa and 4 kPa

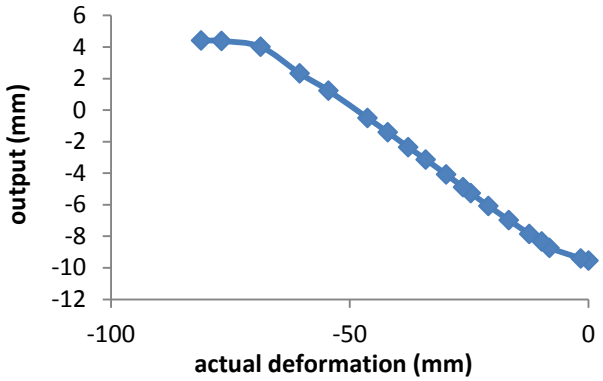

(a) Calibration of LVDT # 3 (Gain=1, offset=0)

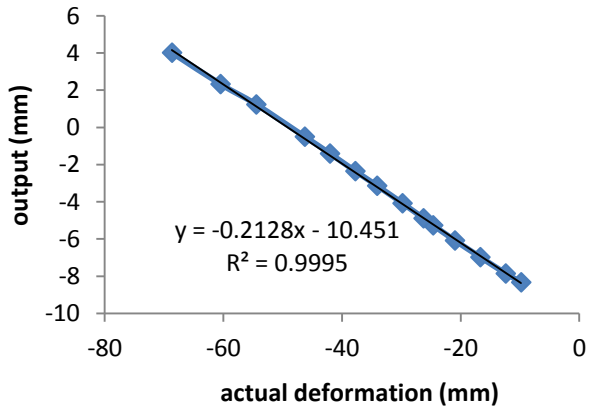

(b) Linear part of the above calibration curve (Gain=1, offset=0)

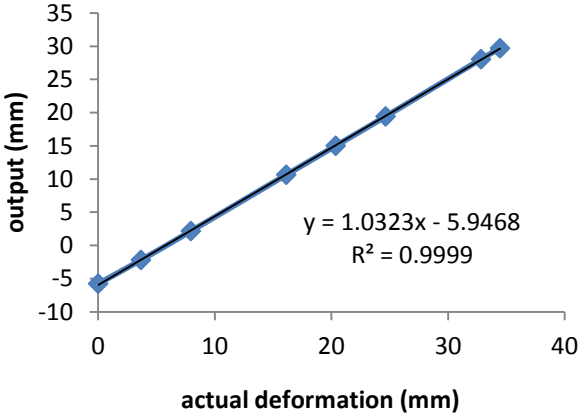

(c) Calibration of LVDT # 3 (Gain=-4.6992, offset=0)

FIGURE 2.7 Procedures for calibration of LVDT

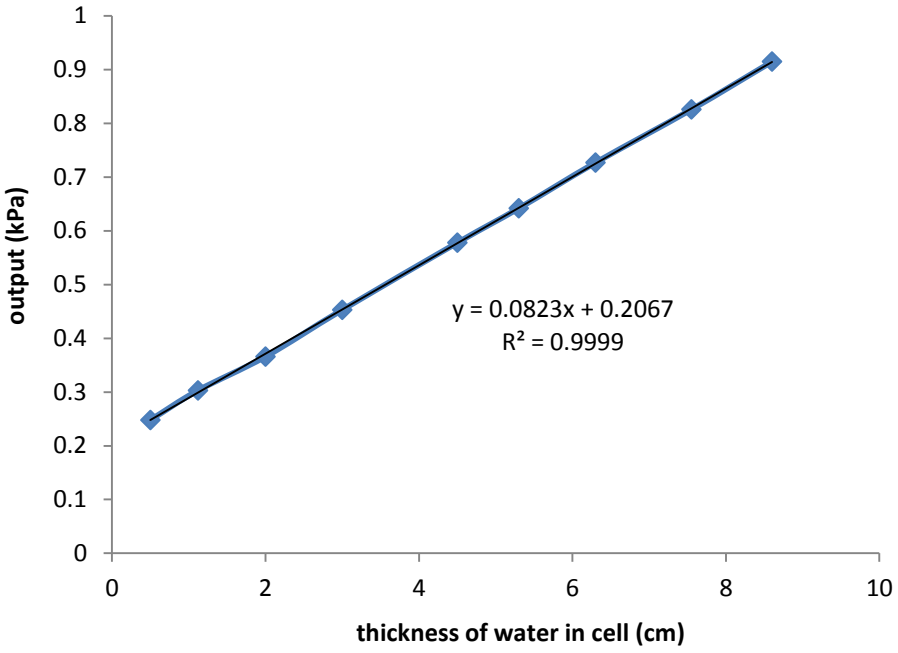

FIGURE 2.8 Calibration of pore pressure transducer # 416631 (Gain=344, offset=7.104)

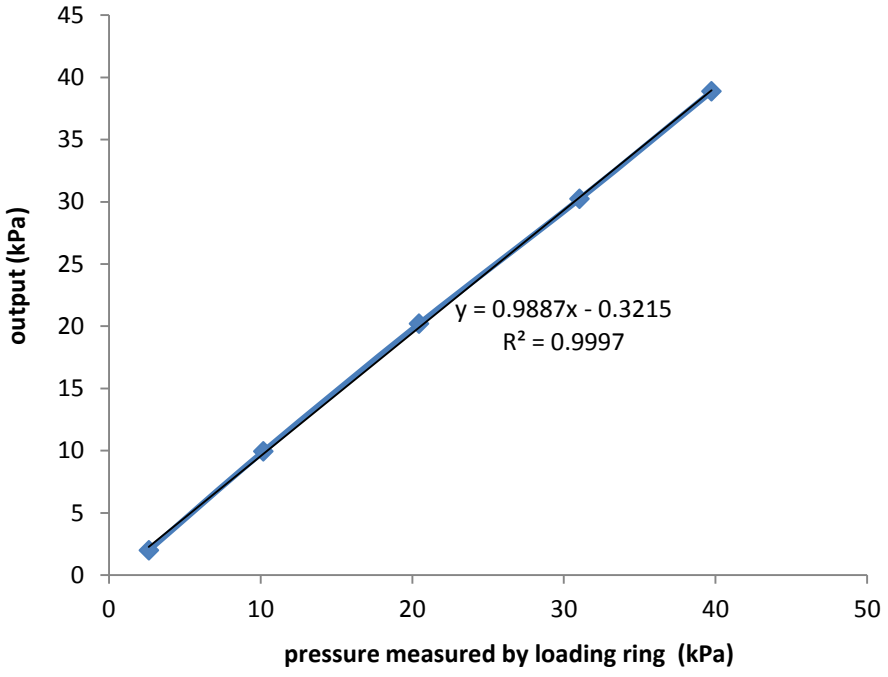

FIGURE 2.9 Calibration of air-pressure loading system (Gain=1323.452, offset=-11.5)

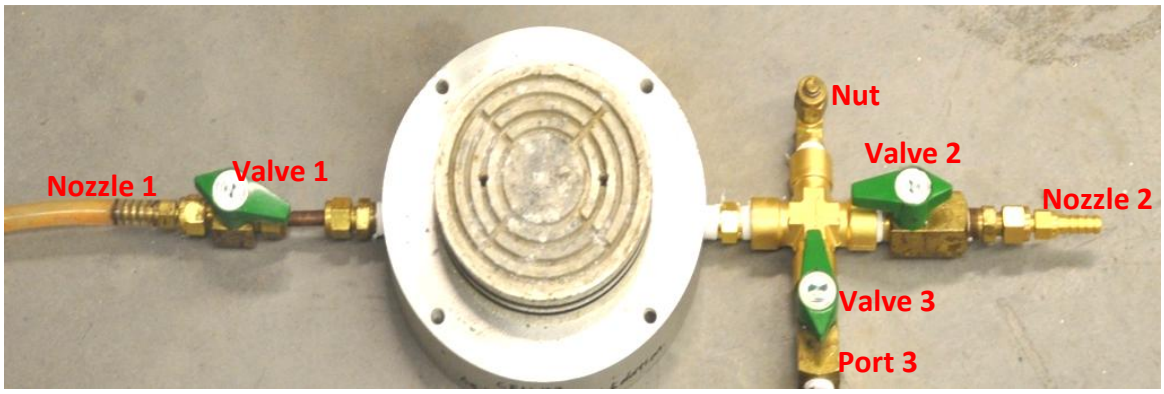

FIGURE 2.10 Design of base plate

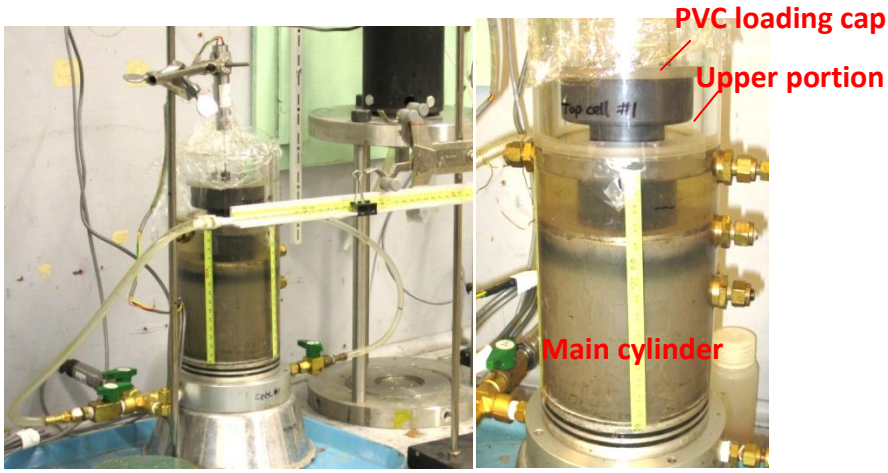

FIGURE 2.11 Consolidometer setup at 0.5 kPa

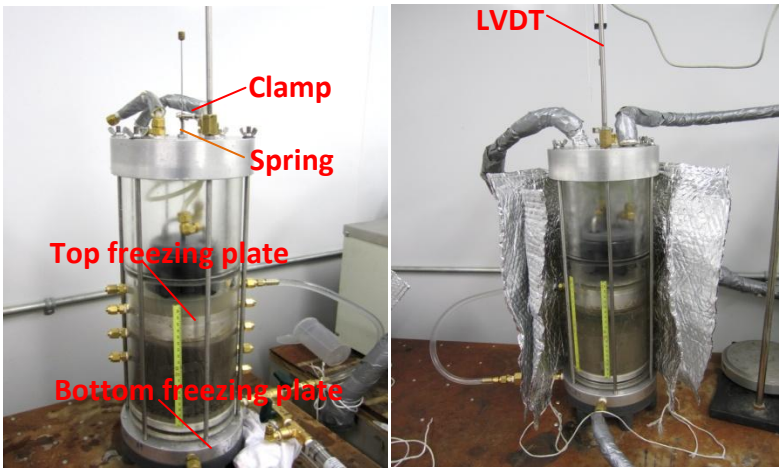

FIGURE 2.12 Freeze/thaw consolidometer

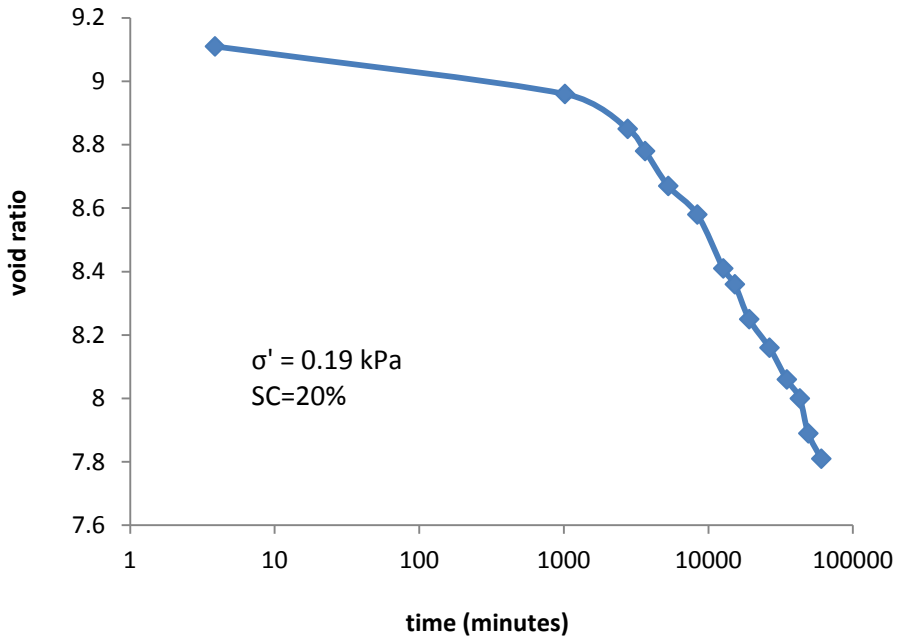

FIGURE 2.13 Deformation curve for Syncrude MFT (after Pollock 1988)

CHAPTER 3

3. TEST RESULTS AND DISCUSSION

3.1 Methods of determining the coefficient of consolidation

The coefficient of consolidation (c_v) implies the rate of consolidation and can be used to predict the consolidation progress of MFT. It is defined as the ratio of permeability (k) to the product of coefficient of volume compressibility (m_v) and unit weight of water (γ_w). The relationships of permeability versus void ratio and effective stress versus void ratio are obtained during the finite strain consolidation tests. The coefficient of volume compressibility (m_v) is estimated as the ratio of the slope of the compressibility curve to the summation of corresponding void ratio and one. Knowing the permeability, the coefficient of consolidation is determined at specific void ratio. In addition, the coefficient of consolidation can also be obtained using curve fitting methods. However, its reliability requires to be checked.

3.2 Selection of proper hydraulic gradient in permeability test

Suthaker (1995) examined the effect of hydraulic gradient on the measured permeability of MFT at the end of consolidation (Figure 3.1). The permeability values were found similar when the hydraulic gradient was less than 0.2, but started to decrease once the hydraulic gradient went beyond 0.2. However, the effect diminished at lower void ratios. Finally, she recommended running permeability test at hydraulic gradient of 0.2.

The heights of the water surface in the consolidometer and the axis of glass tube were simply measured by a ruler with a leveler. The accuracy was questionable if the head difference was too small. In addition, the dissipation rate of excess pore pressure became smaller as the consolidation proceeded. The permeability

can only be initiated when the excess pore pressure was smaller than the applied hydraulic pressure. Much unnecessary time was required for this tiny excess pore pressure to dissipate. Furthermore, the volume of flow through sample should be sufficient to be observed in the glass tube. It took several more days to complete the permeability test under low hydraulic gradient. Also, the evaporation of water in glass tube must be accounted for. Finally, the air-pressure loading system was not stable. The changes in total stress induced variation in pore pressure and sometimes interrupted the permeability test. The effect of variation in pore pressure was relative smaller at larger hydraulic gradient condition. By balancing these factors, a hydraulic gradient of 0.2 was used to measure the permeability at the end of self-weight consolidation. A hydraulic gradient of 0.5 was used to measure the permeability at other stress levels.

The permeability tests were performed from low to high hydraulic gradient during the investigation of the effect of hydraulic gradients. Much less time was required for pore pressure redistribution in this sequence, because pore pressure gaining is much faster than pore pressure dissipation.

3.3 Freezing rate investigation

3.3.1 Results for freezing tests

Samples were separated into a clear aqueous layer and a lower soil layer during thawing and post-thaw consolidation. The final sample height was approximately 9.3 cm and thaw strain was about 36% for those three samples experienced both freeze-thaw and post-thaw self-weight consolidation. The final height was 10.1 cm and the thaw strain was 30.5% for sample four, which were measured at the end of thawing without any additional self-weight consolidation.

Figure 3.2 shows the solids content profiles of MFT before freezing, upon completion of thawing, and after post-thaw consolidation. Profiles of the four samples were enhanced by freeze/thaw. Sample one (top freezing temperature -20°C) and sample two (top freezing temperature -10°C) had similar solids content profiles. Solids content first increased linearly till 4.8 cm and then remained nearly constant to 8 cm. A sudden increase in solids content occurred at the bottom. Sample three was frozen under a lower rate with top temperature of -5°C. The solids content followed the same trend as that of sample one and two, but was higher. The concave part of the curve between 3.7 and 6.7 cm was due to backfill of water[2]. Sample four (-5°C A) was frozen under the same temperature boundary as sample three. The solids content profile was similar as that of sample three till 4.0 cm, and then it decreased with depth.

Figure 3.3 shows the undrained shear strength profiles measured before freezing, upon completion of thawing, and after post-thaw consolidation. Shear strength of the four samples were higher than that of as-received sample. The shear strength profiles of sample one (-20°C), sample two (-10°C), and sample three (-5°C) demonstrate that the higher the freezing rate, the lower the shear strength measured. More specifically, the profiles were close to 3.3 cm and then departed. Shear strength of sample one increased gradually with depth. Shear strength of sample three increased most sharply and reached 1.2 kPa at the bottom. Shear strength of sample four (-5°C A) was the lowest among the four samples. It was almost constant along with depth.

[2] The sample was tested using a viscometer after thawing. However, the strength of MFT was beyond the range of the viscometer. A manual vane shear machine was considered to be used. Some specimen was brought out with the spindle and a channel created. Surface Water was filled back and decreased the solids content at the location occupied by the spindle.

Figure 3.4 presents the relationship between undrained shear strength and solids content for frozen/thawed samples and as-received samples. The shear strengths of frozen/thawed samples were higher than that of as-received samples. In addition, the curves for different frozen/thawed samples were close and followed the same trend. Their shear strength increased slowly till the solids content reached 50%, then the increasing rate became much faster.

3.3.2 Discussion on freezing rate investigation

Freezing induces fractures and over-consolidated soil peds form between the ice-filled fractures. The soil peds settle under self-weight upon thawing and the fractures behave as flow channels to drain water. The top part of MFT thawed first while the lower part was still frozen. The frozen MFT prevented any water from flowing downwards. No drainage port was on the base plate of freeze/thaw cell. Therefore, one way drainage was only allowed both during thawing and post-thaw consolidation. Released water gathered on top of the MFT. The total volume of surface water and final MFT sample equaled the volume of sample before freezing. Sample one, sample two and sample three had approximately 36% thaw strain during thawing and post-thaw consolidation. Sample four experienced 30.5% thaw strain during thawing. The 50 days post-thaw consolidation accounted for the additional 5.5% strain after thawing. Thus, 84.7% thaw strain occurred during thawing and 15.3% thaw strain occurred after thaw via self-weight consolidation.

The solids profile of sample four in Figure 3.2 shows that solids content first increased and then decreased below 4 cm. The solids content profile above 4 cm was similar as that of sample three, which meant the self-weight consolidation occurred as it thawed. The solids content profile of sample four indicates more time (e.g., 120 hours) was required to complete the self-weight consolidation as the solids content was lower below 4 cm. The solids content of sample four at

8.2 cm was 39%, and thus the solids content at 10 cm was expected to be about 36.6%. It implies that 96 hours is a proper thawing time in this investigation. Solids content and shear strength of sample one and sample three were smaller and closer at the upper part than those at the lower part (Figure 3.2 and Figure 3.3). Freezing rate and effective stress were responsible for this phenomenon. The initial temperature of MFT was 0°C before freezing. It took time to achieve a linear temperature distribution with depth. The top part of samples experienced a higher freezing rate. A higher freezing rate froze most pore water in place and ice crystals retarded water from flowing to the freezing front, while lower freezing rate allowed water flow to the freezing front resulting in consolidation of the MFT. In addition, the effective stress was lower in upper part upon the completion of post-thaw self-weight consolidation. Therefore, the upper part of the samples had lower solids content and shear strength. On the other hand, the temperature gradient on sample surface was theoretically infinite by large for both samples and no difference in freezing rate was expected at the beginning of freezing. Along with the stabilization of temperature, the effect of freezing temperature became larger as the temperature gradients were finite and comparable. Shear strength of sample four was lower than that of sample one although its solids content was higher in the upper part. The thixotropic strength gained with time may be the cause of this phenomenon.

Solids content of sample one was expected to be smaller than that of sample two (Figure 3.2). The cause to similar solids content profiles was the errors induced by the balance. Initial negative readings were found on balance before adding wet weights of sample two while they were not recorded. The measured solids content of sample two was therefore smaller than it was. The differences in solids content profiles in Figure 3.2 indicate the final sample heights should not be the same for sample one, sample two and sample three. Since the sample surface was not level after thaw, errors existed in the determination of sample

heights. A light porous plate and filter paper are recommended to place on top of sample to ensure the surface is level during the test.

As shown in Figure 3.4, the shear strengths of frozen/thawed samples were higher than that of as-received samples. Considering the errors in determining the solids content of sample two, the curves of frozen/thawed samples should be closer. The stress history during freeze-thaw and thixotropic behavior were claimed as the causes. Shear strength increased much faster when MFT approached solids contents higher than 50%, because the effect of over-consolidation pressure generated during freezing is more significant in soil than in a water-dominated slurry.

3.4 Finite strain consolidation tests

3.4.1 Compressibility and permeability

One specimen (as-received sample one) was specially prepared to perform self-weight consolidation test. The initial sample height was 130 mm and void ratio was 4.35. The measured initial excess pore pressure was 361 Pa. The investigation lasted for four months and yielded a deformation of 13.86 mm. As a result, the strain was up to 10.7% and void ratio decreased to 3.78. In order to locate the end of primary consolidation, three types of deformation curves were plotted in Figure 3.5. The curve in Figure 3.5a approaches the asymptotic line (y = 14 mm) with relative deformation rate less than 1.28×10^{-3}/day after a period of 80 days. The relative deformation rate (δ_r) is defined as the ratio of deformation rate (mm/day) at specific time to the accumulated deformation (mm) by this time. Since the deformation in one day was so negligible to the total deformation, it can be considered as the end of primary consolidation. Figure 3.5b presents the deformation curve with log-time abscissa. The magnitude of primary consolidation (δ_p = 13.55 mm) was estimated by virtue of Casagrande's

method. The corresponding time (t = 83 days) was then back-determined from the deformation curve. Figure 3.5c shows the curve plotted with rectangular hyperbola method. The linear part represents the deformation at consolidation degree between 60 and 90%. Its slope (m = 0.059) and interception with vertical axis (c = 1.148) were then inputted to the given empirical formulas to calculate the magnitude of primary consolidation (δ_p = 13.42 mm) and the time (t = 78 days) to achieve it. Although magnitude of excess pore pressure is the best guide to judge the end of primary consolidation, the pore pressure transducer did not perform properly during this test.

Another three copies of specimens: as-received sample two, as-received sample three and as-received sample four, were tested to investigate the finite strain consolidation in the stress range of 0.5 kPa to 100 kPa. Self-weight consolidation was ignored for the aim of shortening the test duration. Since as-received MFT is too weak to carry a load of 0.5 kPa, these three specimens were first partially consolidated (e_2 = 3.84, e_3 = 3.45, and e_4 = 3.70) under self-weight and an overburden stress of 0.23 kPa. Figure 3.6 gives the compressibility curves with logarithm stress. The curves appeared to be a function of initial void ratio and converged at higher effective stresses. The compression indexes (C_c) were estimated by curve fitting and their values were 0.182, 0.174 and 0.178, respectively. The void ratios at overburden stress of 100 kPa were 1.23, 1.05, and 1.16, respectively. The permeability curves in Figure 3.7 indicate that permeability varied between 3.3×10^{-7} and 5.2×10^{-9} cm/s during the tests. The data of as-received sample one was plotted on both curves for comparison.

Two copies of specimens: freeze/thaw sample one and freeze/thaw sample two, were used to investigate the freeze/thaw effect on the consolidation behaviors of Albian MFT. The specimens were first frozen and thawed with controlled boundary temperatures. A volumetric expansion of 6.35% was measured during freezing (Figure 3.8) and a thaw strain of 40% was observed during thawing and

post-thaw self-weight consolidation. Table 3.1 summarized the height and void ratio changes upon freeze/thaw. Due to defects of instruments, post-thaw consolidation of freeze/thaw sample one was interrupted after 20 kPa. The compressibility curves in Figure 3.9 are nearly identical and the compression index was estimated to be 0.100. The void ratio at overburden stress of 100 kPa was 1.00. The permeability curves in Figure 3.10 are close to each other and contain three linear segments. The magnitude of permeability was in the range of 5.4×10^{-7} cm/s to 1.0×10^{-8} cm/s.

3.4.2 Pore pressure during consolidation

The initial excess pore pressure was expected to have the same magnitude as the overburden pressure if one-way drainage was applied. However, the pore pressure readings indicated that certain amount of time (between 5 minutes and 3 hours) was required to reach the peak pore pressure at the bottom of sample. Figure 3.11a, Figure 3.11c, and Figure 3.11e denote that the maximum excess pore pressure was smaller than the incremental load. Figure 3.11b shows that pore pressure at the bottom of the specimen instantly decreased to static pore pressure after switching to double drainage. It implied the pore pressure transducer could measure an instant pore pressure. Figure 3.11d and Figure 3.11f present the pore pressure gain and dissipation after applying 20 and 100 kPa. The pore pressure gain rate was much higher than the dissipation rate, and both rates decreased with time. In addition, the pore pressure dissipation rate was higher at higher stress level by comparing Figure 3.11d with Figure 3.11f.

3.4.3 Post consolidation solids content and shear strength

Figure 3.12 presents the solids content profile of as-received sample one after self-weight consolidation. It was found that solids content increased with depth between 37.2% and 43.7%. Figure 3.13 shows the undrained shear strength profile measured at the end of self-weight consolidation. Shear strength

increased with depth between 70.2 Pa and 222 Pa. Figure 3.14 indicates that undrained shear strength increased with the solids content. Table 3.2 summarized the vane shear strength and solids content measured at the end of finite strain consolidation tests. The average solids content increased from initially 36.6% to 68.1% after the MFT was consolidated under stresses up to 100 kPa. The peak shear strength was enhanced from 36 Pa to 23 kPa and residual shear strength increased from 32 Pa to 11.1 kPa. Consequently, the sensitivity changed from 1.13 to 2.09. According to Rosenqvist (1953), Albian MFT can be categorized as slightly sensitive clay.

3.4.4 Effect of hydraulic gradient on permeability

The effect of hydraulic gradient on permeability was studied under three effective stresses. Hydraulic gradients of 0.2, 0.5 and 1.0 were chosen for permeability test at effective stress of 50 kPa and 100 kPa. Hydraulic gradients of 0.05, 0.1 and 0.2 were used for the permeability test at the end of self-weight consolidation. Figure 3.15 indicates that hydraulic gradient barely affected the permeability of MFT as Albian MFT only contains 1.29% wt bitumen. In addition, a hydraulic gradient of 0.2 was proved not capable to measure the permeability at effective stress of 100 kPa.

3.4.5 One way drainage versus double drainage

Figure 3.16a compares the deformation rate of freeze/thaw sample one with that of freeze/thaw sample two at a stress level of 20 kPa. Sample one was consolidated only with upward drainage, while sample two was consolidated with double drainage during the test. The deformation rate with double drainage was 1.56 to 1.44 times that with one-way drainage, and the magnitude of deformation with double drainage was 1.17 times that with one-way drainage. Figure 3.16b shows the deformation rate of as-received sample three and as-received sample four at the stress level of 100 kPa. The deformation rate with

double drainage was 1.54 to 1.2 times that with one-way drainage, and the magnitude of deformation was 1.18 times that with one-way drainage.

3.4.6 Discussion on finite strain consolidation tests

As stated before, MFT has low permeability (k) and high compressibility (m_v). Combined with the effect of its thixotropic behavior and drainage path, most MFT is undergoing self-weight consolidation. The magnitude of existing excess pore pressure equals to the total stress minus the effective stress and static pore pressure. Remolding of MFT during sample preparation would break the existing fabric and bonds between particles. Thus, the effective stress decreases and the excess pore pressure increases. Knowing the density of MFT (ρ = 1.29 Mgm^{-3}) and specimen height (H_0 = 13 cm), the summation of excess pore pressure and effective stress can be calculated as 367 Pa. The initial excess pore pressure at the bottom of as-received sample one was measured as 361 Pa. It implies that negligible effective stress existed in remolded Albian MFT with solids content of 36.6% at the start of the experiment.

The end of primary consolidation was predicted by three methods for as-received sample one in Figure 3.5. The variations in deformation (0.1 mm) and time (5 days) were small. However, the implementation of Casagrande's approach requires that the deformation curve levels out. This approach is not effective for MFT as the test time exceeds 10^5 minutes. The rectangular hyperbola method is straightforward and predicts the magnitude and end of primary consolidation. The observational method is simply and can be used together with the relative deformation rate. Figure 3.17 presents the deformation curves and excess pore pressure data at the stress level of 2 kPa and 50 kPa for as-received sample two. Figure 3.17a claims that the relative deformation rate was 3.79×10^{-3} /day at 37 days at the stress of 2 kPa, which indicated the end of primary consolidation. Besides, the excess pore pressure (U_e

= 92 Pa) implied that the degree of consolidation was 93.9%. The excess pore pressure applied during permeability test would be about 460 Pa. Therefore, the permeability test was carried out without the primary consolidation having been completed. Figure 3.17b shows that more time was required to develop a straight line in the Casagrande's plot. No sign of departure from the linear line was observed in the curve plotted with rectangular hyperbola method (Figure 3.17c). Figure 3.17d declares that the relative deformation rate was 0.9×10^{-3} /day after 17.8 days at a stress of 50 kPa, which implied the completion of primary consolidation. In addition, the degree of consolidation was determined to be 99.6% by knowing the excess pore pressure (U_e = 116 Pa). A permeability test was performed as the excess pore pressure applied was 300 Pa. Casagrande's method would underestimate the time for completion of primary consolidation (Figure 3.17e). And there was no sign to show derivation from the linear line in the rectangular hyperbola plot (Figure 3.17f). All in all, only pore pressure measurement and the direct observation method are recommended in determination of the end of primary consolidation in finite strain consolidation. The Casagrande method and rectangular hyperbola method are based on the Terzaghi's consolidation theory. They should only be used together with the pore pressure measurement and observation method.

Excess pore pressure has fully dissipated and effective stress has reached its peak value at the end of self-weight consolidation. In the center of the specimen, the effective stress equals 0.18 kPa, which is half of the difference between the initial total stress and static pore pressure. The effective stress versus void ratio and permeability versus void ratio for as-received sample one matched the extension of data from the other as-received samples (Figure 3.18 & Figure 3.19). It suggests that similar compressibility and permeability behaviors exist for MFT without having full consolidation under self-weight and 0.23 kPa applied stress.

Although different degrees of consolidation during the early stages exerted negligible effects on the compressibility and permeability, independent compressibility curves were observed in Figure 3.18. As-received sample two had a higher initial void ratio (e_0=3.84) and corresponding higher compressibility index (C_c = 0.182), while as-received sample three had the smallest initial void ratio (e_0=3.45) and the lowest compressibility (C_c=0.173). Creep occurred during the early stage was responsible for the independent compressibility behaviors and its effect eliminated with increasing effective stress. The compressibility for frozen/thawed MFT was identical as these samples started at the same initial void ratio and followed the same stress path. Additional permeability tests and investigations are required to fully understand the differences between permeability curves in Figure 3.19. Table 3.3 summarized the logarithmic curve fits for the compressibility behaviors of both as-received and frozen/thawed MFT samples. Table 3.4 modeled the permeability of as-received MFT with power law relationship and the permeability of frozen/thawed MFT with logarithmic relationship. In addition, logistic curve fits for all samples were presented in Table 3.3 and Table 3.4.

One cycle of freeze-thaw released 45% of initial pore water and significantly decreased the void ratio compared to the as-received Albian MFT. Consequently, the overall compressibility was lowered to about half of the original compressibility in terms of compression index. Figure 3.18 shows the compressibility curves converged with increasing effective stress. The final void ratios were similar for non-frozen/thawed MFT and frozen/thawed MFT. The effect of freeze-thaw diminished at higher effective stress. As stated in chapter one, freezing gives birth to over-consolidated soil peds which are surrounded by a reticulate ice network. Upon thawing, soil peds settle and expel water through fractures created by the ice network. The solids content increases and the compressibility is lowered. Furthermore, the suction created at the freezing front introduces stress gradient that moves water. MFT is over-consolidated by

different effective stresses induced during the freezing. The generated soil peds are therefore not homogeneous. During the post-thaw consolidation, the compressibility of thawed MFT gradually approaches that of as-received samples. Once all the MFT reached its pre-consolidation pressure, the frozen/thawed MFT behaved like as-received MFT. Figure 3.18 indicated that the maximum pre-consolidation pressure induced by freezing in the MFT was about 100 kPa.

The permeability of frozen/thawed MFT was initially about 6 times that as-received MFT at the same void ratio (Figure 3.19). This was attributed to the flow channels (fractures) generated during freeze-thaw. The weights of soil peds and small overburden stress do not fully close the flow channels. Although soil peds are less permeable, excess pore water would escape via the path of least resistance. The overall permeability is higher than that of as-received MFT at the same void ratio and it decreases significantly with decreasing void ratio. When the void ratio was smaller than 1.70, the channels appear to close and the permeability decreases with void ratio similar to that for the as-received MFT. The permeability of the frozen/thawed MFT was still higher even at lower void ratio. It is because some parts of the frozen/thawed MFT were more over-consolidated and the other parts were less consolidated. Water flowed via the more permeable paths. The as-received MFT was homogeneous and its average void ratio was lower than that of the more permeable paths in the frozen/thawed MFT.

Figure 3.20 presents both permeability and coefficient of volume compressibility. The permeability and compressibility decrease during consolidation. The curves for as-received MFT are smooth without sudden changes. The curves for frozen/thawed MFT can be divided into two parts. In the stress range of 1.5 to 4 kPa, the permeability decreased rapidly while the compressibility changed less significantly. At stress higher than 4 kPa, the compressibility of frozen/thawed MFT decreased faster while the permeability shows slower decrease. For the aim

of examining the variation of compressibility and permeability, the data of as-received samples were divided by that of sample one at the end of self-weight consolidation and the data of frozen/thawed samples was divided by that at the end of post-thaw self-weight consolidation. Figure 3.21 presents the normalized permeability and compressibility. It implies that permeability varies 100 times and the compressibility changes about 1000 times. As a result, the coefficient of consolidation varies by 10 fold throughout the tests. Figure 3.22 gives the coefficient of consolidation determined as described in section 3.1. Coefficient of consolidation for as-received MFT increased with decreasing void ratio and became stable at lower void ratio. Its value was in the range of 1.45×10^{-2} to 1.65×10^{-1} m^2/year. The coefficient of consolidation for frozen/thawed MFT generally increased with reduction in void ratio except for void ratio between 1.5 and 2. Its value was between 2.94×10^{-2} and 4.45×10^{-1} m^2/year. In addition, the coefficient of consolidation for as-received MFT was higher at higher void ratio and lower at lower void ratio comparing with that of frozen/thawed MFT. Coefficient of consolidation was also determined using the Casagrande's method and rectangular hyperbola method. The sample height at 50% degree of consolidation was used to determine the drainage path. Figure 3.23 presents the coefficient of consolidation for as-received sample one at self-weight consolidation, as-received sample three at 100 kPa, and freeze/thaw sample one at 20 kPa. It indicated that both curve fitting methods yield similar results.

The average preconsolidation pressure generated during freezing was estimated to be 10 kPa using the graphical approach presented by Chamberlain (1981) in Figure 3.24. It can only represent the average pre-consolidation pressure as a pressure gradient existed during the freezing.

The composition routes of Albian MFT samples during finite strain consolidation are presented in Ternary diagram (Figure 3.25). Regardless of the stress paths and thermal history, the route is roughly identical. The MFT samples, as non-

segregating material, only experienced water dissipation while all solids components remained constant. Besides, the route penetrates the liquid and solid boundary and indicates the final water content (ω=47.6%) is lower than the liquid limit (LI=54%). Besides, the composition profiles of thawed MFT and as-received MFT at the end of self-weight consolidation were also presented in Figure 3.25.

The undrained shear strength of normally consolidated clay was predicted by Skempton's equation:

$$S_u = \left(0.11 + 0.0037 I_p\right)\sigma_v'$$

Where S_u is the undrained shear strength (kPa), $I_p$is the plasticity index (%), σ_v' is the vertical effective stress (kPa). The plasticity index of Albian MFT is 26.7%. Figure 3.26 compared the predicted undrained shear strength with measured values at the stress level of 20 and 100 kPa. Vane shear test is supposed to be carried out under overburden pressure. The removal of overburden pressure in laboratory would reduce the undrained shear strength of MFT. Even though, the measured undrained shear strength is higher than the predicted value. Suthaker (1995) declared that MFT has a much higher thixotropic ratio compared to kaolinite, illite, and bentonite. Thixotropic behavior is the main cause of the higher undrained shear strength of MFT than other normally consolidated clay.

Banas (1991) proved residual undrained shear strength of Syncrude MFT could be predicted using Leoueil et al.'s (1983) equation over a liquidity index range of 0.5 to 2.5. The relationship between residual shear strength and liquidity index can be written as:

$$S_{ur} = \left(\frac{25.9}{I_L}\right)^{2.27}$$

where S_{ur} is the residual undrained shear strength (Pa), I_L is the liquidity index. The liquidity index of freeze/thaw sample two at 20 kPa is 0.91. Figure 3.27 compared the predicted residual shear strength of Albian MFT with laboratory measured values. The measured residual shear strengths appear to be much larger than the predicted values. The effect of stress history is responsible for the higher residual strength, since MFT was sheared directly after remolding in Banas' (1991) vane shear tests.

TABLE 3.1 Freeze expansion and thaw strain of freeze/thaw sample one and sample two

specimens	H_i (mm)	e_i	H_f (mm)	H_t (mm)	ε_t (%)	e_f
freeze/thaw one	130	4.35	138.2	83	39.96	2.416
freeze/thaw two	130	4.35	138.5	83	40.05	2.416

H_i, H_f, and H_t: initial height, frozen height, and thawed height; ε_t: thaw strain; e_i , e_f : initial/ final void ratio.

TABLE 3.2 Post consolidation solids content and vane shear strength

specimens	σ' (kPa)	SC (%)	e	S_{up} (kPa)	S_{ur} (kPa)	S_t
as-received two	100	68.19	1.23	19.46	10.17	1.91
as-received three	100	68.73	1.05	26.38	14.78	1.78
as-received four	100	67.5	1.16	23.07	8.36	2.76
freeze/thaw one	20	65.94	1.36	9.59	7.28	1.32
freeze/thaw two	100	69.93	1.00	22.08	12.35	1.79

SC: solids content; S_{up}: peak shear strength; S_{ur}: residual shear strength; S_t: sensitivity.

TABLE 3.3 Curve fits for compressibility behaviors

specimens	logarithmic	logistic
as-received two	$y = -0.42 \ln x + 3.085$, $R^2 = 0.989$	$y=3.525/[1+(x/3.193)^{0.579}]+0.817$, $R^2 = 0.999$
as-received three	$y = -0.41 \ln x + 2.853$, $R^2 = 0.992$	$y=3.247/[1+(x/4.033)^{0.598}]+0.647$, $R^2 = 0.999$
as-received four	$y = -0.40 \ln x + 2.921$, $R^2 = 0.994$	$y=10.91/[1+(x/13.64)^{0.147}]-3.529$, $R^2 = 0.999$
freeze/thaw one	$y = -0.23 \ln x + 2.037$, $R^2 = 0.995$	$y=1.393/[1+(x/2.177)^{0.842}]+1.178$, $R^2 = 0.999$
freeze/thaw two	$y = -0.23 \ln x + 2.042$, $R^2 = 0.994$	$y=1.946/[1+(x/3.975)^{0.580}]+0.755$, $R^2 = 0.999$

TABLE 3.4 Curve fits for permeability behaviors

specimens	power/logarithmic	logistic
as-received two	$y = 143.2\ x^{0.251}$, $R^2 = 0.995$	$y=-7.639/[1+(x/1.03E^{-6})^{0.408}]+8.042$, $R^2 = 0.995$
as-received three	$y = 306.8\ x^{0.298}$, $R^2 = 0.997$	$y=-6.196/[1+(x/3.71E^{-7})^{0.535}]+6.656$, $R^2 = 0.999$
as-received four	$y = 242.2\ x^{0.281}$, $R^2 = 0.990$	$y=-2.708/[1+(x/6.05E^{-8})^{1.111}]+3.698$, $R^2 = 0.999$
freeze/thaw one	$y = -0.334 \ln x + 7.315$, $R^2 = 0.989$	$y=-3.821/[1+(x/1.12E^{-8})^{0.451}]+3.004$, $R^2 = 0.995$
freeze/thaw two	$y = -0.358 \ln x + 7.617$, $R^2 = 0.982$	$y=-5.648/[1+(x/3.15E^{-9})^{0.341}]+3.225$, $R^2 = 0.989$

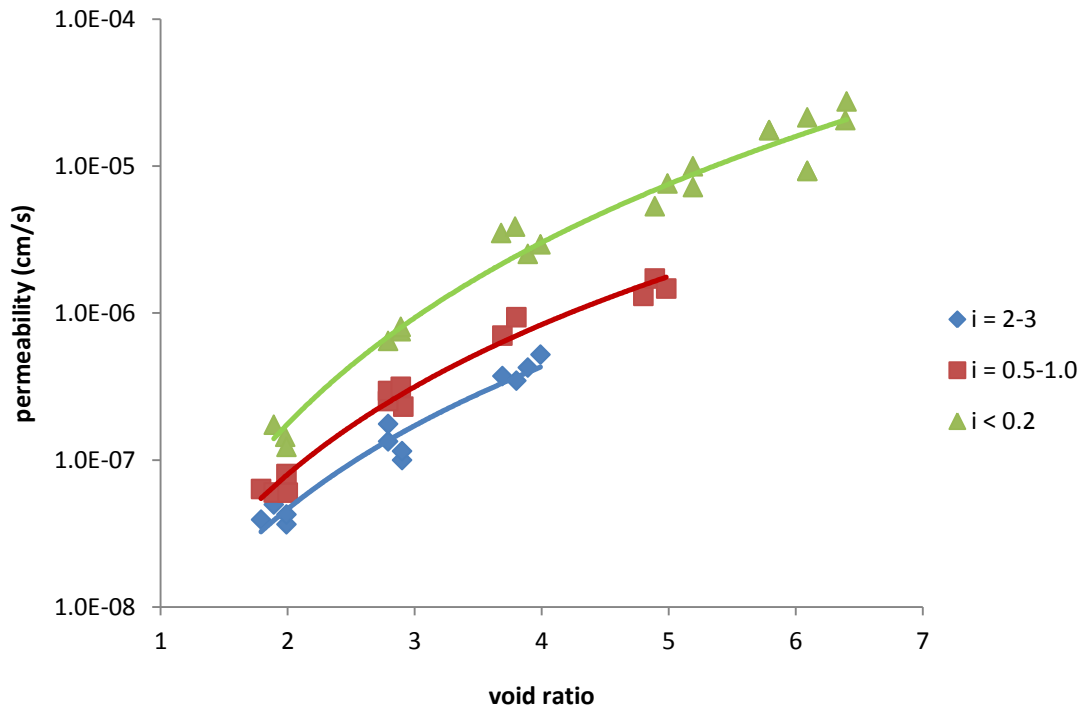

FIGURE 3.1 Effect of hydraulic gradient on the permeability of MFT (after Suthaker 1995)

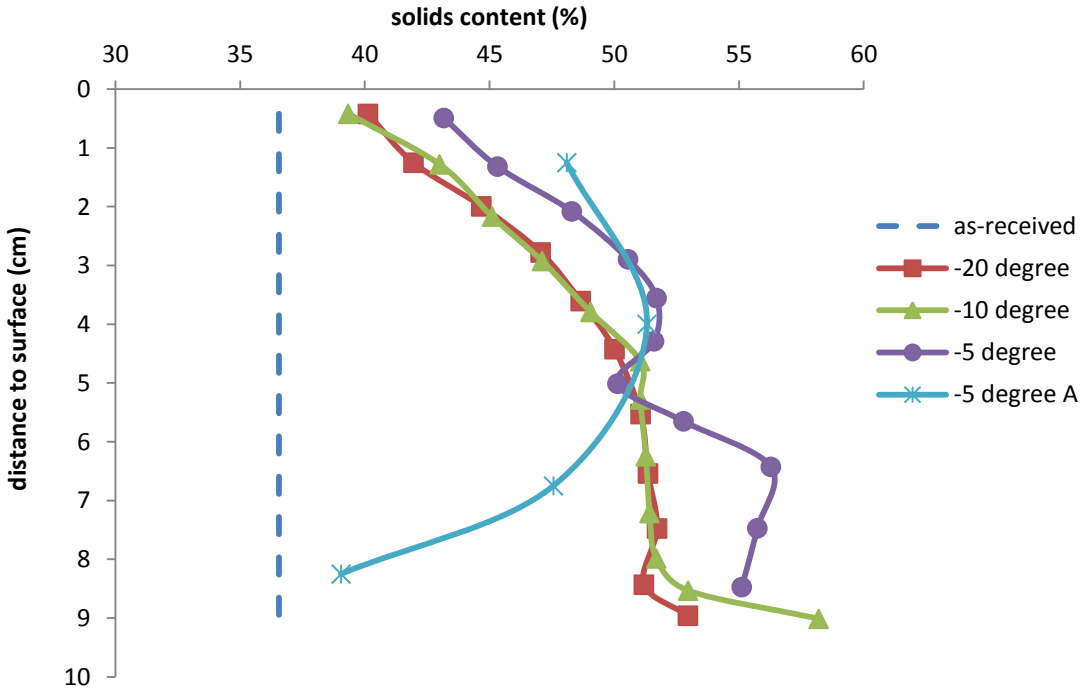

FIGURE 3.2 Solids content profiles after freeze-thaw

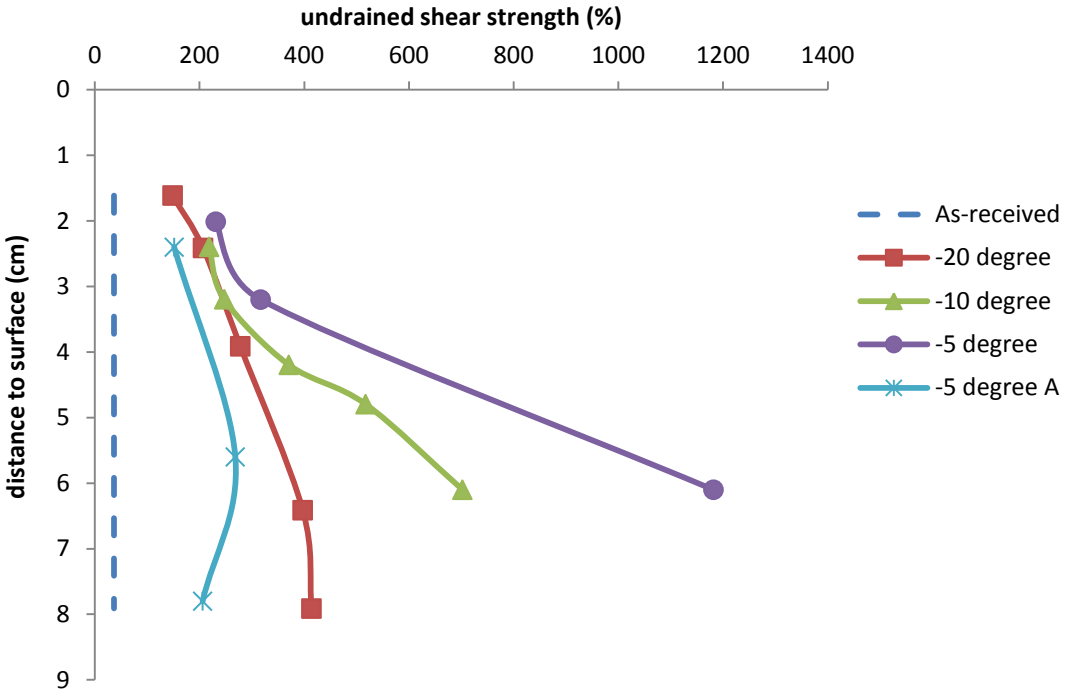

FIGURE 3.3 Undrained shear strength profiles after freeze-thaw

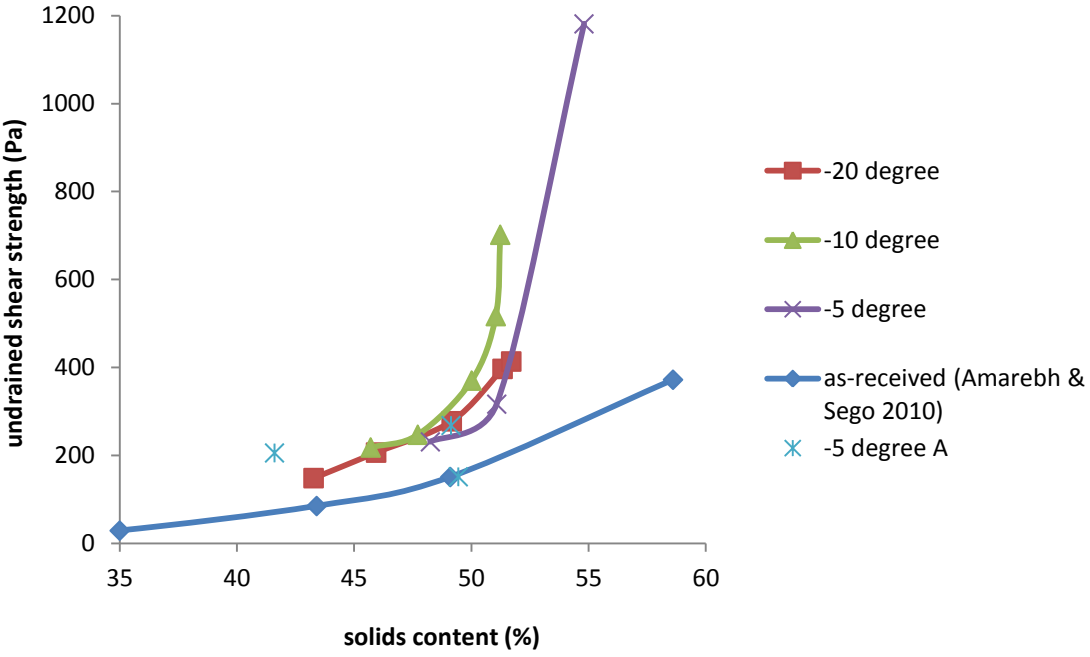

FIGURE 3.4 The relationship between undrained shear strength and solids content

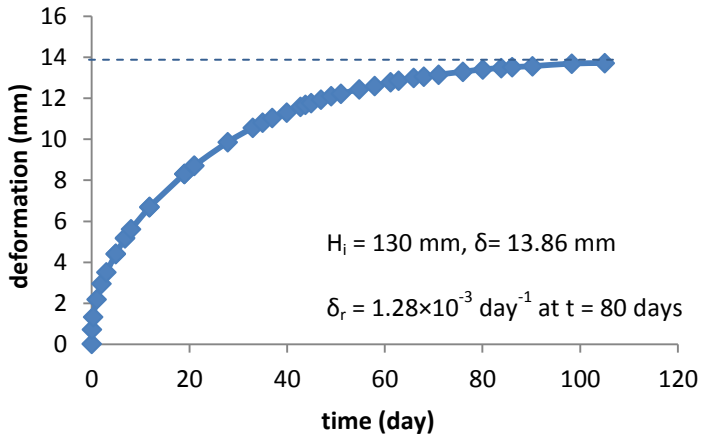

(a) Observational method

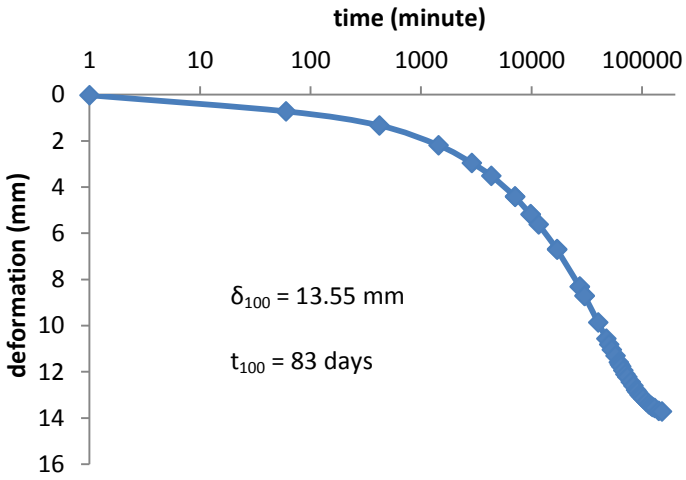

(b) Casagrande's method

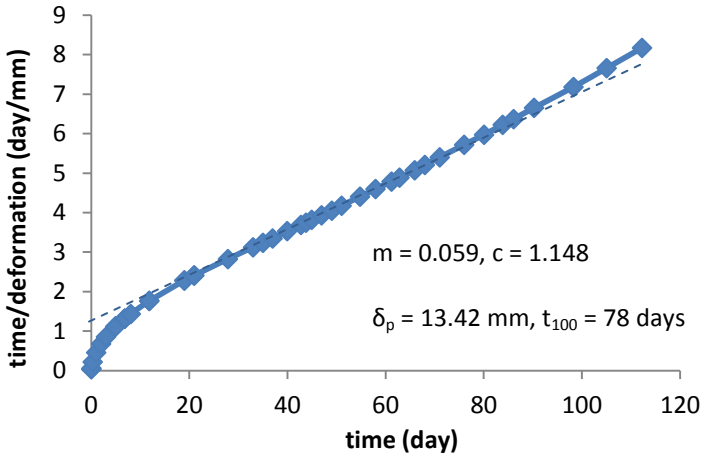

(c) Rectangular hyperbola method

FIGURE 3.5 Self-weight consolidation curves of as-received one

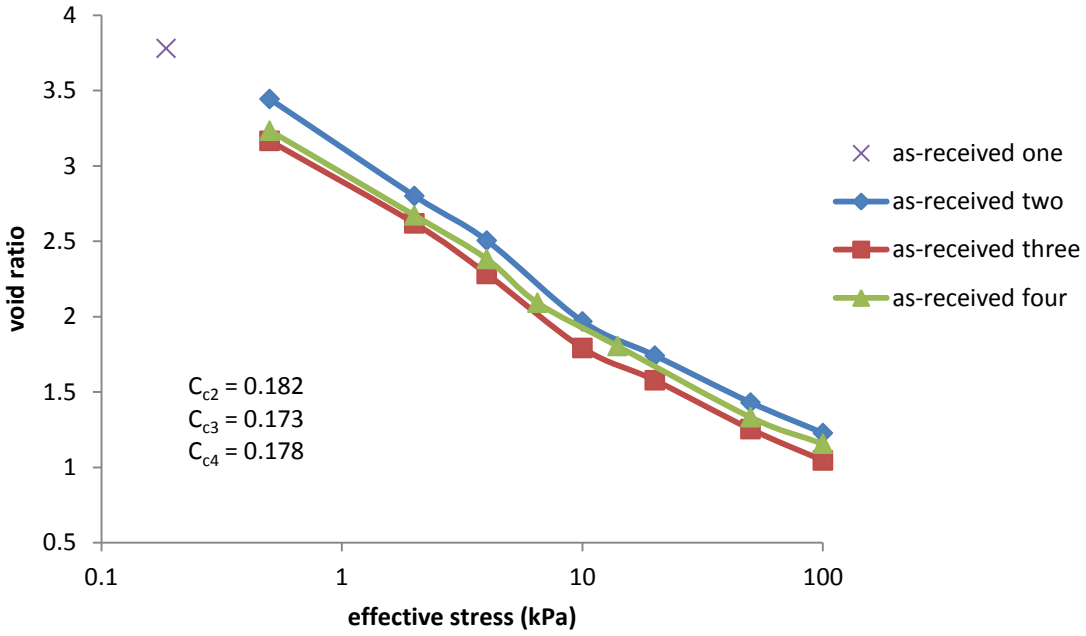

FIGURE 3.6 Compressibility results for as-received, never frozen Albian MFT

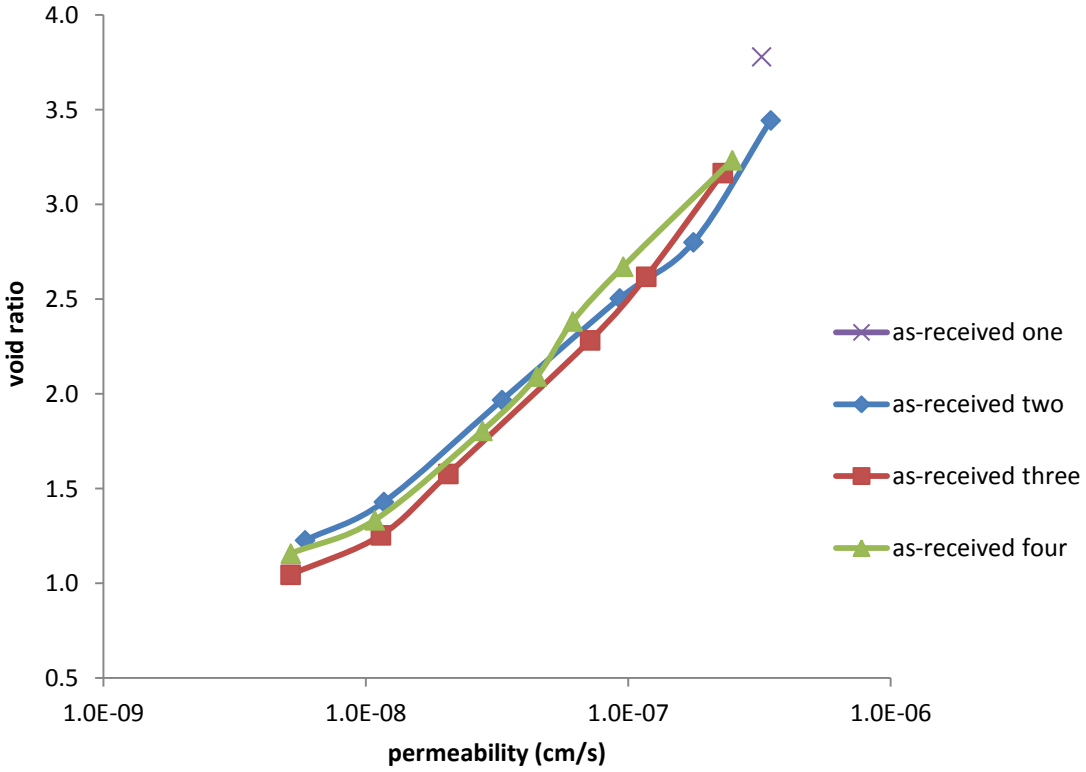

FIGURE 3.7 Permeability test results for as-received, never frozen Albian MFT

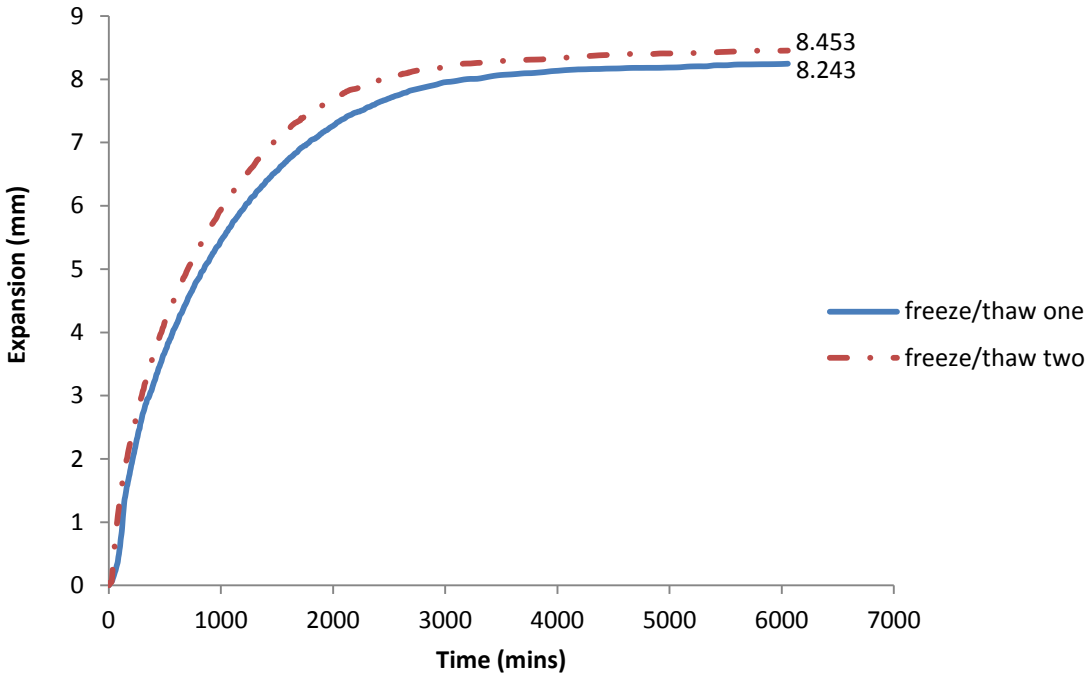

FIGURE 3.8 Sample expansions during freezing

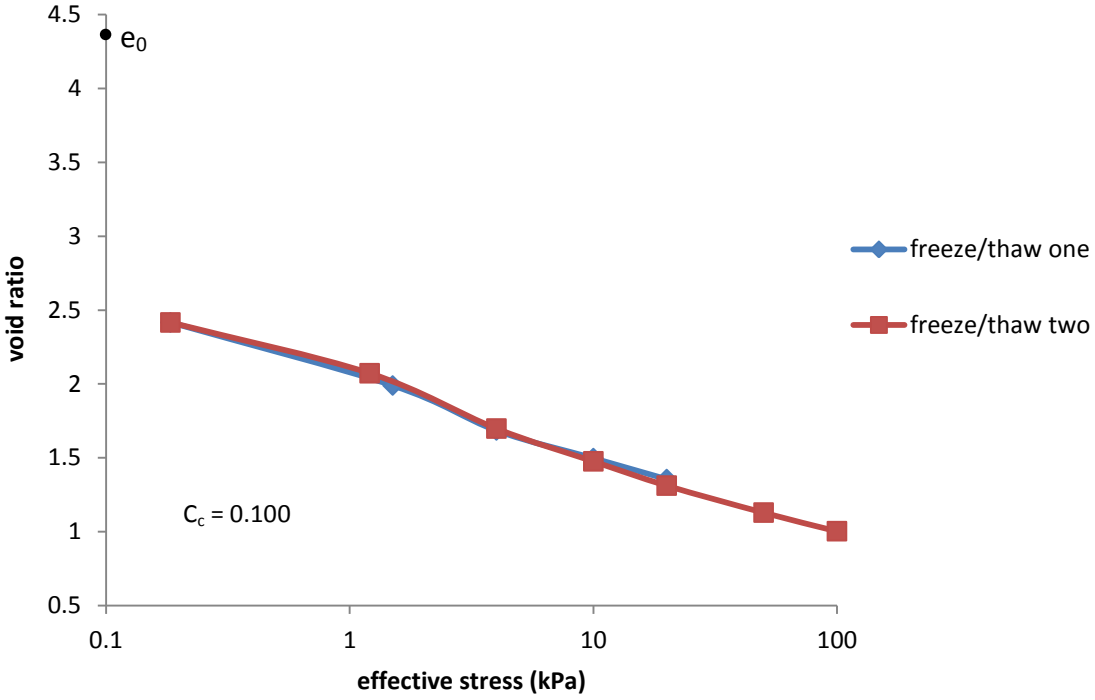

FIGURE 3.9 Compressibility results for as-received, frozen/ thawed Albian MFT

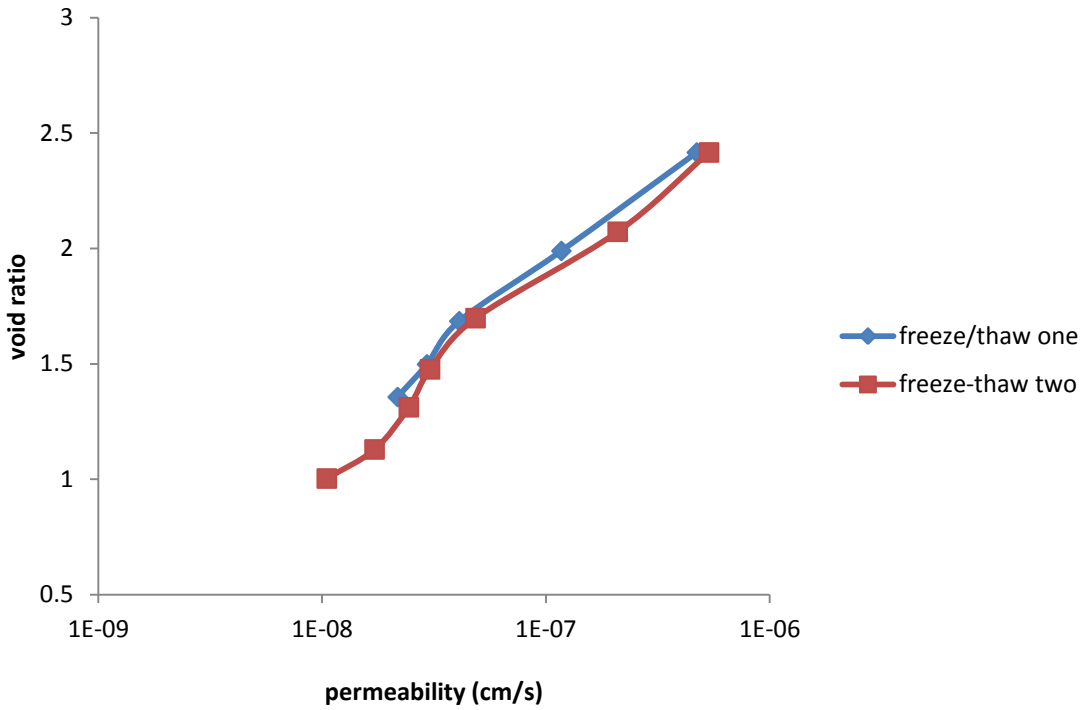

FIGURE 3.10 Permeability results for as-received, frozen/ thawed Albian MFT

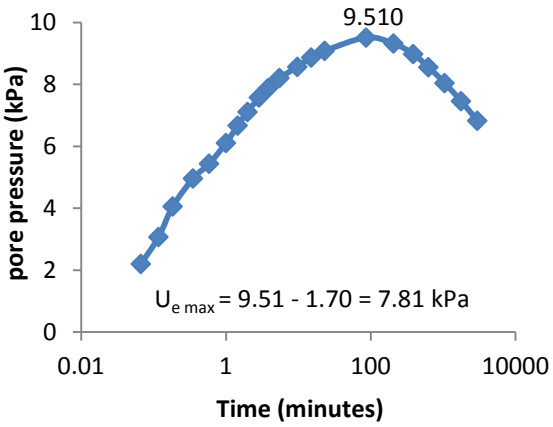

(a) Pore pressure of as-received four after applying 20 kPa

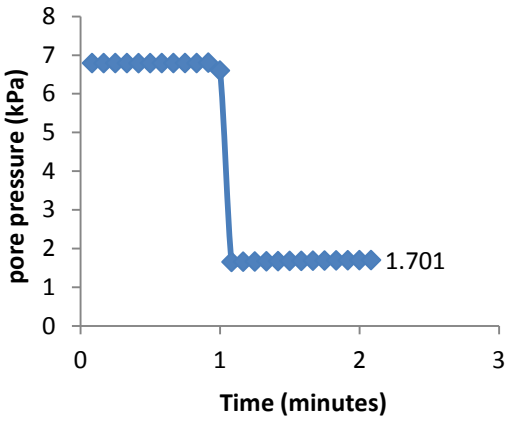

(b) Pore pressure of as-received four upon changing into double drainage at 20 kPa

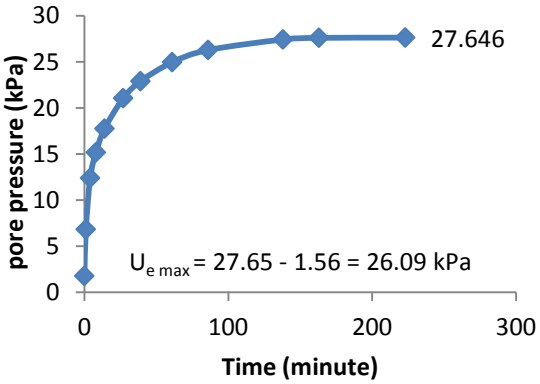

(c) Pore pressure gaining of as-received four after applying 100 kPa

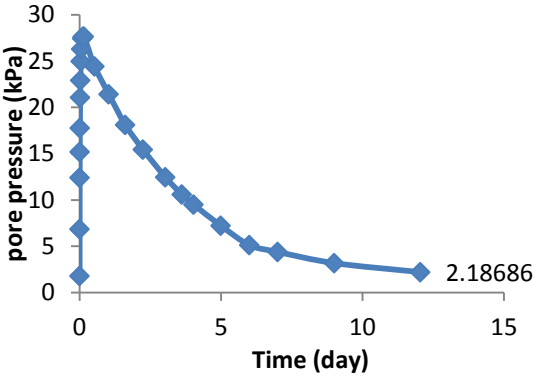

(d) Pore pressure of as-received four after applying 100 kPa

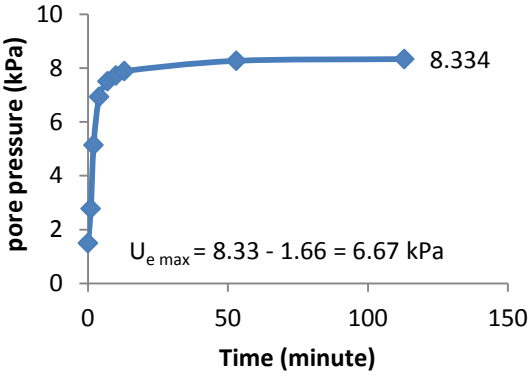

(e) Pore pressure gaining of freeze/thaw one after applying 20 kPa

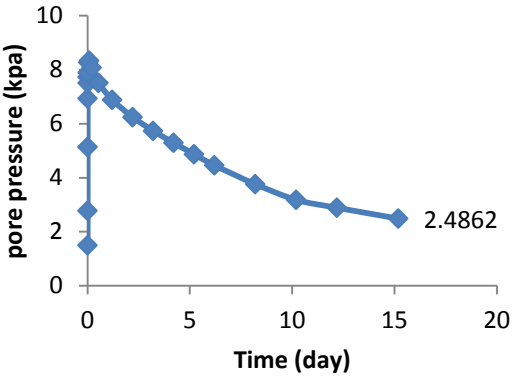

(f) Pore pressure of freeze/thaw one after applying 20 kPa

FIGURE 3.11 Pore pressure during post-thaw consolidation

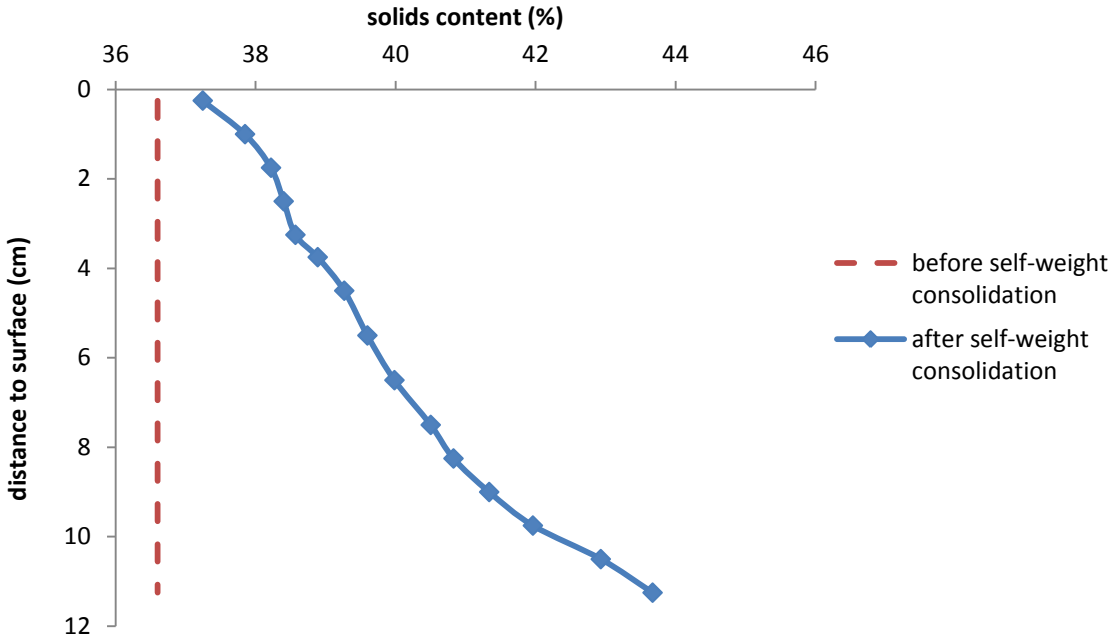

FIGURE 3.12 Solids content profile of as-received one

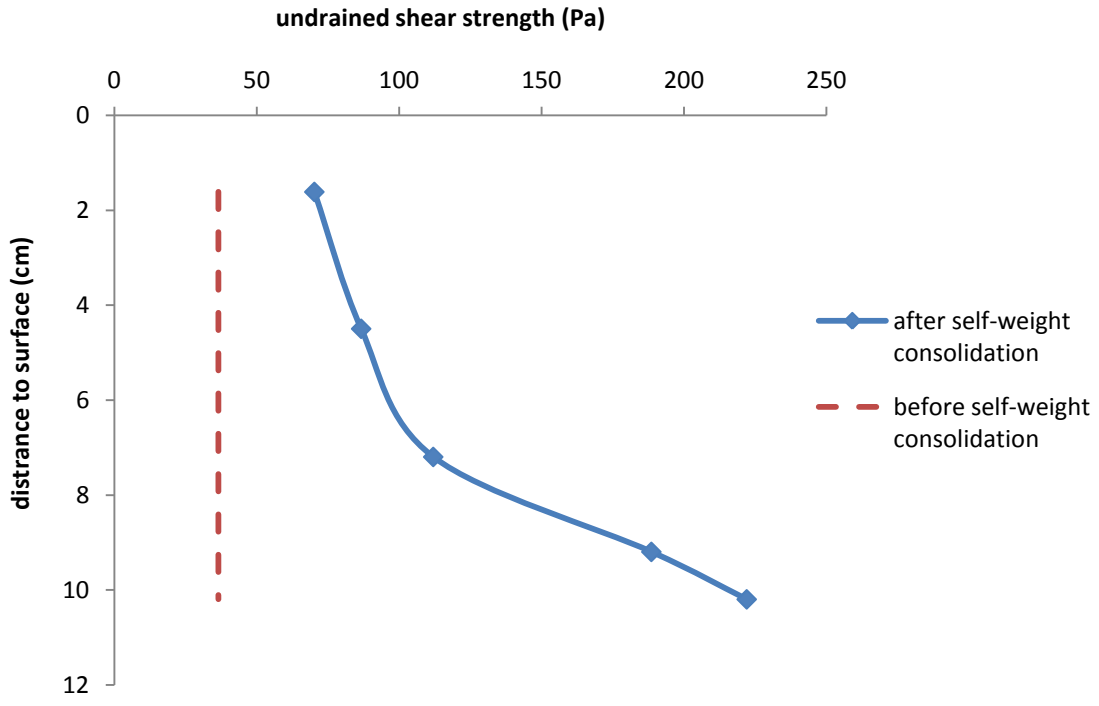

FIGURE 3.13 Undrained shear strength profile of as-received one

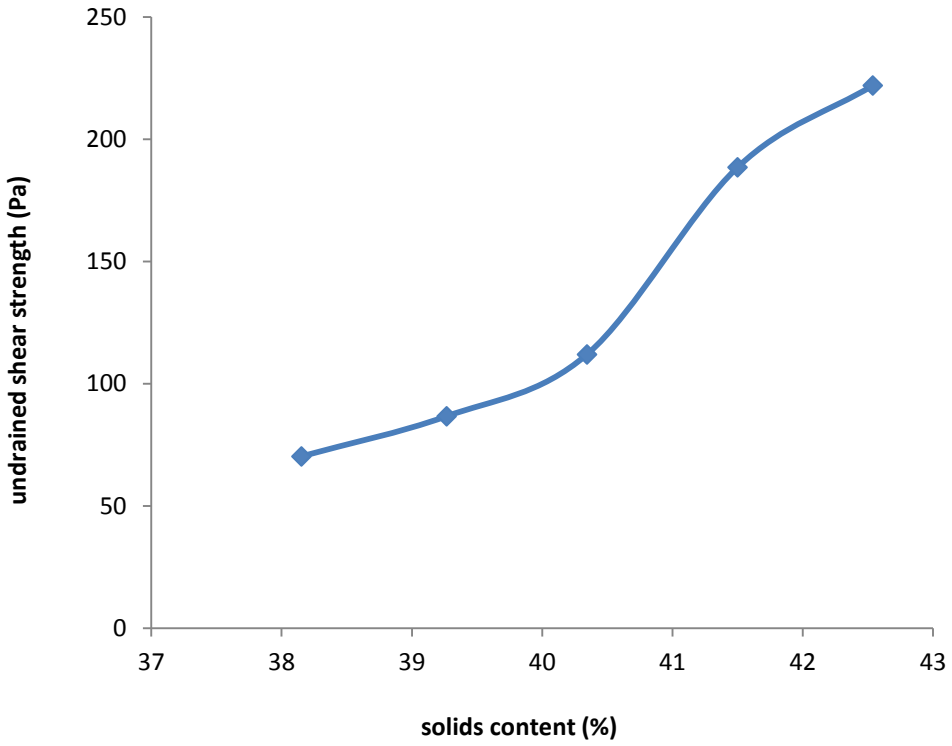

FIGURE 3.14 The relationship between solids content and undrained shear strength

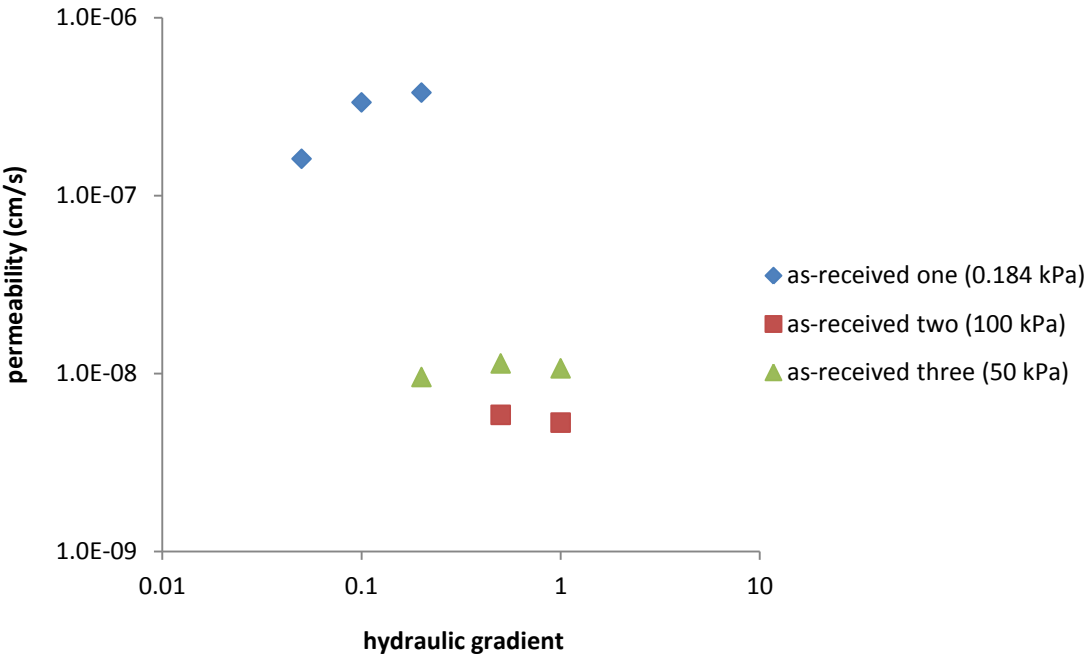

FIGURE 3.15 Variation of permeability with hydraulic gradient

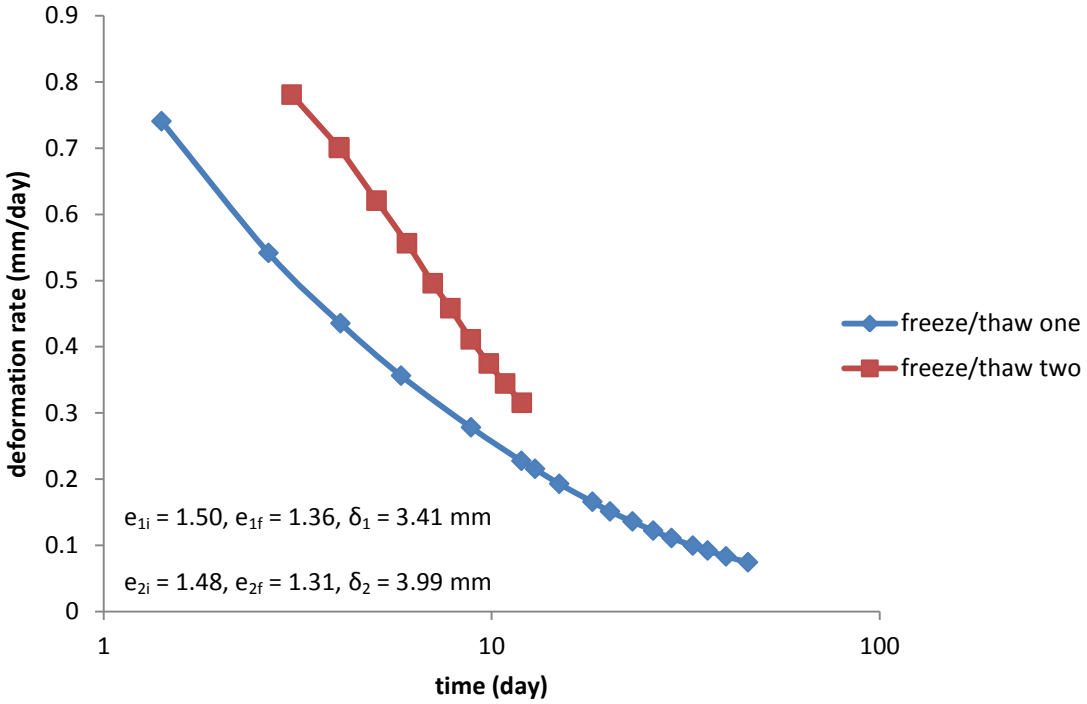

(a) Deformation rate for one way and double drainage under 20 kPa

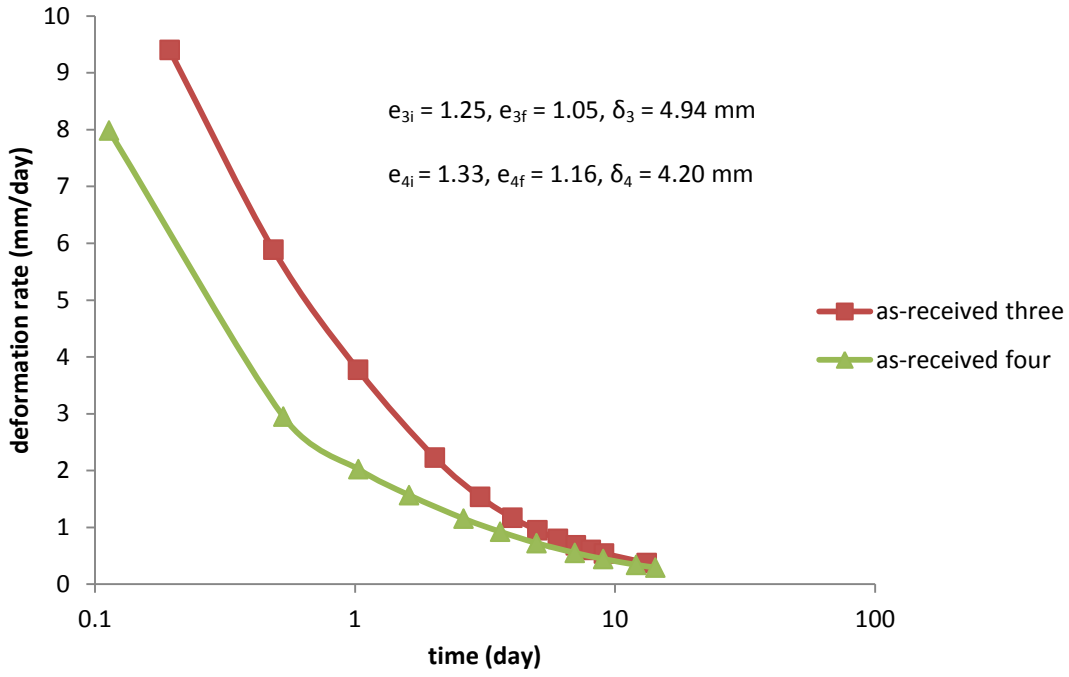

(b) Deformation rate for one way and double drainage under 100 kPa

FIGURE 3.16 Effect of drainage path on deformation rate and magnitude

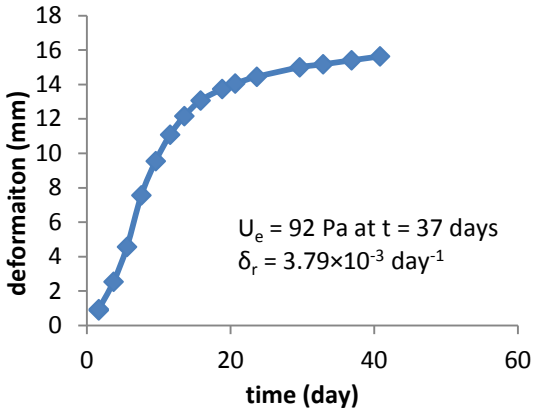

(a) Observational method at 2 kPa

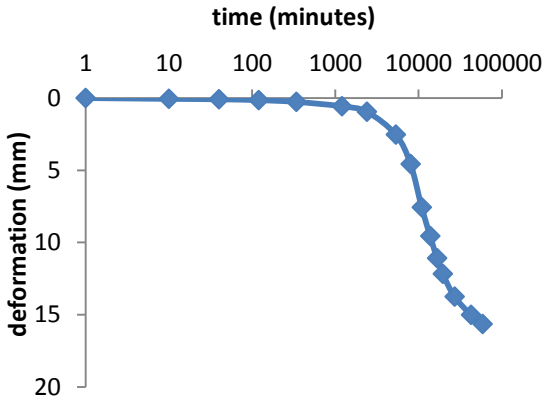

(b) Casagrande's method at 2 kPa

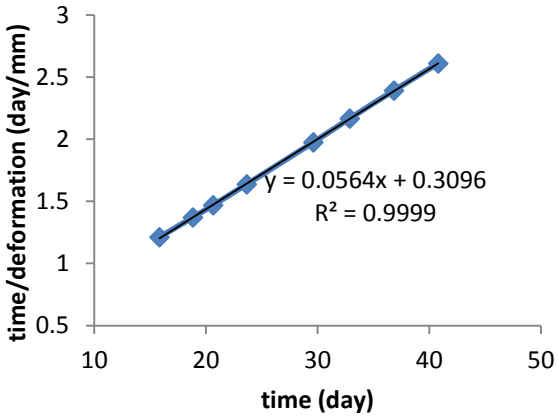

(c) Rectangular hyperbola method at 2 kPa

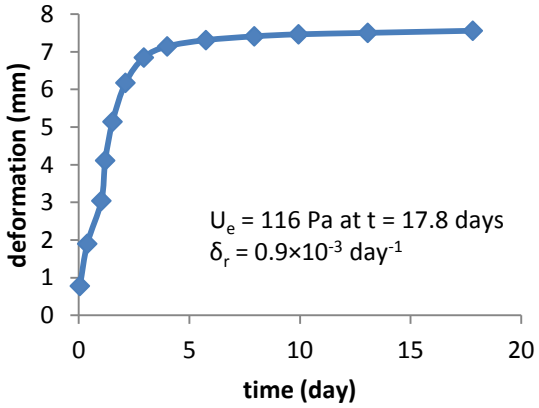

(d) Observation method at 50 kPa

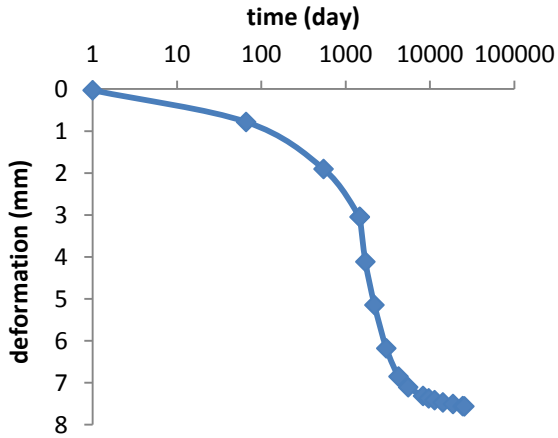

(e) Casagrande's method at 50 kPa

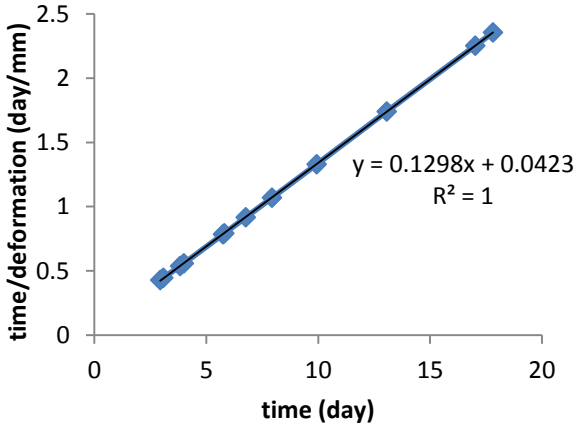

(f) Rectangular hyperbola method at 50 kPa

FIGURE 3.17 Determination of completion of consolidation

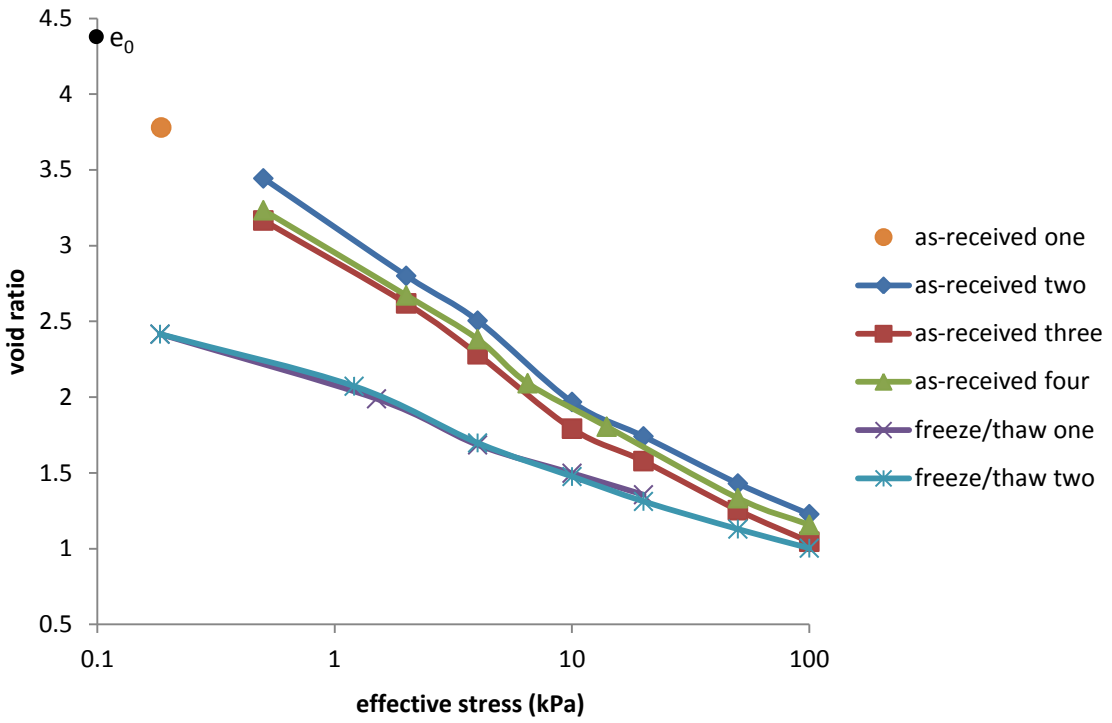

FIGURE 3.18 Compressibility curves for all the Albian MFT samples

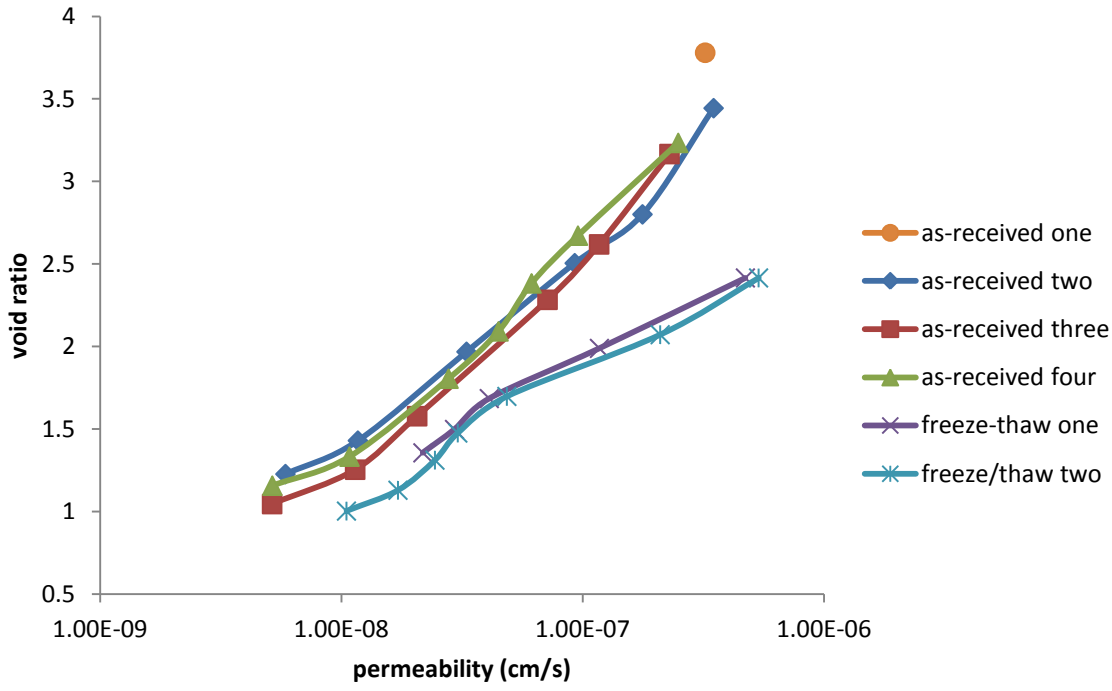

FIGURE 3.19 Permeability curves for all the Albian MFT samples

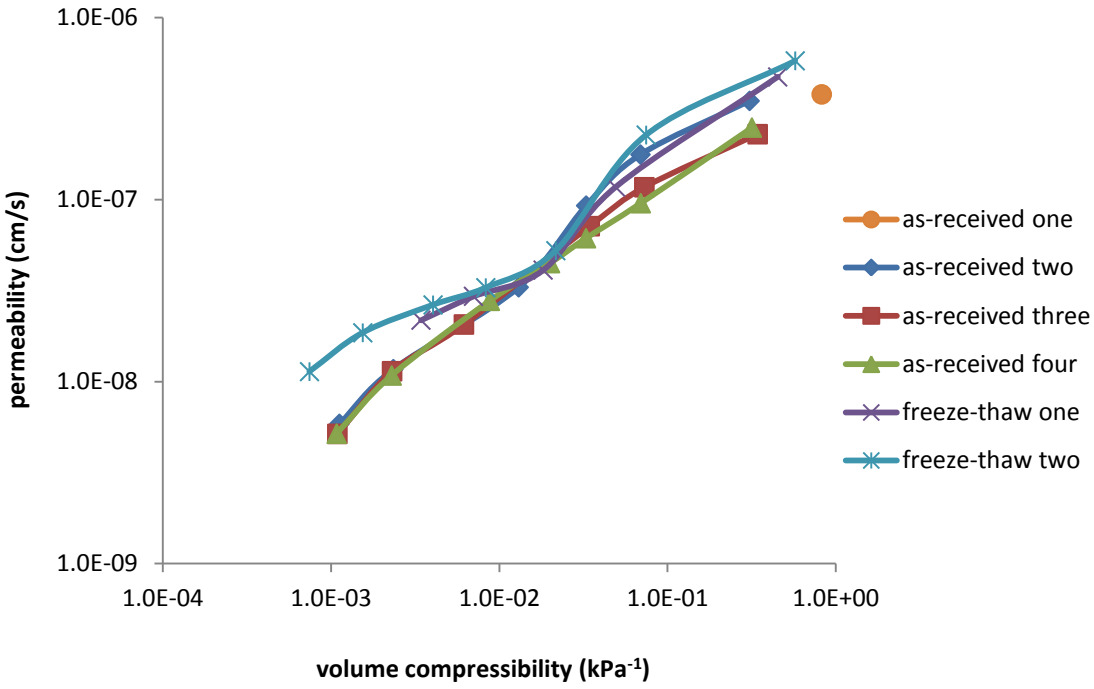

FIGURE 3.20 The corresponding permeability and coefficient of volume compressibility

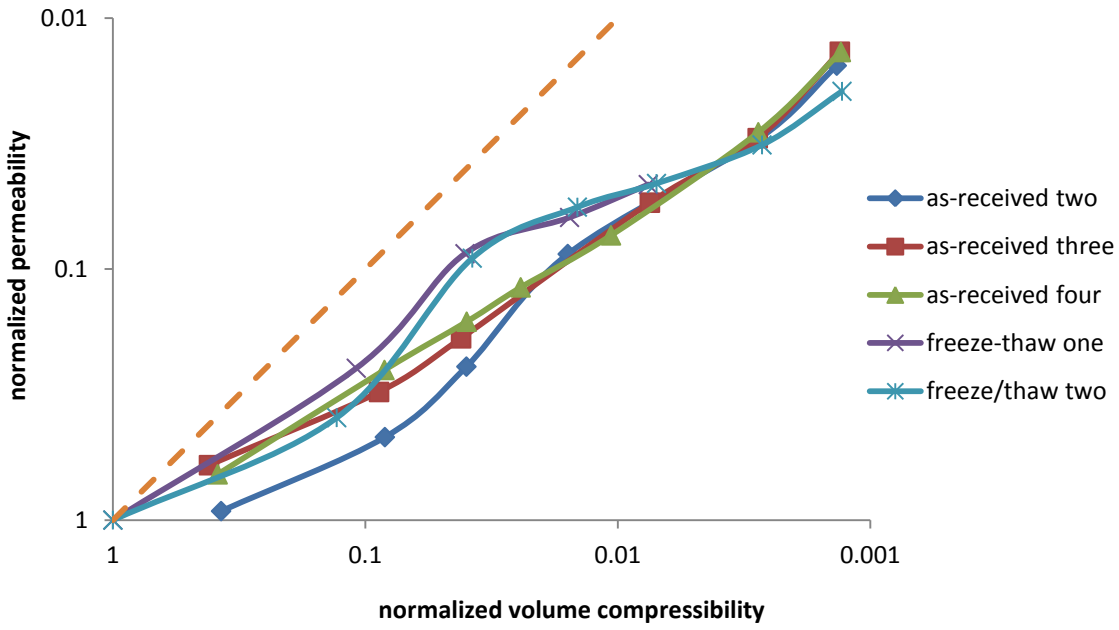

FIGURE 3.21 The normalized permeability and coefficient of volume compressibility

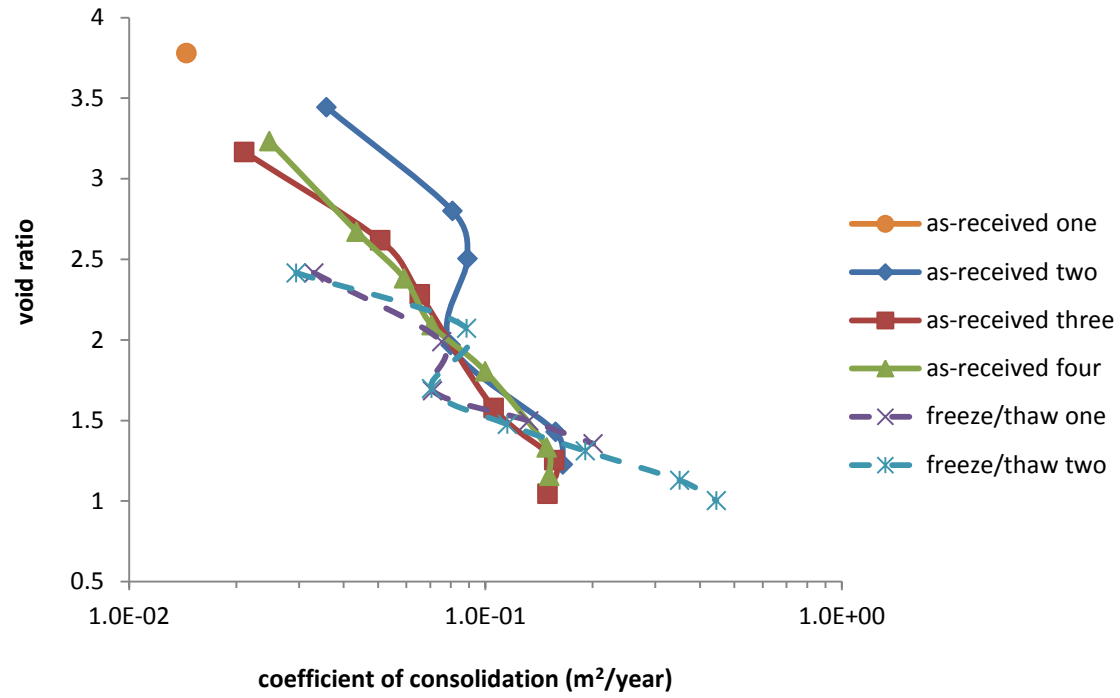

FIGURE 3.22 Variation of coefficient of consolidation with void ratio

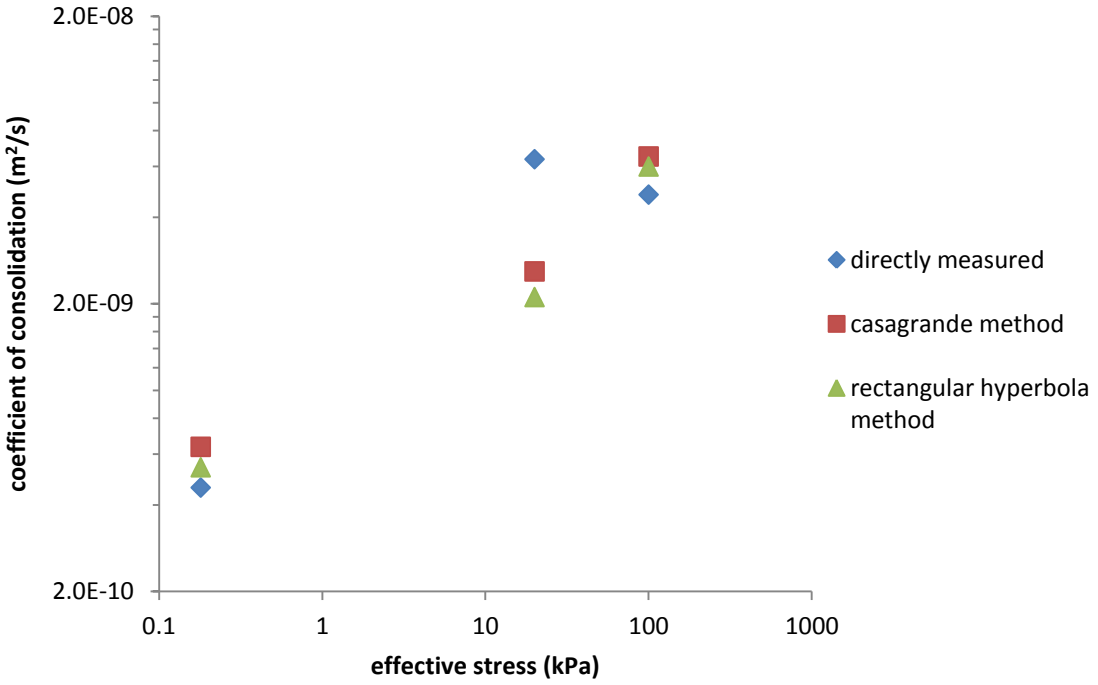

FIGURE 3.23 Coefficient of consolidation obtained by different methods

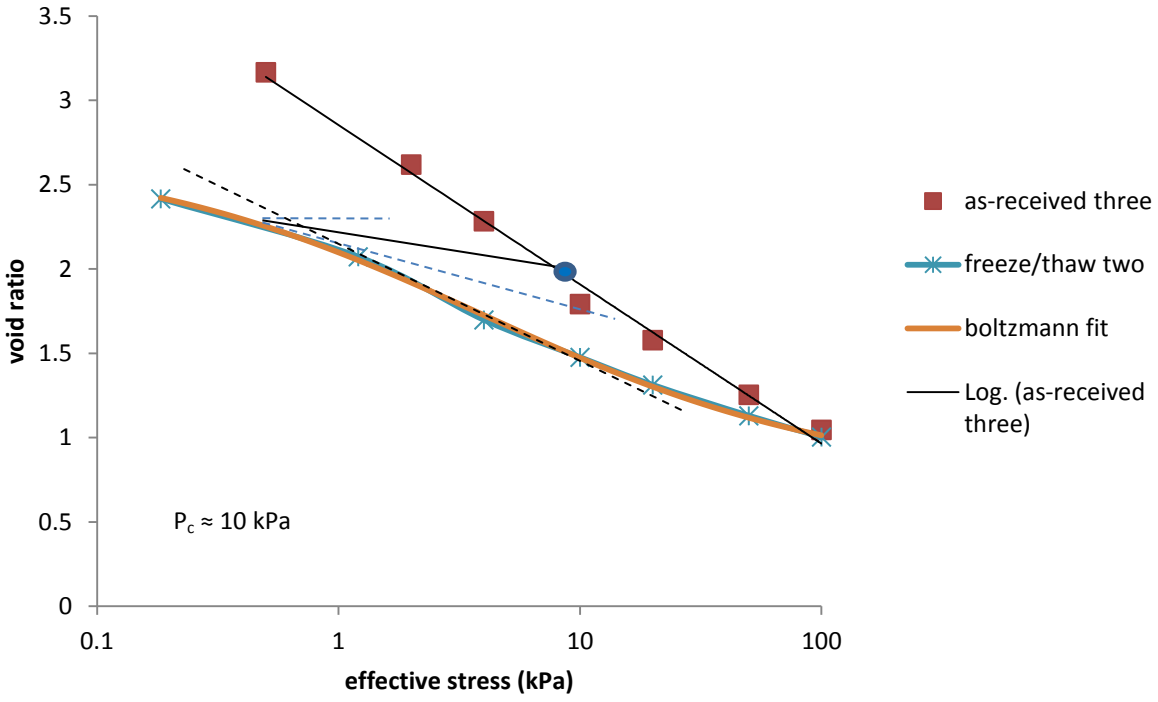

FIGURE 3.24 Determination of preconsolidation pressure generated during freezing

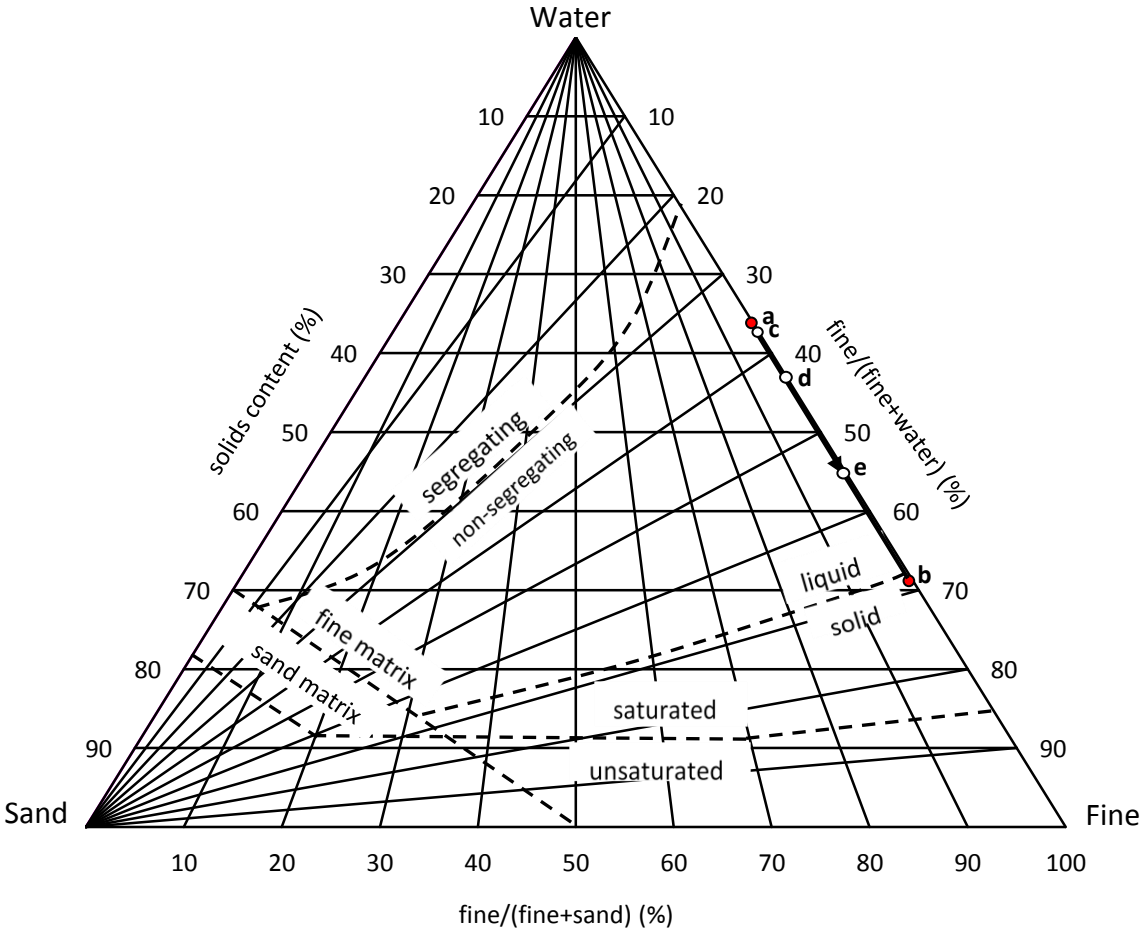

FIGURE 3.25 Albian MFT presented in Ternary diagram. a-b: the route of finite strain consolidation for both as-received and frozen/thawed Albian MFT; c-d: composition profile of as-received MFT after self-weight consolidation; d-e: composition profile of thawed MFT (top freezing temperature: -5°C) (after Azam & Scott 2005)

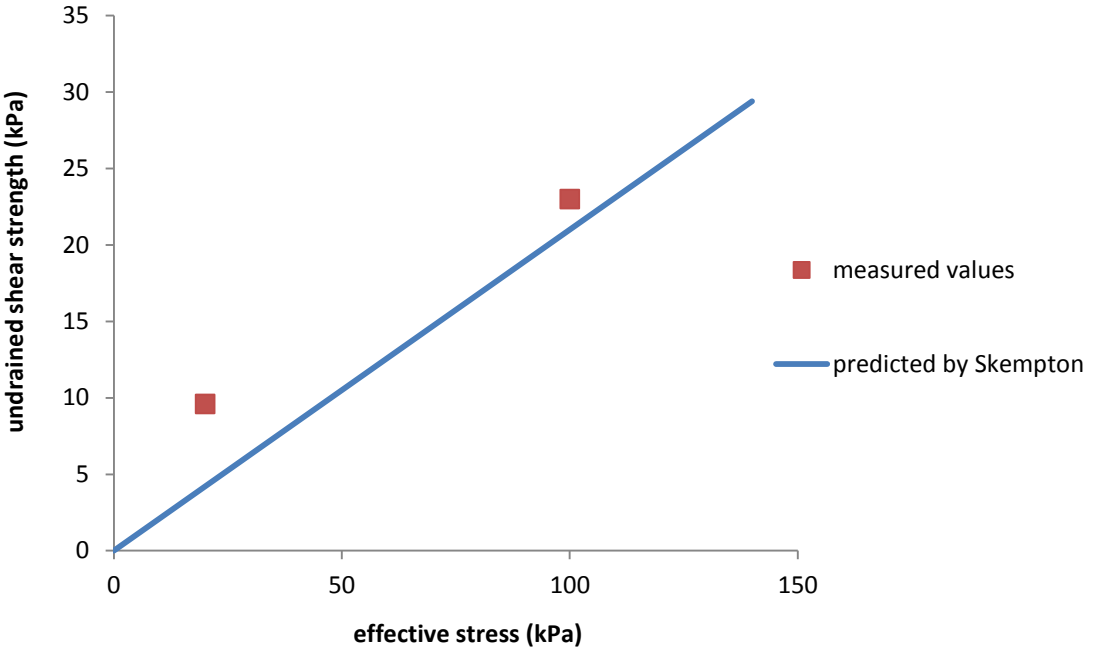

FIGURE 3.26 Comparison between predicted and measured undrained shear strength

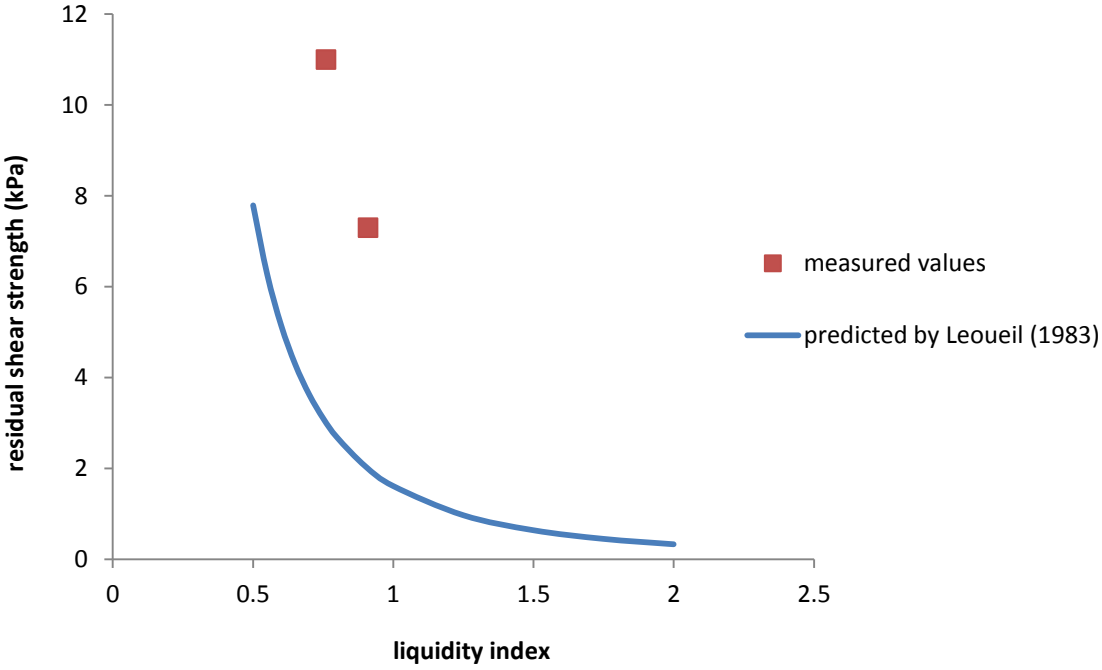

FIGURE 3.27 Comparison between predicted and measured residual shear strength

CHAPTER 4

4. CONCLUSIONS AND RECOMMENDATIONS

4.1 Summary and Conclusions

Detailed testing procedures for freezing tests were developed to provide guidance on the selection of temperature boundaries, duration of freeze-thaw and post-thaw self-weight consolidation. The selection of vane shear instruments, the deployment of test points, and the correction of torque induced by spindle rod were also discussed in details.

Detailed testing procedures were generated for finite strain consolidation of both as-received and frozen/thawed MFT. The procedures presented all the preparation work including saturation of the consolidometer and calibration of instruments. In addition, weight discs were designed to apply load during early consolidation stages of as-received MFT. Those discs permitted instant deformation measurement and there was no need to remove them before switching to air pressure load. Moreover, the methods of determining the end of primary consolidation and coefficient of consolidation were discussed.

One dimensional freeze-thaw tests were conducted with various freezing rates (top temperatures of -5, -10 and -20°C, respectively) to investigate the effect on dewatering. Freeze-thaw separated MFT into a clear aqueous layer and a soil layer. Around 36% thaw strain occurred to the MFT sample with a height of 13.6 cm. Lower freezing rate resulted in higher solids content and higher shear strength. Shear strength increasing rate became larger at solids content higher than 50%.

Slurry consolidation tests were performed on four as-received MFT samples to determine the compressibility, permeability, and consolidation rate. One sample

was only consolidated under self-weight, while the other three were consolidated up to 100 kPa. Solids content and shear strength increased with depth at the end of self-weight consolidation. Solids content of MFT (SC=68%) at the end of consolidation under 100 kPa was higher than the liquid limit (SC=65%). Regardless of accomplishment of self-weight consolidation, the compressibility and permeability curves were almost identical for as-received MFT.

Two MFT samples were tested to study the effect of freeze-thaw on the consolidation behaviors. Freeze-thaw reduced the compressibility to about half that of as-received MFT and increased the permeability by 6 times comparing with as-received MFT with same void ratio. Both compressibility curves and permeability curves converged at higher effective stress (σ'=100 kPa). Meanwhile, the coefficient of consolidation became larger with increasing in effective stress. In addition, it was larger at lower effective stress and smaller at higher effective stress for frozen/thawed MFT comparing with that of as-received MFT.

Pore pressure readings were recorded during consolidation, which indicated that a variable amount of time (5 minutes to 3 hours) was required to reach the peak pore pressure at the bottom of samples. The pore pressure dissipation rate decreased with the magnitude of pore pressure. In addition, the deformation rate of MFT with two-way drainage was about 1.5 times that with one-way drainage. Furthermore, hydraulic gradient did not affect the permeability of Albian MFT.

4.2 Recommendations

1. Another freezing test with top freezing temperature of -2.5°C is recommended to check the relationship between solids content and undrained shear strength, in order to verify the relationship follows the same trend in Figure 3.4.

2. The solids content profile of decanted water content after freeze-thaw should be checked, since pond water with high solids content may cause severe erosion to extraction facilities.

3. The effect of hydraulic gradient on permeability of MFT at the stress level between 0.5 kPa and 20 kPa should be examined to verify the conclusions that hydraulic gradient does not affect the permeability of Albian MFT.

4. More tests are required to study the difference between deformation rates with one-way drainage and two-way drainage.

5. Undrained shear strength at the end of consolidation under stress between 0.5 and 50 kPa are needed to study the relationship between undrained shear strength and solids content.

6. More efforts should be devoted to investigate the mechanisms controlling the permeability of MFT to identify the factors affecting permeability.

7. A large scale laboratory test is suggested to check the thermal models.

REFERENCES

Andersland, O.B., Ladanyi, B. 2004. Frozen ground engineering, 2nd edition. John wiley and sons, Inc., New York.

ASTM. 2005. Standard test method for laboratory miniature vane shear test for saturated fine-grained clayey soil. D4648-05, American Society for Testing and Materials, West Conshohocken. Pp. 1-7.

ASTM. 2007. Standard test method for particle-size analysis of soils. D422-63, American Society for Testing and Materials, West Conshohocken. Pp. 1-8.

ASTM. 2010a. Standard test methods for laboratory determination of water (moisture) content of soil and rock by mass. D2216-10, American Society for Testing and Materials, West Conshohocken. Pp. 1-7.

ASTM. 2010b. Standard test methods for Liquid limit, Plastic limit, and plasticity index of soils. D4318-10, American Society for Testing and Materials, West Conshohocken. Pp. 1-16.

ASTM. 2010c. Standard test methods for specific gravity of soil solids by water pycnometer. D854-10, American Society for Testing and Materials, West Conshohocken. Pp. 1-7.

Chamberlain, E.J. 1981. Overconsolidation effects of ground freezing. Engineering geology, 18: 97-110.

Dawson, R.F. 1994. Mine waste geotechnics. Ph.D. dissertation. University of Alberta.

Environment Canada. 2011. Canada Climate Normals: Fort McMurray. Government of Canada. [Accessed online 22 June 2011 at http://climate.weatheroffice.gc.ca/climate_normals/results_e.html?stnID=2519

&prov=&lang=e&dCode=1&dispBack=1&StationName=Fort_Mcmurray&SearchType=Contains&province=ALL&provBut=&month1=0&month2=12]

Fourie, A. 2009. Enhanced dewatering of fine tailings using electrokinetics. Proceeding of the thirteenth international conference on tailings and mine waste, November 1-4, 2009, Banff, Alberta, Canada. Pp. 269-280.

Gibson, R.E., England, G.L., Hussey, M.J.L. 1967. The theory of one-dimensional consolidation of saturated clays. I. Finite non-linear consolidation of thin homogeneous layers. Geotechnique, 17 (3): 261-273.

Gibson, R.E., Schiffman, R.L., Cargill, K.W. 1981. The theory of one-dimensional consolidation of saturated clays. II. Finite nonlinear consolidation of thick homogeneous layers. Canadian geotechnical journal, 18 (2): 280-293.

Government of Alberta. 2011a. Oil sands: the resources. [Accessed online 20 June 2011 at http://www.oilsands.alberta.ca/facts.html]

Government of Alberta. 2011b. Alberta's oil sands: facts about the resources. [Accessed online 20 June 2011 at http://www.oilsands.alberta.ca/facts.html]

Government of Alberta. 2011c. Alberta's oil sands: facts about tailings management. [Accessed online 20 June 2011 at http://www.oilsands.alberta.ca/facts.html]

Imai, G. 1979. Development of a new consolidation test procedure using seepage force. Japanese society of soil mechanics and foundation engineering, 2 (3): 45-60.

International Energy Agency. 2007. Renewables in global energy supply. [Accessed online 20 June 2011 at http://www.iea.org/publications/free_new_Desc.asp?PUBS_ID=1596]

Johnson, R.L., Bork, P., Allen, E.A.D., James, W.H., Koverny, L. 1993. Oil sands sludge dewatering by freeze-thaw and evapotranspiration.

Long, M.R., Ulrich, A.C., Sego, D.C. 2010. A review of methods developed to solve the issue of weak mature fine tailings. Proceeding of the second international oil sands tailings conference, December 5-8, 2010, Edmonton, Alberta, Canada. Pp. 355-364.

Martel, C.J. 1988. Predicting freezing design depth of sludge-freezing beds. Journal of cold regions engineering, 2 (2): 145-156.

Martel, C.J. 1989. Development and design of sludge freezing beds. Journal of environmental engineering, 115 (4):799-808.

Martel, C.J. 1993. Fundamentals of sludge dewatering in freezing beds. Water Science and Technology, 28 (1): 29-35.

Mihiretu, Y., Chalaturnyk, R., Scott, J.D. 2008. Tailings segregation fundamentals from flow behavior perspective. Proceeding of the first international oil sands tailings conference, December 7-10, 2008, Edmonton, Alberta, Canada. Pp. 112-120.

Mikula, R.J., Munoz, V.A., Lam, W.W., and Payette, C. 1993. Structure in oil sands fine tailings. Proceeding of oil sands: our petroleum future conference, April 4-7, 1993, Edmonton, Alberta, Canada. F4.

Mitchell, J.K., Soga, K. 2005. Fundamentals of soil behavior, 3rd edition. John Wiley and Sons, Inc., New York.

Nixon, J.F., Morgenstern, N.R. 1973. The residual stress in thawing soils. Canadian geotechnical journal, 10 (4): 571-580.

Nixon, J.F., McRoberts, E.C. 1973. A study of some factors affecting the thawing of frozen soils. Canadian geotechnical journal, 10 (3): 439-452.

Pollock, G.W. 1988. Large strain consolidation of oil sand tailings sludge. M.Sc. thesis. University of Alberta.

Proskin, S. 1998. A geotechnical investigation of freeze-thaw dewatering of oil sands fine tailings. Ph.D. dissertation, University of Alberta.

Qiu, Y. 2000. Optimum deposition for sub-aerial tailings disposal. Ph.D. dissertation, University of Alberta.

Rosenqvist, I.Th. 1953. Considerations of sensitivity of Norwegian quick-clays. Geotechnique, 3(5): 195-200.

Sego, D.C. 1992. Influence of pore fluid chemistry on freeze-thaw behavior of Suncor oil sand fine tails (Phase I). Submitted to reclamation research technical advisory committee, Alberta Environment, Pp35.

Sego, D.C. and Dawson, R.F. 1992. Influence of freeze-thaw on behavior of oil sand fine tails. Submitted to Alberta oil sand technology and research authority.

Sobkowicz, J.C. and Morgenstern, N.R. 2009. A geotechnical perspective on oil sands tailings. Proceeding of the thirteenth international conference on tailings and mine waste, November 1-4, 2009, Banff, Alberta, Canada. Keynote presentation.

Sridharan, A. and Sreepada Rao, A. 1981. Rectangular hyperbola fitting method for one dimensional consolidation. Geotechnical testing journal, 4(4): 161-168.

Sridharan, A., Murthy, N.S., and Prakash, K. 1987. Rectangular hyperbola method of consolidation analysis. Geotechnique, 37(3): 355-368.

Suthaker, N.N. 1995. Geotechnics of oil sand fine tailings. Ph.D. dissertation, University of Alberta.

Abazari Torghabeh, E. 2012. Personal communication.

Zhang, C., Alostaz, M., Beier, N., and Sego, D.C. 2009. Cross flow filtration of oil sand total tailings. Proceeding of the thirteenth international conference on tailings and mine waste, November 1-4, 2009, Banff, Alberta, Canada. Pp. 799-812.

Znidarcic, D., Croce, P., Pane, V., Ko, H.Y., Olsen H.W. and Schiffman R.L. 1984. The theory of one-dimensional consolidation of saturated clays, III, existing testing procedures and analyses. Geotechnical testing journal, 7 (3): 123-133.

APPENDIX A Instruments Calibration

A.1 Loading system for frozen/thawed samples

As shown in Figure A1, two independent air pressure systems were used to apply loads on frozen/thawed samples in slurry consolidometers. The ranges of dial gauge and regulator in the main line are 0-1100 kPa and 2-120 psi, respectively. The range of dial gauge and regulator in the branch lines are 0-100 kPa and 0-20 psi, respectively. BenchLink data logger 3 was chosen to record data of air-pressure, deformation, pore pressure, and temperature. The air pressure transducers were calibrated with Omega DPI 610 pressure calibrator (Figure A2 and Figure A3). The obtained values of gain and offset were input in the software.

A.2 Loading system for as-received samples

Three belloframs were used to apply higher loads on as-received samples and load ring was used in the calibration (Figure A4). Friction exists between piston and the air chamber of bellofram. In order to ensure the pressure applied on the MFT sample is the same as the readings from data logger, the bellofram and pressure transducer were calibrated as a whole. Place load ring in the frame and adjust the regulator to apply pressure. The range of the load ring is 0 lb to 500 lb and 9.5 divisions represent 1 kg. The pressure (kPa) applied on samples equals to the force (kN) measured by load ring over the area of cell cross section (m^2). The force (N) equals to the number of divisions divided by 9.5 and multiplied by 9.81. Table A1 presents the details of calculation. Figure A5 to Figure A7 show the relationship between the pressure measured and the readings from data logger.

A.3 LVDT

Totally six LVDT were calibrated and used for measuring deformation during consolidation. The relationship between actual deformation and output readings was first determined and then the linear part was found. The calibrations of all LVDT are shown in FIGURE A8 to FIGURE A16.

A.4 Pore pressure transducer

Six pore pressure transducers were used to determine excess pore pressure during consolidation. Figure A17 presents the calculation graphs supplied by the transducer manufacture. In addition, all transducers were re-calibrated by changing the water heights in consolidometer. Figure A18 to Figure A23 are the relationships between changes in thickness of water and pore pressure readings. All pressure readings are very small and errors exist in measuring the thickness. Pressure transducer is considered as satisfied when the slope of curve is close to 0.1.

TABLE A1 The details of bellofram systems Calculation

	NO.	Divisions of load ring	Force of load ring (kg)	Pressure on sample (kPa)	Readings from software (kPa)
BELLO ONE	1	14.20	1.49	1.80	1.90
	2	83.90	8.83	10.66	10.30
	3	162.10	17.06	20.60	19.70
	4	243.20	25.60	30.90	29.92
	5	327.10	34.43	41.56	40.72
BELLO TWO	1	20.70	2.18	2.63	1.99
	2	80.10	8.43	10.18	9.94
	3	160.90	16.94	20.44	20.20
	4	244.20	25.71	31.03	30.23
	5	312.70	32.92	39.73	38.87
BELLO THREE	1	26.10	2.75	3.32	2.50
	2	88.20	9.28	11.21	10.80
	3	156.00	16.42	19.82	19.50
	4	222.20	23.39	28.23	27.40
	5	306.10	32.22	38.89	38.15

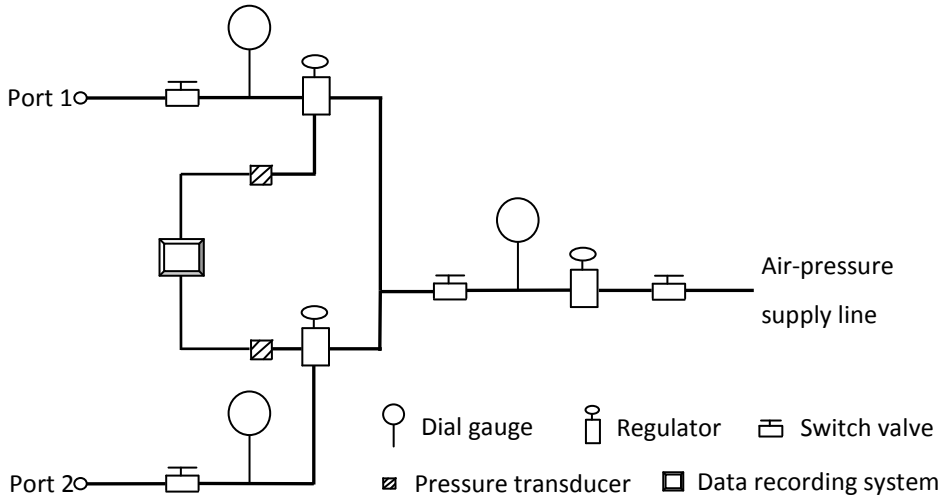

FIGURE A1 Design of air-pressure loading systems

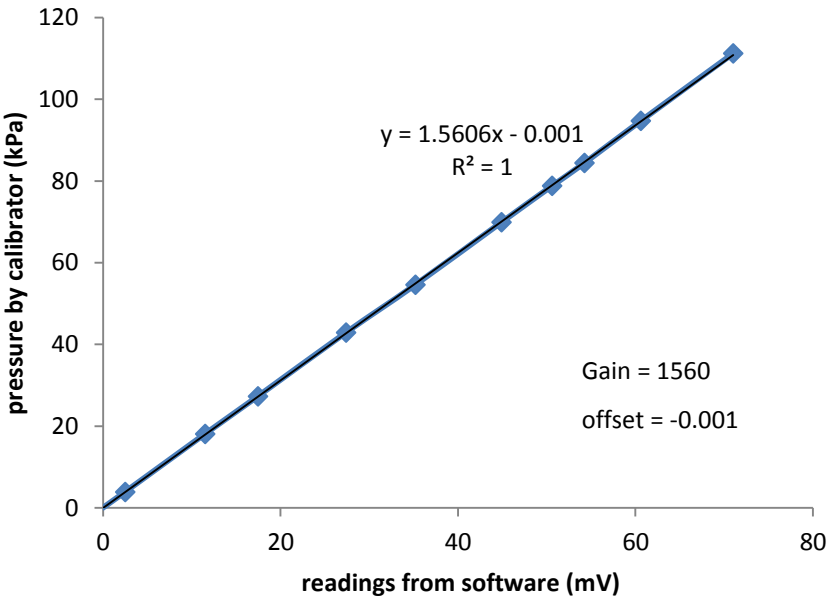

FIGURE A2 The relationship between output readings and actual pressure of transducer one

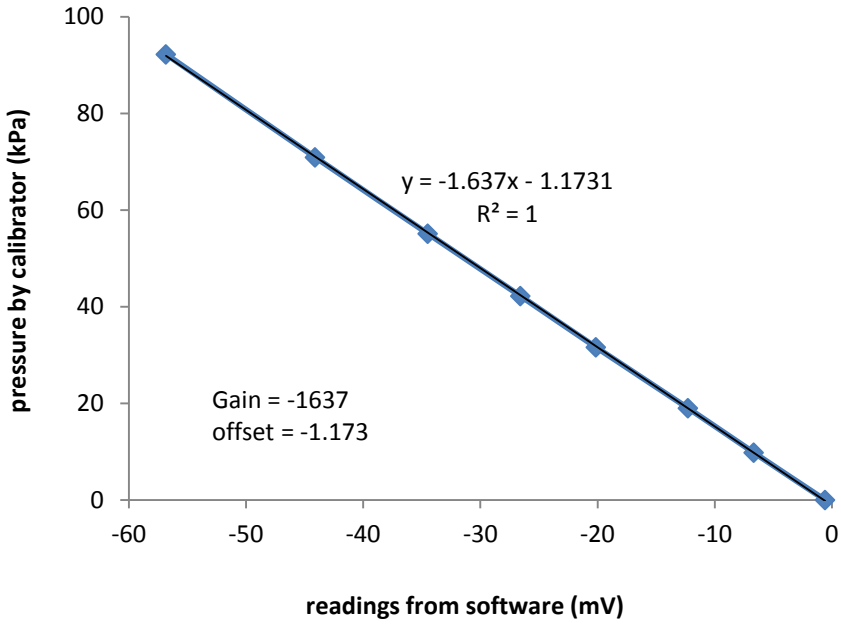

FIGURE A3 The relationship between output readings and actual pressure of transducer two

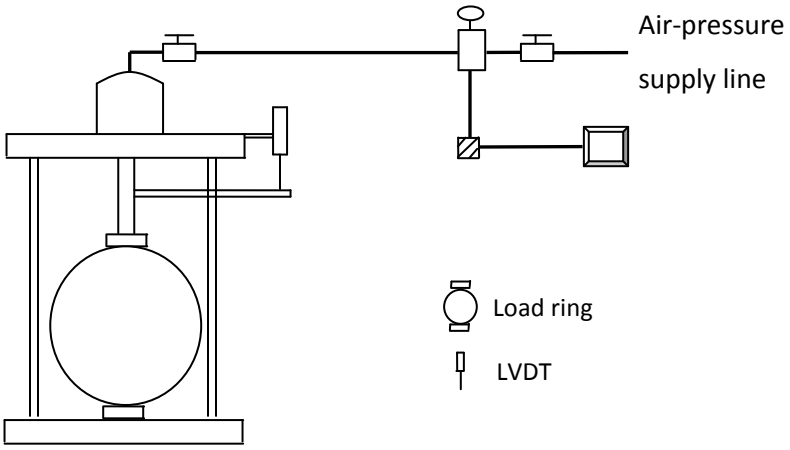

FIGURE A4 Layout of bellofram loading system and load ring

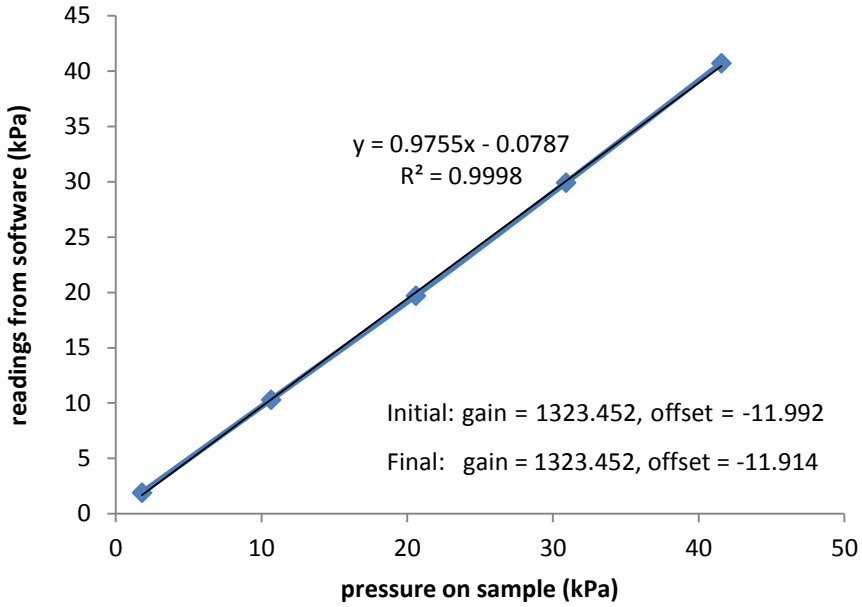

FIGURE A5 The relationship between measured pressure and pressure readings from data logger for bellofram one

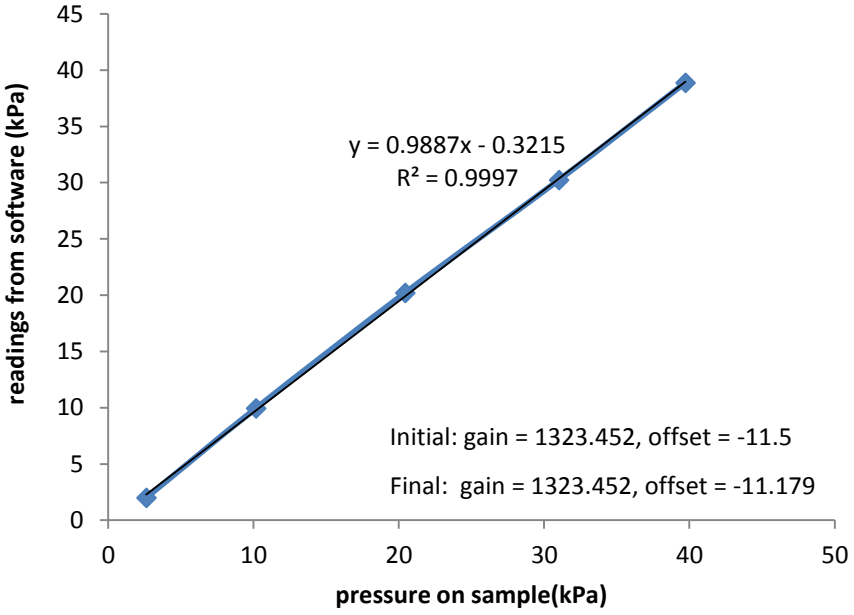

FIGURE A6 The relationship between measured pressure and pressure readings from data logger for bellofram two

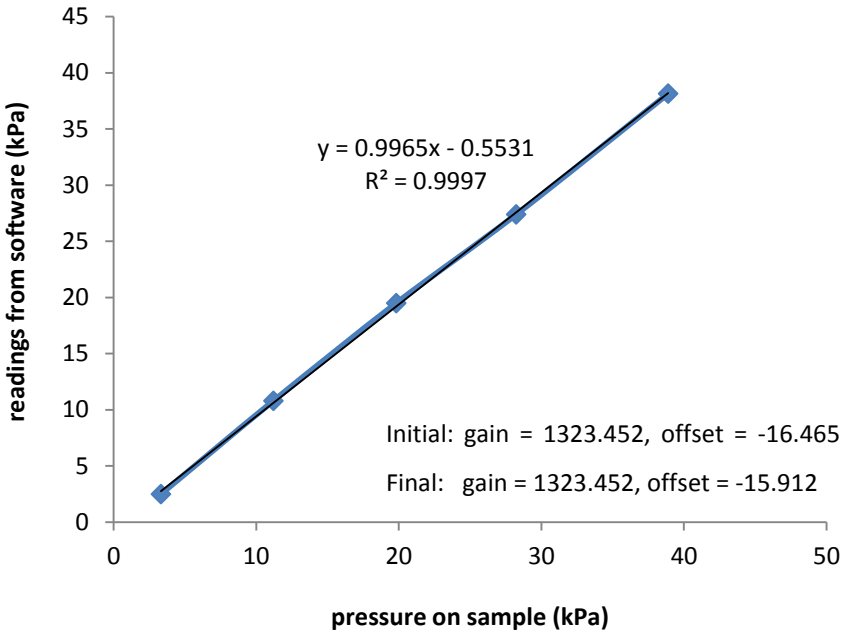

FIGURE A7 The relationship between measured pressure and pressure readings from data logger for bellofram three

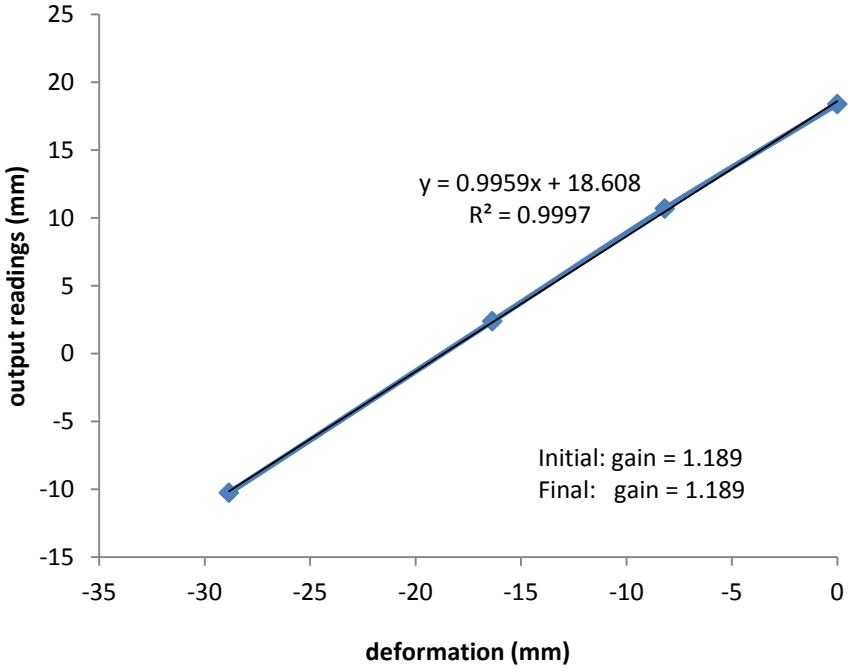

FIGURE A8 Calibration of LVDT for as-received sample one

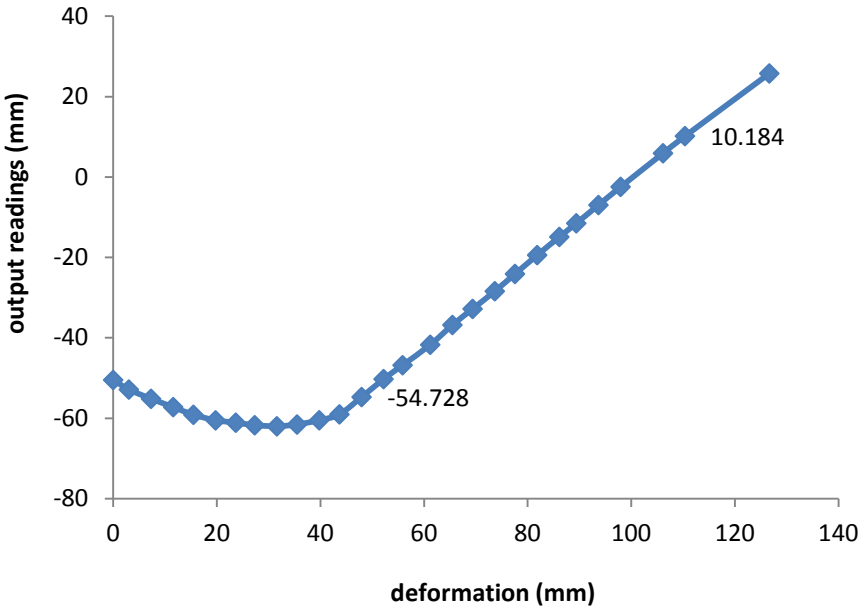

FIGURE A9 Calibration of LVDT for as-received sample two

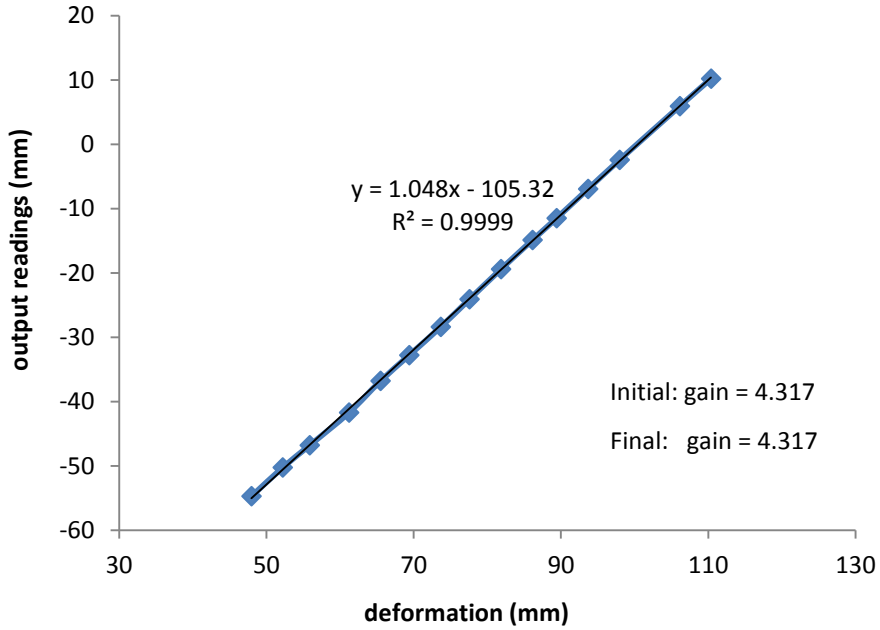

FIGURE A10 Calibration of LVDT for as-received sample two

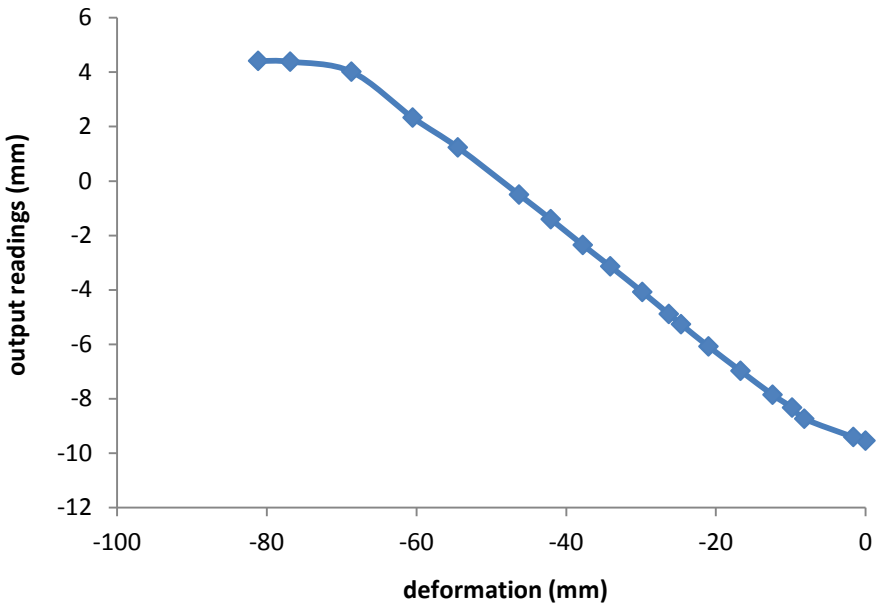

FIGURE A11 Calibration of LVDT for as-received sample three

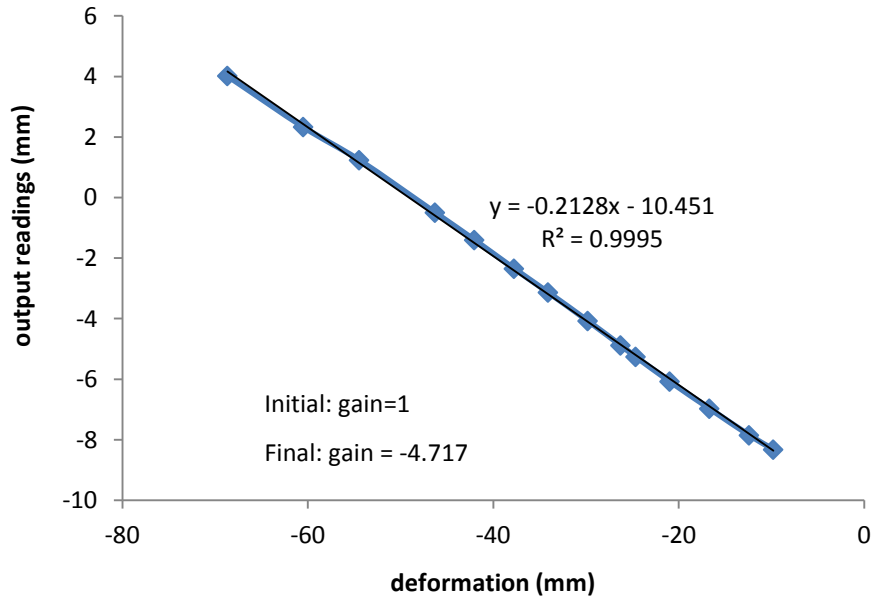

FIGURE A12 Calibration of LVDT for as-received sample three

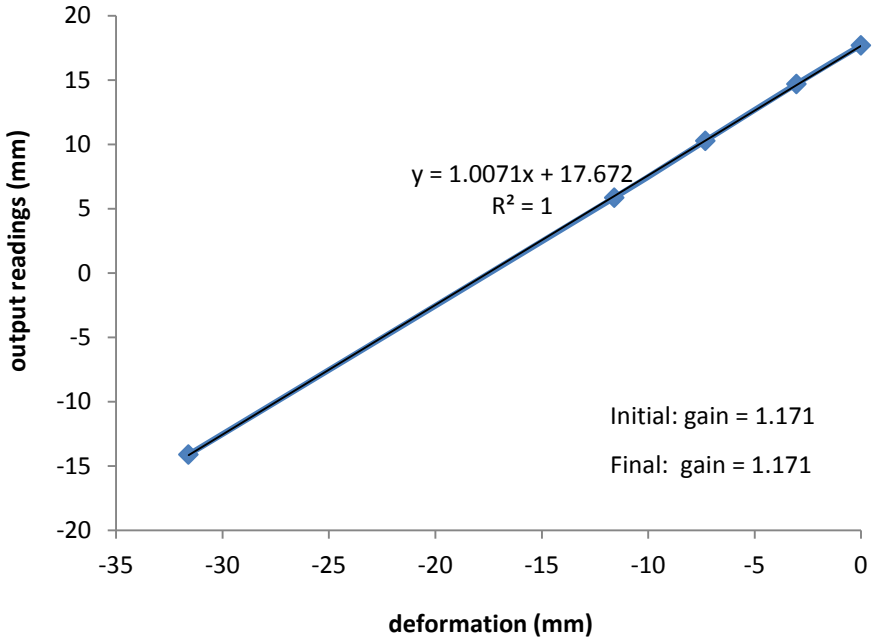

FIGURE A13 Calibration of LVDT for as-received sample four

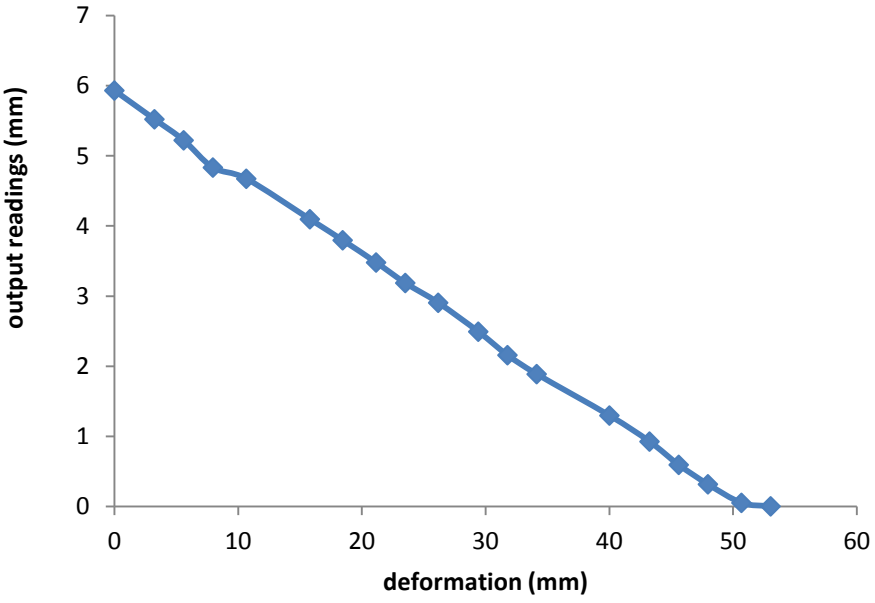

FIGURE A14 Calibration of LVDT for frozen/thawed sample one

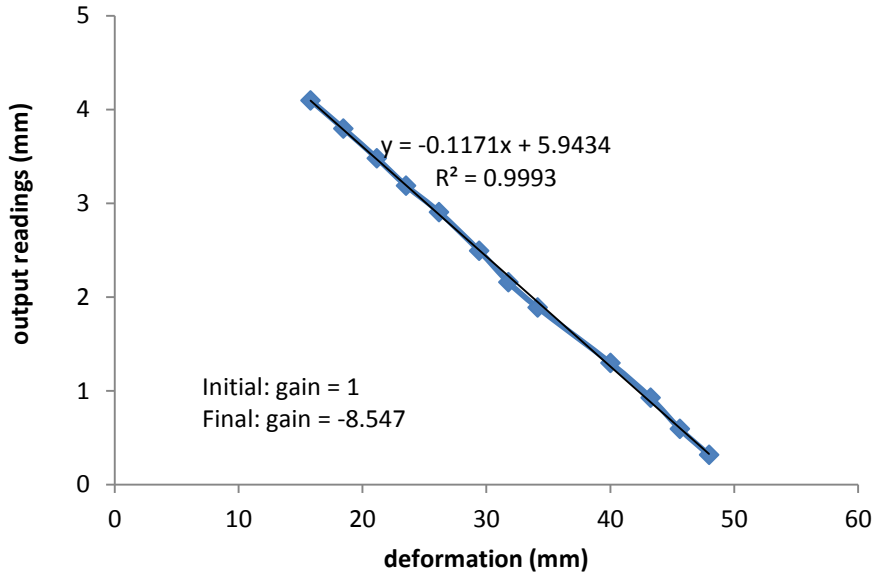

FIGURE A15 Calibration of LVDT for frozen/thawed sample one

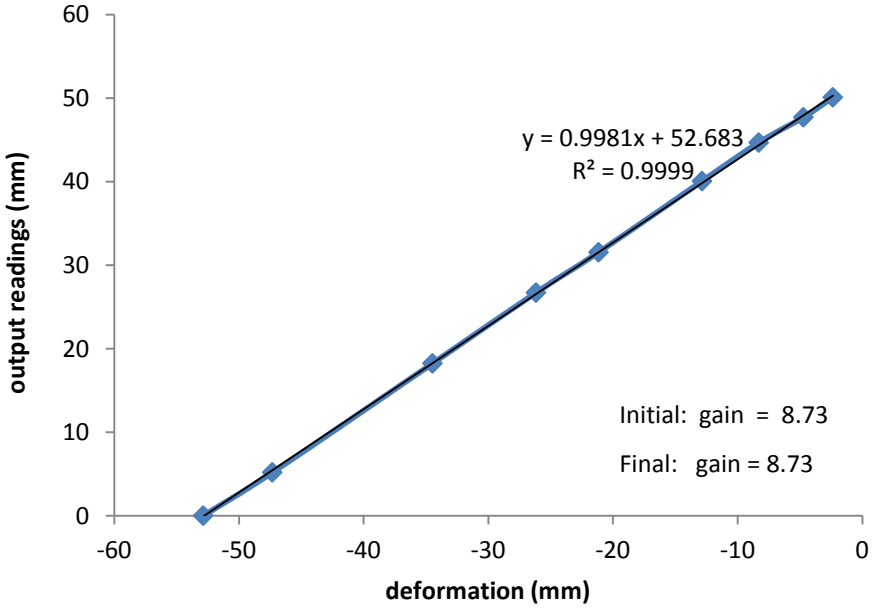

FIGURE A16 Calibration of LVDT for frozen/thawed sample two

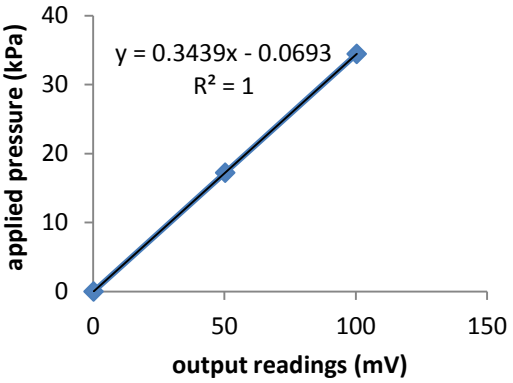

(a) as-received sample one

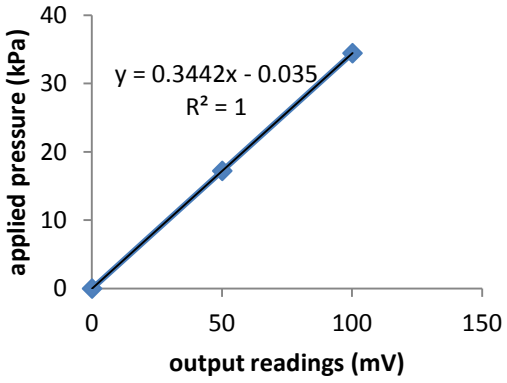

(b) as-received sample two

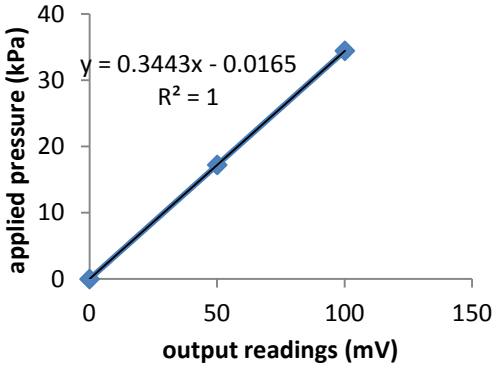

(c) as-received sample three

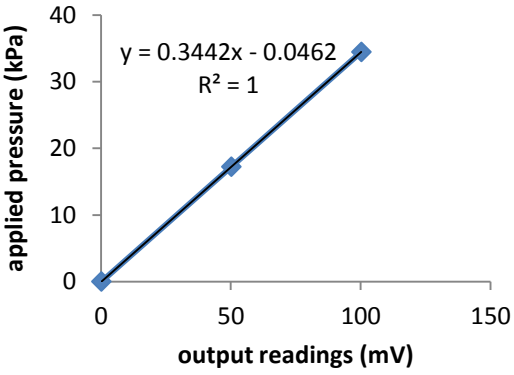

(d) as-received sample four

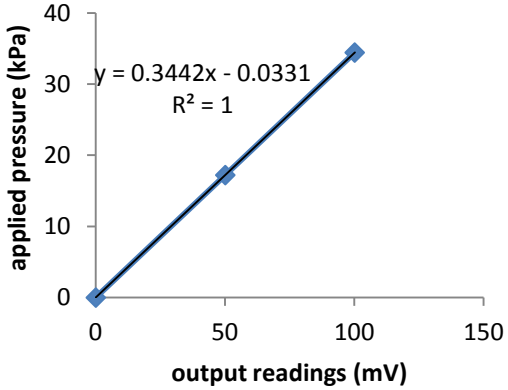

(e) frozen/thawed sample one

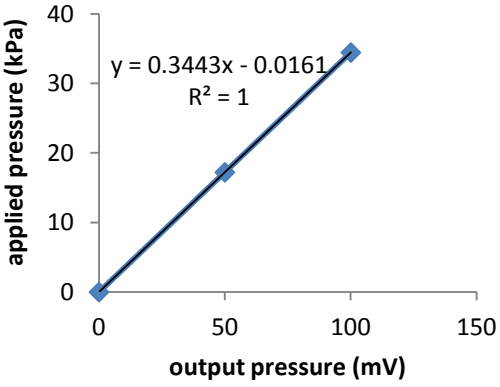

(f) frozen/thawed sample two

FIGURE A17 Supplied calibration with pore pressure transducer

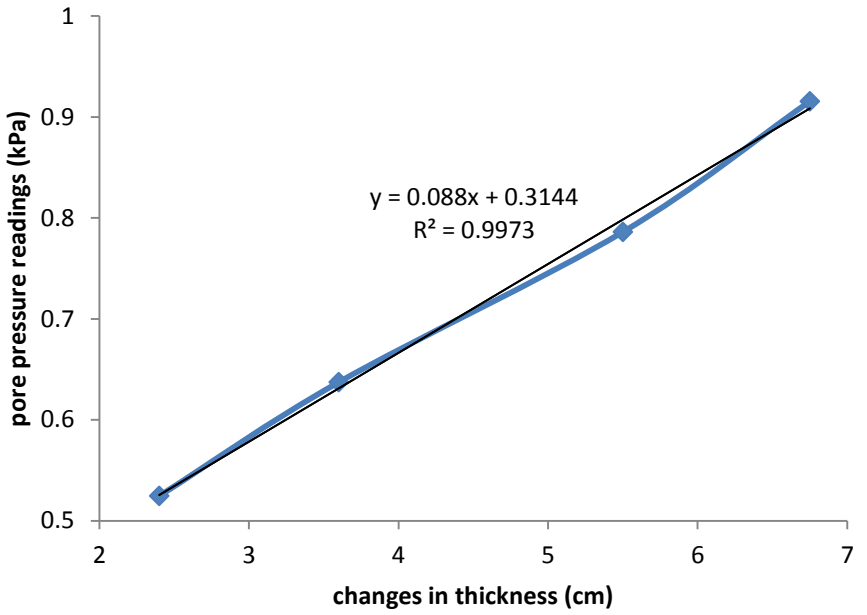

FIGURE A18 Calibration of pore pressure transducer for as-received sample one

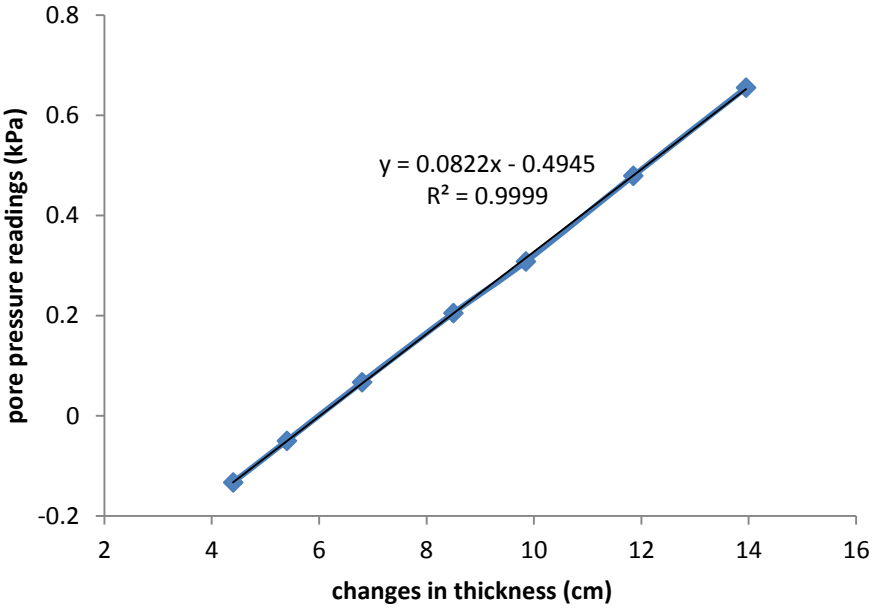

FIGURE A19 Calibration of pore pressure transducer for as-received sample two

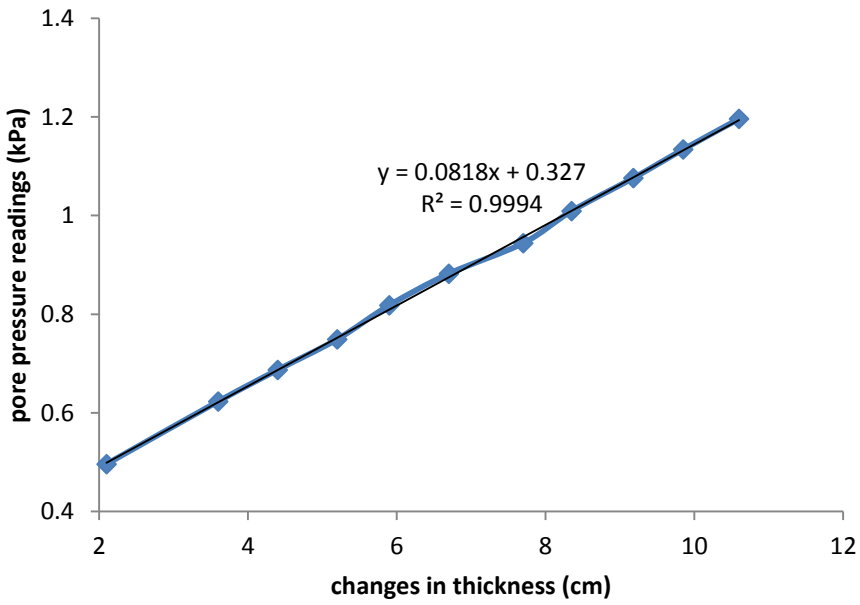

FIGURE A20 Calibration of pore pressure transducer for as-received sample three

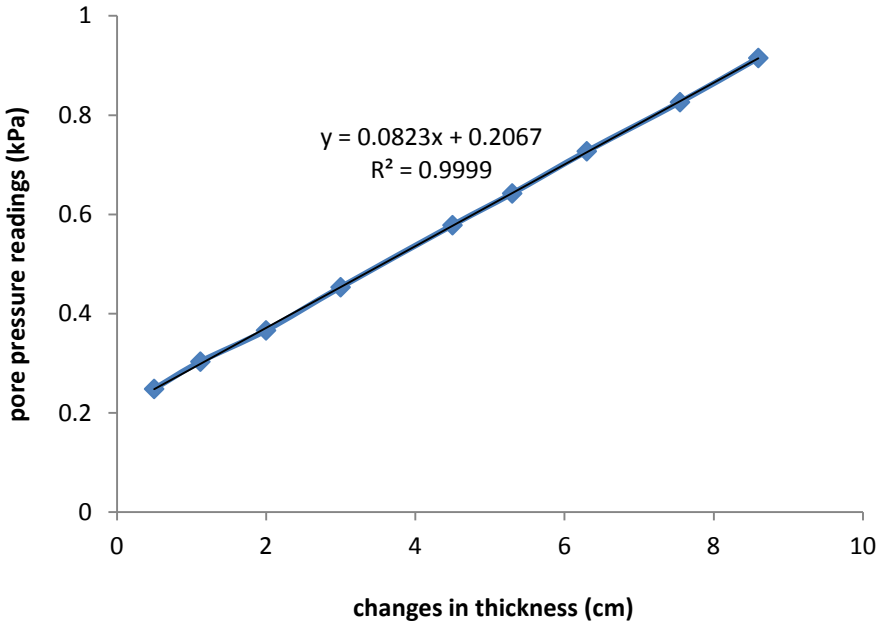

FIGURE A21 Calibration of pore pressure transducer for as-received sample four

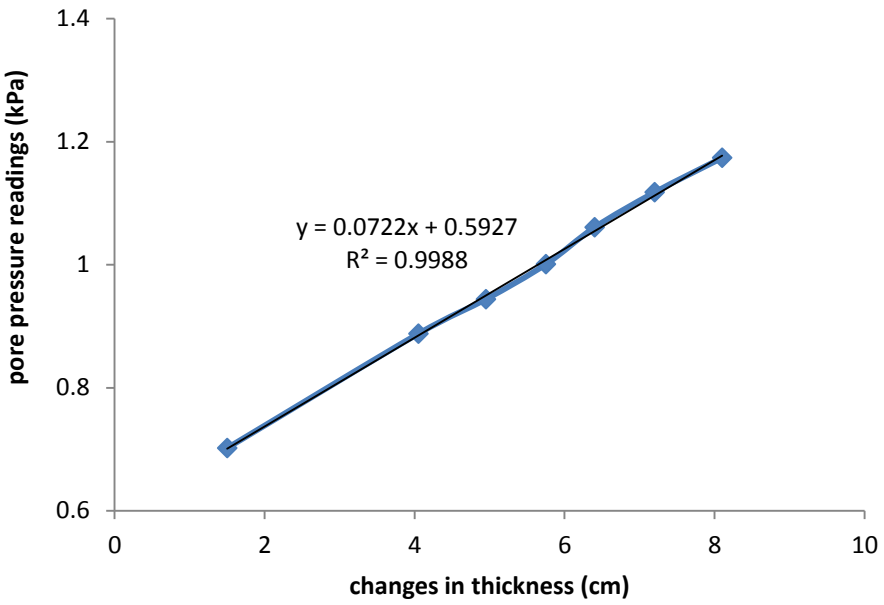

FIGURE A22 Calibration of pore pressure transducer for frozen/thawed sample one

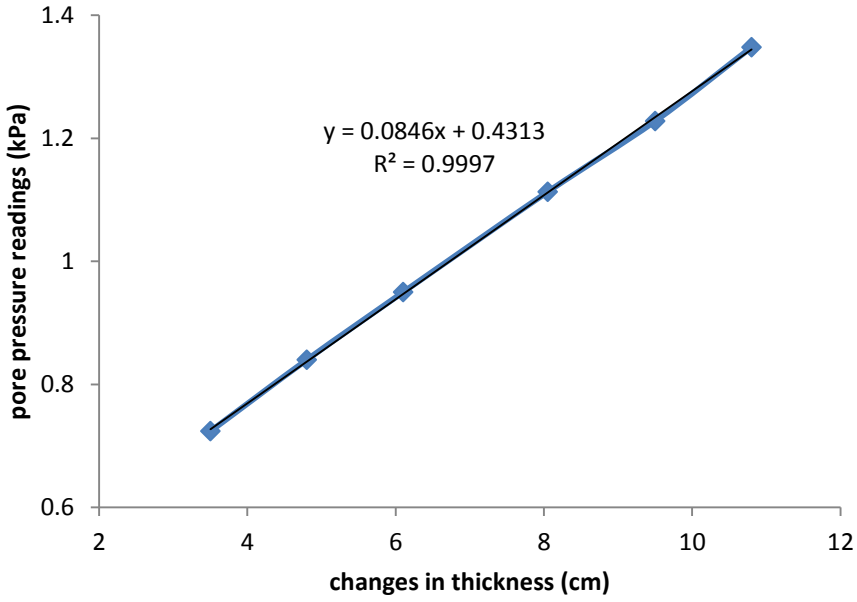

FIGURE A23 Calibration of pore pressure transducer for frozen/thawed sample two

APPENDIX B Design and Modification

B.1 Dead weight design for consolidation of as-received MFT

Dead weights were designed to consolidate as-received MFT at stress level smaller than 10 kPa. A porous plastic plate (Figure B1) was used during the early stages as its buoyant weight is negligible. The threaded needle of LVDT was screwed into the central hole. A tiny nut was mounted on top of the plate to keep the plate perpendicular to the needle. To avoid any interaction between the surface water and dead weights, a plastic platform (Figure B2) was designed to carry load of 0.23 kPa. The PVC loading cap in Figure B3 was designated to carry higher loads. The rod besides it is used to lift and lower the loading. LVDT needle can be placed on top of the cap of the rod for displacement measurement. The weight of loading cap is 5.3 N and it has two layers of porous stone. The buoyant weight of the loading cap is about 0.5 kPa as it submerged in surface water about 3 cm to 4 cm at stress level of 0.5 kPa. The design of load discs for overburden at 2 kPa and 4 kPa are shown in Table B1. Figure B4 shows the dimensions of base cell and top cell. The cell can accommodate sample with height of 13 to 15 cm, and 10 cm. Figure B5 presents the side view of the aluminum base plate.

B.2 Buoyant weight of freezing plate

The first overburden stress after freeze-thaw is the buoyant weight of the freezing plate (Figure B6). Its gravity weight is 14.22 N and the uplift force generated by water equals to 4.35 N. Therefore, the buoyant weight is 9.87N and the average effective pressure applied on sample is 1.23 kPa. In order to ensure free upward drainage, gaskets were placed between porous stone and freezing plate (Figure B7). In addition, the holes on bottom of rolling diaphragm (Figure B8) should be punched exactly to ensure the air tightness.

B.3 Vane shear tests

Undrained shear strength was measured by programmable viscometer and manual vane shear machine. Figure B8 shows the location and sequence of testing points using small spindles (e.g., spindle #75). The number of testing points should be less to ensure the accuracy when using larger spindles. Figure B9 gives the geometry of designed spindle for manual vane shear machine. Figure B10 presents the conversion between torque measured by spring and stress around spindle. Linear/constant stress distribution around spindle is assumed and stress around the rod is ignored. The surface area of inserted rod becomes relative large to the surface area of spindle column when testing shear strength at deeper points. It should be considered during the result analysis. Table B2 and Table B3 summarize the ranges of stress that viscometer and manual vane shear machine can measure using various spindles and springs.

B.4 Procedures of Freezing Tests

Three freeze/thaw cells and two temperature controlling systems (BATHs) were used to investigate the effect of freezing rate on dewatering. Samples were frozen in a series connection and thawed together. Figure B11 shows the procedure and boundary condition of freezing tests.

TABLE B1 Design of dimensions of load discs

Overburden (kPa)	Added load (kPa)	Added weight (kg)	Disc H (cm)	Disc D (cm)
2	1.5	1.23	2.45	9
4	2	1.63	3.25	9

NOTE: density of steel disc $\rho = 7.8\ g/cm^3$, inner diameter of cell d = 10.1 cm, inner area of cell A = 80 cm^2.

TABLE B2 Determinable shear stress with various spindles and springs (Manual Vane Shear)

Spindle No.	H (mm)	D (mm)	K (mm^3)	τ (kPa) at T_{min} = 0.25	τ (kPa) at T_1 = 1.75	τ (kPa) at T_2 = 4.75	τ (kPa) at T_3 = 6	τ (kPa) at T_4 = 7.5
1	25	12.5	7159	3.49	24.45	66.35	83.82	104.77
2	15	12.5	4704	5.31	37.20	100.97	127.55	159.43
3	12.5	12.5	4091	6.11	42.78	116.12	146.68	183.35
4	38	19	25140	0.99	6.96	18.89	23.87	29.83

Note: T_{min} is the minimum torque (kg·cm) that can be measured. T1, T2, T3 and T4 are the maximum torque that can be measured by corresponding springs.

TABLE B3 Range of undrained shear strength measured by viscometer

Spindle No.	H (mm)	D (mm)	K (cm^3)	T_{max} ($\times 10^{-6}$ N·m)	τ (Pa)
# 71	68.78	34.39	145.00	718.7	4.82
# 72	43.38	21.67	37.31	718.7	19.26
# 73	25.35	12.67	7.45	718.7	96.43
# 74	11.76	5.89	0.75	718.7	961.52
# 75	16.1	8.03	1.90	718.7	378.09

Note: T_{max} is the maximum torque the spring can bear.

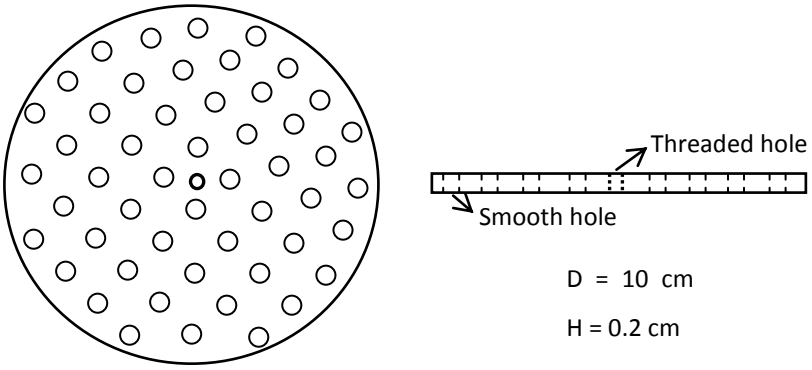

(a) Plan view (b) Side view

FIGURE B1 porous plastic plate

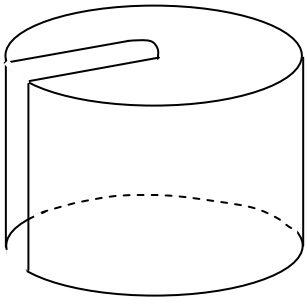

FIGURE B2 Design of plastic platform

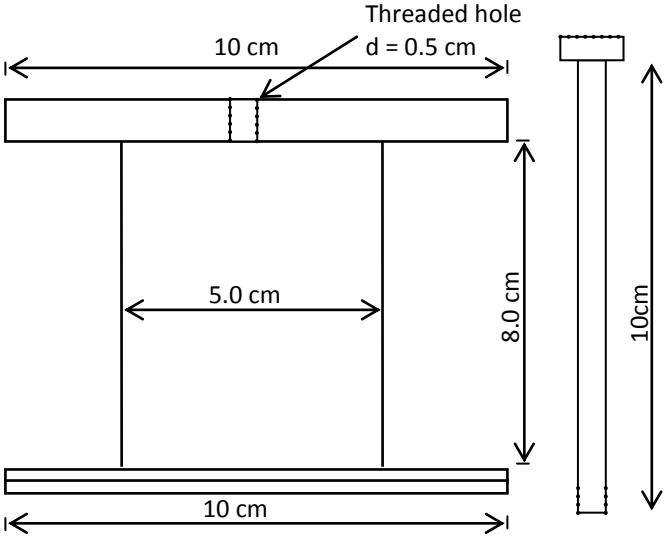

FIGURE B3 Design of PVC loading cap and rod

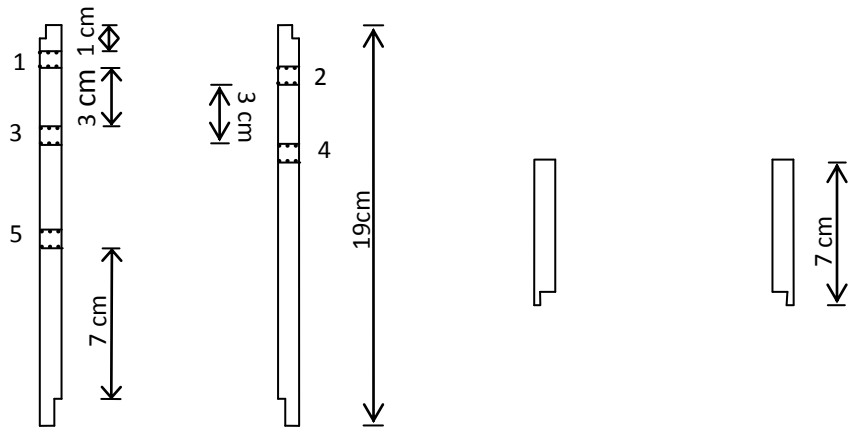

NOTE: Thickness of cell wall is half inch. Diameter of side ports = ¼ inch. Port 2 is right beneath port 1 in elevation, similarly for port 3 and port 4. Port 5 is used to drain water out at the end of the test. Solid screw is used in port 5. The bottom cut of base cell is used to hold porous stone and base plate. The top cut of base cell is used to hold top cell in place.

FIGURE B4 Design of base cell and top cell of consolidometer

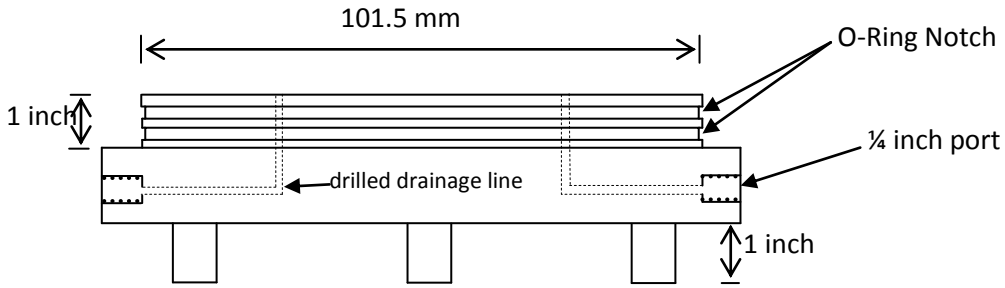

FIGURE B5 Side view of aluminum base plate

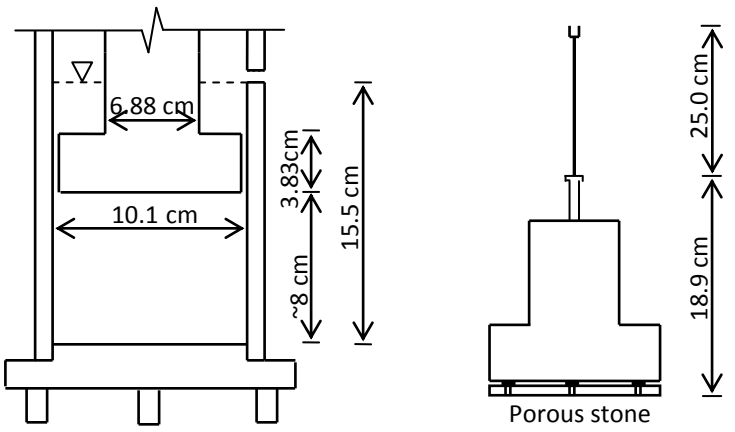

FIGURE B6 Information for determining the buoyant weight of freezing plate

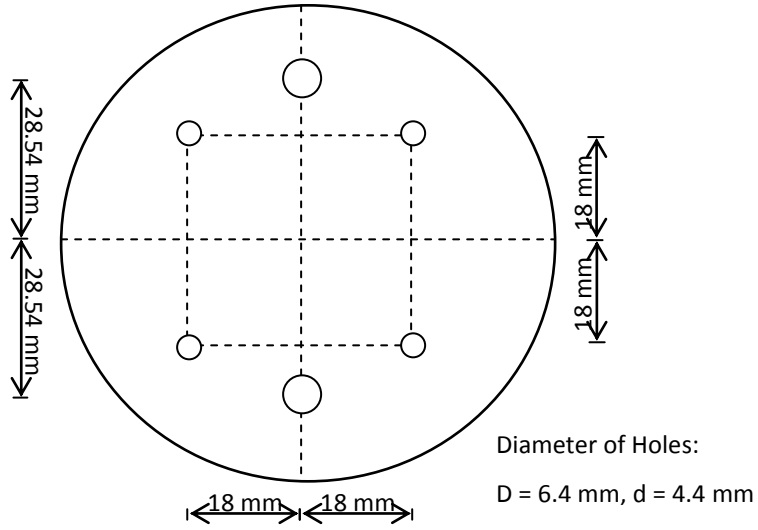

FIGURE B7 Deployment of holes on bottom of rolling diaphragm

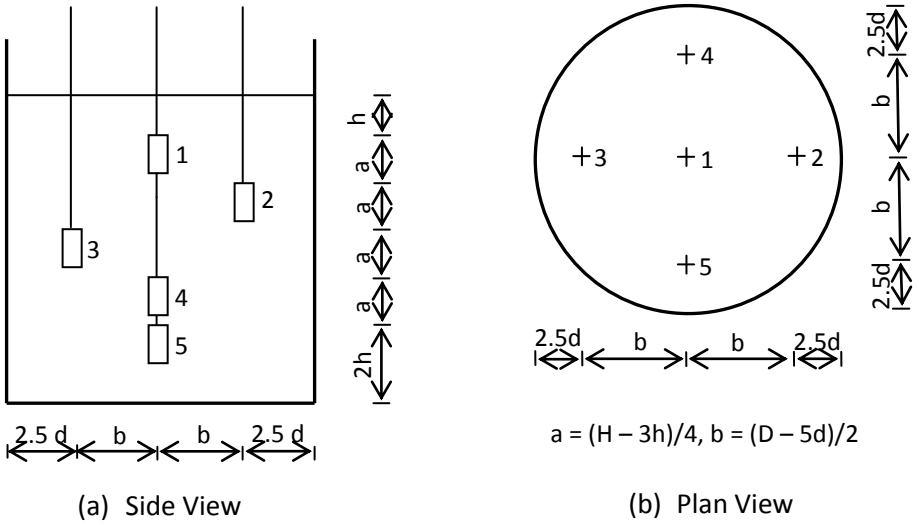

FIGURE B8 Deployment and sequence of vane shear testing points

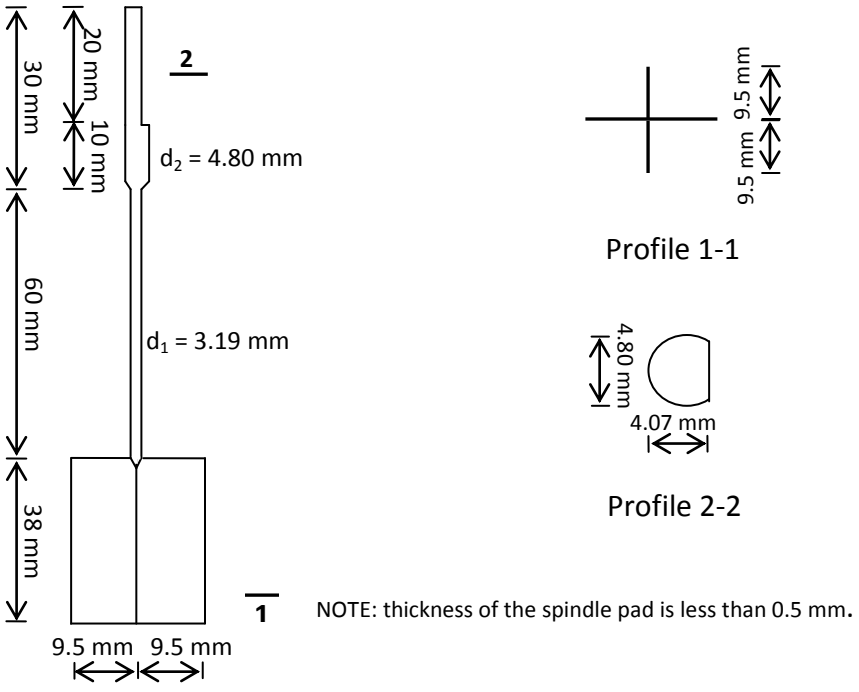

FIGURE B9 Design of spindle for manual vane shear instrument

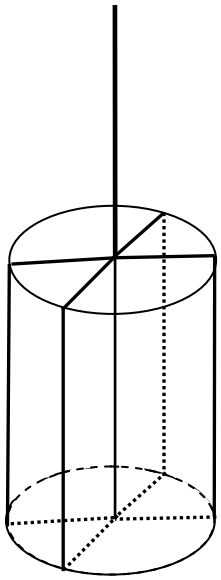

$T = \tau \times A$, τ = constant;

Assume no torque around the rod.

$T_{total} = T_{side} + T_{top} + T_{bottom}$;

$$T = \frac{\pi D^3}{2}\left(\frac{H}{D} + \frac{1}{3}\right)\tau;$$

$$K = \frac{\pi D^3}{2}\left(\frac{H}{D} + \frac{1}{3}\right);$$

FIGURE B10 Determination of undrained shear strength in vane shear test

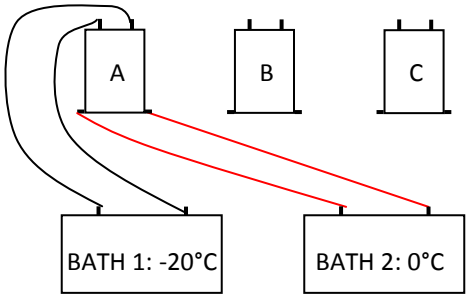

(a) Duration t = 3 days

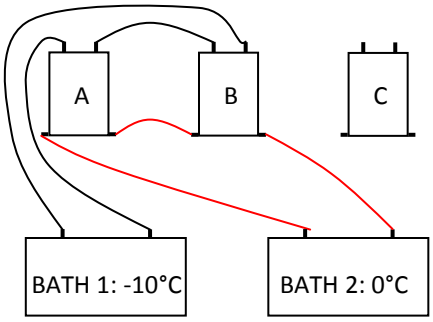

(b) Duration t = 3 days

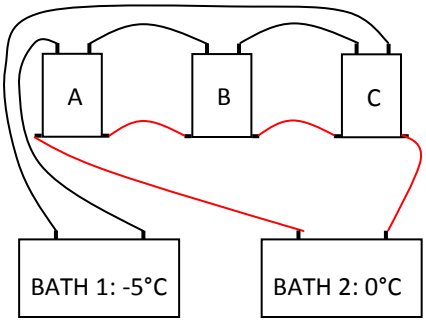

(c) Duration t = 3 days

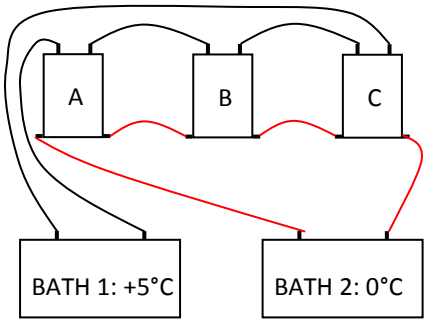

(d) Duration t = 4 days

FIGURE B11 Procedures of freezing tests

APPENDIX C Material Properties

The basic properties of MFT, including water content/solids content (Table C1), void ratio, liquid limit (Figure C1 & Table C2), plastic limits (Table C3), fines content (Table C4), specific gravity (Table C5), bitumen content (Table C6), bulk density (Table C7), and particle size distribution (Table C8) were determined in accordance with ASTM standards.

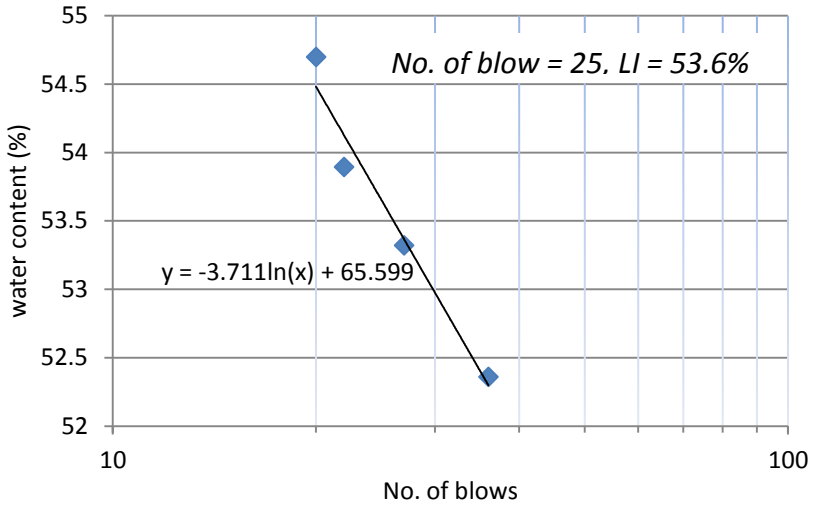

FIGURE C1 The relationship between No. of blows and water content

TABLE C1 Moisture content and solids content of Albian MFT

#	Tare (g)	Tare+Wet (g)	Tare+Dry (g)	SC (%)	MC (%)
1	1.59	65.87	25.09	36.56	173.53
2	1.59	59.02	22.59	36.57	173.47
3	1.59	64.55	24.61	36.56	173.50
			AVG	*36.56*	*173.50*

NOTE: SC = solids content, MC = moisture content.

TABLE C2 Liquid limit of Albian MFT

#	Tare (g)	Tare+Wet (g)	Blows	Tare+Dry (g)	MC (%)
1	1.59	19.02	36	13.03	52.36014
2	1.59	18.44	27	12.58	53.3212
3	1.58	16.4	22	11.21	53.89408
4	1.59	20.03	20	13.51	54.69799

TABLE C3 Plastic limit of Albian MFT

#	Tare (g)	Tare+Wet (g)	Tare+Dry (g)	MC (%)
1	1.59	7.78	6.47	26.84
2	1.59	7.15	5.97	26.94
			AVG	*26.89*

TABLE C4 Fines content of Albian MFT

		Before washing		After washing		
#	Beaker	Beaker+Wet (g)	Dry (g)	Tare (g)	Tare+Dry	f (%)
1	160.38	825.49	243.18	1.54	1.87	0.999
2	216.86	931.11	261.15	1.6	2.08	0.998
					AVG	*0.998*

NOTE: fine content =100 %×(1-(dry weight after washing/dry weight before washing)).

TABLE C5 Specific gravity of Albian MFT (De-air by suction)

	Preparation		Drying			
Pyc (g)	Pyc+H_2O	Phc+H_2O+MFT (g)	Tray (g)	Tray+Dry (g)	G_t	G_{20}
169.38	667.48	695.1	46.65	92.53	2.51	2.51

NOTE: T = 23.1°C, ρ_w = 0.998 g/cm^3, K = 0.999.

Calculate the specific gravity at soil solids the test temperature, G_t as follows,

$$G_t = \frac{\rho_s}{\rho_{w,t}} = \frac{M_s}{\left(M_{\rho w,t} - \left(M_{\rho ws,t} - M_s\right)\right)}$$

Where: ρ_s = the density of the soil solids (g/cm^3), $\rho_{w,t}$ = the density of water at the test temperature (g/cm^3), M_s = the mass of the oven dry soil solids (g), and $M_{\rho ws,t}$ = the mass of pycnometer, water, and soil solids at the test temperature (g).

Calculate the specific gravity of soil solids at 20°C as follows:

$$G_{20°C} = K \cdot G_t$$

Where: K = the temperature coefficient.

TABLE C6 Bitumen content of Albian MFT

#	Thimble (g)	Thimble+Dry MFT (g)	Thimble+bitumen removed MFT (g)	Bitumen Content (%)
1	6.4	81.37	80.38	1.32
2	4.9	82.34	81.37	1.25
			AVG	*1.29*

NOTE: bitumen content = 100 % × (bitumen/dry MFT)

TABLE C7 Density of Albian MFT

#	cylinder (g)	Cylinder+MFT (g)	Volume (cm3)	Density (g/m3)
1	594.8	1882.9	1000	1.29

TABLE C8 Size distribution of Albian MFT (Hydrometer 152H)

t (min)	Reading	T (°C)	R	%	K	L	D (μm)
2	55	23.6	48	97.03	0.01367	7.325	26.2
5	54.4	23.6	47.4	95.82	0.01367	7.423	16.7
15	51.1	23.6	44.1	89.15	0.01367	7.961	10.0
30	48.2	23.5	41.2	83.29	0.01367	8.433	7.2
60	46	23.6	39	78.84	0.01367	8.792	5.2
120	42.5	23.4	35.5	71.76	0.0137	9.363	3.8
250	39.1	23.6	32.1	64.89	0.01367	9.917	2.7
480	36	23.6	29	58.62	0.01367	10.422	2.0
1440	30.9	23.6	23.9	48.31	0.01367	11.253	1.2

For hydrometer 152H:

$$P = (Ra/W) \times 100$$

Where: $a =$ correction faction, $P =$ percentage of soil remaining in suspension at the level at which the hydrometer measures the density of the suspension, $R =$ hydrometer reading with composite correction applied, $W =$ oven-dry mass of soil in a total test sample represented by mass of soil dispersed.

$$D = K\sqrt{L/T}$$

Where: $D =$ diameter of particle (mm), $K =$ constant depending on the temperature of the suspension and the specific gravity of the soil particles.

APPENDIX D Vane Shear Strength & Solids Content

D.1 Vane shear strength

Vane shear tests were carried out to obtained undrained shear strength of MFT at different states. Figure D1 shows the shear stress versus time curve of remolded as-received MFT. Figure D2 shows the shear stress versus time curves at different depth of as-received MFT at the end of self-weight consolidation. The torque induced by the spindle rod was also considered. Figure D3 shows the geometry information of viscometer spindle and designed extension rod. Table D1 presents the correction for undrained shear strength. The calculation details are as follows:

$$S_{u\,corrected} = \frac{\left(\frac{S_u}{S_{u\,peak}}\right) \cdot T_{peak} - \Delta K \cdot S_{ur}}{K_{spindle}}$$

Where: $S_u =$ measured peak undrained shear strength, $S_{u\,peak} =$ the maximum shear strength that the viscometer can measure, $T_{peak} =$ the maximum torque that the spring can bear, $\Delta K =$ rod surface constant, $S_{ur} =$ the average residual shear strength around rod, $K_{spindle} =$ spindle constant.

In the investigation of the effect of freezing rate on dewatering, the thaw strain was determined (TABLE D2) as below:

$$H_{cal} = {M_w}\Big/{\left(\pi/_4\, D^2 \cdot \rho_w\right)}$$

$$H_f = H_0 + 9\% \times H_0 \times (1 - SC)$$

$$\varepsilon_t = 100\% \times {\Big(H_f - (H_0 - (H_{cal} + H_{mea})/2)\Big)}\Big/{H_f}$$

Where: $M_w =$ weight of surface water, $D =$ inner diameter of cell, $H_0 =$ initial sample height, $SC =$ solids content.

In addition, the undrained shear strengths of frozen/thawed MFT were measured. Figure D4 shows the shear stress versus time curves of frozen/thawed sample one. Figure D5 and Table D3 give the shear test results of frozen/thawed sample two. Figure D6 and Table D4 present the shear test results of frozen/thawed sample three. Figure D7 plotted the shear stress versus time relationship of frozen/thawed sample four. Table D5 summarized the shear tests results of both as-received MFT and frozen/thawed MFT at the end of consolidation under 20kPa/100 kPa.

D.2 Solids content

Solids content profiles were determined by measuring solids content by layer. Table D6 shows the solids content test results of as-received MFT at the end of self-weight consolidation. Table D7 to Table D10 present the solids content test results of frozen/thawed samples in the freezing rate investigation. Table D 11 to Table D15 are the solids content test results of both as-received and frozen/thawed MFT at the end of consolidation under 20 kPa/100 kPa.

TABLE D1 Correction for undrained shear strength by considering surface area of rod

#	Spindle	Depth (cm)	S_u (Pa)	S_{ur} (Pa)	ΔK (cm^3)	$S_{u\ corrected}$ (Pa)
1	74	1.6	74	44.9	0.064	70
2	75	4.5	99	50.1	0.456	87
3	75	7.2	124	44.9	1.470	112
4	75	9.2	244	59.3	1.755	189
5	75	10.2	284	61.2	1.924	222

TABLE D2 Thaw strain of all four samples in the freezing rate investigation

Cell No.	Con (g)	Con + H_2O (g)	H_{cal} (cm)	$H_{measured}$ (cm)	H_f (cm)	ε_t (%)
1	23.1	373.6	4.33	4.27	14.60	*36.31*
2	23.7	366	4.23	4.37	14.60	*36.30*
3	23.4	369.9	4.28	4.10	14.60	*35.56*
4	33.96	320.9	3.46	N/A	14.60	*30.55*

NOTE: Con = container, Con + H_2O = container plus surface water, H_{cal} = calculated water thickness, $H_{measured}$ = measured water thickness, H_f = frozen sample height, ε_t = thaw strain.

TABLE D3 Vane shear strength of sample two at 6.1 cm (manual vane shear instrument)

R_i (°)	R_f (°)	ΔR(°)	S_u (Pa)
164.5	190.3	25.8	702

NOTE: R_i = initial reading, R_f = final reading, ΔR = reading difference. Self-designed spindle and spring No. 1 were used.

TABLE D4 Vane shear strength of sample three at 6.1 cm (manual vane shear instrument)

R_i (°)	R_f (°)	ΔR(°)	S_u (Pa)
162.1	205.5	43.4	1182

NOTE: R_i = initial reading, R_f = final reading, ΔR = reading difference. Self-designed spindle and spring No. 1 were used.

TABLE D5 Shear strength of all samples at the end of consolidation

Sample #	R_i (°)	R_f (°)	ΔR (°)	T (kg·cm)	S_{up} (kPa)	S_{ur} (kPa)
AS – 2	169	325	156	1.39	19.46	—
	145.5	227	81.5	0.73	—	10.17
AS – 3	257	108.5	211.5	1.89	26.38	—
	166	284.5	118.5	1.06	—	14.78
AS – 4	163	348	185	1.65	23.07	—
	151	218	67	0.60	—	8.36
F/T – 1	47.8	170	122.2	3.14	9.59	—
	45	140	95	2.39	—	7.28
F/T – 2	73	250	177	1.58	22.08	—
	71	170	99	0.88	—	12.35

NOTE: AS = as-received sample, F/T = frozen/thawed sample, T = torque. Spring No. 2 and self-designed spindle were used for F/T – 2; spring No. 1 and spindle (H = 25 mm and D = 12.5 mm) were used for all other samples.

TABLE D6 Solids content of as-received sample at the end of self-weight consolidation

#	depth	depth	Tare (g)	Tare+wet	Tare+dry	SC (%)	WC (%)
1	4.0-4.5	0.25	1.76	62.6	24.42	37.25	168.49
2	4.5-5.5	1	2.11	80.13	31.64	37.85	164.21
3	5.5-6.0	1.75	1.67	77.31	30.58	38.22	161.64
4	6.0-7.0	2.5	1.6	78.55	31.15	38.40	160.41
5	7.0-7.5	3.25	2	78.59	31.54	38.57	159.28
6	7.5-8.0	3.75	1.67	87.61	35.09	38.89	157.15
7	8.0-9.0	4.5	1.59	85.86	34.68	39.27	154.67
8	9.0-10.0	5.5	1.59	91.09	37.03	39.60	152.54
9	10.0-11.0	6.5	1.57	100.51	41.13	39.98	150.10
10	11.0-12.0	7.5	1.58	85.65	35.63	40.50	146.90
11	12.0-12.5	8.25	1.62	93.96	39.32	40.83	144.93
12	12.5-13.5	9	1.58	82.96	35.22	41.34	141.91
13	13.5-14	9.75	1.61	94.91	40.76	41.96	138.31
14	14-15	10.5	1.61	103.4	45.31	42.93	132.93
15	15-15.5	11.25	1.61	47.91	21.83	43.67	128.98

TABLE D7 Solid content profile of frozen/thawed sample one (-20°C)

#	Depth	Tare (g)	Tare+Wet (g)	Tare+Dry	MC (%)	SC (%)
1	4.21	1.33	68.72	28.37	149.22	40.12
2	12.52	1.33	70.84	30.49	138.37	41.95
3	19.94	1.33	75.70	34.55	123.87	44.67
4	27.79	1.33	96.15	45.94	112.55	47.05
5	36.05	1.33	101.90	50.26	105.54	48.65
6	44.23	1.33	113.47	57.41	99.96	50.01
7	55.28	1.33	117.01	60.39	95.87	51.05
8	65.39	1.33	102.05	53.05	94.74	51.35
9	74.74	1.33	98.77	51.72	93.37	51.71
10	84.31	1.33	103.35	53.55	95.37	51.19
11	89.58	1.33	102.12	54.70	88.85	52.95

NOTE: MC = moisture content, SC = solids content.

TABLE D8 Solids content profile of frozen/thawed sample two (-10°C)

#	Depth	Tare (g)	Tare+Wet	Tare+Dry (g)	MC (%)	SC (%)
1	4.20	1.33	66.47	26.95	154.25	39.33
2	12.80	1.33	79.20	34.81	132.59	42.99
3	21.67	1.33	76.14	35.07	121.72	45.10
4	29.24	1.33	101.47	48.50	112.30	47.10
5	37.90	1.33	97.77	48.63	103.89	49.05
6	46.27	1.33	100.98	52.19	95.93	51.04
7	52.80	1.33	65.37	34.02	95.90	51.05
8	62.45	1.33	111.80	57.96	95.07	51.26
9	72.12	1.33	102.49	53.34	94.50	51.41
10	79.84	1.33	105.84	55.34	93.50	51.68
11	85.33	1.33	33.43	18.33	88.82	52.96
12	90.11	1.33	81.10	47.75	71.84	58.19

TABLE D9 Solids content profile of frozen/thawed sample three (-5°C)

#	Depth	Tare (g)	Tare+Wet	Tare+Dry (g)	MC (%)	SC (%)
1	4.90	1.33	72.27	31.95	131.68	43.16
2	13.17	1.33	71.37	33.07	120.67	45.32
3	20.80	1.33	104.36	51.09	107.05	48.30
4	28.94	1.33	113.81	58.19	97.82	50.55
5	35.55	1.33	73.37	38.57	93.45	51.69
6	42.89	1.33	60.37	31.79	93.83	51.59
7	50.11	1.33	88.09	44.82	99.49	50.13
8	56.51	1.33	68.71	36.89	89.48	52.78
9	64.26	1.33	93.91	53.43	77.70	56.28
10	74.71	1.33	123.75	69.56	79.42	55.73
11	84.71	1.33	84.93	47.40	81.46	55.11

TABLE D10 Solids content profile of frozen/thawed sample four (-5°C a)

Depth	#	Tare (g)	Tare+wet (g)	Tare+Dry (g)	MC (%)	SC (%)
0 – 2.5	1	1.61	64.4	31.18	110.07	47.09
	2	1.6	72	35.59	108.40	48.28
	3	1.64	83.9	41.88	108.08	48.92
2.5 – 5.5	4	1.62	65	34.15	102.32	51.33
	5	1.61	59.8	31.66	105.55	51.64
	6	1.65	98.4	50.97	105.47	50.98
5.5 – 7.0	7	1.62	59.9	29.48	135.32	47.80
	8	1.61	66.7	32.41	140.48	47.32
	9	1.63	82.9	34.97	184.56	41.02
7.0 – 9.5	10	1.65	65.1	25.7	250.96	37.90
	11	1.61	67.2	26.68	258.42	38.22
	12	1.6	53.7	21.45	341.27	38.10

TABLE D11 Solids content profile of as-received sample two at end of consolidation

No.	Tare (g)	Tare+Wet (g)	Tare +Dry	SC (%)	MC (%)
2	1.58	75.1	51.47	67.86	47.75
3	1.6	83.03	57.20	68.28	47.20
1	1.6	97.47	67.05	68.27	47.27
4	1.58	106.92	73.40	68.18	46.91
5	1.6	78.29	53.95	68.26	47.63
7	1.77	89.81	61.78	68.16	47.00
8	1.65	74.96	51.52	68.03	48.56
9	1.6	79.53	54.69	68.13	48.20
10	1.61	30.6	21.61	68.99	48.89
			AVG	*68.19*	*47.71*

TABLE D12 Solids content profile of as-received sample three at end of consolidation

No.	Tare (g)	Tare +Wet	Tare +Dry	SC (%)	MC (%)
b	1.57	3.05	2.62	70.95	40.95
c	1.6	111.05	76.08	68.05	46.95
d	1.6	103.19	71.07	68.38	46.24
e	1.6	111.19	77.51	69.27	44.37
f	1.6	105.62	73.59	69.21	44.49
g	1.69	128.44	88.84	68.76	45.44
h	1.87	131.68	88.64	66.84	49.60
			AVG	*68.73*	*45.43*

TABLE D13 Solids content profile of as-received sample four at end of consolidation

No.	Tare (g)	Tare+Wet (g)	Tare+Dry (g)	SC (%)	MC (%)
2	1.58	2.46	2.17	67.05	49.15
3	1.6	36.23	24.79	66.97	49.33
4	1.58	105.14	71.99	67.99	47.08
5	1.6	89.13	61.02	67.89	47.31
6	1.6	81.42	55.68	67.75	47.60
7	1.6	118.53	80.79	67.72	47.66
8	1.69	96.22	65.54	67.54	48.05
9	1.63	97.36	66.15	67.40	48.37
10	1.65	98.25	66.56	67.19	48.82
			AVG	*67.50*	*48.15*

TABLE D14 Solids content profile of frozen/thawed sample one at end of consolidation

No.	Tare (g)	Tare+ Wet	Tare+ Dry	SC (%)	MC (%)
1	1.57	48.13	31.47	64.22	55.72
2	1.61	55.78	37.45	66.16	51.14
3	1.6	71.68	48.08	66.32	50.77
4	1.6	84.53	56.68	66.42	50.56
5	1.58	61.11	41.04	66.29	50.86
6	1.58	67.39	45.19	66.27	50.91
7	1.57	46.7	31.35	65.99	51.54
8	1.62	72.25	47.94	65.58	52.48
9	1.6	66.62	44.13	65.41	52.88
10	1.59	65.11	43.39	65.81	51.96
11	1.6	81.41	54.46	66.23	50.98
			AVG	65.94	51.66

TABLE D15 Solids content profile of frozen/thawed sample two at end of consolidation

#	Tare	Tare+ Wet	Tare+ Dry (g)	SC (%)	MC (%)
a	1.56	34.63	23.6	66.65	33.35
b	1.58	68.14	47.99	69.73	30.27
c	1.6	97.05	68.7	70.30	29.70
d	1.59	100.93	71.56	70.43	29.57
e	1.59	143.91	101.96	70.52	29.48
f	1.6	111.64	77.94	69.37	30.63
g	1.91	145.78	102.27	69.76	30.24
h	1.69	5.91	4.62	69.43	30.57
			AVG	69.94	30.48

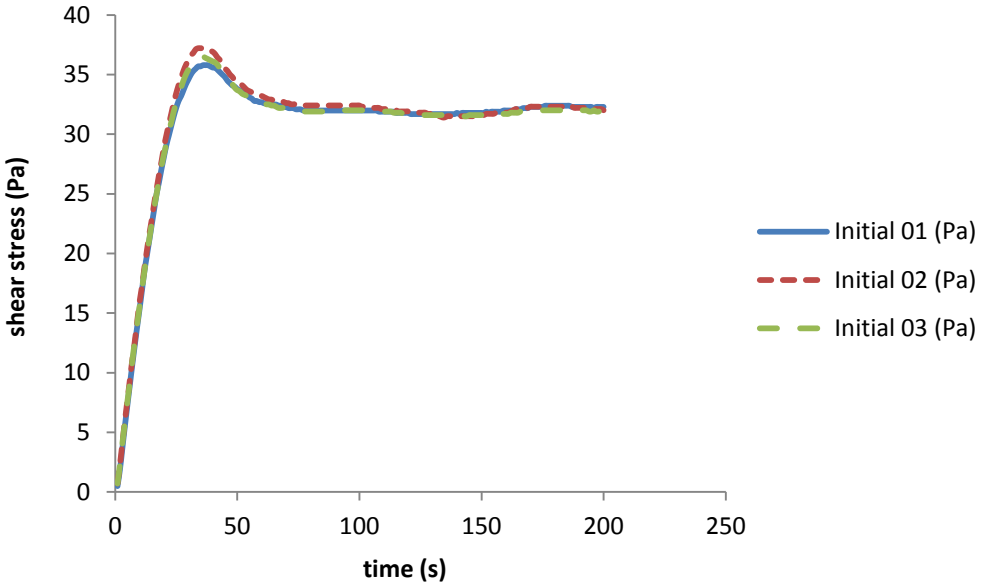

FIGURE D1 Initial shear stress versus time for as-received Albian MFT

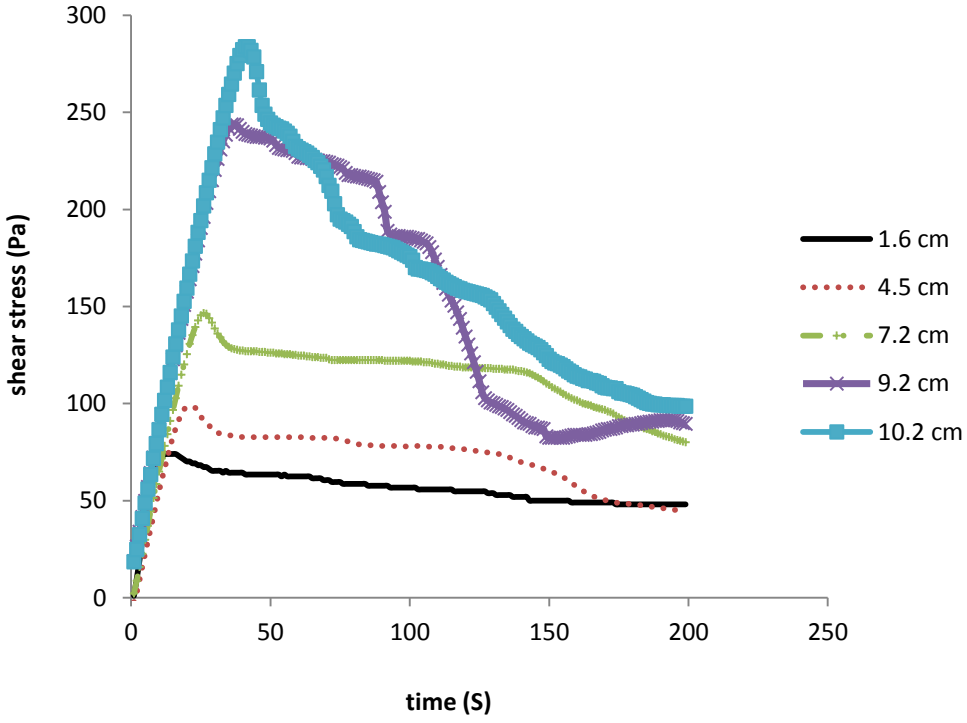

FIGURE D2 Shear stress versus time for as-received Albian MFT at the end of self-weight consolidation

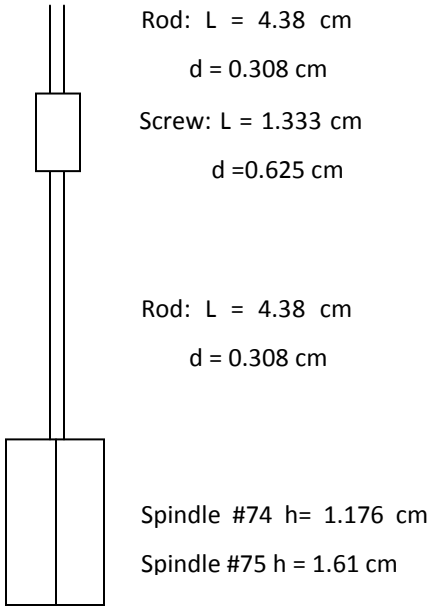

FIGURE D3 Geometry of spindles

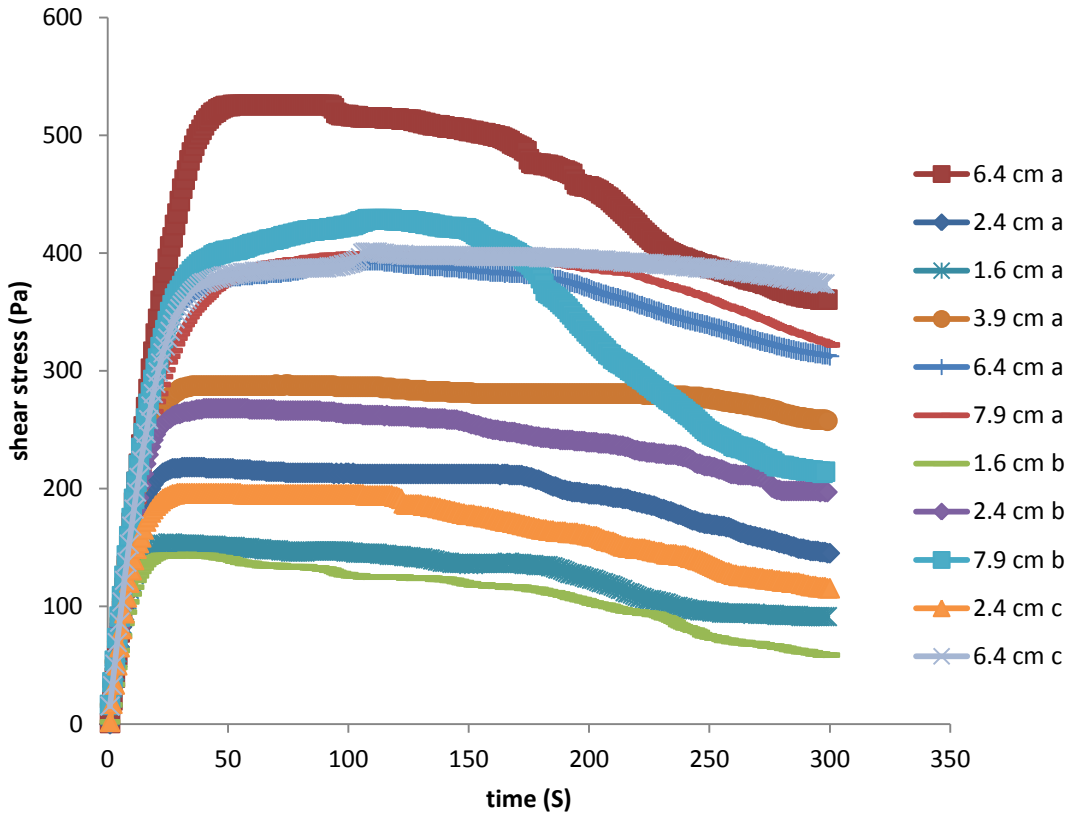

FIGURE D4 Shear stress versus time for frozen/thawed sample one (-20°C)

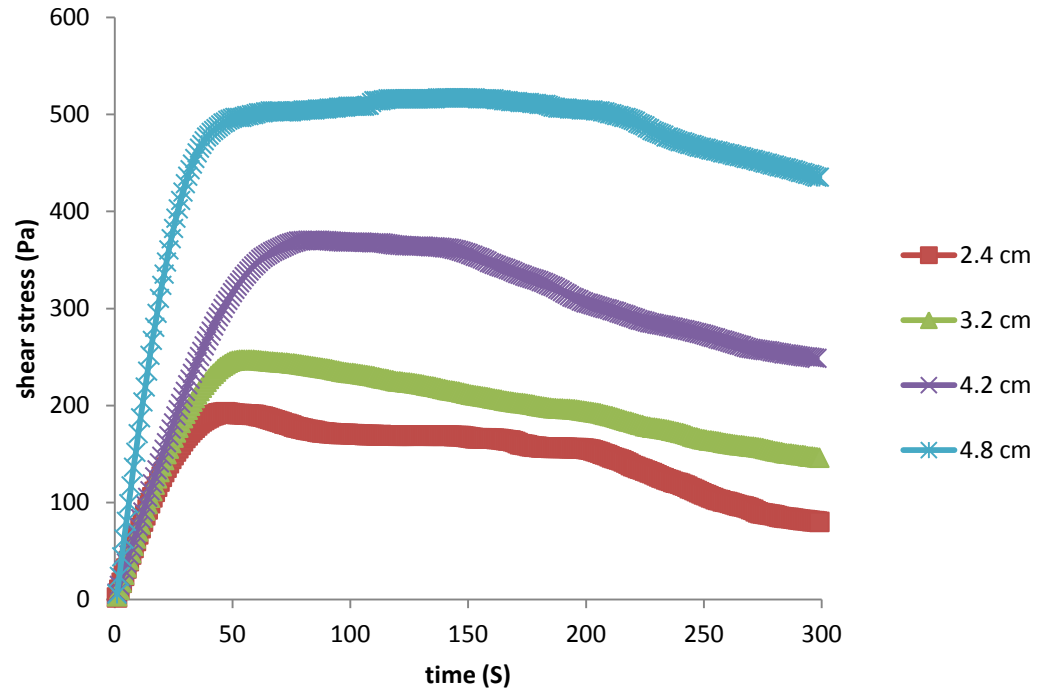

FIGURE D5 shear stress versus time for frozen/thawed sample two (-10°C)

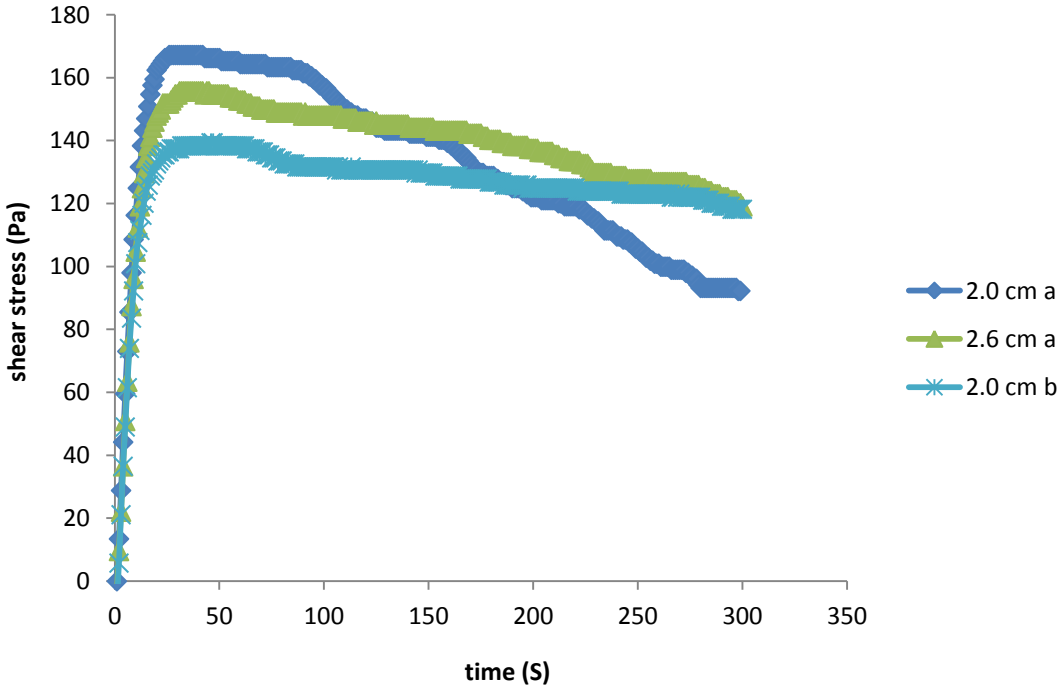

FIGURE D6 Shear stress versus time for frozen/thawed sample three (-5°C)

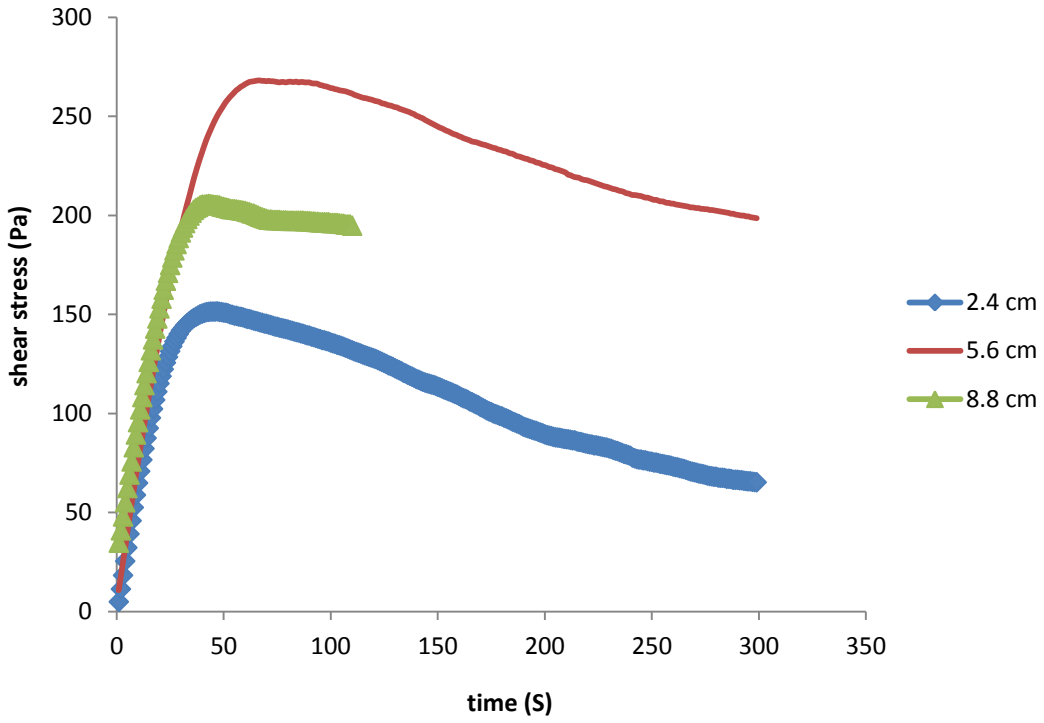

FIGURE D7 Shear stress versus time for frozen/thawed sample four (-5°C A)

APPENDIX E Finite Strain Consolidation Tests

E.1 Determination of permeability and hydraulic gradient

Constant head tests with upward flow were used to determine the permeability of MFT at different effective stresses. Figure E1 shows the test setup and information required for determining permeability. The permeability can be calculated as follows:

$$i = {\Delta H}/{H}, \Delta H = H_1 - H_2$$

$$Q = \left(R_i - R_f\right) \cdot a, a = \frac{\pi}{4} d^2$$

$$Q = k_t \cdot i \cdot A \cdot t, A = \frac{\pi}{4} D^2$$

$$k_{20°C} = k_t\left({\mu_t}/{\mu_{20°C}}\right), k_t = \frac{\left(R_i - R_f\right) \cdot a}{i \cdot A \cdot t}$$

Where: $i =$ hydraulic gradient, $a =$inner cross section area of glass tube, $d =$ inner diameter of glass tube, $Q =$ amount of flow, $t =$ duration of test, $A =$ inner cross section area of cell, $D =$ inner diameter of cell, $k_t =$ permeability at ambient temperature, $k_{20°C} =$ permeability at 20°C, $\mu_t =$ viscosity of water at ambient temperature, $\mu_{20°C} =$ viscosity of water at 20°C.

In order to prevent piping, the hydraulic gradient should satisfy:

$$\sigma' = \gamma_t H_0 - \gamma_w H_0 + P > i \cdot H_f \gamma_w = F_{up}$$

Where: $\sigma' =$ effective stress at bottom of sample at the end of consolidation, $\gamma_t =$ bulk density before self-weight consolidation, $H_0 =$ sample height before self-weight consolidation, $P =$ overburden pressure, $i =$ applied hydraulic gradient during permeability test, $H_f =$ sample height during permeability test, $F_{up} =$ uplift pressure generated by constant head water table in permeability test.

At the end of self-weight consolidation, assume $H_0 = 13$ cm, $\gamma_t = 12.65$ kN/m^3, $H_f = 11.61$ cm, and $P = 0$ kPa, the applied hydraulic gradient $i < 0.324$.

At the end of consolidation under 0.5 kPa, assume $H_f = 10.0$ cm, the applied hydraulic gradient $i < 0.879$.

E.2 Deformation curves

Deformation during consolidation was recorded throughout all tests. Figure E2 shows the deformation curve of as-received sample one. Figure E3 to Figure E10 present the deformation curves of as-received sample two. Figure E11 to Figure E18 show the deformation curves of as-received sample three. Figure 19 to Figure E26 are the deformation curves of as-received sample four. Figure E27 shows the frozen expansion curves of frozen/thawed samples. Figure E28 to Figure E31 present the deformation curves of frozen/thawed sample one. Figure E32 to Figure E36 are the deformation curves of frozen/thawed sample two.

E.3 Results of permeability tests

Permeability tests were performed at the end of consolidation under each load increment. Table E1 to Table E3 present the permeability results of as-received sample one with different hydraulic gradient. Table E4 to Table E11 summarized the permeability results of as-received sample two, among which Table E10 and Table E11 show the permeability results at 100 kPa. Table E12 to Table E 20 give the permeability results of as-received sample three, in which Table 17 to Table19 present the permeability results under 50 kPa. Table E21 to Table E27 give the permeability results of as-received sample four. Table E28 to Table E31 show the permeability results of frozen/thawed sample one. Table E32 to TableE37 present the permeability results of frozen/thawed sample two.

E.4 Pore pressure readings

Pore pressure readings were recorded throughout all consolidation tests. Significant data was plotted and given in this section. Figure E37 and Figure E38 are pore pressure readings for as-received sample one. Figure E39 to Figure E57 and Table E38 are pore pressure readings for as-received sample two. Figure E58 to Figure E76 are pore pressure readings for as-received sample three. Figure E77 to Figure E78 are pore pressure readings for as-received sample four. Figure E87 to Figure E90 are pore pressure readings for frozen/thawed sample one. Figure E91 to Figure E95 are pore pressure readings for frozen/thawed sample two.

TABLE E1 Permeability of as-received sample one ($i = 0.05$)

Test No.	t_i	R_i (cm)	t_f	R_f (cm)	t (sec)	Q (mm^3)	q (cm^3/s)	k_t (cm/s)
1	8/11/2011 11:37	6.87	8/11/2011 12:52	6.9	4500	-3.69E+00	-8.21E-07	-2.09E-07
2	8/11/2011 12:52	6.9	8/14/2011 18:00	6.69	277680	2.59E+01	9.31E-08	2.37E-08
3	8/14/2011 18:00	6.69	8/15/2011 13:00	6.39	68400	3.69E+01	5.40E-07	1.38E-07
4	8/15/2011 13:00	6.39	8/17/2011 10:26	5.55	163560	1.03E+02	6.32E-07	1.61E-07
5	8/17/2011 10:26	5.55	8/18/2011 14:14	5.03	100080	6.40E+01	6.40E-07	1.63E-07

NOTE: H_1 = 27.78 cm, H_2 = 27.20 cm, d = 3.96 mm, t_i = starting time, t_f = ending time, R_i = initial reading, R_f = final reading, t = test duration.

TABLE E2 Permeability of as-received sample one ($i = 0.1$)

Test No.	t_i	R_i (cm)	t_f	R_f (cm)	t (sec)	Q (mm^3)	q (cm^3/s)	k_t (cm/s)
1	8/18/2011 15:11	4.9	8/18/2011 16:06	4.61	3300	3.57E+01	1.08E-05	1.38E-06
2	8/18/2011 16:06	4.61	8/19/2011 10:22	2.89	65760	2.12E+02	3.22E-06	4.10E-07
3	8/19/2011 10:22	2.89	8/19/2011 13:42	2.61	12000	3.45E+01	2.87E-06	3.66E-07
4	8/19/2011 13:42	2.61	8/20/2011 10:51	1.1	76140	1.86E+02	2.44E-06	3.11E-07
5	8/20/2011 11:06	24.97	8/20/2011 11:09	24.93	180	4.92E+00	2.74E-05	3.48E-06
6	8/20/2011 11:09	24.93	8/21/2011 13:26	22.99	94620	2.39E+02	2.52E-06	3.22E-07
7	8/21/2011 13:26	22.99	8/21/2011 17:13	22.7	13620	3.57E+01	2.62E-06	3.34E-07

TABLE E3 Permeability of as-received sample one ($i = 0.2$)

Test No.	t_i	R_i (cm)	t_f	R_f (cm)	t (sec)	Q (mm^3)	q (cm^3/s)	k_t (cm/s)
1	8/21/2011 17:22	22.51	8/21/2011 17:24	22.41	120	1.23E+01	1.03E-04	6.53E-06
2	8/21/2011 17:24	22.41	8/21/2011 17:40	22.2	960	2.59E+01	2.69E-05	1.72E-06
3	8/21/2011 17:40	22.2	8/21/2011 20:12	21.39	9120	9.97E+01	1.09E-05	6.96E-07
4	8/21/2011 20:12	21.39	8/22/2011 11:52	18.3	54780	3.80E+02	6.94E-06	4.42E-07
5	8/22/2011 11:52	18.3	8/23/2011 15:10	13.55	98280	5.85E+02	5.95E-06	3.79E-07

TABLE E4 Permeability of as-received sample two at 0.5 kPa ($i = 0.5$)

Test No.	t_i	R_i (cm)	t_f	R_f (cm)	t (sec)	Q (mm^3)	q (cm^3/s)	k_t (cm/s)
1	1/15/2011 15:02	88.400	15:27	87.8	1500	7.39E+01	4.92E-05	1.25E-06
2	15:27	87.800	15:51	87.5	1440	3.69E+01	2.56E-05	6.53E-07
3	15:51	87.5	17:05	86.91	4440	7.26E+01	1.64E-05	4.17E-07
4	17:05	86.91	18:22	86.22	4620	8.49E+01	1.84E-05	4.68E-07
5	18:22	86.22	19:20	85.9	3480	3.94E+01	1.13E-05	2.88E-07
6	19:20	85.9	20:22	85.5	3720	4.92E+01	1.32E-05	3.37E-07
a	1/18/2011 10:23	84.25	13:19	82.62	10560	2.01E+02	1.90E-05	4.84E-07
b	13:19	82.62	16:57	81.19	13080	1.76E+02	1.35E-05	3.43E-07
c	16:57	81.19	19:00	80.4	7380	9.72E+01	1.32E-05	3.36E-07
d	19:00	80.4	22:06	79.1	11160	1.60E+02	1.43E-05	3.65E-07

NOTE: a to d are the permeability results re-performed.

TABLE E5 Permeability of as-received sample two at 2 kPa ($i = 0.5$)

Test No.	t_i	R_i (cm)	t_f	R_f (cm)	t (sec)	Q (mm^3)	q (cm^3/s)	k_t (cm/s)
1	2/28/2011 16:00	24.53	17:56	24.08	6960	5.54E+01	7.96E-06	2.03E-07
2	17:56	24.08	20:11	23.6	8100	5.91E+01	7.29E-06	1.86E-07
3	20:11	23.6	22:09	23.2	7080	4.92E+01	6.95E-06	1.77E-07

TABLE E6 Permeability of as-received sample two at 4 kPa ($i = 0.5$)

Test No.	t_i	R_i (cm)	t_f	R_f (cm)	t (sec)	Q (mm^3)	q (cm^3/s)	k_t (cm/s)
1	3/24/2011 11:20	18.3	13:03	18.03	6180	3.32E+01	5.38E-06	1.36E-07
2	13:03	18.03	17:16	17.45	15180	7.14E+01	4.70E-06	1.19E-07
3	17:16	17.45	3/25/2011 10:56	15.57	63600	2.31E+02	3.64E-06	9.22E-08

TABLE E7 Permeability of as-received sample two at 10 kPa ($i = 0.5$)

Test No.	t_i	R_i (cm)	t_f	R_f (cm)	t (sec)	Q (mm^3)	q (cm^3/s)	k_t (cm/s)
1	4/19/2011 10:01	13.55	11:00	13.51	3540	4.92E+00	1.39E-06	3.54E-08
2	11:00	13.51	13:33	13.4	9180	1.35E+01	1.48E-06	3.76E-08
3	13:33	13.4	4/20/2011 13:18	12.5	85500	1.11E+02	1.30E-06	3.30E-08

TABLE E8 Permeability of as-received sample two at 20 kPa ($i = 0.5$)

Test No.	t_i	R_i (cm)	t_f	R_f (cm)	t (sec)	Q (mm^3)	q (cm^3/s)	k_t (cm/s)
1	5/4/2011 15:38	9.9	20:36	9.85	17880	6.16E+00	3.44E-07	8.77E-09
2	20:36	9.85	5/5/2011 15:38	9.71	68520	1.72E+01	2.52E-07	6.41E-09
3	5/5/2011 15:38	9.71	5/6/2011 14:03	9.49	80700	2.71E+01	3.36E-07	8.55E-09

TABLE E9 Permeability of as-received sample two at 50 kPa ($i = 0.5$)

Test No.	t_i	R_i (cm)	t_f	R_f (cm)	t (sec)	Q (mm^3)	q (cm^3/s)	k_t (cm/s)
1	5/24/2011 16:22	7.9	5/25/2011 12:00	7.51	70680	4.80E+01	6.79E-07	1.73E-08
2	5/25/2011 12:00	7.51	5/26/2011 11:08	7.6	83280	-1.11E+01	-1.33E-07	-3.39E-09
3	5/26/2011 11:08	7.6	5/27/2011 15:02	7.32	100440	3.45E+01	3.43E-07	8.74E-09
4	5/27/2011 15:02	7.32	5/28/2011 14:47	7	85500	3.94E+01	4.61E-07	1.17E-08

TABLE E10 Permeability of as-received sample two at 100 kPa ($i = 0.5$)

Test No.	t_i	R_i (cm)	t_f	R_f (cm)	t (sec)	Q (mm^3)	q (cm^3/s)	k_t (cm/s)
4	6/24/2011 13:42	27.41	6/24/2011 16:43	27.35	10860	7.39E+00	6.80E-07	1.73E-08
5	6/24/2011 16:43	27.35	6/25/2011 17:45	27.1	90120	3.08E+01	3.41E-07	8.70E-09
6	6/25/2011 17:45	27.1	6/26/2011 17:59	26.72	87240	4.68E+01	5.36E-07	1.37E-08
9	6/28/2011 20:22	27.41	6/30/2011 15:20	27.21	154680	2.46E+01	1.59E-07	4.06E-09
10	6/30/2011 15:20	27.21	7/3/2011 17:37	26.71	267420	6.16E+01	2.30E-07	5.86E-09

TABLE E11 Permeability of as-received sample two at 100 kPa ($i = 1$)

Test No.	t_i	R_i (cm)	t_f	R_f (cm)	t (sec)	Q (mm^3)	q (cm^3/s)	k_t (cm/s)
1	7/3/2011 17:48	26.6	7/4/2011 22:26	26.01	103080	7.26E+01	7.05E-07	8.98E-09
2	7/4/2011 22:26	26.01	7/5/2011 12:11	25.7	49500	3.82E+01	7.71E-07	9.82E-09
3	7/5/2011 12:11	25.7	7/6/2011 21:33	25.51	120120	2.34E+01	1.95E-07	2.48E-09
4	7/6/2011 21:33	25.51	7/7/2011 14:48	25.3	62100	2.59E+01	4.16E-07	5.30E-09

TABLE E12 Permeability of as-received sample three at 0.5 kPa ($i = 0.5$)

Test No.	t_i	R_i (cm)	t_f	R_f (cm)	t (sec)	Q (mm^3)	q (cm^3/s)	k_t (cm/s)
1	2/19/2011 11:42	91.4	13:31	90.72	6540	8.37E+01	1.28E-05	3.29E-07
2	13:31	90.72	15:29	90.2	7080	6.40E+01	9.04E-06	2.33E-07
3	15:29	90.2	18:08	89.52	9540	8.37E+01	8.77E-06	2.26E-07

TABLE E13 Permeability of as-received sample three at 2 kPa ($i = 0.5$)

Test No.	t_i	R_i (cm)	t_f	R_f (cm)	t (sec)	Q (mm^3)	q (cm^3/s)	k_t (cm/s)
1	3/24/2011 11:20	47.7	13:03	47.41	6180	3.57E+01	5.78E-06	1.49E-07
2	13:03	47.41	17:16	46.87	15180	6.65E+01	4.38E-06	1.13E-07
3	17:16	46.87	3/25/2011 10:56	44.5	63600	2.92E+02	4.59E-06	1.18E-07

TABLE E14 Permeability of as-received sample three at 4 kPa ($i = 0.5$)

Test No.	t_i	R_i (cm)	t_f	R_f (cm)	t (sec)	Q (mm^3)	q (cm^3/s)	k_t (cm/s)
1	4/19/2011 10:01	41.68	11:00	41.6	3540	9.85E+00	2.78E-06	7.18E-08
2	11:00	41.6	13:33	41.42	9180	2.22E+01	2.41E-06	6.23E-08
3	13:33	41.42	4/20/2011 13:18	39.47	85500	2.40E+02	2.81E-06	7.25E-08

TABLE E15 Permeability of as-received sample three at 10 kPa ($i = 0.5$)

Test No.	t_i	R_i (cm)	t_f	R_f (cm)	t (sec)	Q (mm^3)	q (cm^3/s)	k_t (cm/s)
1	5/4/2011 20:36	38.49	5/5/2011 15:38	38	68520	6.03E+01	8.80E-07	1.87E-08
2	5/5/2011 15:38	38	5/6/2011 14:03	37.4	80700	7.39E+01	9.15E-07	1.95E-08

TABLE E16 Permeability of as-received sample three at 20 kPa ($i = 0.5$)

Test No.	t_i	R_i (cm)	t_f	R_f (cm)	t (sec)	Q (mm^3)	q (cm^3/s)	k_t (cm/s)
1	5/24/2011 16:22	35.7	5/25/2011 12:00	35.00	70680	8.62E+01	1.22E-06	2.56E-08
2	5/25/2011 12:00	35.00	5/26/2011 11:08	34.71	83280	3.57E+01	4.29E-07	9.01E-09
3	5/26/2011 11:08	34.71	5/27/2011 15:01	33.91	100380	9.85E+01	9.81E-07	2.06E-08
4	5/27/2011 15:01	33.91	5/28/2011 14:47	32.87	85560	1.28E+02	1.50E-06	3.14E-08

TABLE E17 Permeability of as-received sample three at 50 kPa ($i = 0.2$)

Test No.	t_i	R_i (cm)	t_f	R_f (cm)	t (sec)	Q (mm^3)	q (cm^3/s)	k_t (cm/s)
1	6/24/2011 16:43	30	6/25/2011 17:45	29.80	90120	2.46E+01	2.73E-07	1.77E-07
2	6/25/2011 17:45	29.80	6/26/2011 17:59	29.51	87240	3.57E+01	4.09E-07	2.66E-07
3	6/28/2011 20:22	29.53	6/30/2011 15:20	29.35	154680	2.22E+01	1.43E-07	9.30E-08
4	6/30/2011 15:20	29.35	7/3/2011 17:37	29.03	267420	3.94E+01	1.47E-07	9.56E-08

TABLE E18 Permeability of as-received sample three at 50 kPa ($i = 0.5$)

Test No.	t_i	R_i (cm)	t_f	R_f (cm)	t (sec)	Q (mm^3)	q (cm^3/s)	k_t (cm/s)
1	6/21/2011 15:37	30.81	6/22/2011 14:59	30.48	84120	4.06E+01	4.83E-07	1.25E-07
2	6/22/2011 14:59	30.48	6/23/2011 14:15	30.19	83760	3.57E+01	4.26E-07	1.11E-07
3	6/23/2011 14:15	30.19	6/24/2011 13:42	29.91	84420	3.45E+01	4.08E-07	1.06E-07

TABLE E19 Permeability of as-received sample three at 50 kPa ($i = 1.0$)

Test No.	t_i	R_i (cm)	t_f	R_f (cm)	t (sec)	Q (mm^3)	q (cm^3/s)	k_t (cm/s)
1	7/3/2011 17:48	28.9	7/4/2011 22:26	28.05	103080	1.05E+02	1.02E-06	1.33E-07
2	7/4/2011 22:26	28.05	6/5/2011 12:11	27.5	49500	6.77E+01	1.37E-06	1.79E-07
3	6/5/2011 12:11	27.5	7/6/2011 21:33	26.7	120120	9.85E+01	8.20E-07	1.07E-07
4	7/6/2011 21:33	26.7	7/7/2011 14:48	26.29	62100	5.05E+01	8.13E-07	1.07E-07

TABLE E20 Permeability of as-received sample three at 100 kPa ($i = 0.5$)

Test No.	t_i	R_i (cm)	t_f	R_f (cm)	t (sec)	Q (mm^3)	q (cm^3/s)	k_t (cm/s)
1	7/26/2011 12:26	25.11	7/27/2011 21:25	24.91	118740	2.46E+01	2.07E-07	5.40E-09
2	7/27/2011 21:25	24.91	7/28/2011 12:57	24.82	55920	1.11E+01	1.98E-07	5.16E-09
3	7/29/2011 17:39	24.83	8/2/2011 12:01	24.7	238920	1.60E+01	6.70E-08	1.75E-09

TABLE E21 Permeability of as-received sample four at 0.5 kPa ($i = 0.5$)

Test No.	t_i	R_i (cm)	t_f	R_f (cm)	t (sec)	Q (mm^3)	q (cm^3/s)	k_t (cm/s)
1	2/28/2011 16:00	79.91	17:56	79.2	6960	8.74E+01	1.26E-05	3.24E-07
2	17:56	79.2	20:11	78.56	8100	7.88E+01	9.73E-06	2.51E-07
3	20:11	78.56	22:09	78.01	7080	6.77E+01	9.56E-06	2.46E-07

TABLE E22 Permeability of as-received sample four at 2 kPa ($i = 0.5$)

Test No.	t_i	R_i (cm)	t_f	R_f (cm)	t (sec)	Q (mm^3)	q (cm^3/s)	k_t (cm/s)
1	4/4/2011 15:04	72.31	16:48	72.02	6240	3.57E+01	5.72E-06	1.48E-07
2	16:48	72.02	17:55	71.9	4020	1.48E+01	3.67E-06	9.49E-08
3	17:55	71.9	9:52	70.1	57420	2.22E+02	3.86E-06	9.96E-08
4	9:52	70.1	16:32	69.4	24000	8.62E+01	3.59E-06	9.27E-08
5	16:32	69.4	10:21	67.52	64140	2.31E+02	3.61E-06	9.32E-08

TABLE E23 Permeability of as-received sample four at 4 kPa ($i = 0.5$)

Test No.	t_i	R_i (cm)	t_f	R_f (cm)	t (sec)	Q (mm^3)	q (cm^3/s)	k_t (cm/s)
1	5/4/2011 15:38	63.1	20:36	62.68	17880	5.17E+01	2.89E-06	7.47E-08
2	20:36	62.68	5/5/2011 15:38	61.35	68520	1.64E+02	2.39E-06	6.18E-08
3	5/5/2011 15:38	61.35	5/6/2011 14:03	59.8	80700	1.91E+02	2.36E-06	6.11E-08

TABLE E24 Permeability of as-received sample four at 10 kPa ($i = 0.5$)

Test No.	t_i	R_i (cm)	t_f	R_f (cm)	t (sec)	Q (mm^3)	q (cm^3/s)	k_t (cm/s)
1	6/1/2011 18:45	56.85	6/2/2011 9:46	56.5	54060	4.31E+01	7.97E-07	2.47E-08
2	6/2/2011 9:46	56.5	6/3/2011 13:22	55.01	99360	1.83E+02	1.85E-06	5.72E-08
3	6/3/2011 13:22	55.01	6/4/2011 12:59	54.01	85020	1.23E+02	1.45E-06	4.49E-08

TABLE E25 Permeability of as-received sample four at 20 kPa ($i = 0.5$)

Test No.	t_i	R_i (cm)	t_f	R_f (cm)	t (sec)	Q (mm^3)	q (cm^3/s)	k_t (cm/s)
1	6/21/2011 15:44	51.81	6/22/2011 14:59	50.71	84120	1.35E+02	1.61E-06	4.17E-08
2	6/22/2011 14:59	50.71	6/23/2011 14:15	49.98	83760	8.99E+01	1.07E-06	2.78E-08
3	6/23/2011 14:15	49.98	6/24/2011 13:42	49.1	84420	1.08E+02	1.28E-06	3.33E-08

TABLE E26 Permeability of as-received sample four at 50 kPa ($i = 0.5$)

Test No.	t_i	R_i (cm)	t_f	R_f (cm)	t (sec)	Q (mm^3)	q (cm^3/s)	k_t (cm/s)
1	7/15/2011 15:10	46.62	7/17/2011 15:33	45.2	174180	1.75E+02	1.00E-06	1.31E-08
2	7/17/2011 15:33	45.2	7/20/2011 20:34	43.91	277260	1.59E+02	5.73E-07	7.45E-09
3	7/20/2011 20:34	43.91	7/21/2011 10:08	43.58	48840	4.06E+01	8.32E-07	1.08E-08

TABLE E27 Permeability of as-received sample four at 100 kPa ($i = 2$)

Test No.	t_i	R_i (cm)	t_f	R_f (cm)	t (sec)	Q (mm^3)	q (cm^3/s)	k_t (cm/s)
1	8/9/2011 10:55	30.59	8/9/2011 15:35	30.5	16800	1.11E+01	6.59E-07	4.30E-09
2	8/9/2011 15:35	30.5	8/10/2011 10:14	30	67140	6.16E+01	9.17E-07	5.97E-09
3	8/10/2011 10:14	30	8/11/2011 10:46	29.48	88320	6.40E+01	7.25E-07	4.72E-09

TABLE E28 Permeability of frozen/thawed sample one at 1.3 kPa ($i = 0.5$)

Test No.	t_i	R_i (cm)	t_f	R_f (cm)	t (sec)	Q (mm^3)	q (cm^3/s)	k_t (cm/s)
1	4/8/2011 10:38	42.2	10:51	42.3	780	1.23E+01	1.58E-05	4.09E-07
2	10:51	42.3	12:49	42.65	7080	4.31E+01	6.09E-06	1.58E-07
3	12:49	42.65	15:25	42.8	9360	1.85E+01	1.97E-06	5.11E-08
4	15:25	42.8	18:17	43.05	10320	3.08E+01	2.98E-06	7.72E-08
5	18:17	43.05	4/9/2011 15:43	44.65	77160	1.97E+02	2.55E-06	6.61E-08
6	4/8/2011 10:38	42.2	10:51	42.3	780	1.23E+01	1.58E-05	4.09E-07

TABLE E29 Permeability of frozen/thawed sample one at 4 kPa ($i = 0.5$)

Test No.	t_i	R_i (cm)	t_f	R_f (cm)	t (sec)	Q (mm^3)	q (cm^3/s)	k_t (cm/s)
1	5/8/2011 18:07	37.6	5/9/2011 13:03	38.1	68160	6.16E+01	9.03E-07	2.30E-08
2	5/9/2011 13:03	38.1	5/10/2011 10:24	38.61	76860	6.28E+01	8.17E-07	2.08E-08

TABLE E30 Permeability of frozen/thawed sample one at 10 kPa ($i = 0.5$)

Test No.	t_i	R_i (cm)	t_f	R_f (cm)	t (sec)	Q (mm^3)	q (cm^3/s)	k_t (cm/s)
1	6/7/2011 10:24	35.1	6/8/2011 13:47	35.62	98580	6.40E+01	6.49E-07	1.65E-08
2	6/8/2011 13:47	35.62	6/9/2011 11:07	35.9	76800	3.45E+01	4.49E-07	1.14E-08
3	6/9/2011 11:07	35.9	6/10/2011 15:35	36.3	102480	4.92E+01	4.80E-07	1.22E-08

TABLE E31 Permeability of frozen/thawed sample one at 20 kPa ($i = 0.5$)

Test No.	t_i	R_i (cm)	t_f	R_f (cm)	t (sec)	Q (mm^3)	q (cm^3/s)	k_t (cm/s)
1	7/26/2011 14:22	56.4	7/27/2011 21:34	56.51	112320	-1.35E+01	-1.21E-07	-3.07E-09
2	7/27/2011 21:34	56.51	7/28/2011 13:05	56.5	55860	1.23E+00	2.20E-08	5.61E-10
3	7/28/2011 13:05	56.5	7/29/2011 17:44	56.1	103140	4.92E+01	4.77E-07	1.22E-08
4	7/29/2011 17:44	56.1	8/2/2011 12:13	55.11	239340	1.22E+02	5.09E-07	1.30E-08
5	8/2/2011 12:13	55.11	8/4/2011 10:33	54.52	166800	7.26E+01	4.35E-07	1.11E-08

TABLE E32 Permeability of frozen/thawed sample two at 1.3 kPa ($i = 0.5$)

Test No.	t_i	R_i (cm)	t_f	R_f (cm)	t (sec)	Q (mm^3)	q (cm^3/s)	k_t (cm/s)
1	2/26/2011 11:28	25.9	13:58	26.62	9000	8.86E+01	9.85E-06	2.32E-07
2	13:58	26.62	16:04	26.95	7560	4.06E+01	5.37E-06	1.27E-07
3	16:04	26.95	22:49	28.01	24300	1.30E+02	5.37E-06	1.27E-07

TABLE E33 Permeability of frozen/thawed sample two at 4 kPa ($i = 0.5$)

Test No.	t_i	R_i (cm)	t_f	R_f (cm)	t (sec)	Q (mm^3)	q (cm^3/s)	k_t (cm/s)
1	4/4/2011 16:47	29.5	18:00	29.64	4380	1.72E+01	3.93E-06	1.00E-07
2	18:00	29.64	10:02	29.89	57720	3.08E+01	5.33E-07	1.36E-08
3	10:02	29.89	17:11	30.05	25740	1.97E+01	7.65E-07	1.79E-08
4	17:11	30.05	10:59	30.9	64080	1.05E+02	1.63E-06	3.81E-08
5	4/6/2011 14:12	30.9	4/7/2011 17:10	31.7	97080	9.85E+01	1.01E-06	2.37E-08

TABLE E34 Permeability of frozen/thawed sample two at 10 kPa ($i = 0.5$)

Test No.	t_i	R_i (cm)	t_f	R_f (cm)	t (sec)	Q (mm^3)	q (cm^3/s)	k_t (cm/s)
1	4/28/2011 17:45	28.83	18:28	28.89	2580	7.39E+00	2.86E-06	6.63E-08
2	18:28	28.89	21:02	29.17	9240	3.45E+01	3.73E-06	8.64E-08
3	21:02	29.17	4/29/2011 10:01	29.32	46800	1.85E+01	3.95E-07	9.14E-09
4	4/29/2011 10:01	29.32	5/2/2011 14:17	31.09	274560	2.18E+02	7.94E-07	1.84E-08

TABLE E35 Permeability of frozen/thawed sample two at 20 kPa ($i = 0.5$)

Test No.	t_i	R_i (cm)	t_f	R_f (cm)	t (sec)	Q (mm^3)	q (cm^3/s)	k_t (cm/s)
1	5/24/2011 16:22	41.7	5/26/2011 12:10	42.3	71280	7.39E+01	1.04E-06	2.39E-08
2	5/26/2011 12:10	42.3	5/26/2011 11:18	42.65	83280	4.31E+01	5.17E-07	1.19E-08
3	5/26/2011 11:18	42.65	5/27/2011 15:16	43.19	100680	6.65E+01	6.60E-07	1.52E-08
4	5/27/2011 15:16	43.19	5/28/2011 14:33	43.7	83820	6.28E+01	7.49E-07	1.72E-08

TABLE E36 Permeability of frozen/thawed sample two at 50 kPa ($i = 0.5$)

Test No.	t_i	R_i (cm)	t_f	R_f (cm)	t (sec)	Q (mm^3)	q (cm^3/s)	k_t (cm/s)
1	6/18/2011 18:09	49.11	6/19/2011 16:01	49.23	78720	1.48E+01	1.88E-07	4.29E-09
2	6/19/2011 16:01	49.23	6/20/2011 15:04	49.51	82980	3.45E+01	4.15E-07	9.49E-09
3	6/20/2011 15:04	49.51	6/21/2011 16:45	49.91	92460	4.92E+01	5.33E-07	1.22E-08
4	6/21/2011 16:45	49.91	6/22/2011 14:30	50.2	78300	3.57E+01	4.56E-07	1.04E-08

TABLE E37 Permeability of frozen/thawed sample two at 100 kPa ($i = 0.5$)

Test No.	t_i	R_i (cm)	t_f	R_f (cm)	t (sec)	Q (mm^3)	q (cm^3/s)	k_t (cm/s)
1	7/26/2011 14:22	38.9	7/27/2011 21:34	39.5	112320	7.39E+01	6.58E-07	1.49E-08
2	7/27/2011 21:34	39.5	7/28/2011 13:05	39.65	55860	1.85E+01	3.31E-07	7.50E-09
3	7/28/2011 13:05	39.65	7/29/2011 17:39	39.9	103140	3.08E+01	2.98E-07	6.77E-09
4	7/29/2011 17:39	39.9	8/2/2011 12:13	40.7	239340	9.85E+01	4.11E-07	9.34E-09
5	8/2/2011 12:13	40.7	8/4/2011 10:33	41.08	166800	4.68E+01	2.80E-07	6.36E-09

TABLE E38 Excess pore pressure of as-received sample two (0.5 kPa)

Overburden stress (kPa)	Time (day)	U_e (kPa)
0.23	0.7	0.253
0.5	0.8	0.391
0.5	20.0	0.067

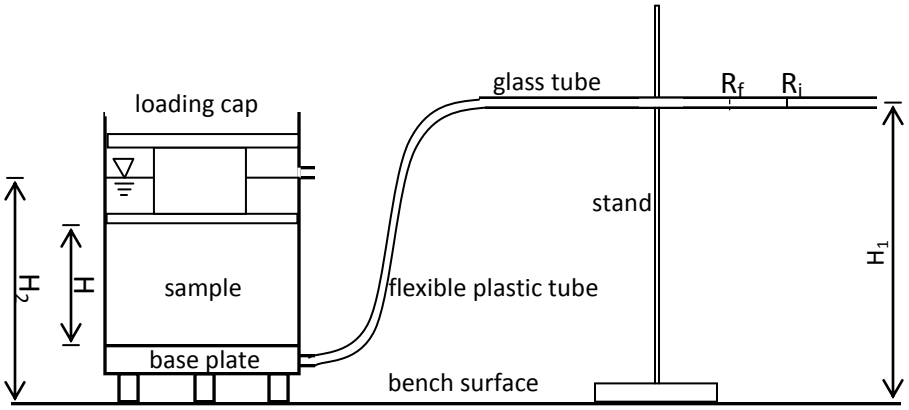

FIGURE E1 Constant head permeability testing setup

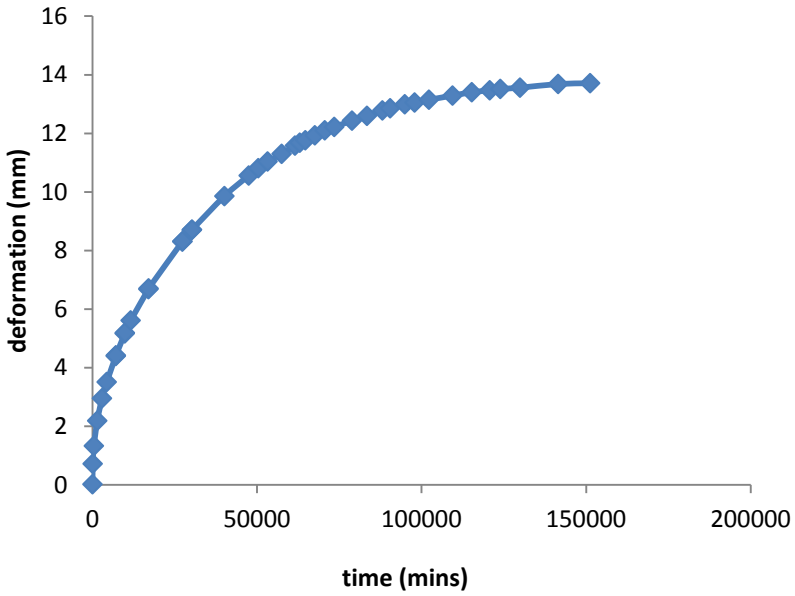

FIGURE E2 Deformation curve of as-received sample one

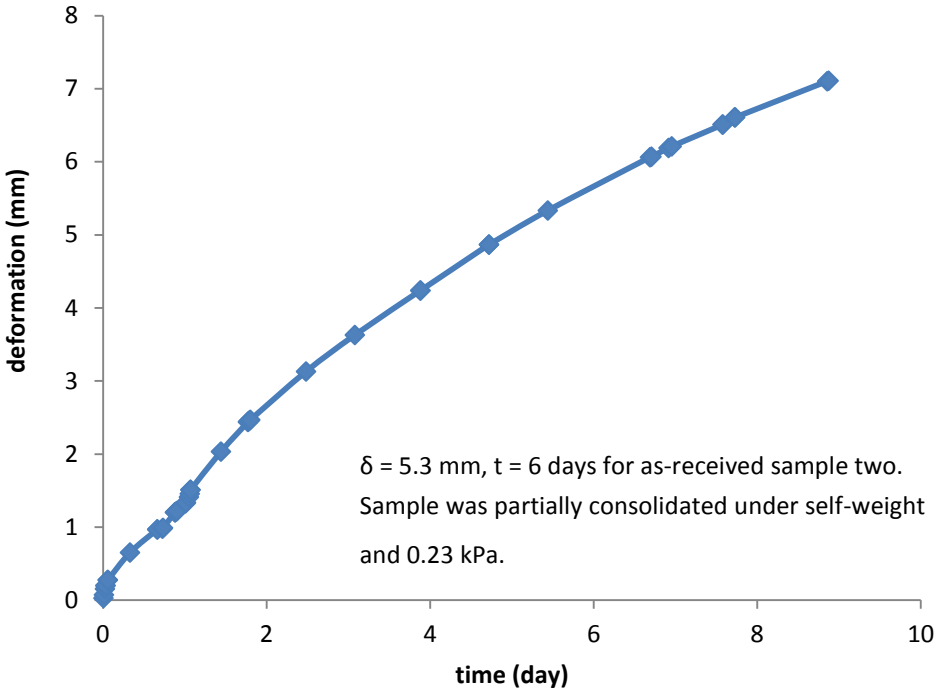

FIGURE E3 Deformation curve of as-received sample two (0.23 kPa)

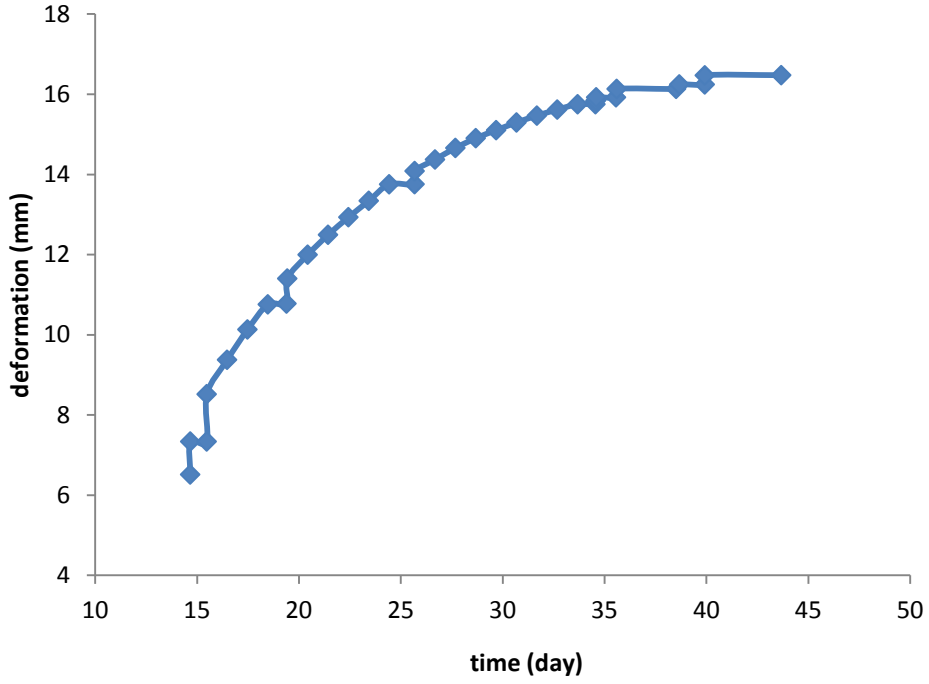

FIGURE E4 Deformation curve of as-received sample two (0.5 kPa)

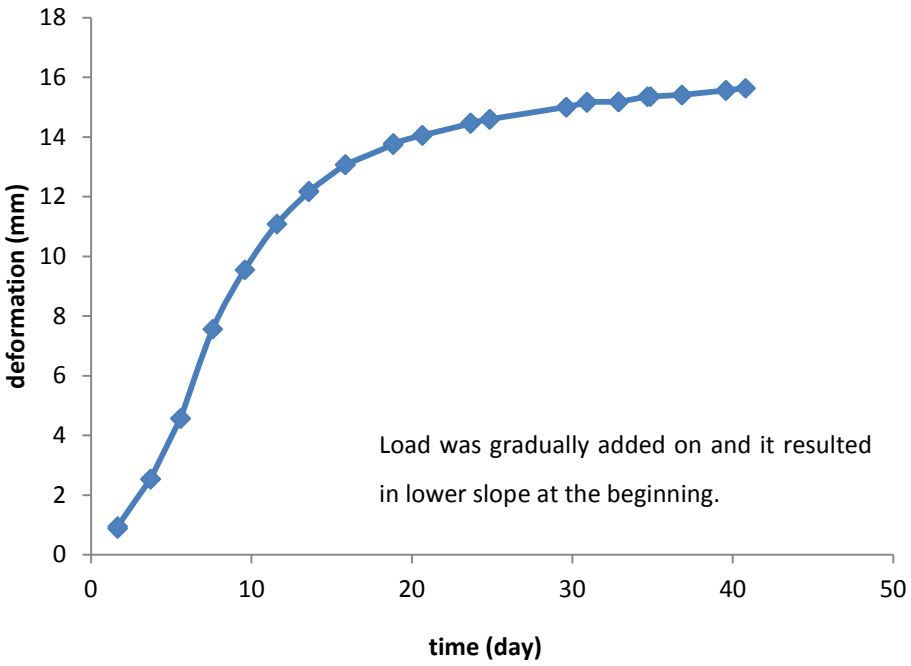

FIGURE E5 Deformation curve of as-received sample two (2 kPa)

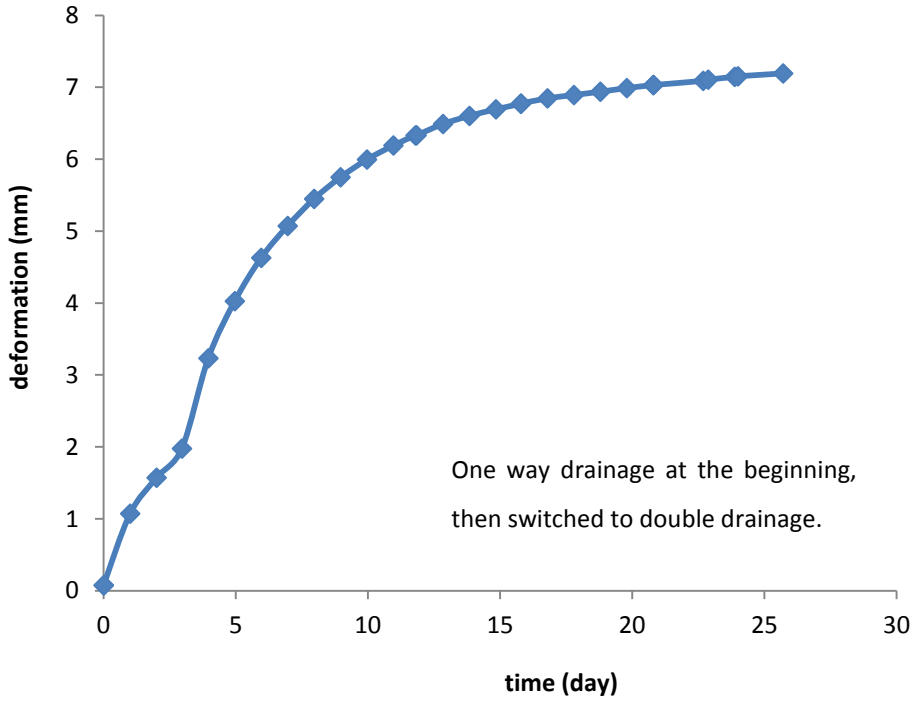

FIGURE E6 Deformation curve of as-received sample two (4 kPa)

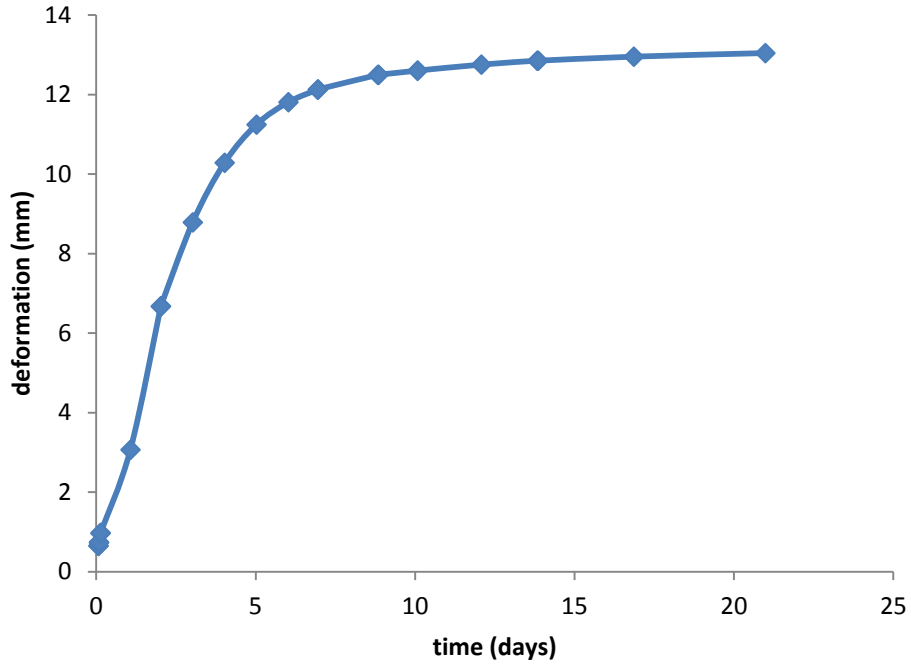

FIGURE E7 Deformation curve of as-received sample two (10 kPa)

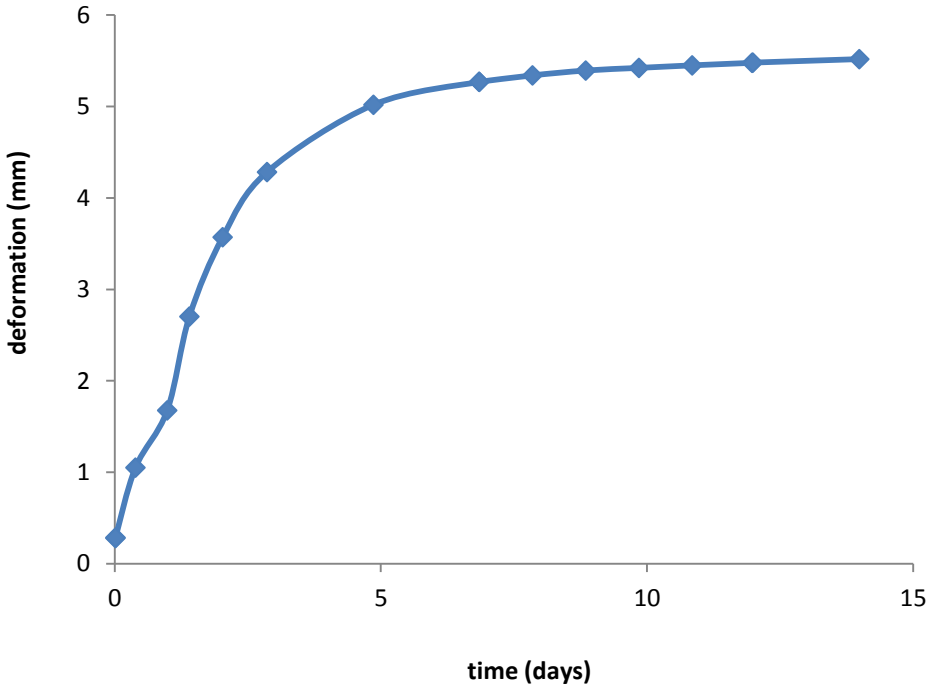

FIGURE E8 Deformation curve of as-received sample two (20 kPa)

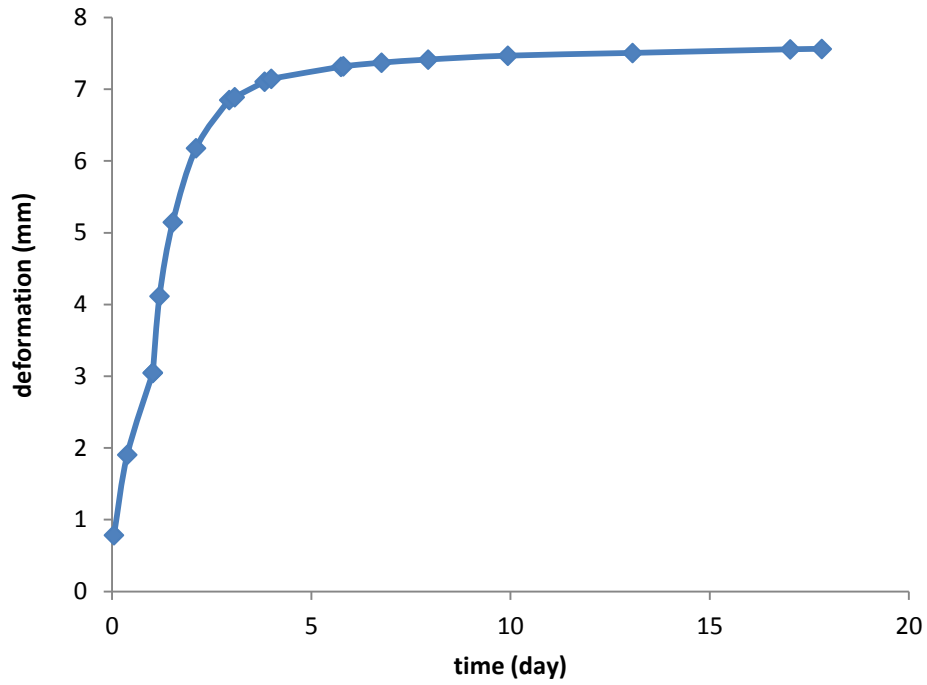

FIGURE E9 Deformation curve of as-received sample two (50 kPa)

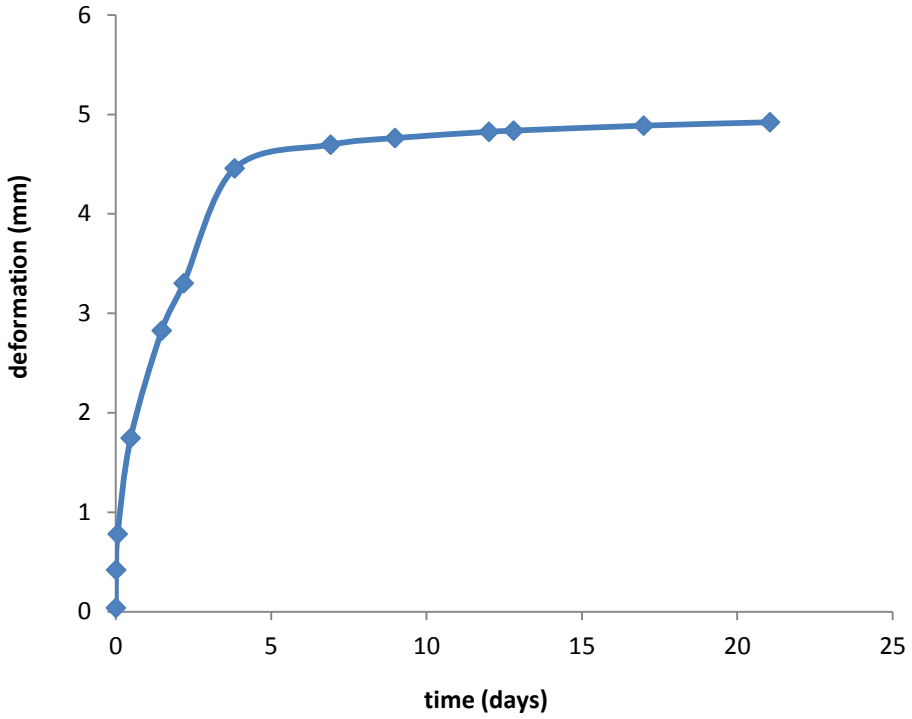

FIGURE E10 Deformation curve of as-received sample two (100 kPa)

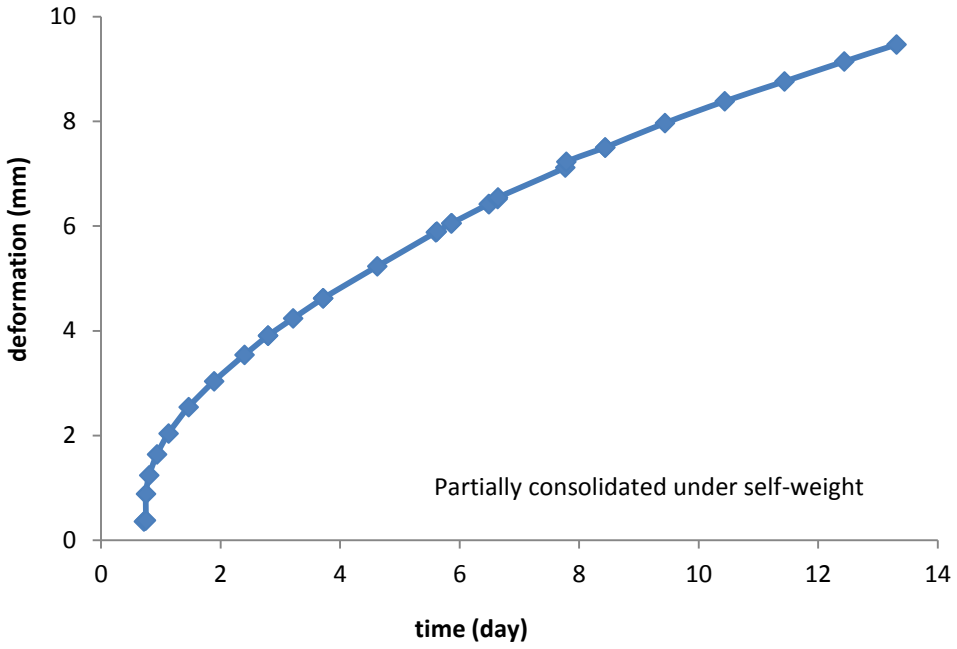

FIGURE E11 Deformation curve of as-received sample three (self-weight)

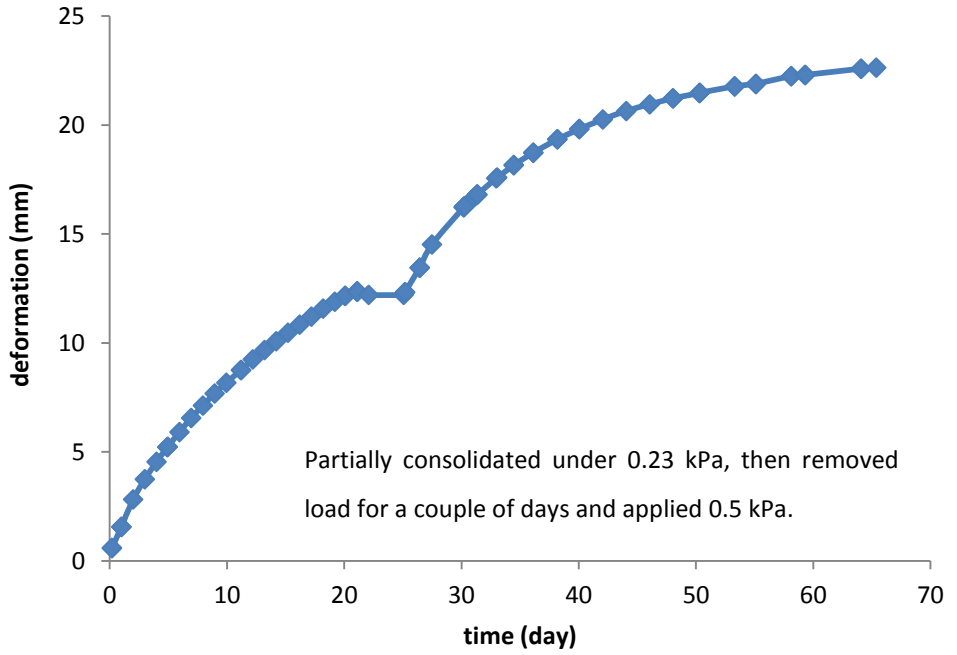

FIGURE E12 Deformation curve of as-received sample three (0.23kPa and 0.5 kPa)

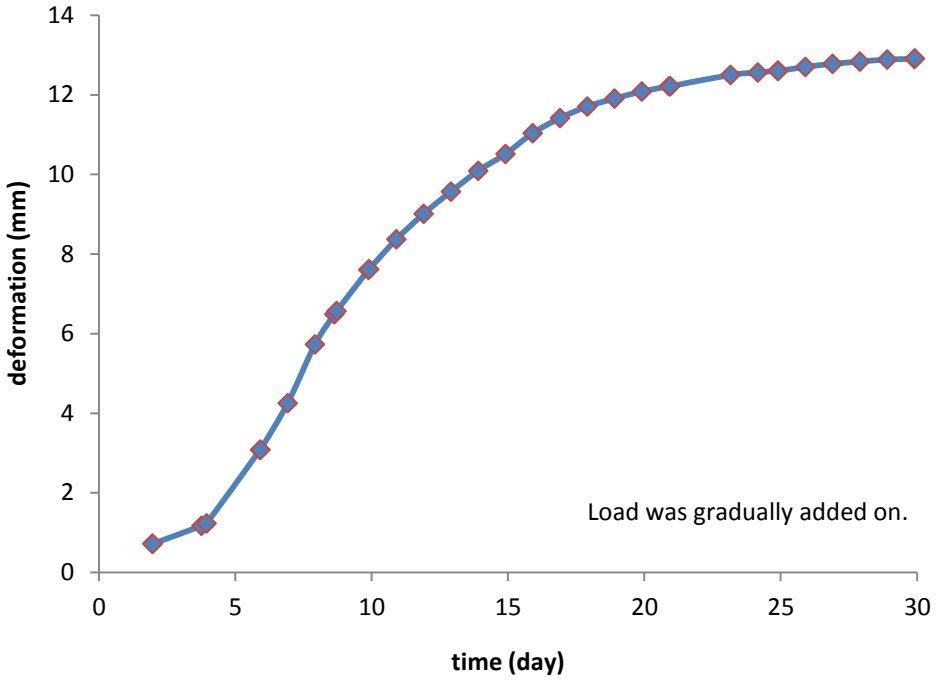

FIGURE E13 Deformation curve of as-received sample three (2 kPa)

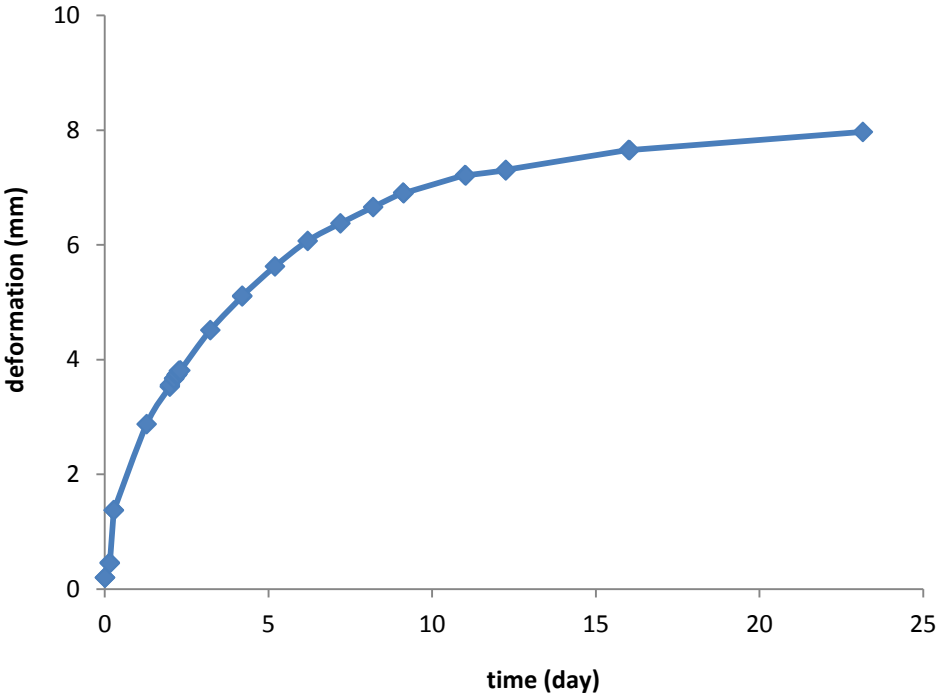

FIGURE E14 Deformation curve of as-received sample three (4 kPa)

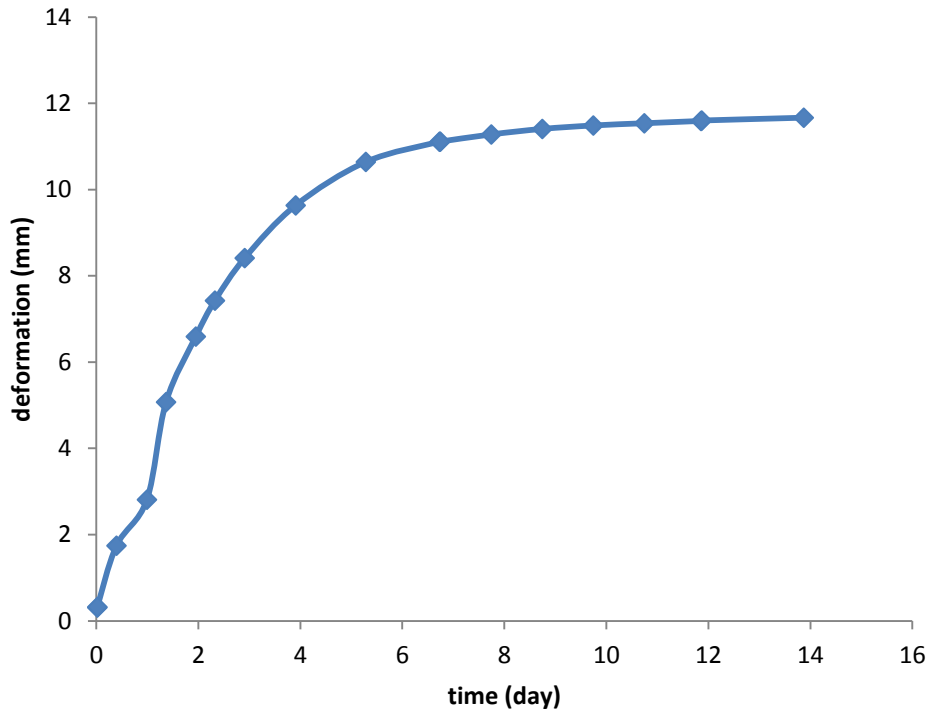

FIGURE E15 Deformation curve of as-received sample three (10 kPa)

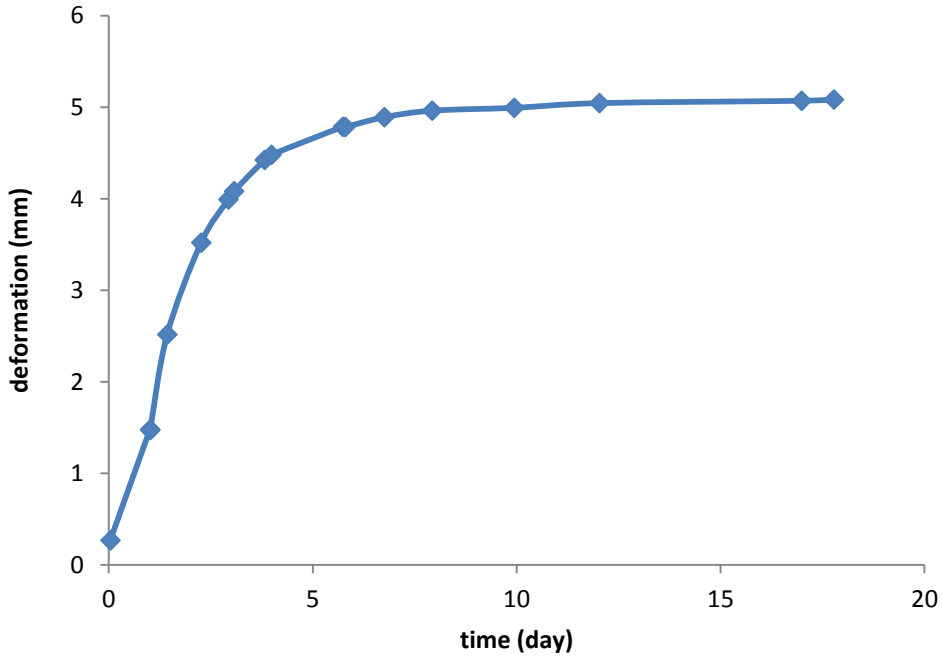

FIGURE E16 Deformation curve of as-received sample three (20 kPa)

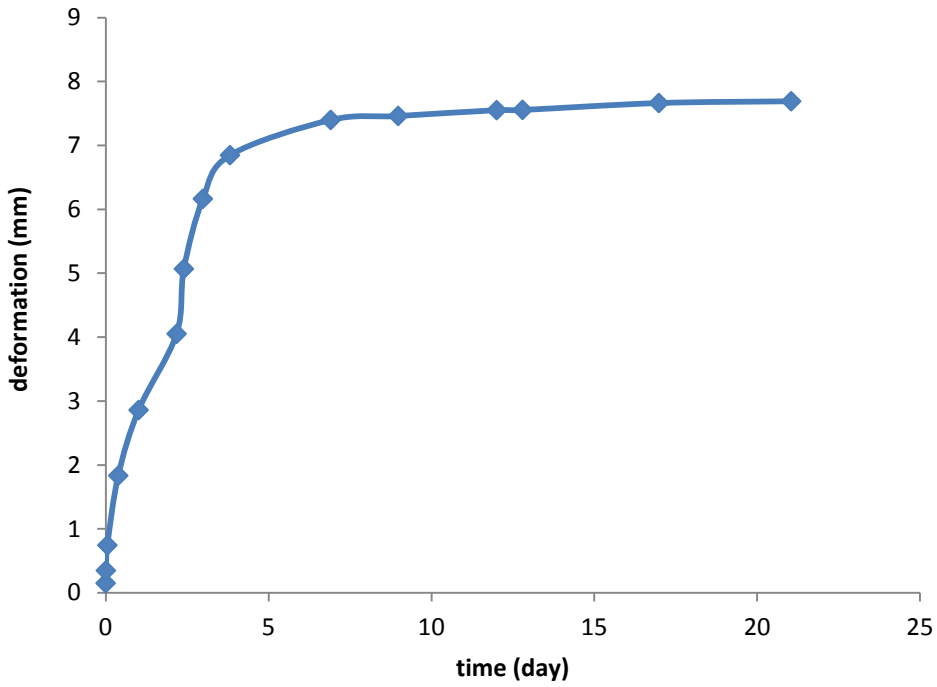

FIGURE E17 Deformation curve of as-received sample three (50 kPa)

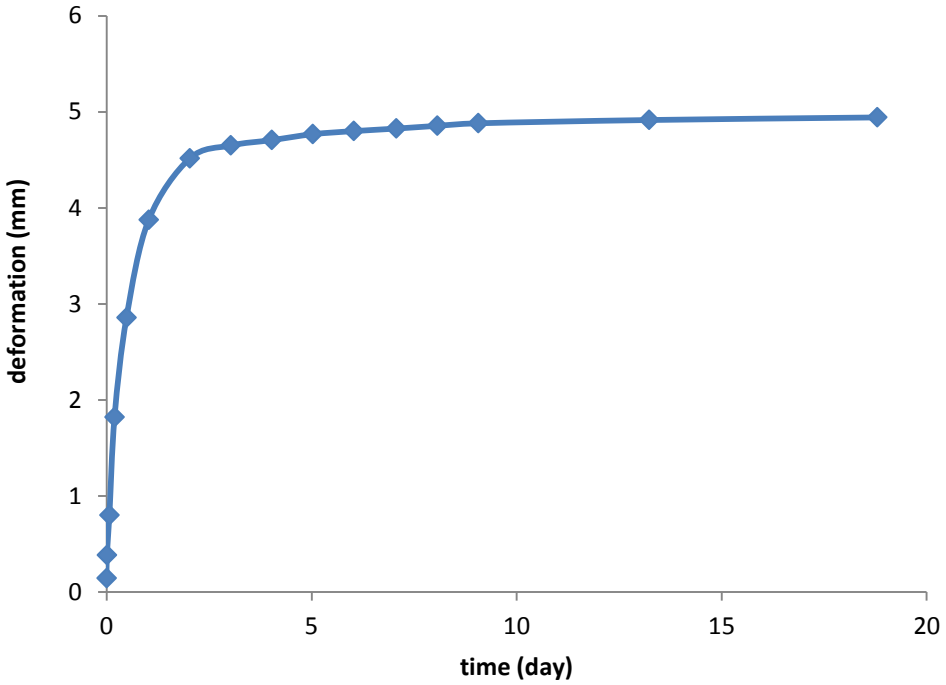

FIGURE E18 Deformation curve of as-received sample three (100 kPa)

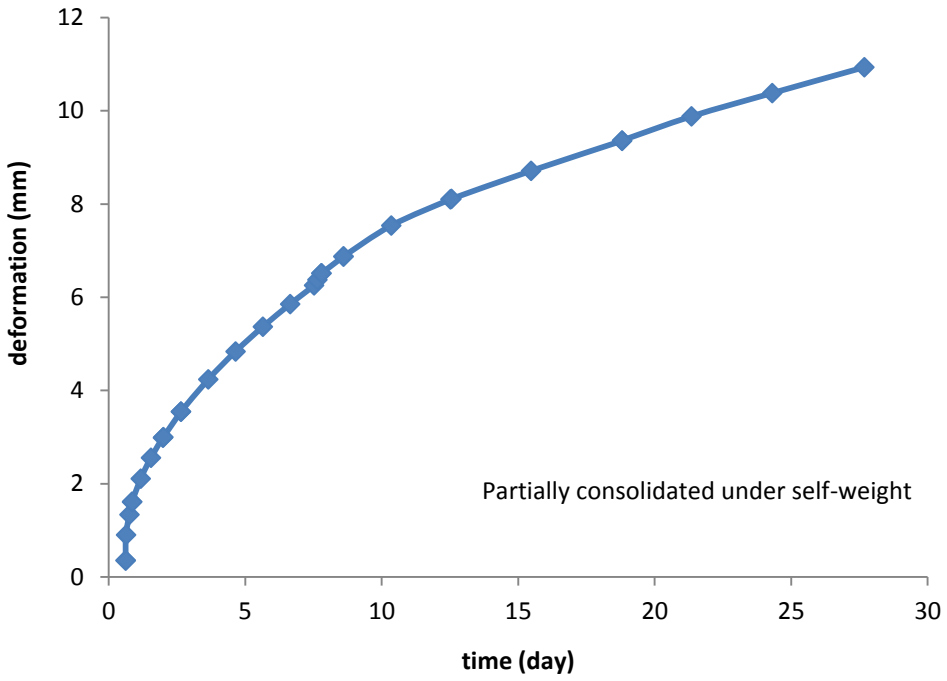

FIGURE E19 Deformation curve of as-received sample four (self-weight)

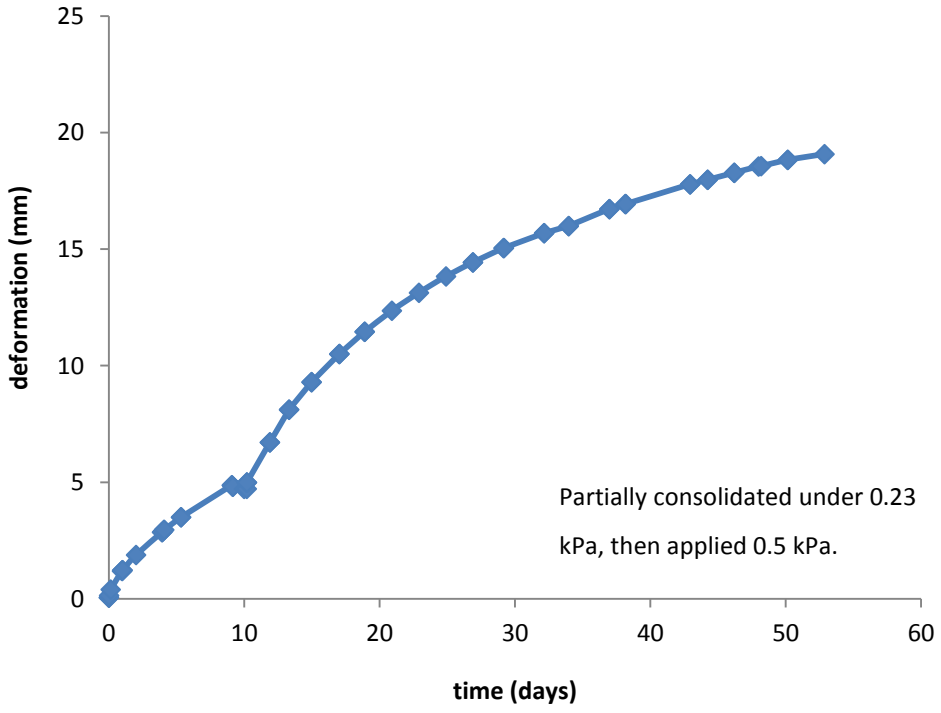

FIGURE E20 Deformation curve of as-received sample four (0.23 kPa and 0.5 kPa)

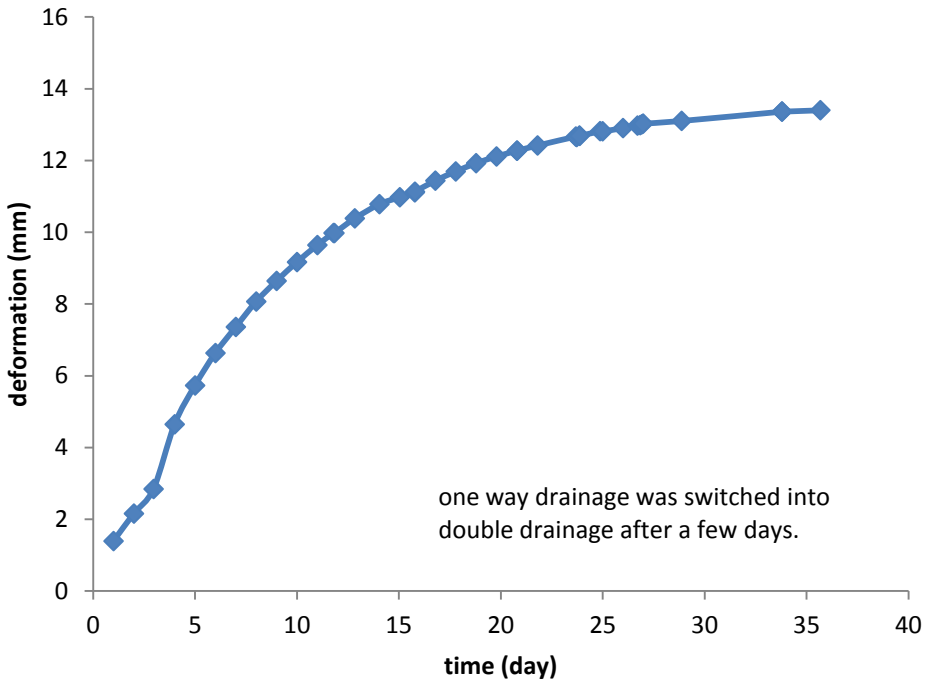

FIGURE E21 Deformation curve of as-received sample four (2 kPa)

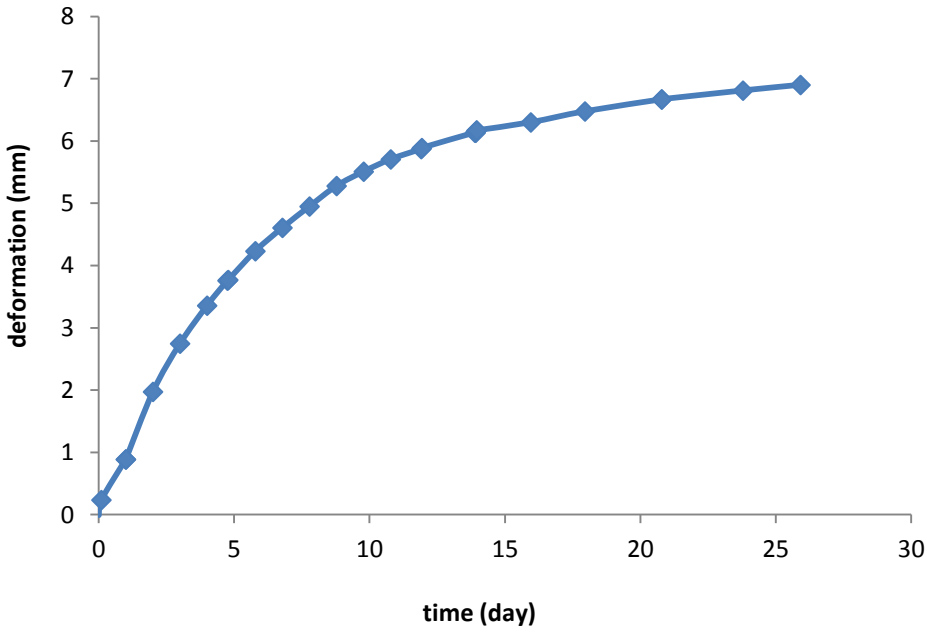

FIGURE E22 Deformation curve of as-received sample four (4 kPa)

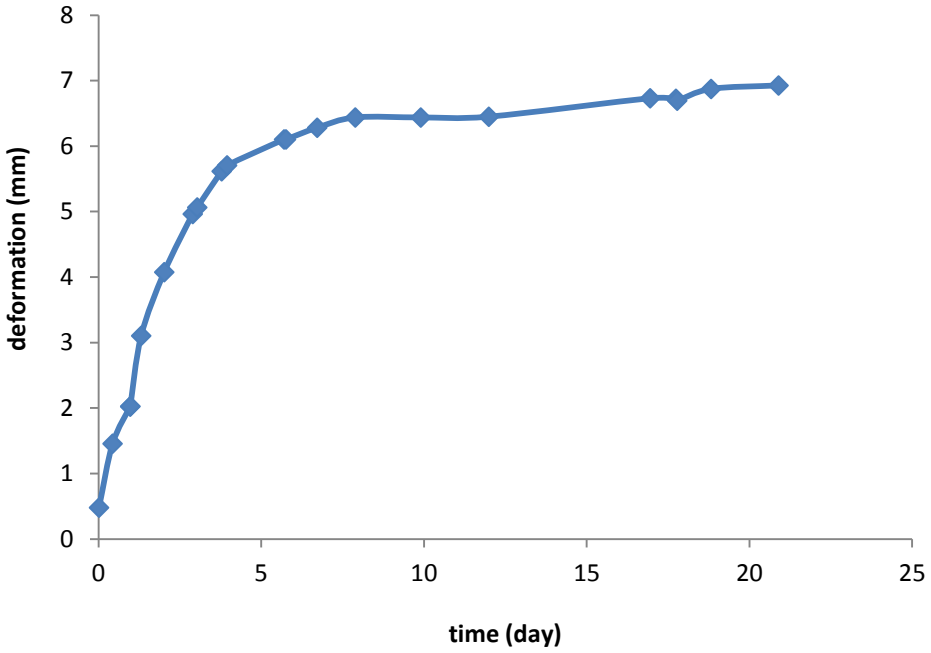

FIGURE E23 Deformation curve of as-received sample four (10 kPa)

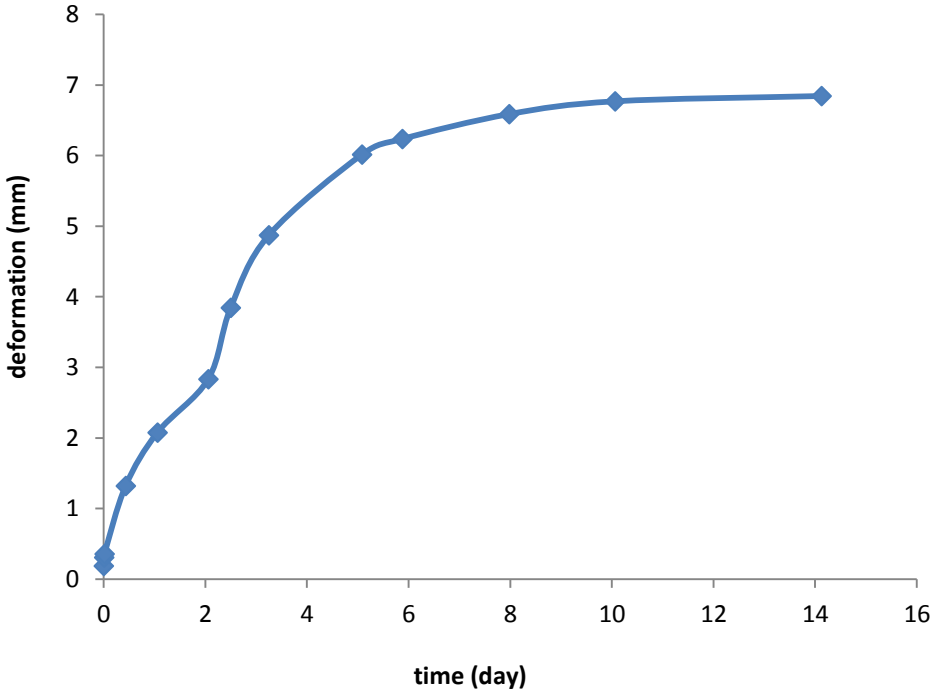

FIGURE E24 Deformation curve of as-received sample four (20 kPa)

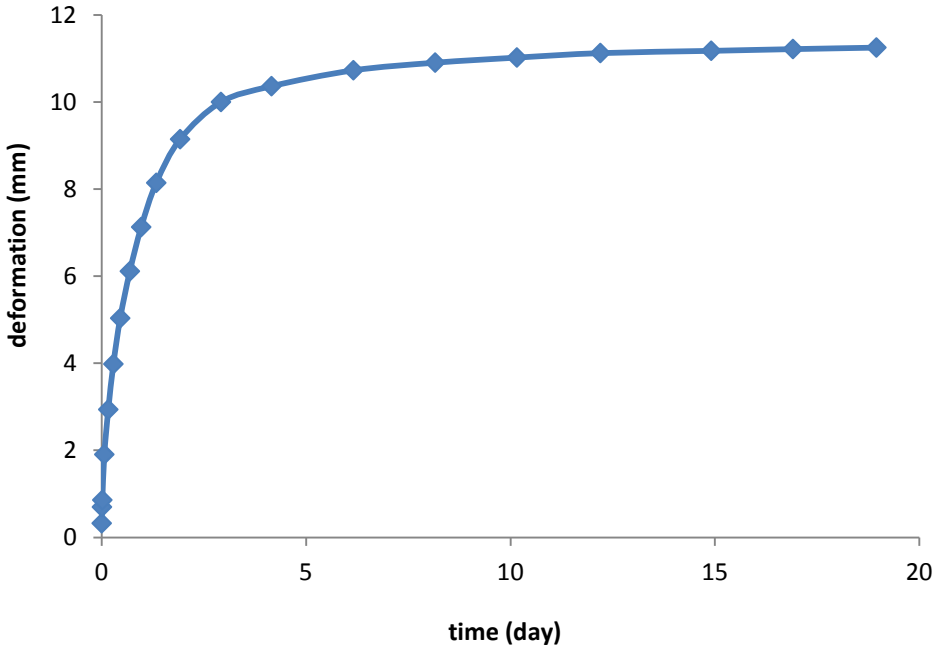

FIGURE E25 Deformation curve of as-received sample four (50 kPa)

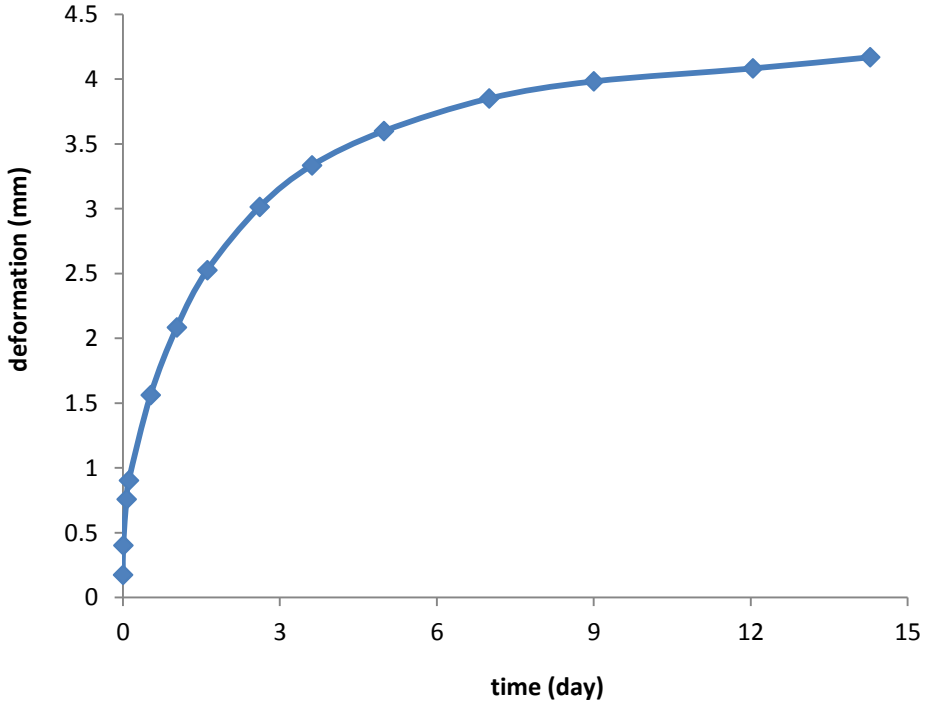

FIGURE E26 Deformation curve of as-received sample four (100 kPa)

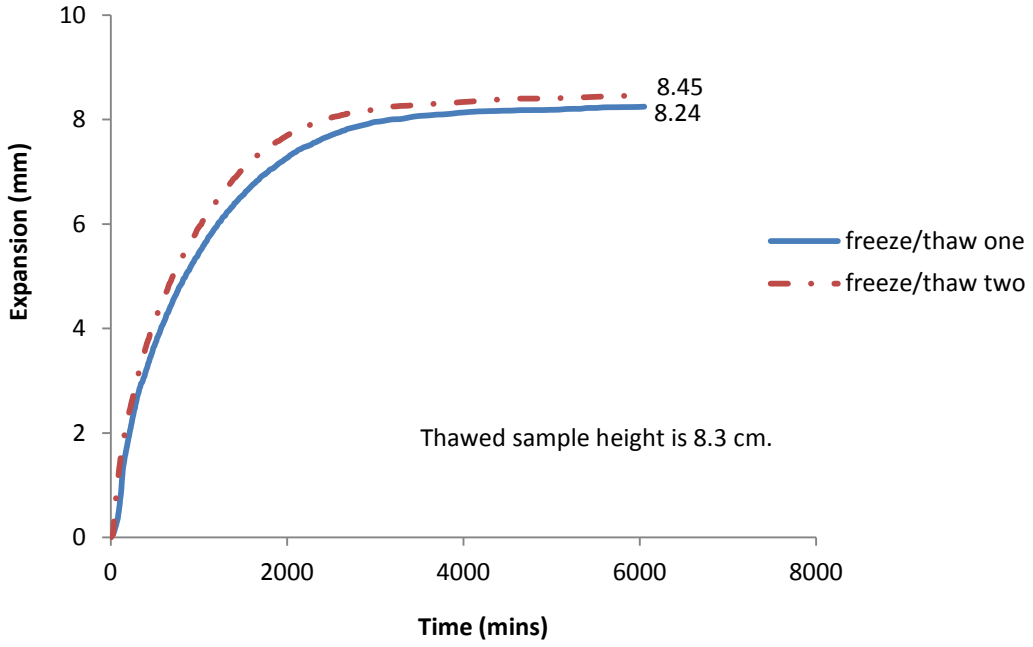

FIGURE E27 Expansion of both samples during freezing

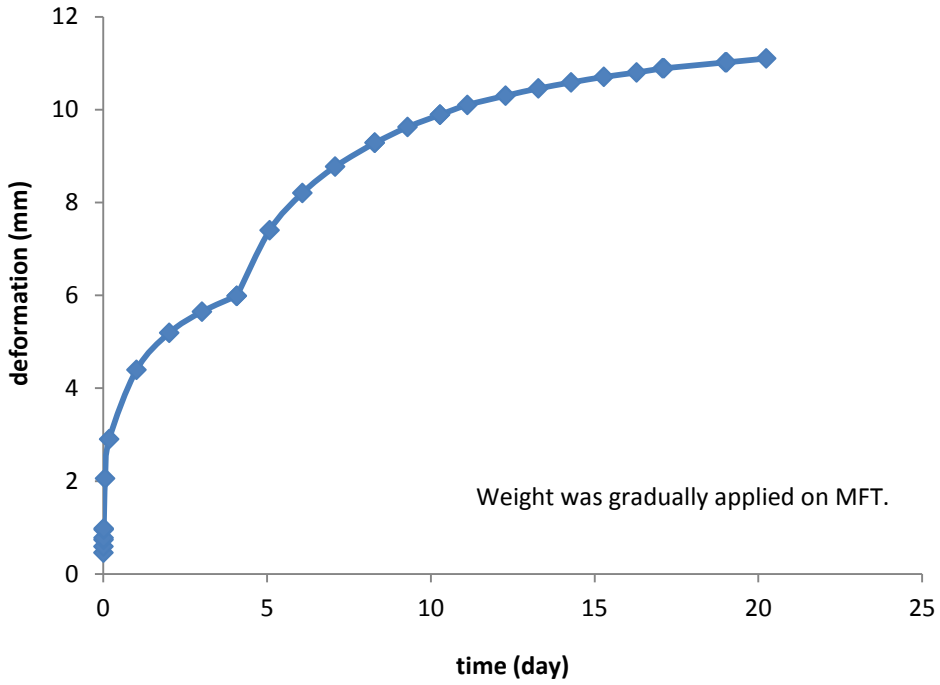

FIGURE E28 Deformation curve of frozen/thawed sample one (1.3 kPa)

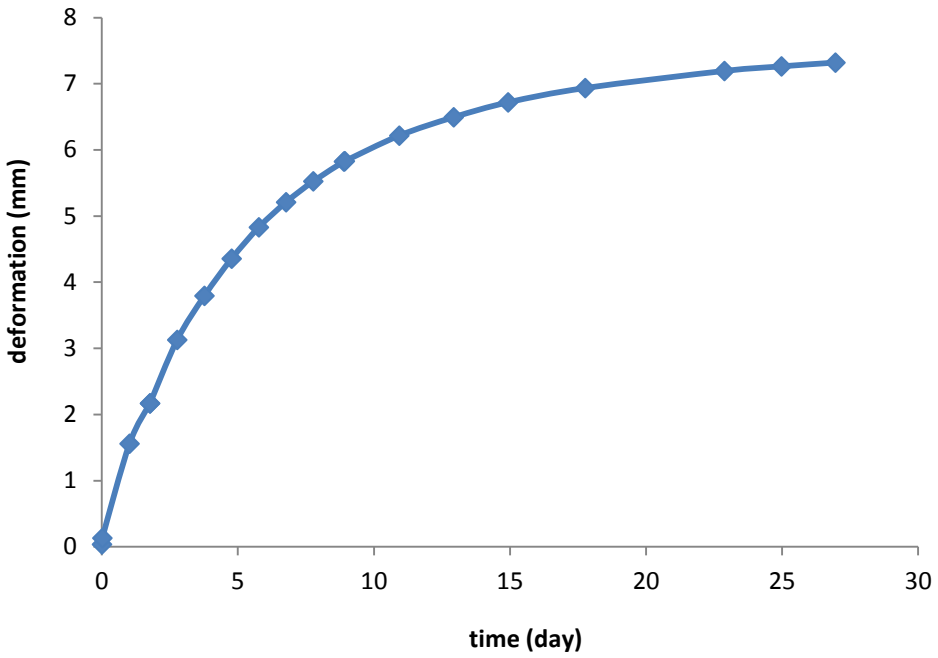

FIGURE E29 Deformation curve of frozen/thawed sample one (4 kPa)

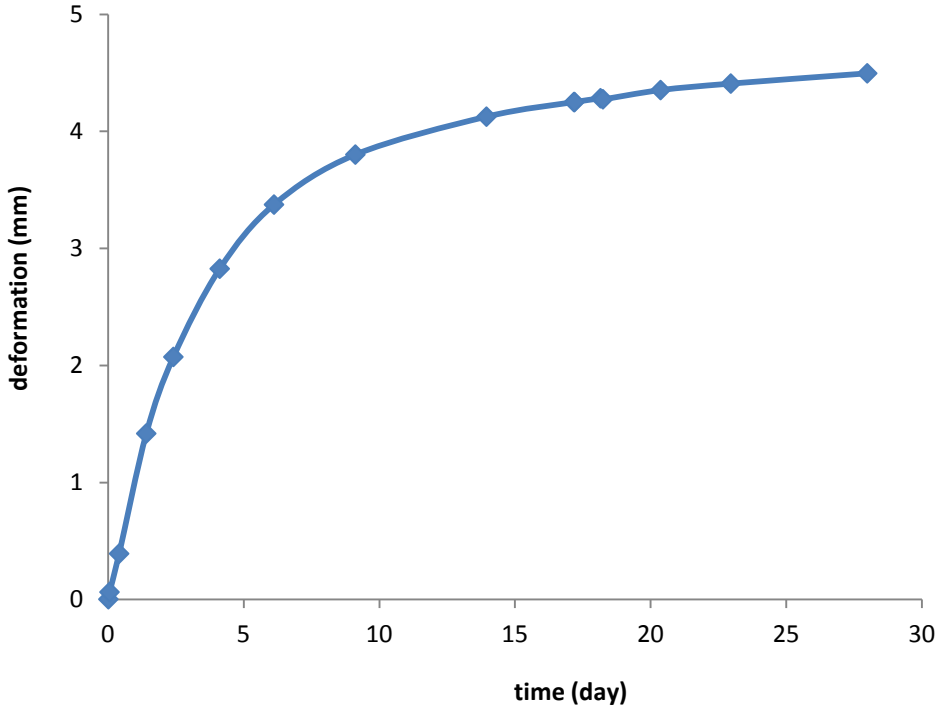

FIGURE E30 Deformation curve of frozen/thawed sample one (10 kPa)

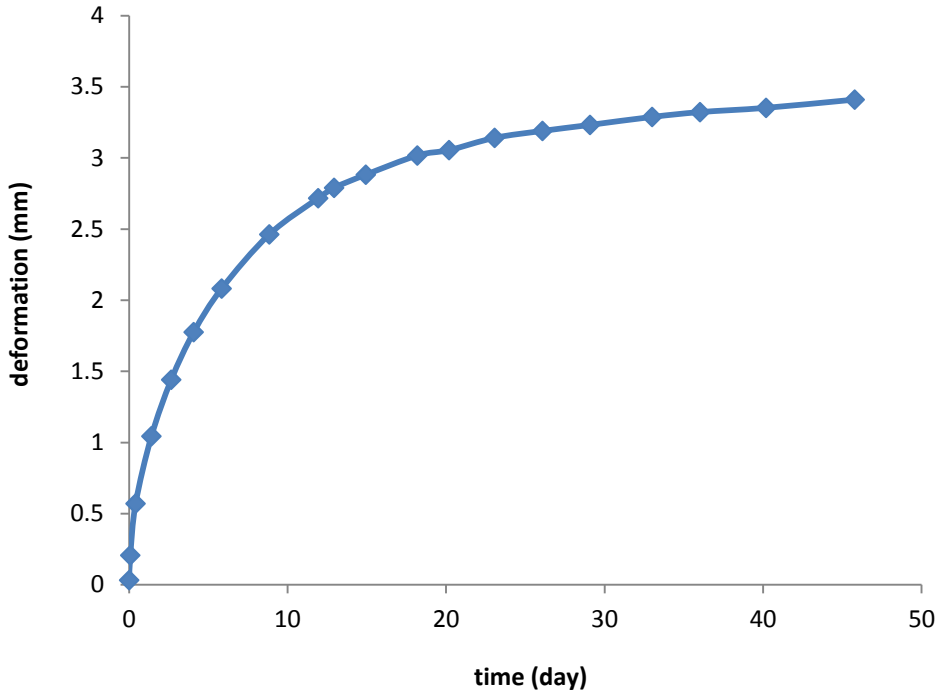

FIGURE E31 Deformation curve of frozen/thawed sample one (20 kPa)

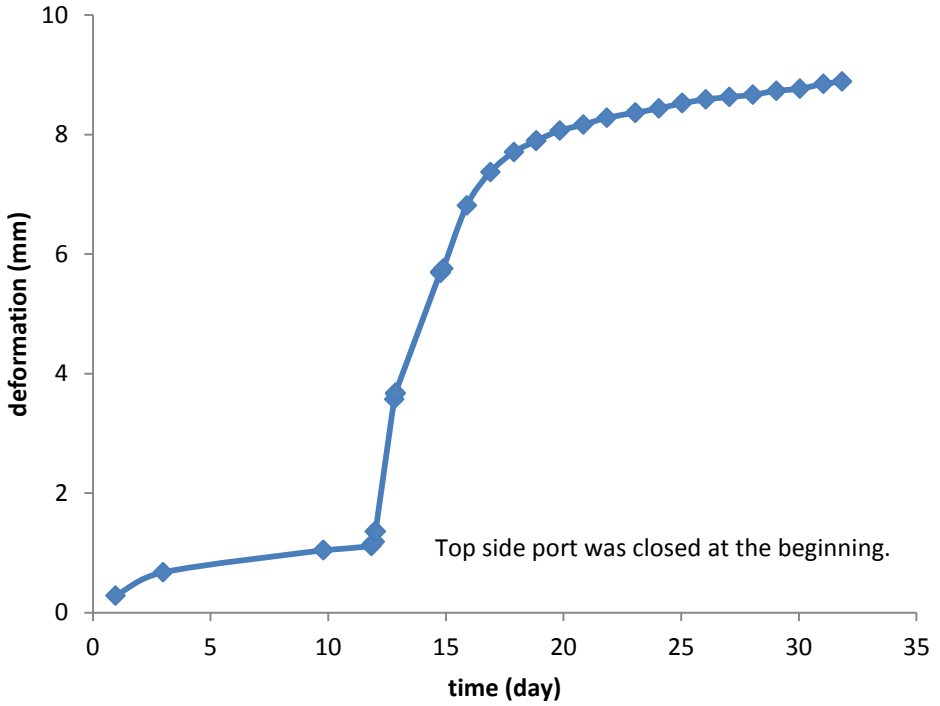

FIGURE E32 Deformation curve of frozen/thawed sample two (4 kPa)

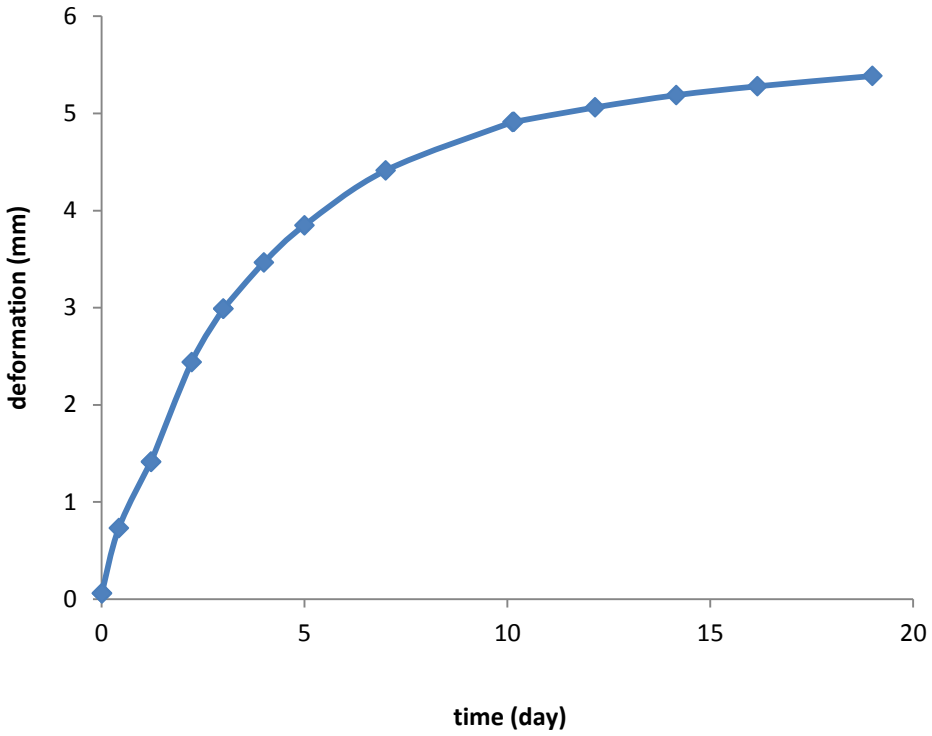

FIGURE E33 Deformation curve of frozen/thawed sample two (10 kPa)

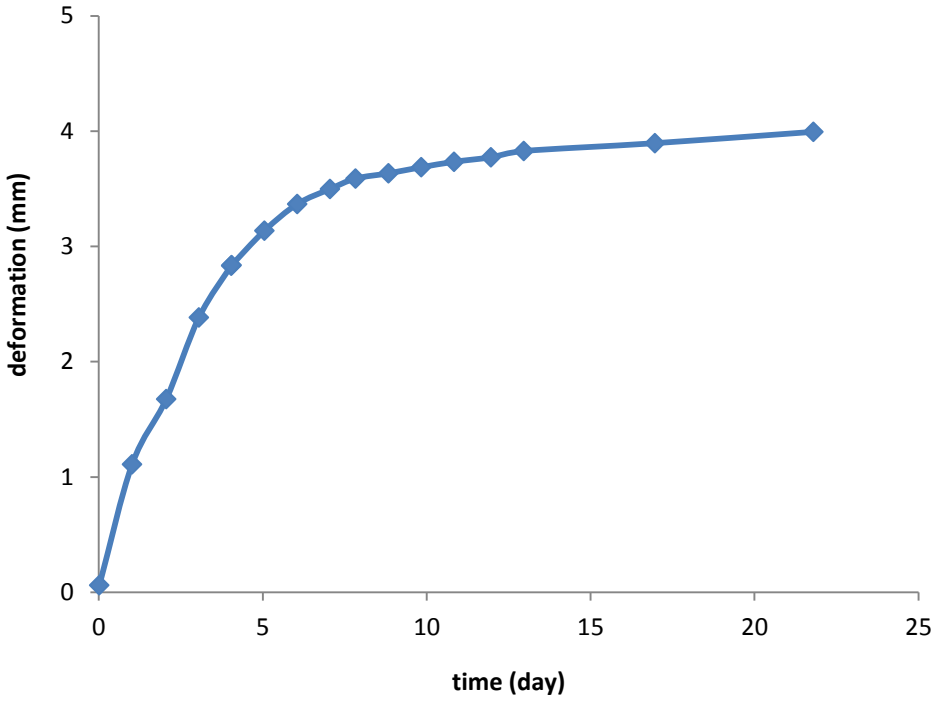

FIGURE E34 Deformation curve of frozen/thawed sample two (20 kPa)

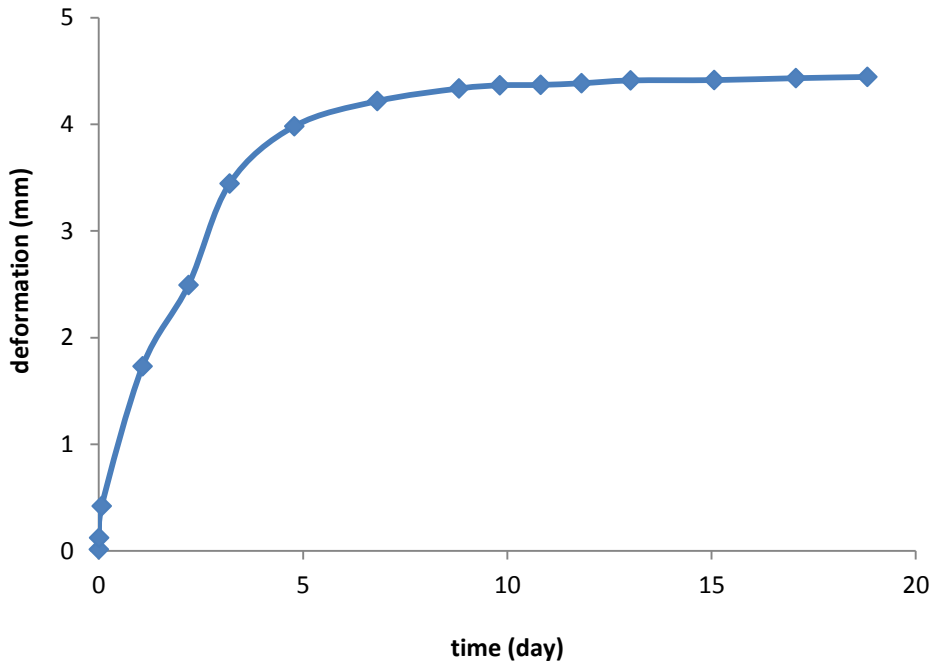

FIGURE E35 Deformation curve of frozen/thawed sample two (50 kPa)

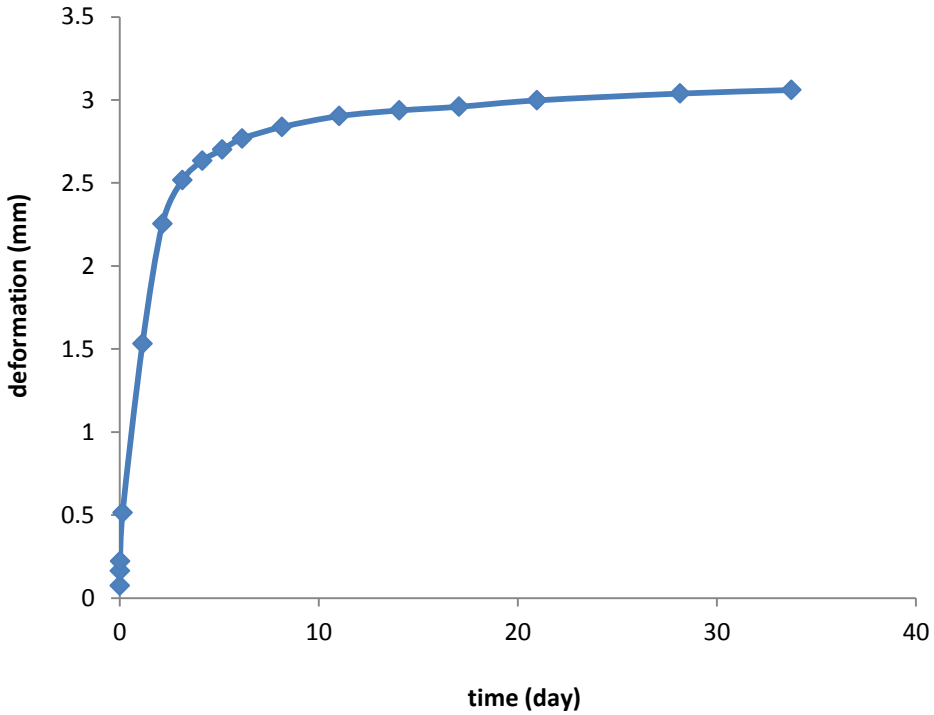

FIGURE E36 Deformation curve of frozen/thawed sample two (100 kPa)

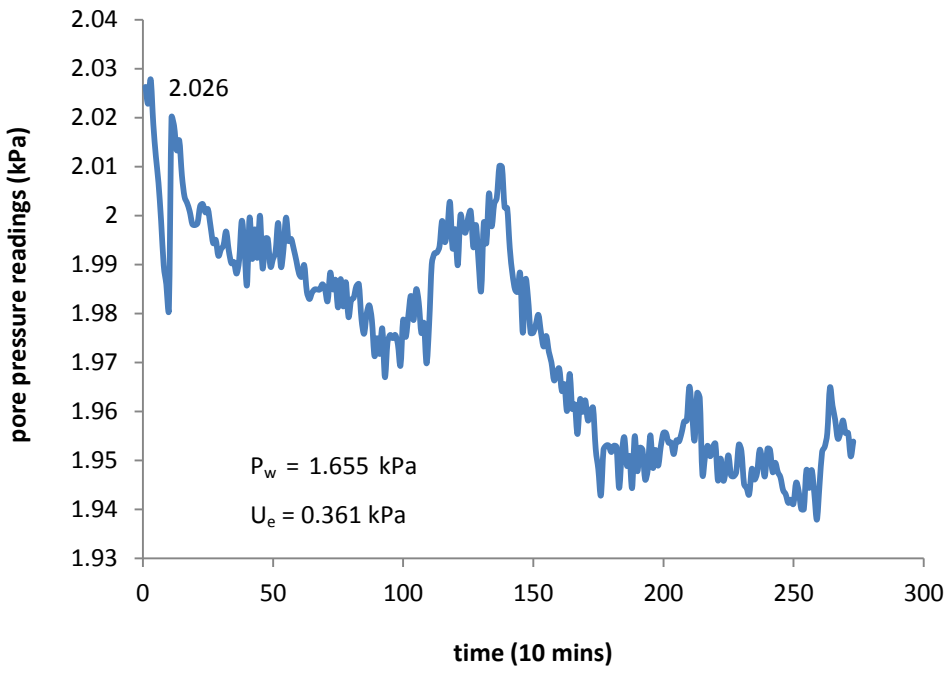

FIGURE E37 Pore pressure of as-received sample one at the beginning

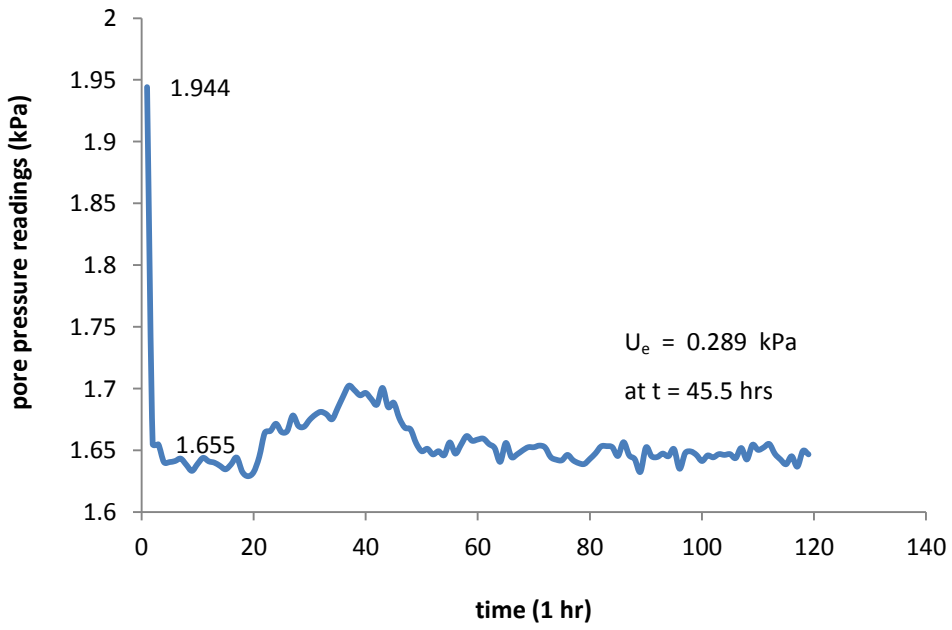

FIGURE E38 Pore pressure of as-received sample one after switching into double drainage

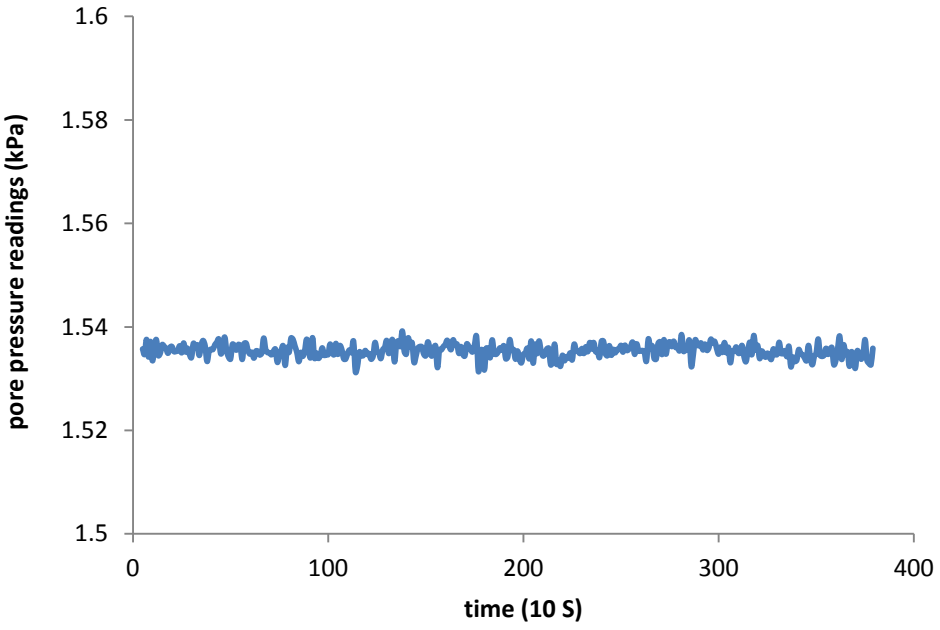

FIGURE E39 Pore pressure of as-received sample two with double drainage at the beginning (self-weight)

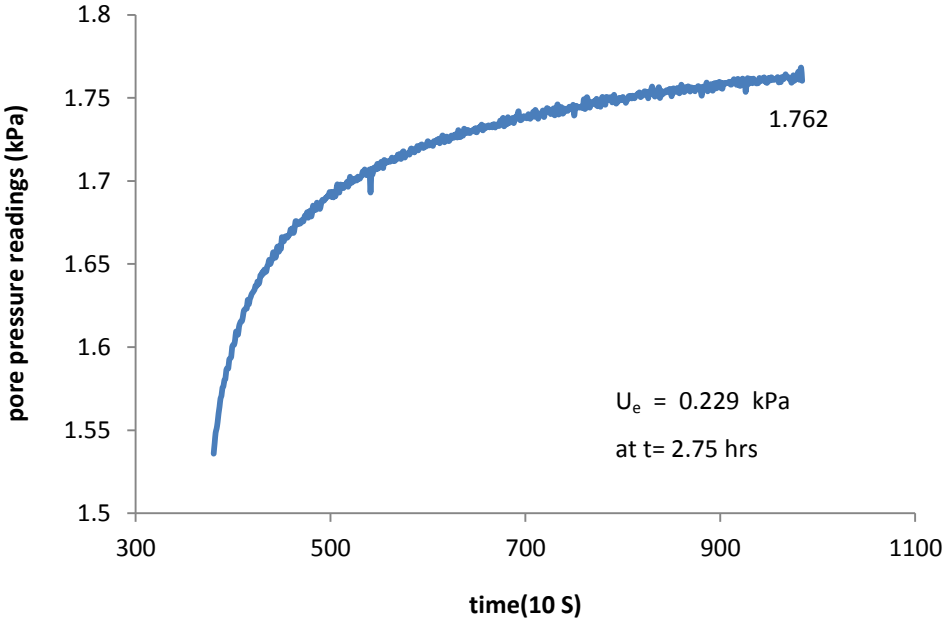

FIGURE E40 Pore pressure of as-received sample two after switching into one-way drainage (self-weight)

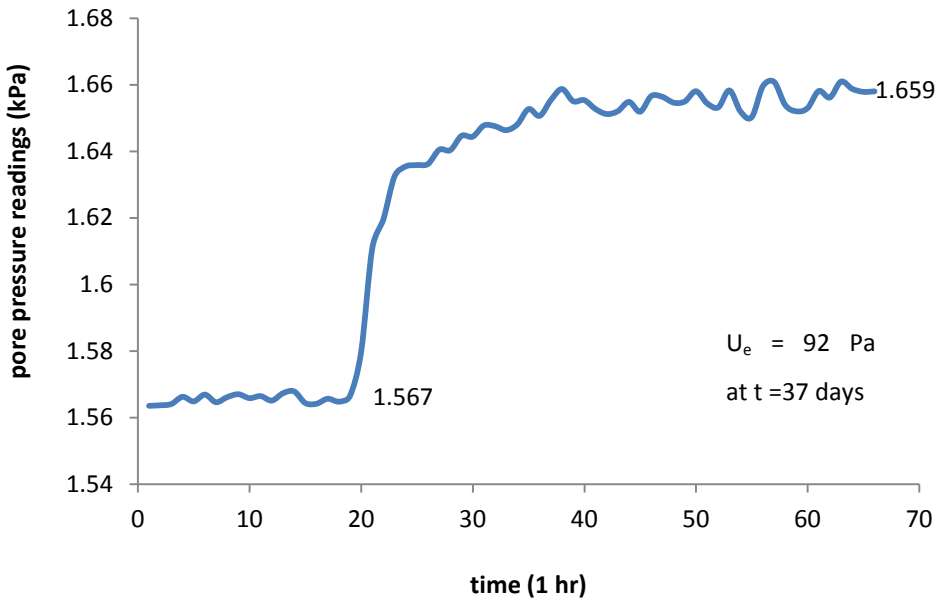

FIGURE E41 Pore pressure of as-received sample two after switching into one-way drainage (2 kPa)

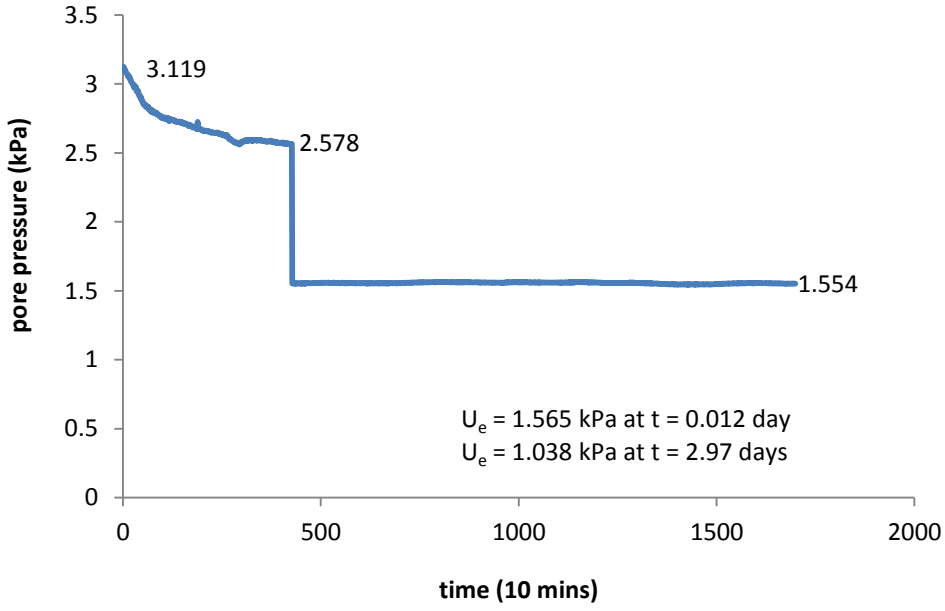

FIGURE E42 Pore pressure of as-received sample two after switching into double drainage (4 kPa)

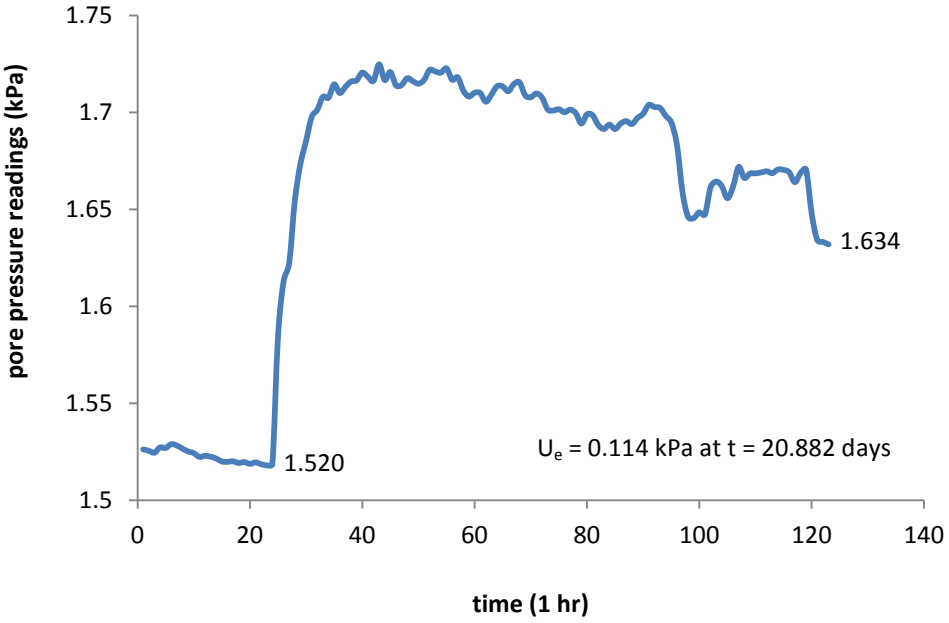

FIGURE E43 Pore pressure of as-received sample two after switching into one-way drainage (4 kPa)

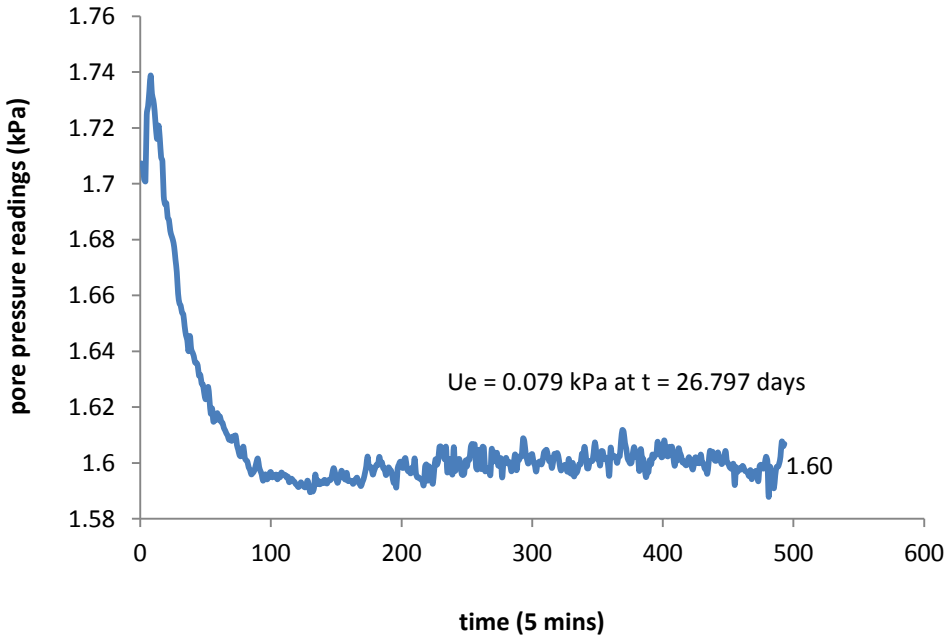

FIGURE E44 Pore pressure of as-received sample two with one-way drainage (4 kPa)

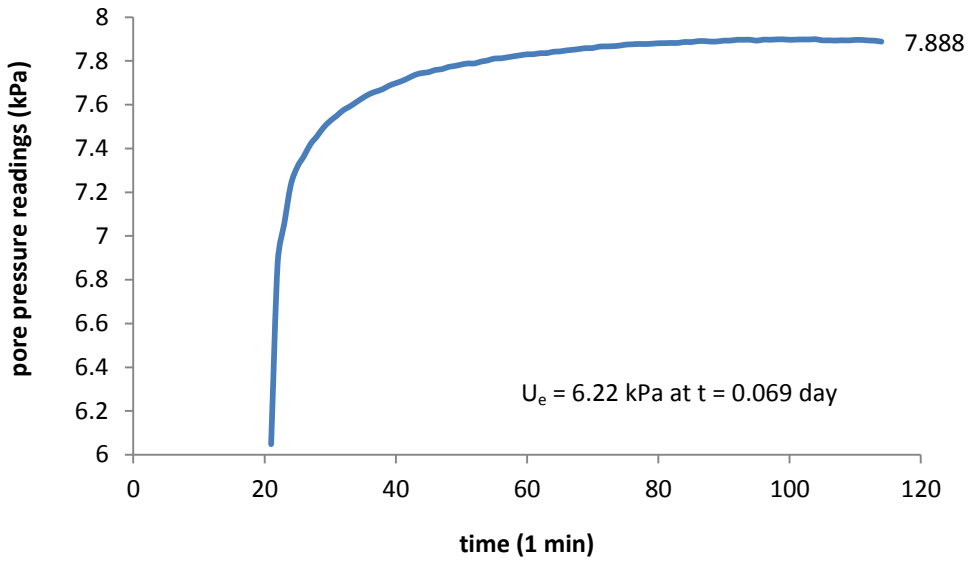

FIGURE E45 Pore pressure of as-received sample two at the beginning with one way drainage (10 kPa)

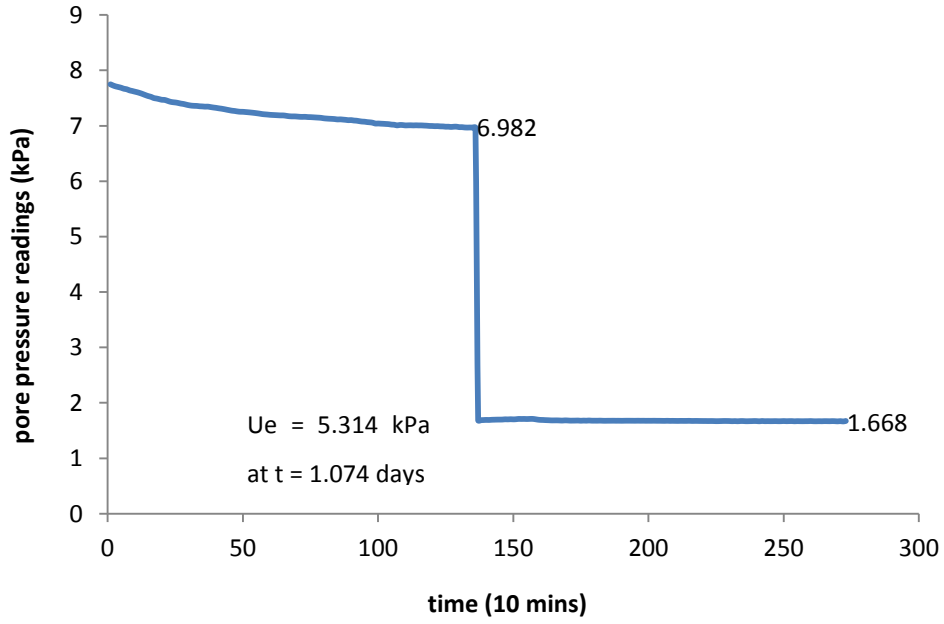

FIGURE E46 Pore pressure of as-received sample two after switching into one way drainage (10 kPa)

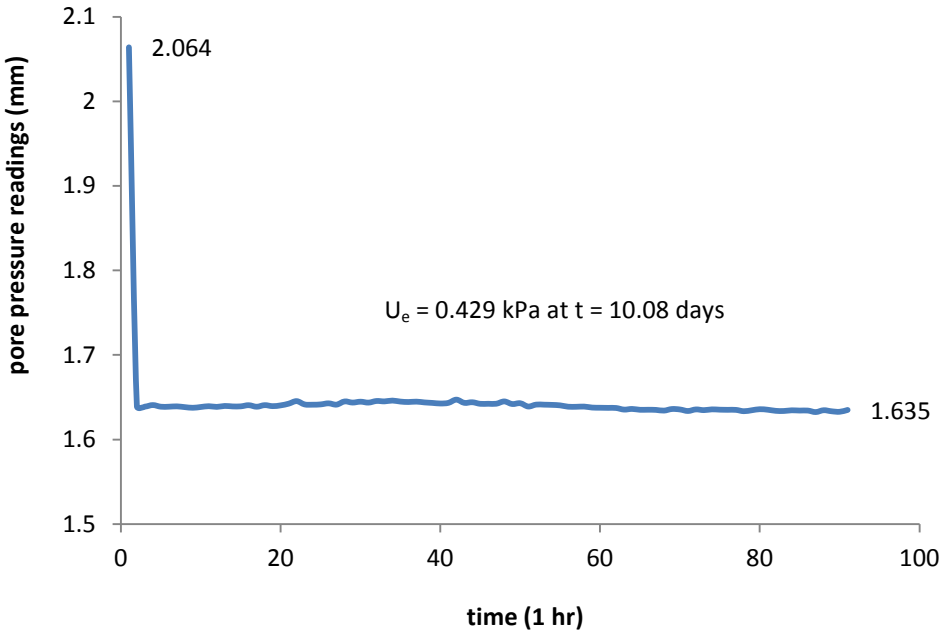

FIGURE E47 Pore pressure of as-received sample two after switching into double drainage (10 kPa)

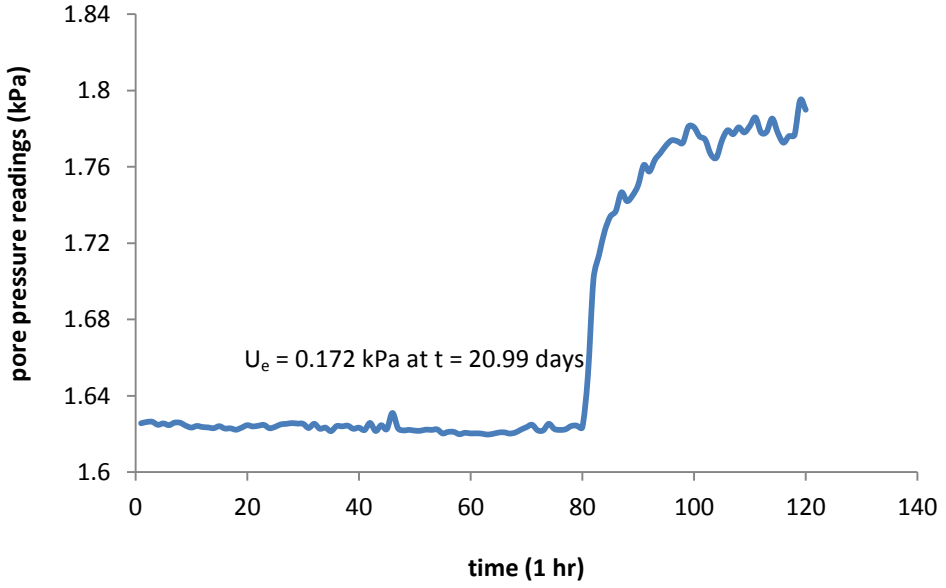

FIGURE E48 Pore pressure of as-received sample two after switching into one way drainage (10 kPa)

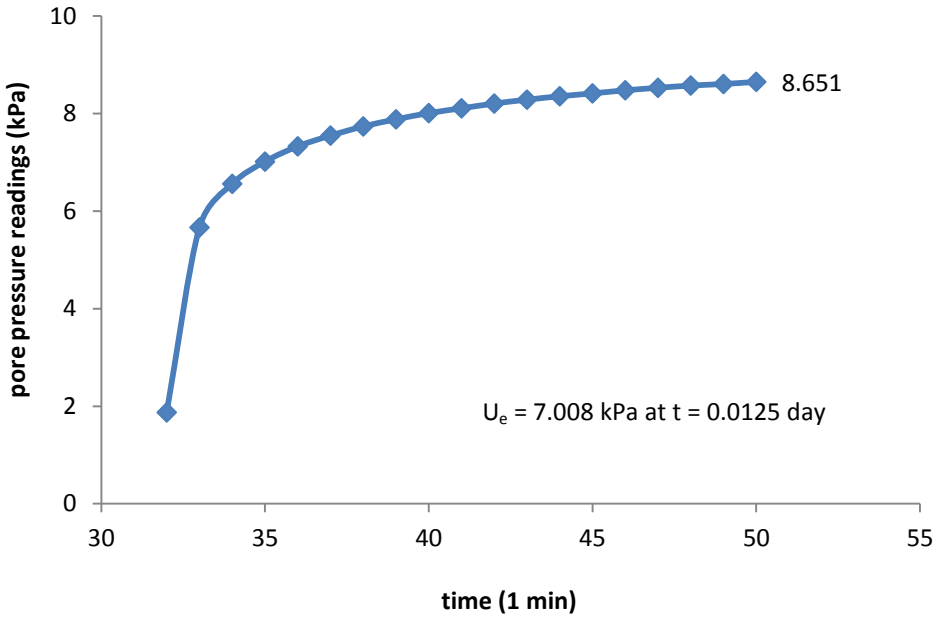

FIGURE E49 Pore pressure of as-received sample two at the beginning with one way drainage (20 kPa)

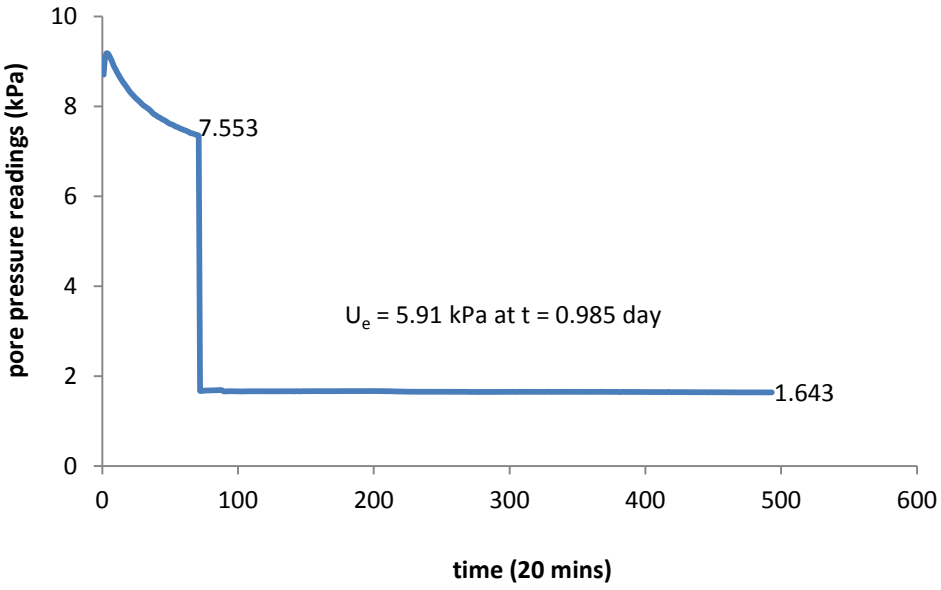

FIGURE E50 Pore pressure of as-received sample two after switching into double drainage (20 kPa)

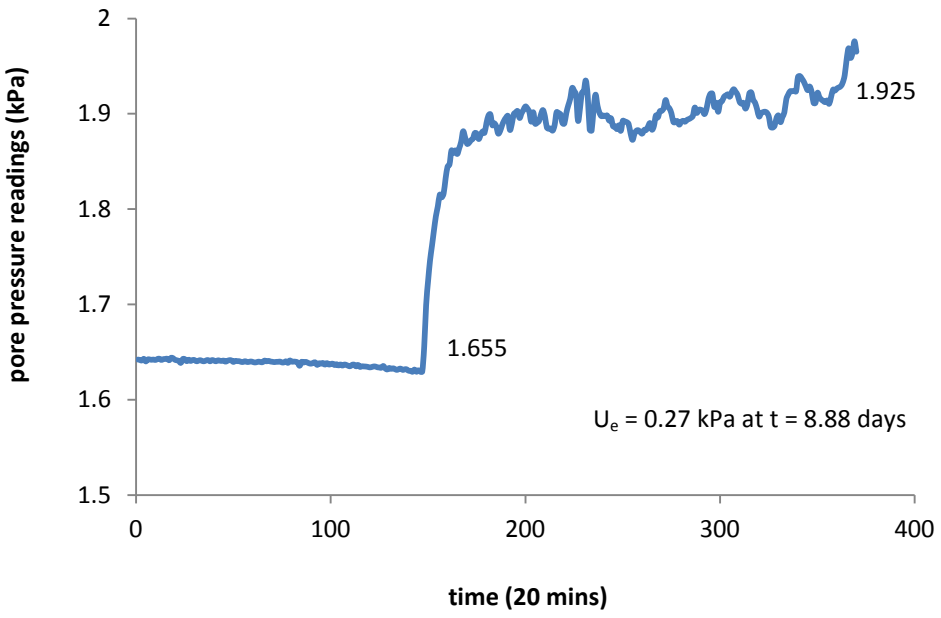

FIGURE E51 Pore pressure of as-received sample two after switching into one way drainage (20 kPa)

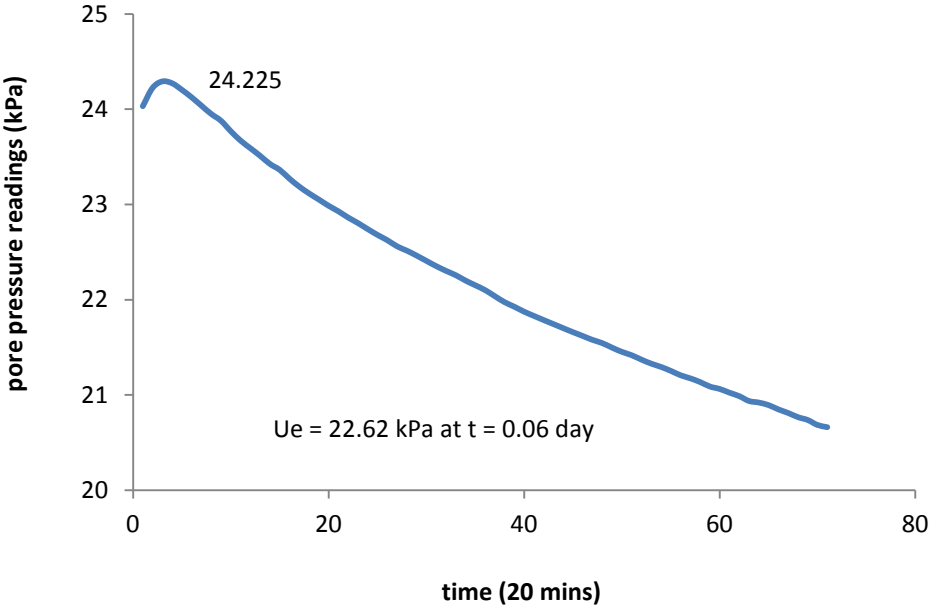

FIGURE E52 Pore pressure of as-received sample two at the beginning with one way drainage (50 kPa)

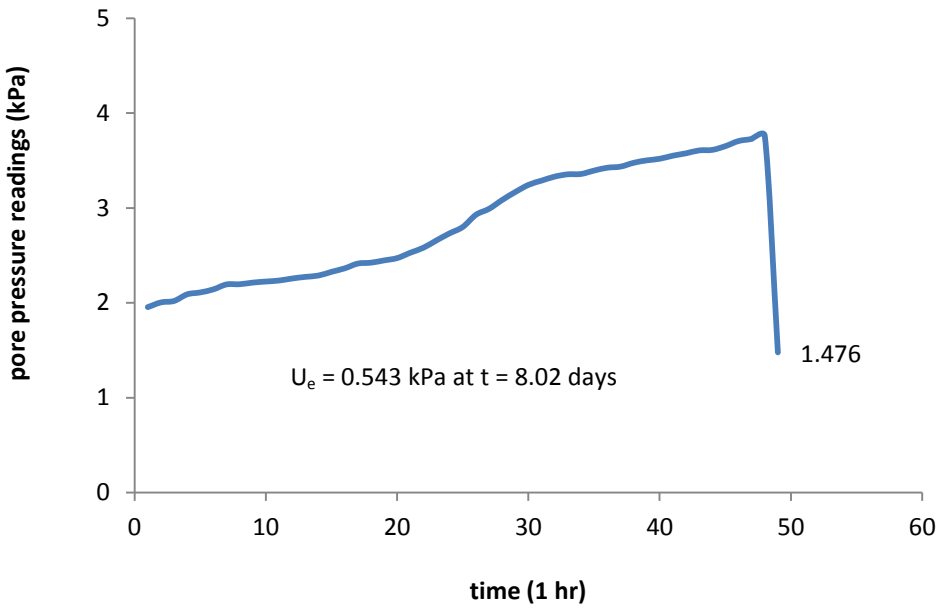

FIGURE E53 Pore pressure of as-received sample two after switching into double drainage (50 kPa)

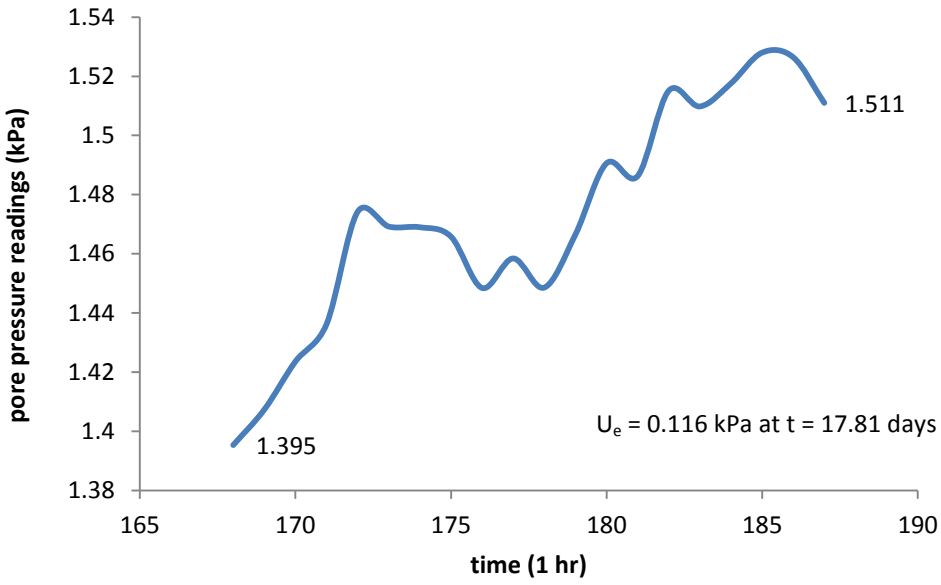

FIGURE E54 Pore pressure of as-received sample two after switching into one-way drainage (50 kPa)

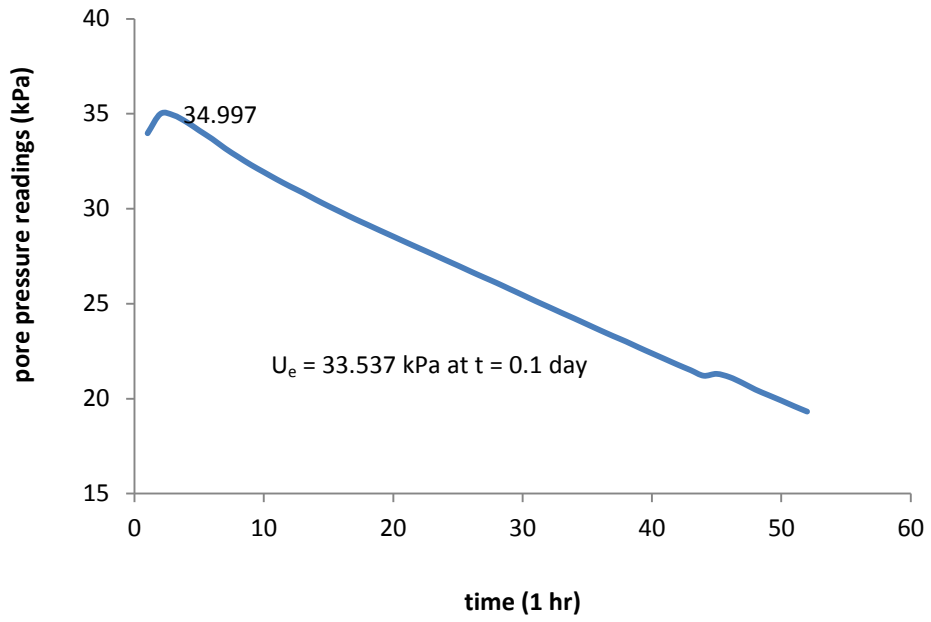

FIGURE E55 Pore pressure of as-received sample two at the beginning with one-way drainage (100 kPa)

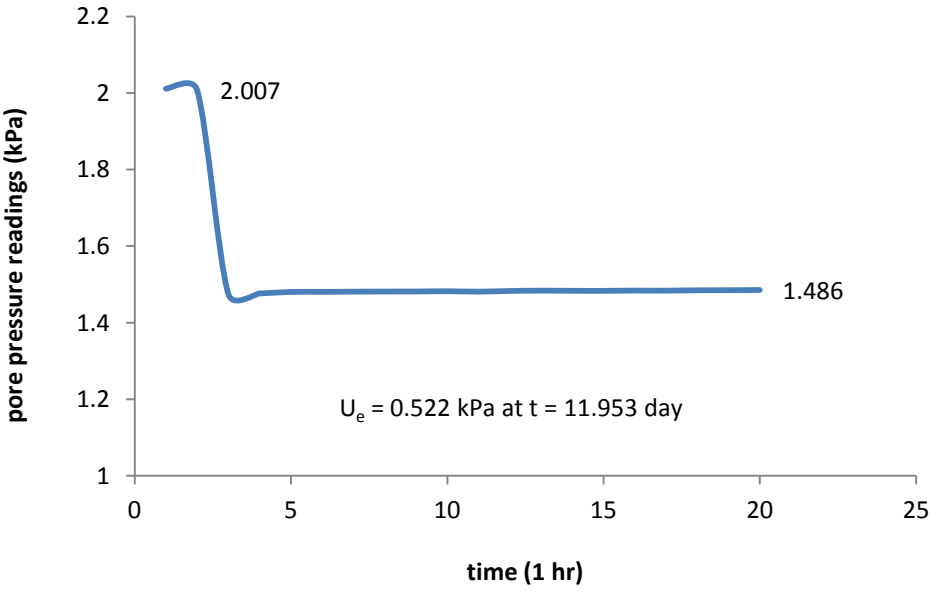

FIGURE E56 Pore pressure of as-received sample two after switching into double drainage (100 kPa)

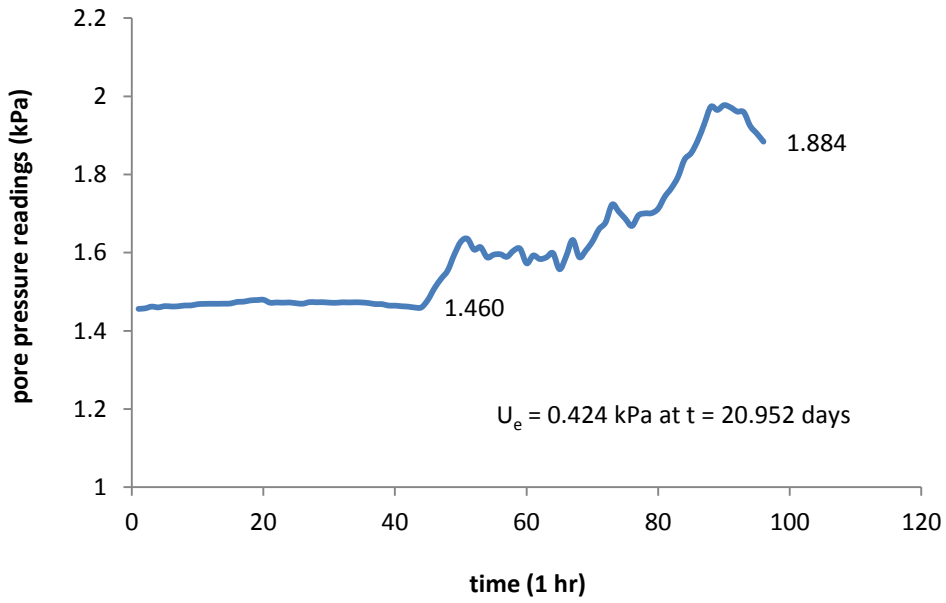

FIGURE E57 Pore pressure of as-received sample two after switching into one-way drainage (100 kPa)

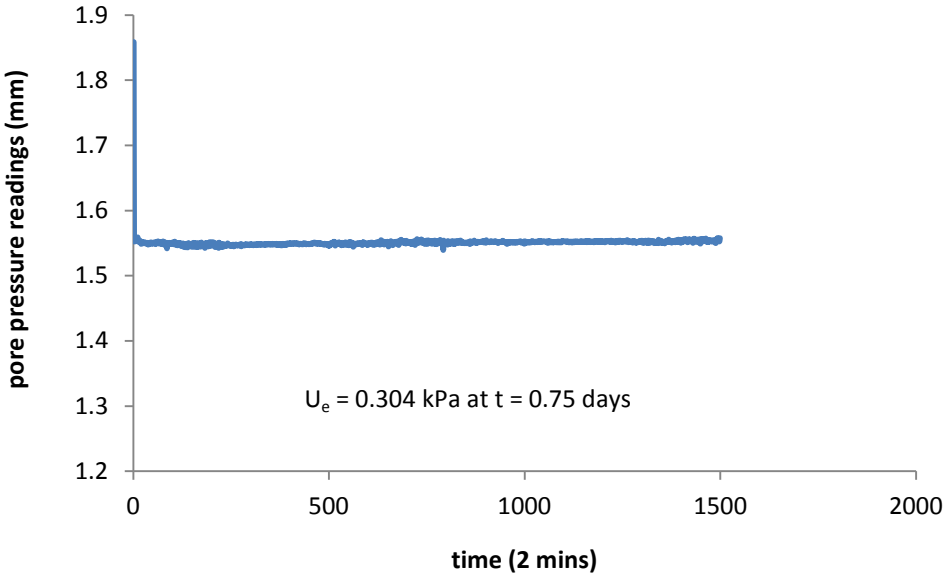

FIGURE E58 Pore pressure of as-received sample three after switching into double drainage (self-weight)

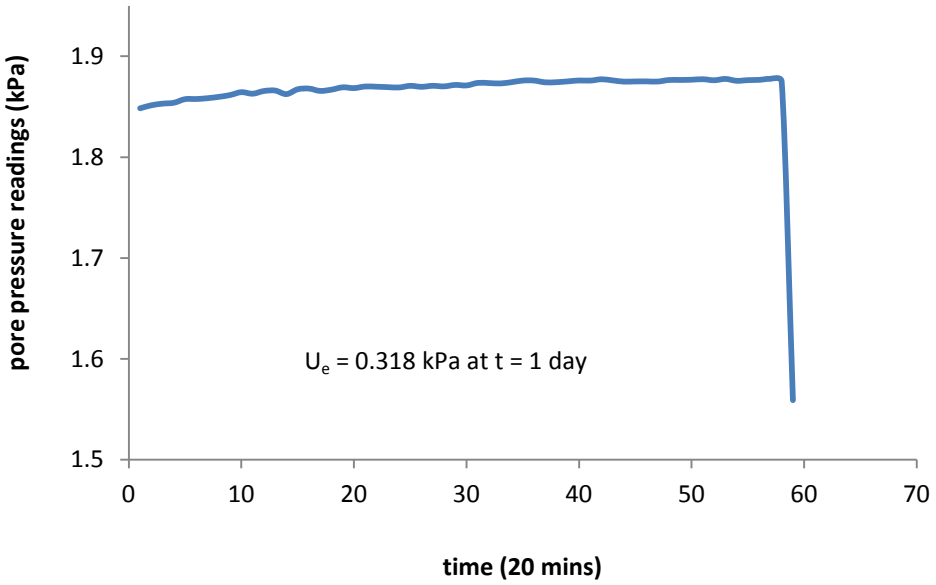

FIGURE E59 Pore pressure of as-received sample three after switching into double drainage (0.23 kPa)

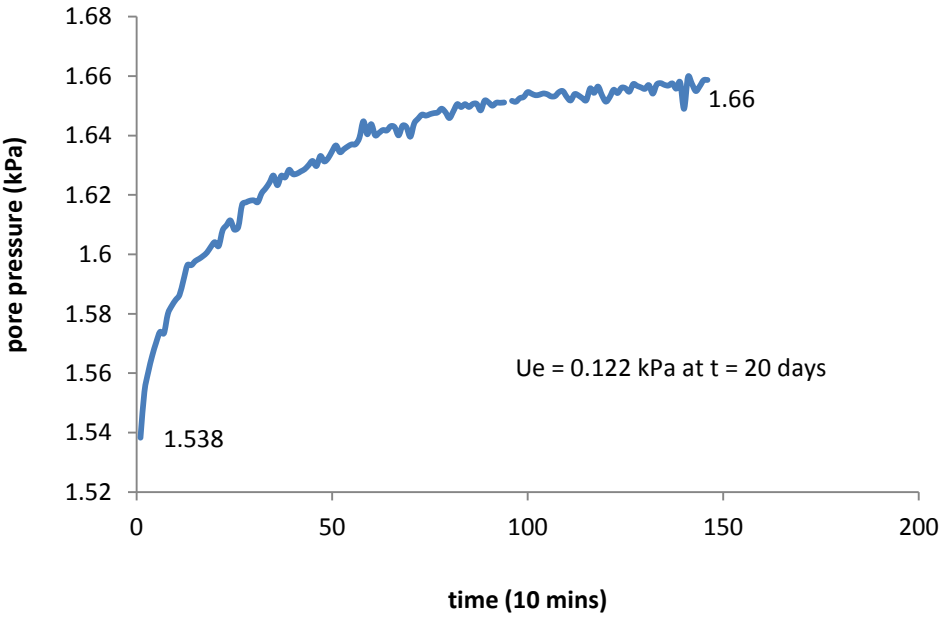

FIGURE E60 Pore pressure of as-received sample three after switching into one-way drainage (0.23 kPa)

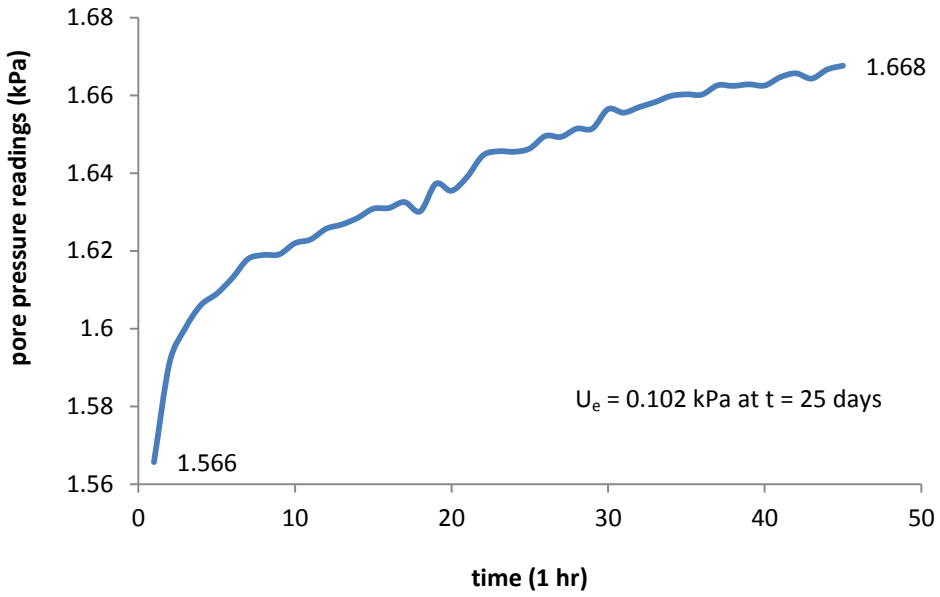

FIGURE E61 Pore pressure of as-received sample three after switching into one-way drainage (0.5 kPa)

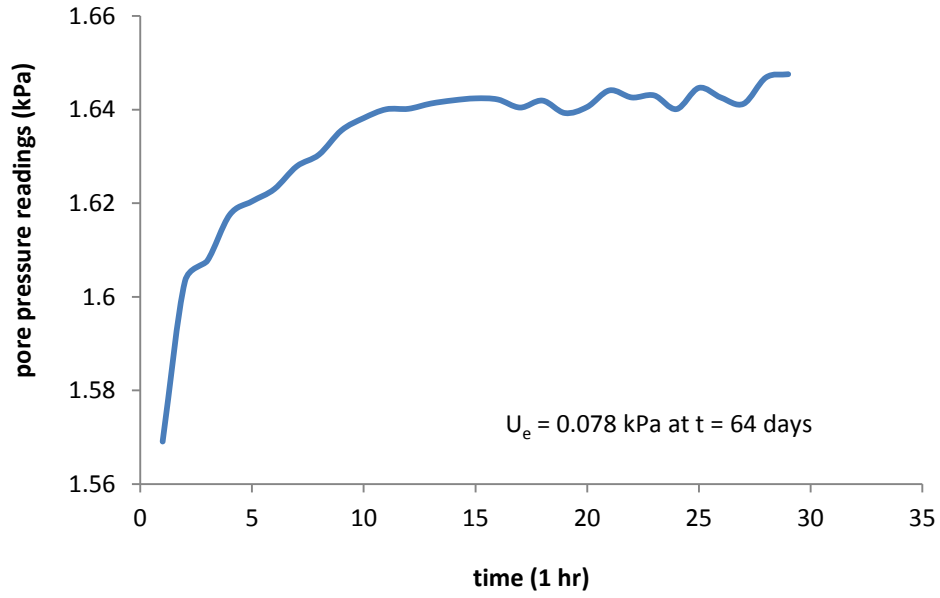

FIGURE E62 Pore pressure of as-received sample three after switching into one-way drainage (0.5 kPa)

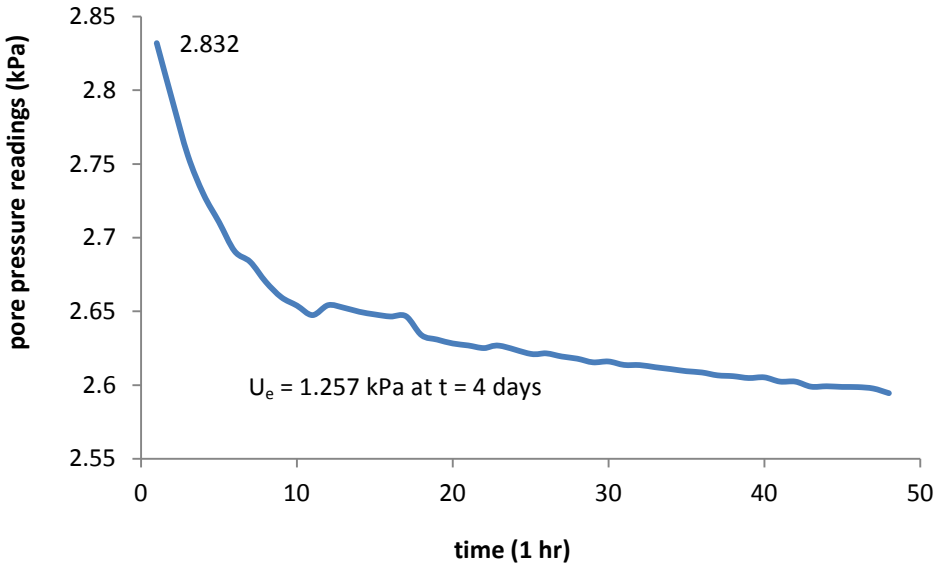

FIGURE E63 Pore pressure of as-received sample three with one-way drainage (2 kPa)

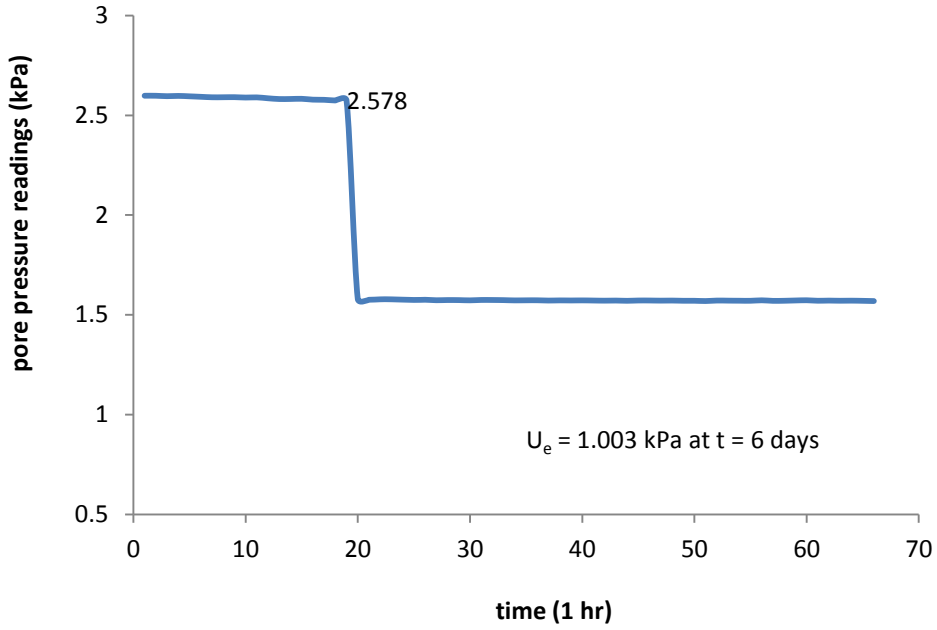

FIGURE E64 Pore pressure of as-received sample three after switching into double drainage (2 kPa)

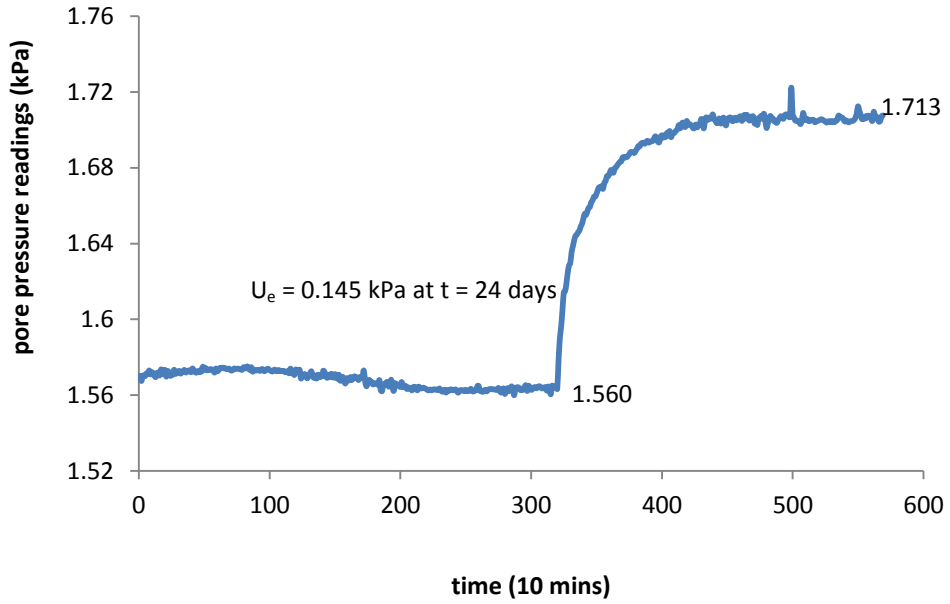

FIGURE E65 Pore pressure of as-received sample three after switching into one-way drainage (2 kPa)

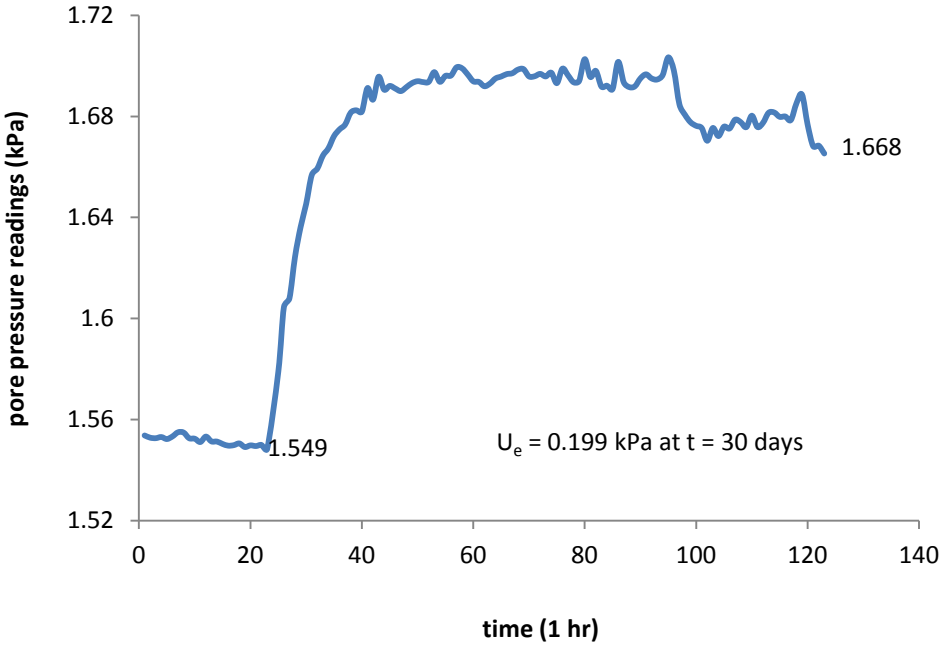

FIGURE E66 Pore pressure of as-received sample three after switching into one-way drainage (2 kPa)

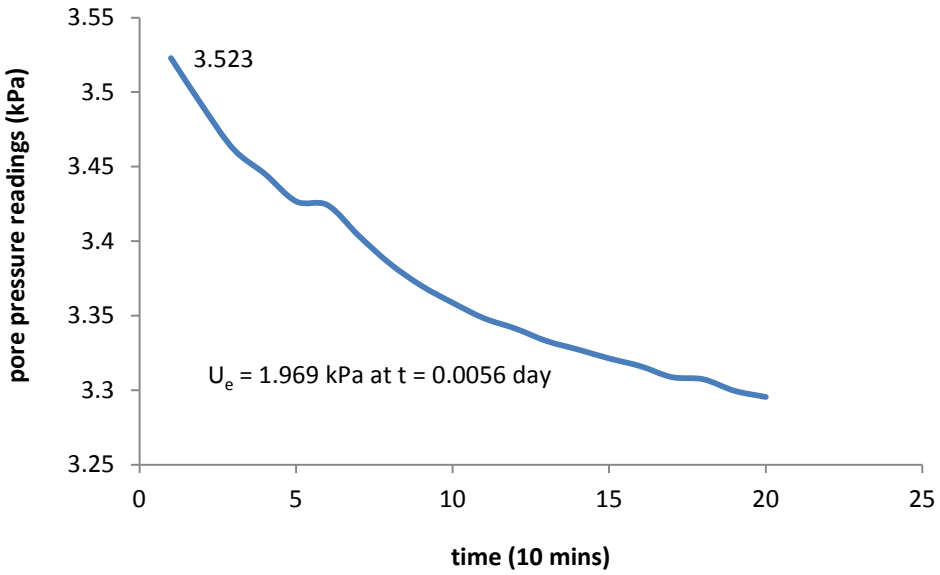

FIGURE E67 Pore pressure of as-received sample three with one-way drainage (4 kPa)

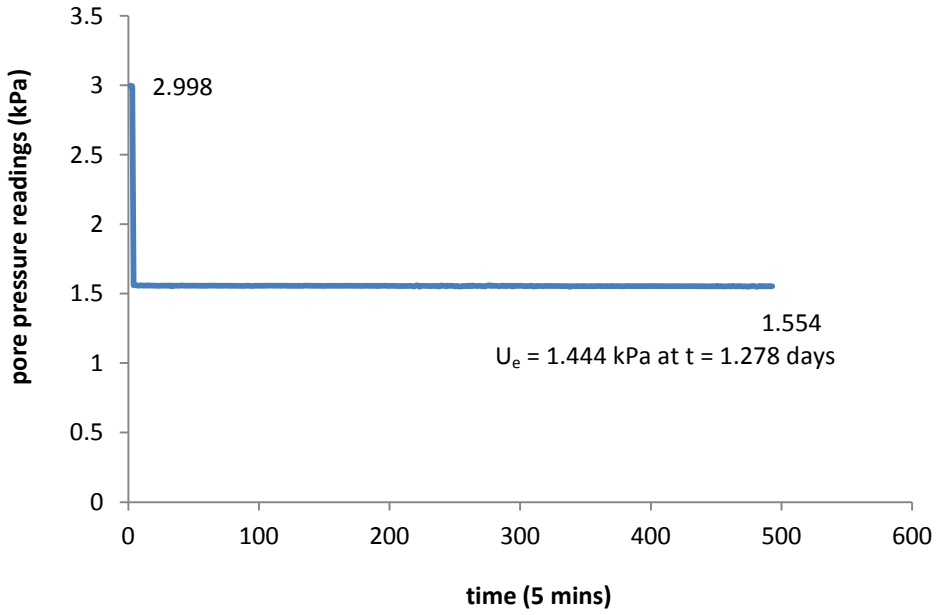

FIGURE E68 Pore pressure of as-received sample three after switching into double drainage (4 kPa)

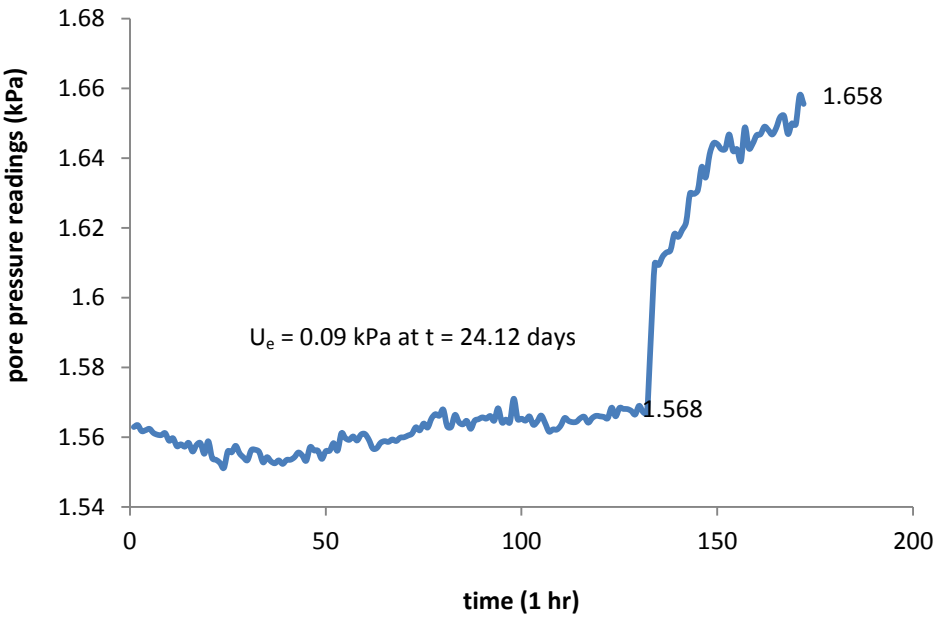

FIGURE E69 Pore pressure of as-received sample three after switching into one-way drainage (4 kPa)

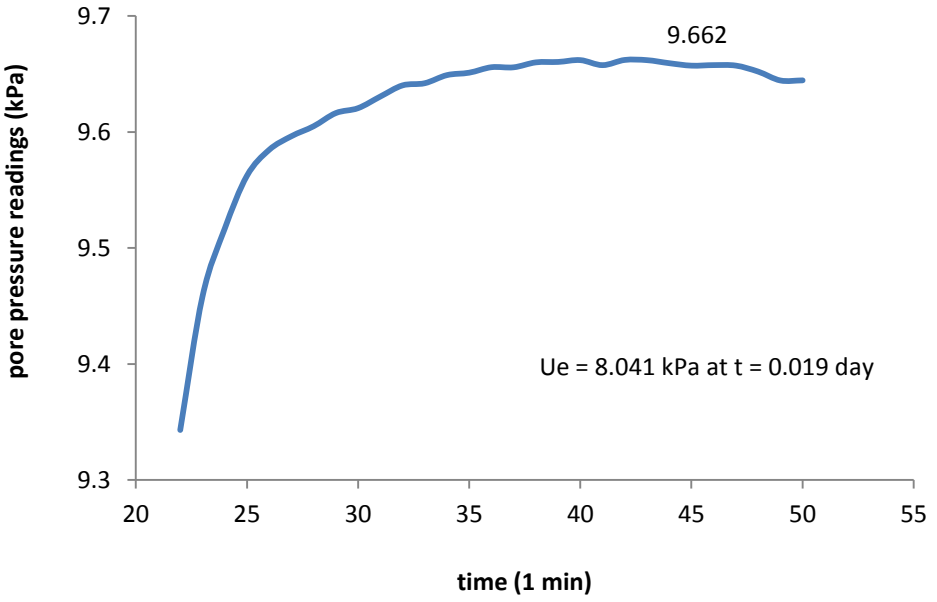

FIGURE E70 Pore pressure of as-received sample three with one-way drainage (10 kPa)

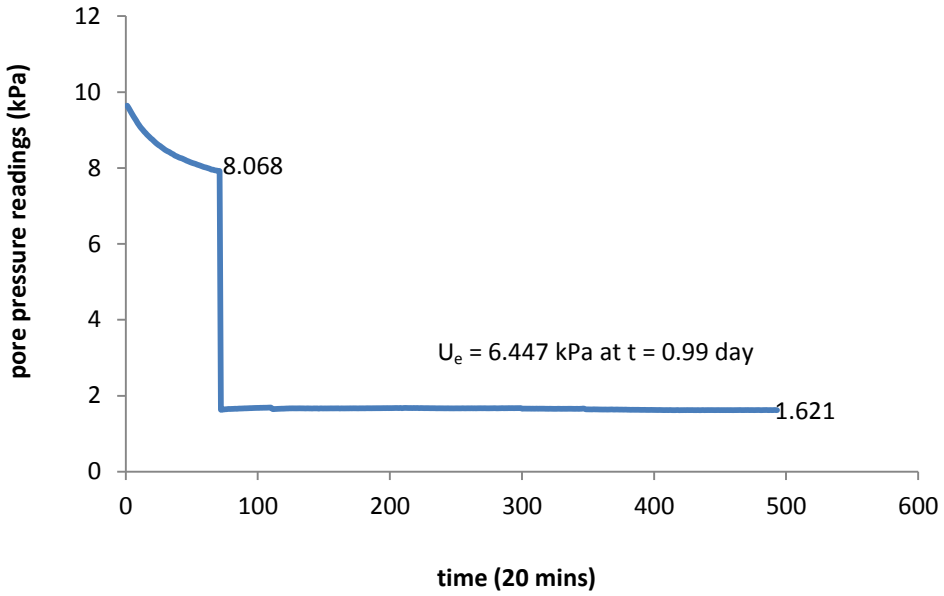

FIGURE E71 Pore pressure of as-received sample three after switching into double drainage (10 kPa)

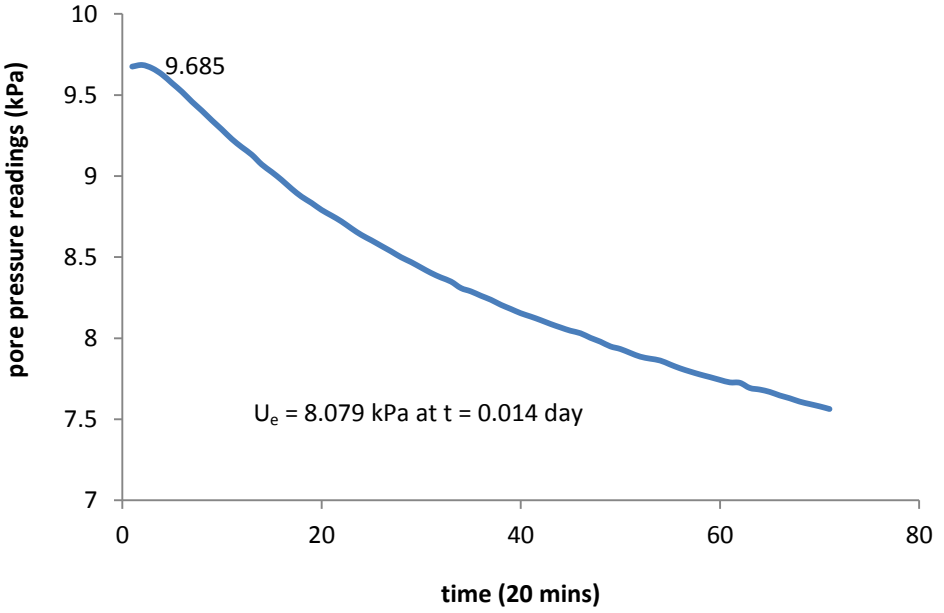

FIGURE E72 Pore pressure of as-received sample three at the beginning with one-way drainage (20 kPa)

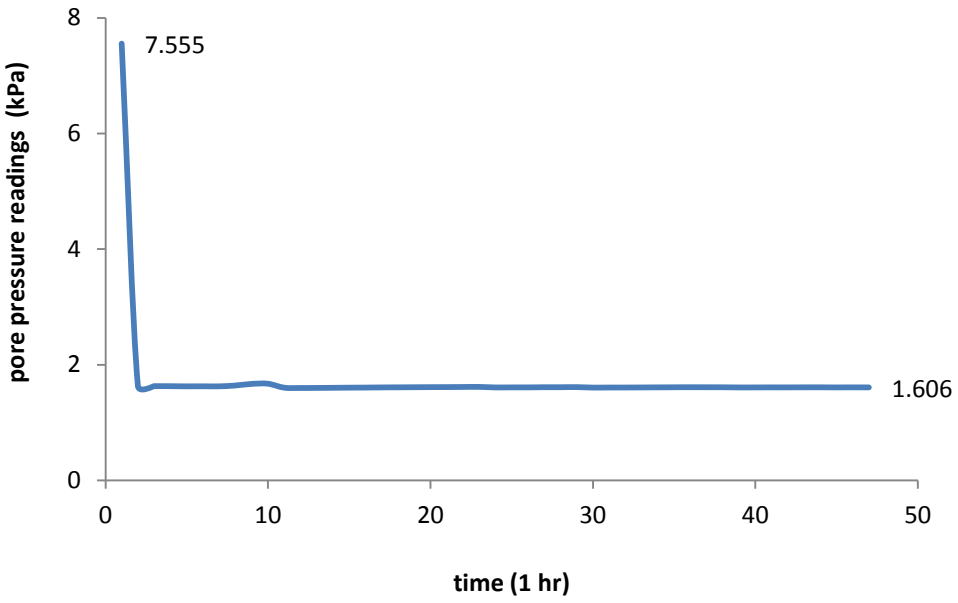

FIGURE E73 Pore pressure of as-received sample three after switching into double drainage (20 kPa)

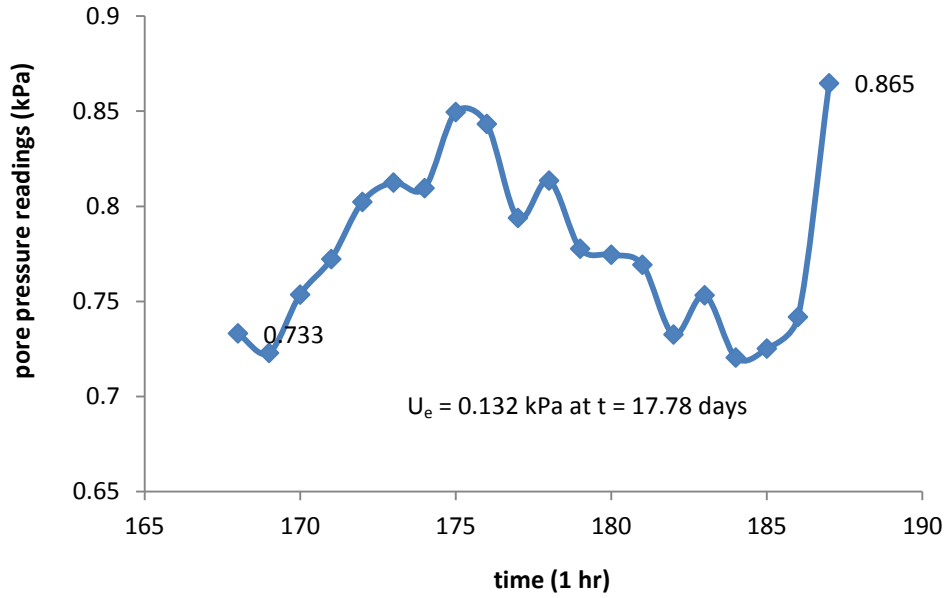

FIGURE E74 Pore pressure of as-received sample three after switching into one-way drainage (20 kPa)

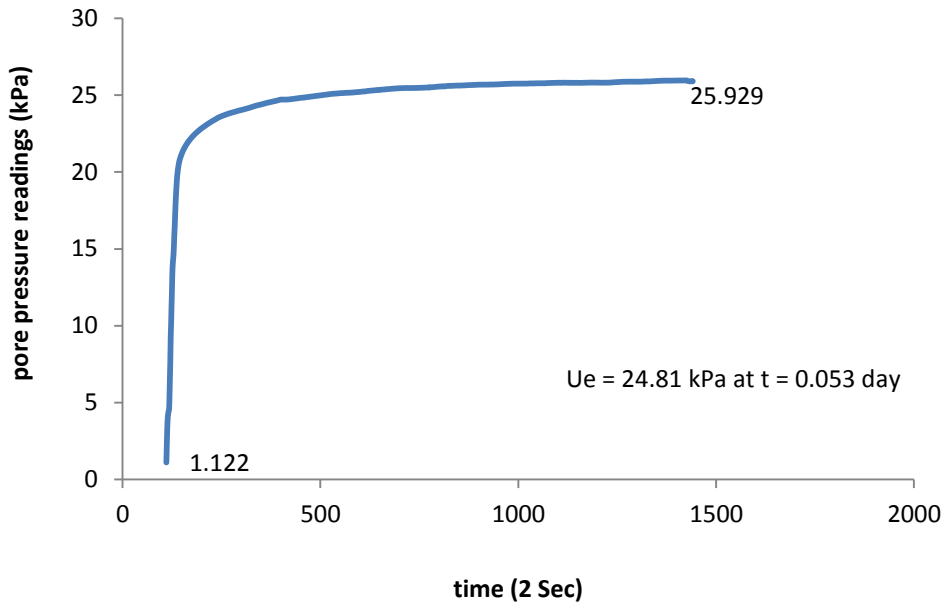

FIGURE E75 Pore pressure of as-received sample three at the beginning with one-way drainage (50 kPa)

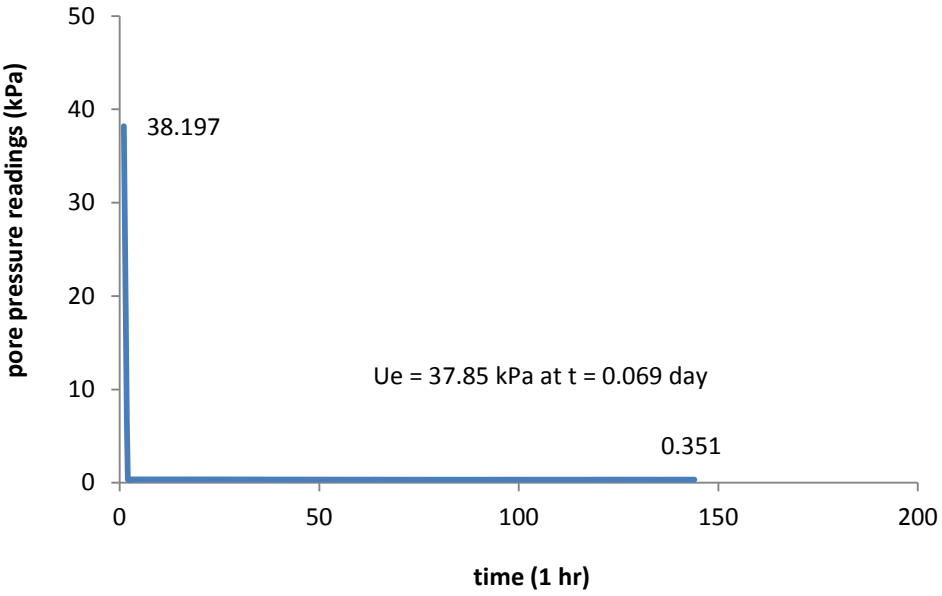

FIGURE E76 Pore pressure of as-received sample three after switching into double drainage (100 kPa)

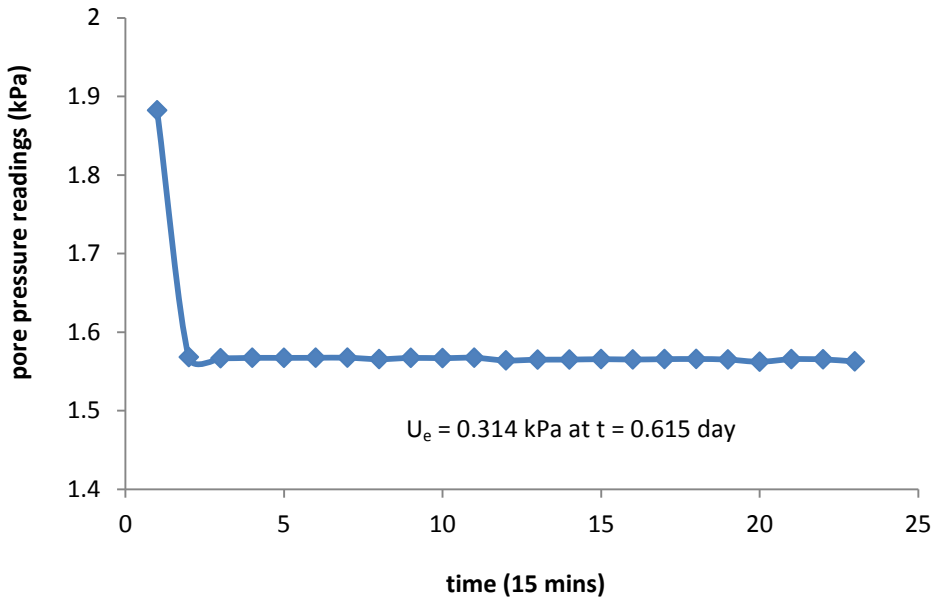

FIGURE E77 Pore pressure of as-received sample four after switching into double drainage (self-weight)

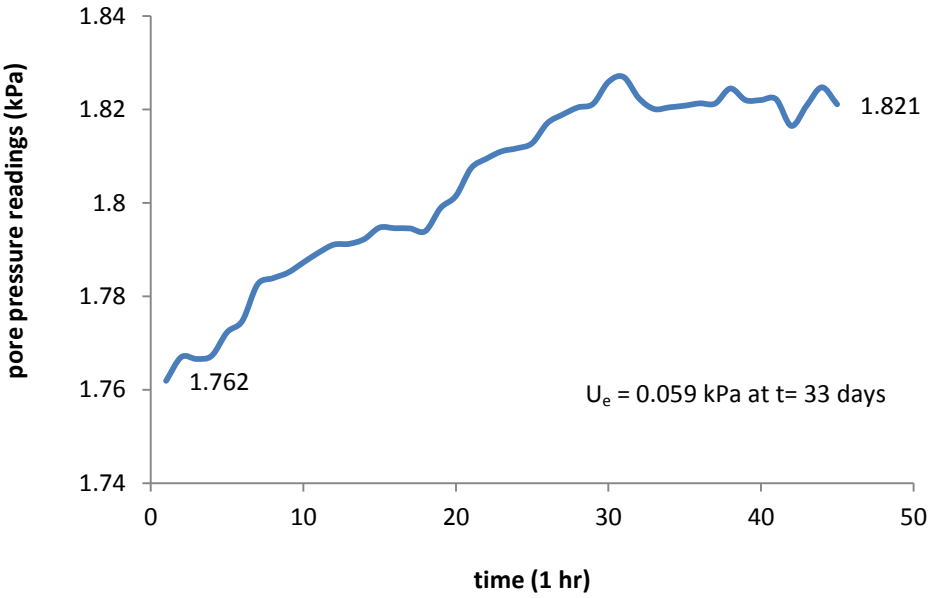

FIGURE E78 Pore pressure of as-received sample four after switching into one-way drainage (0.5 kPa)

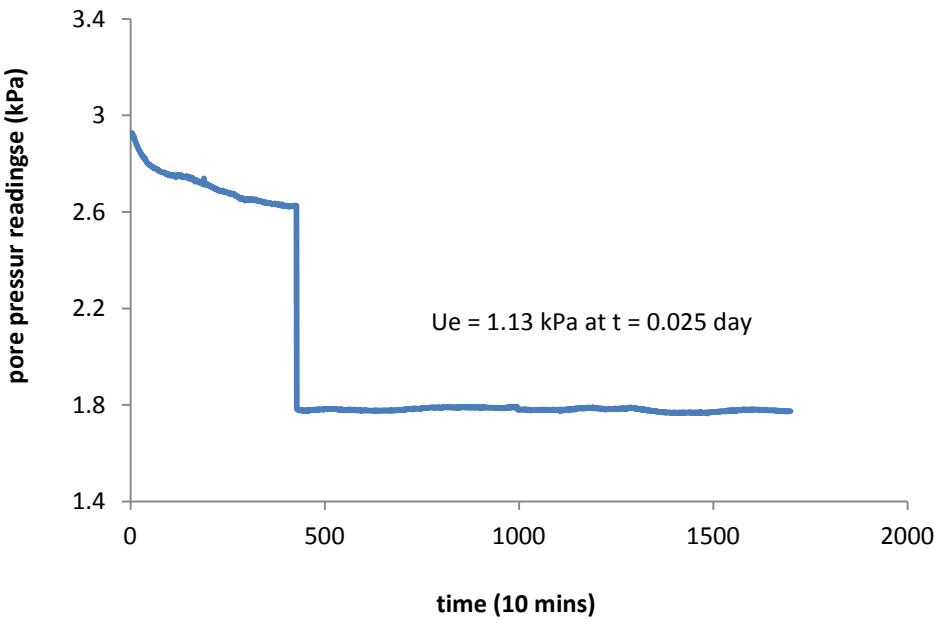

FIGURE E79 Pore pressure of as-received sample four after switching into double drainage (2 kPa)

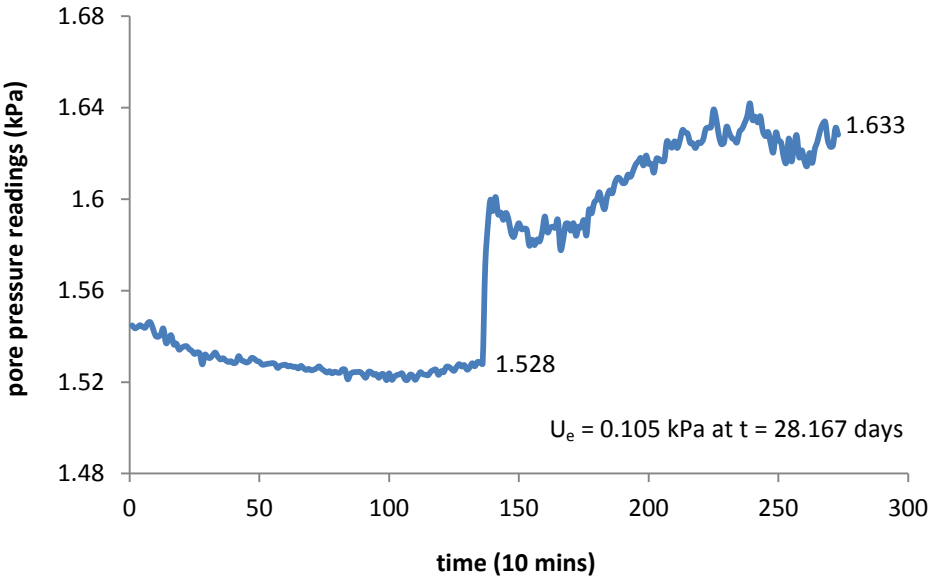

FIGURE E80 Pore pressure of as-received sample four after switching into one-way drainage (2 kPa)

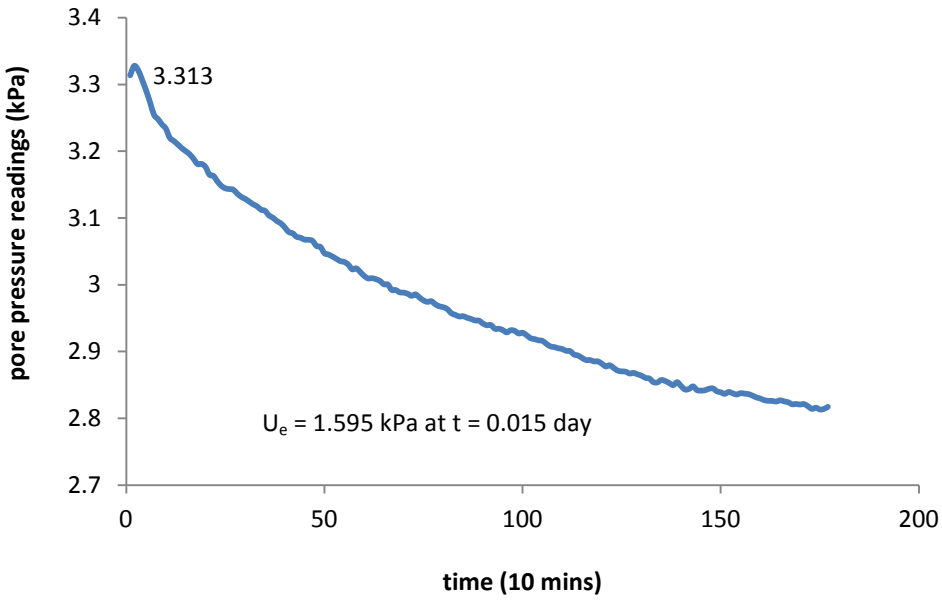

FIGURE E81 Pore pressure of as-received sample four at the beginning with one-way drainage (4 kPa)

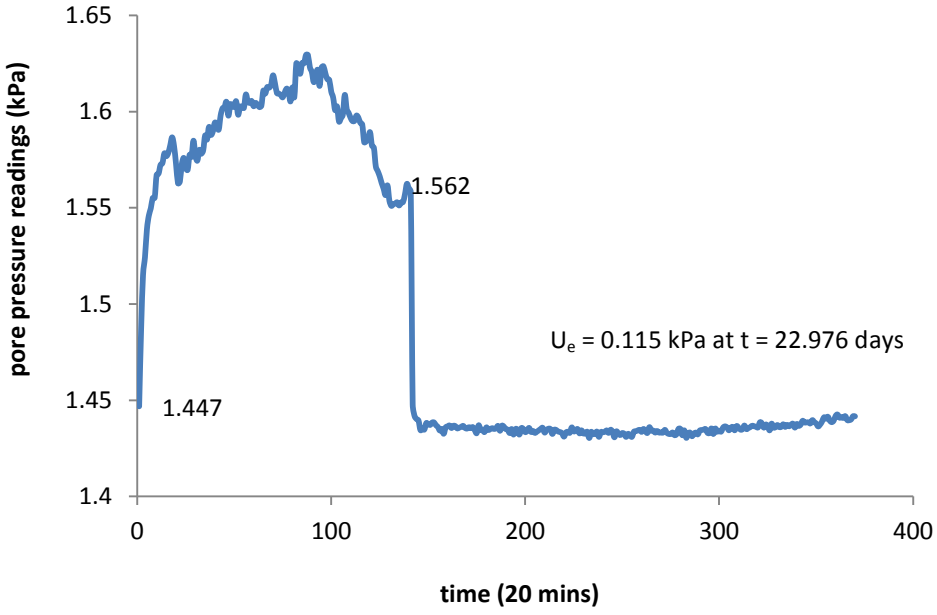

FIGURE E82 Pore pressure of as-received sample four after switching into double drainage (4 kPa)

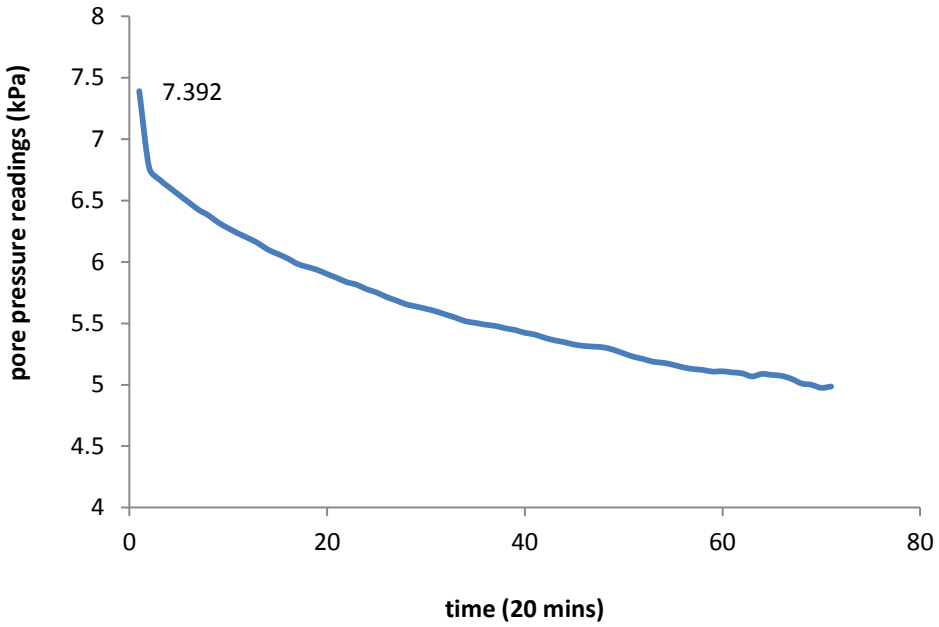

FIGURE E83 Pore pressure of as-received sample four at the beginning with one-way drainage (10 kPa)

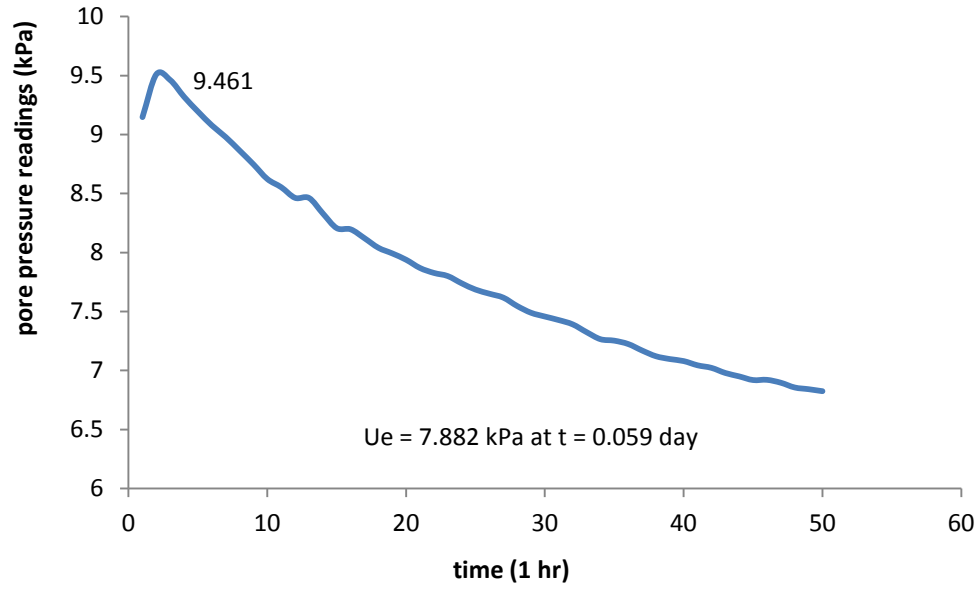

FIGURE E84 Pore pressure of as-received sample four at the beginning with one-way drainage (20 kPa)

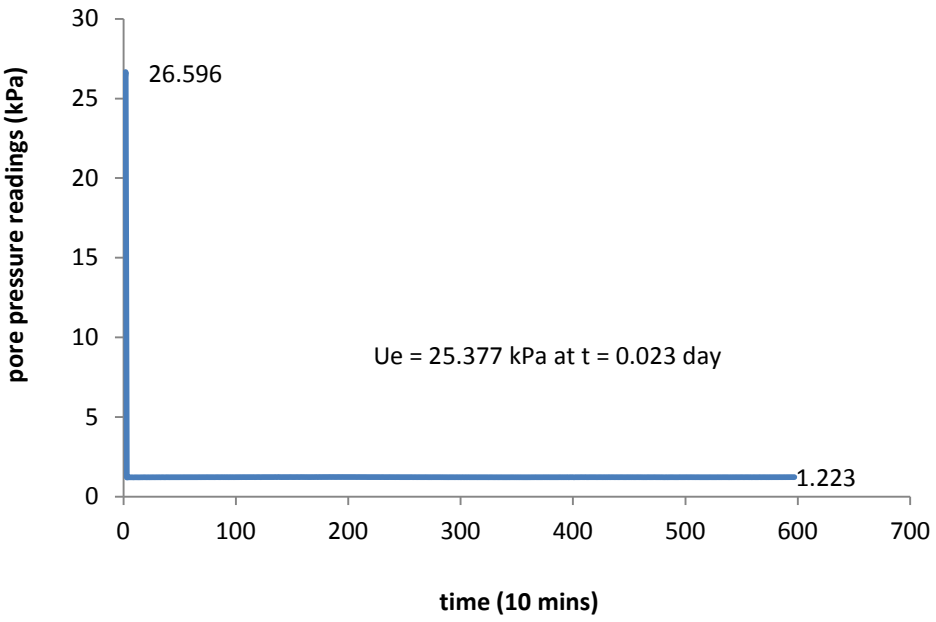

FIGURE E85 Pore pressure of as-received sample four after switching into double drainage (50 kPa)

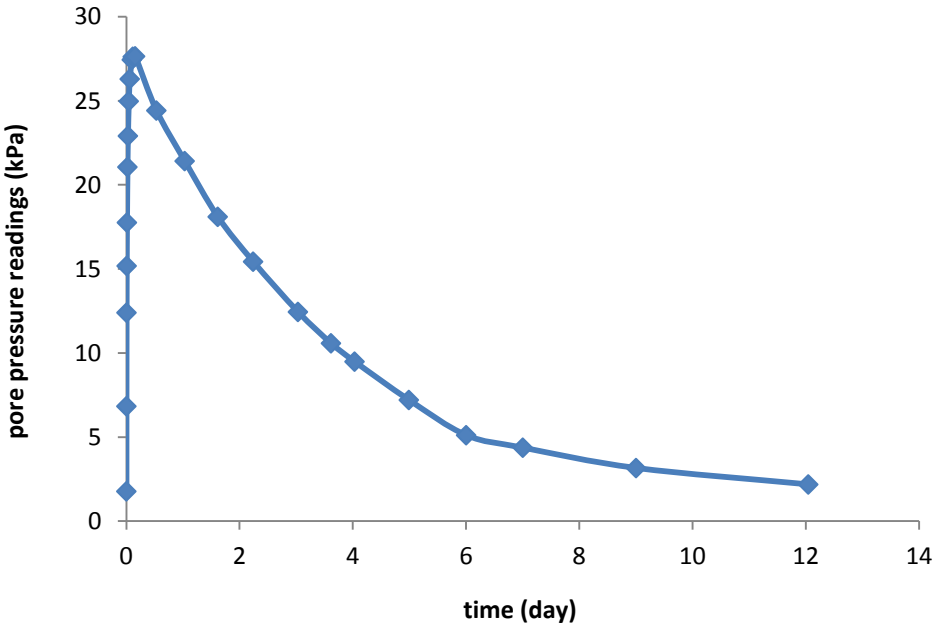

FIGURE E86 Pore pressure of as-received sample four with one-way drainage (100 kPa)

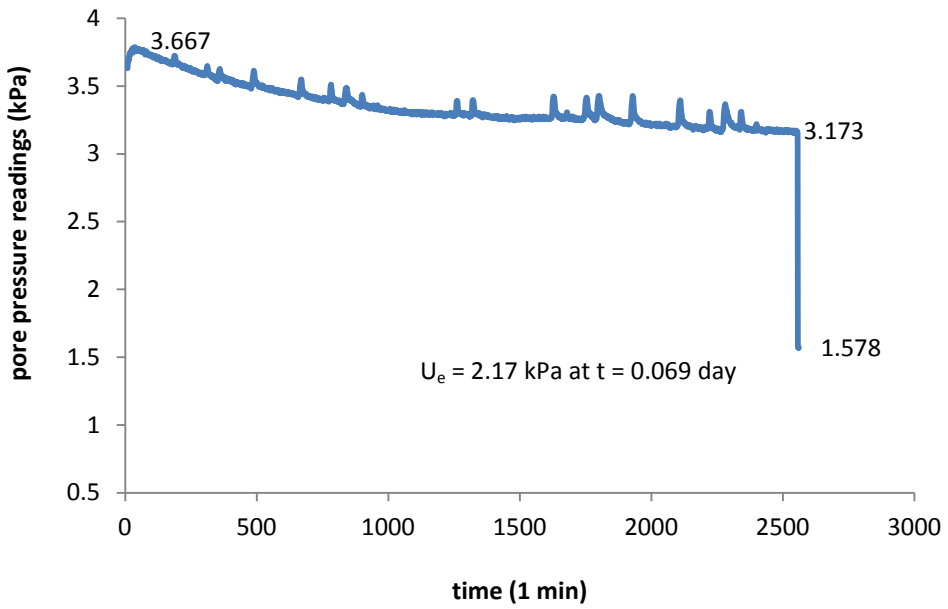

FIGURE E87 Pore pressure of frozen/thawed sample one after switching into double drainage (4 kPa)

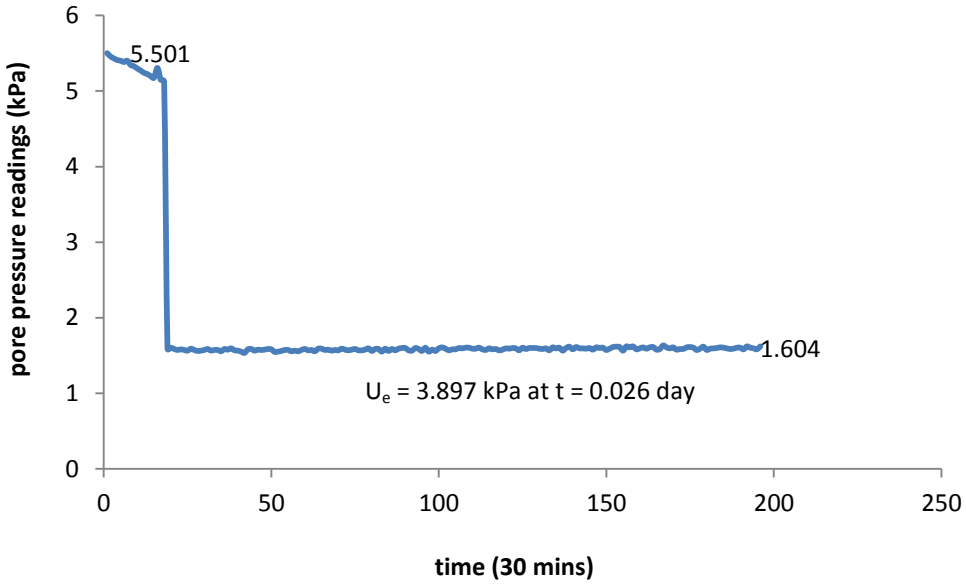

FIGURE E88 Pore pressure of frozen/thawed sample one after switching into double drainage (10 kPa)

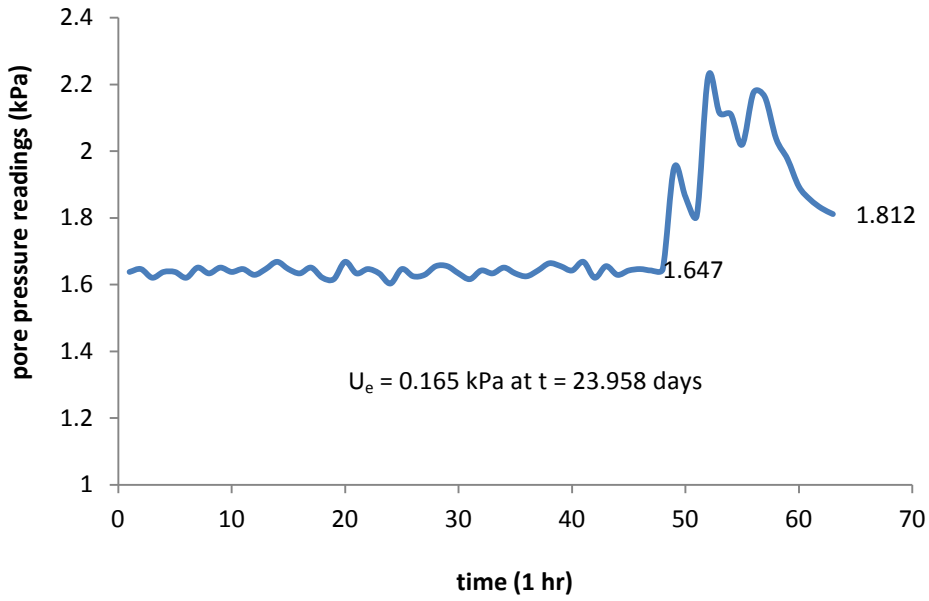

FIGURE E89 Pore pressure of frozen/thawed sample one after switching into one-way drainage (10 kPa)

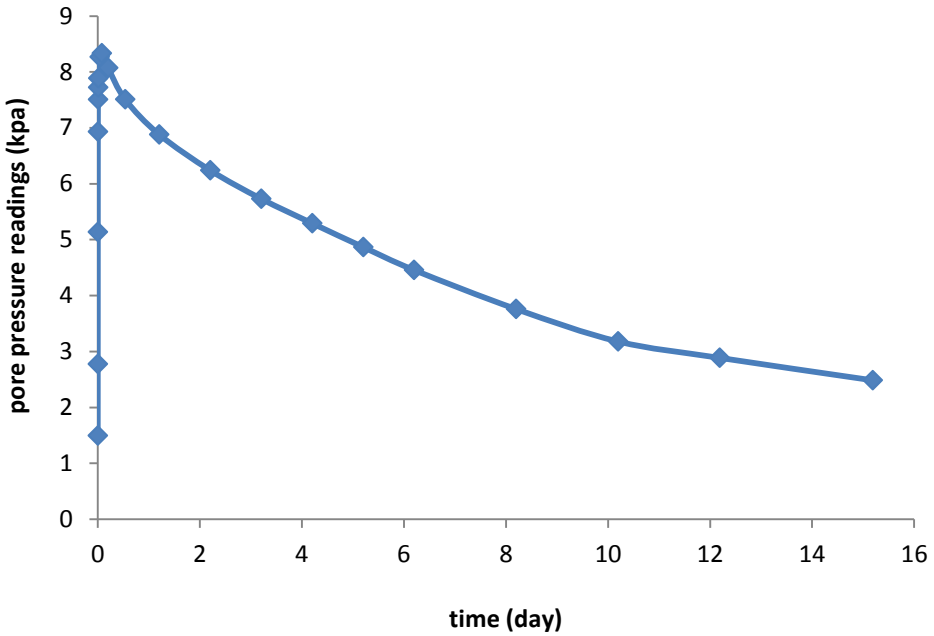

FIGURE E90 Pore pressure of frozen/thawed sample one with one-way drainage (20 kPa)

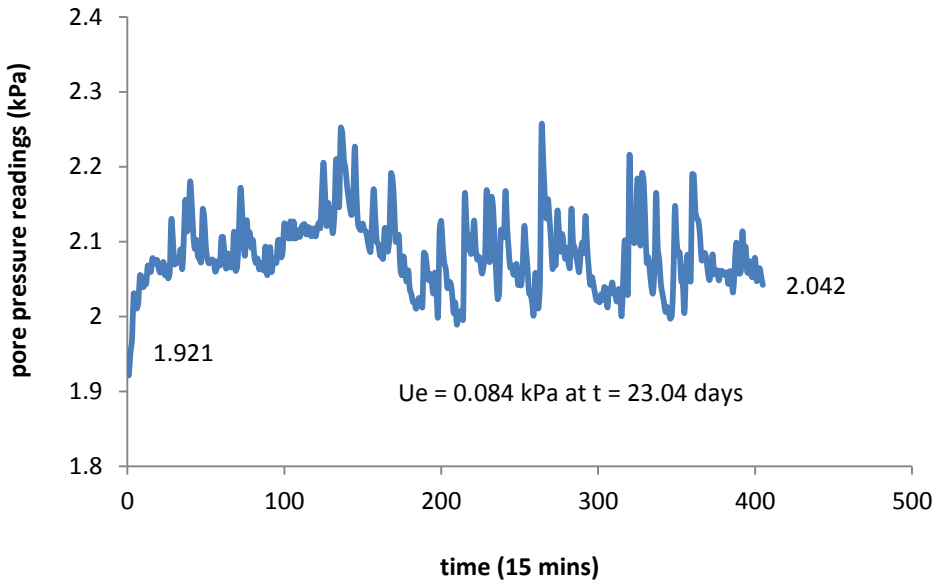

FIGURE E91 Pore pressure of frozen/thawed sample two after switching into one-way drainage (4 kPa)

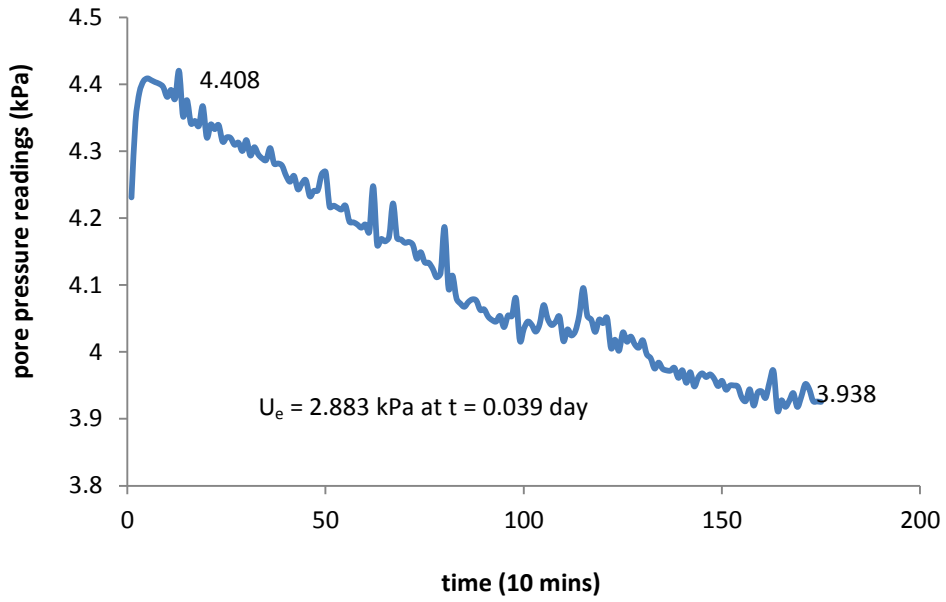

FIGURE E92 Pore pressure of frozen/thawed sample two at the beginning with one-way drainage (10 kPa)

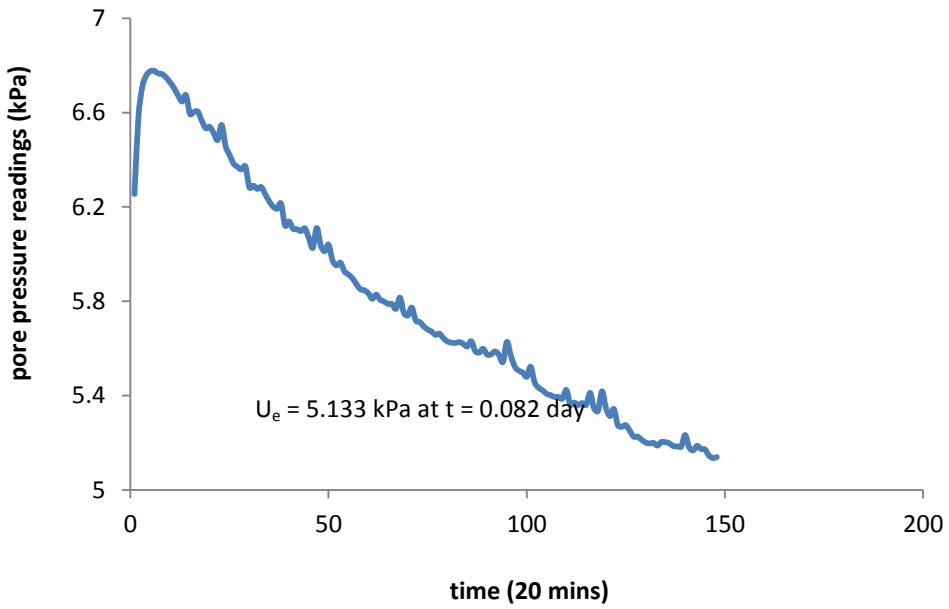

FIGURE E93 Pore pressure of frozen/thawed sample two at the beginning with one-way drainage (20 kPa)

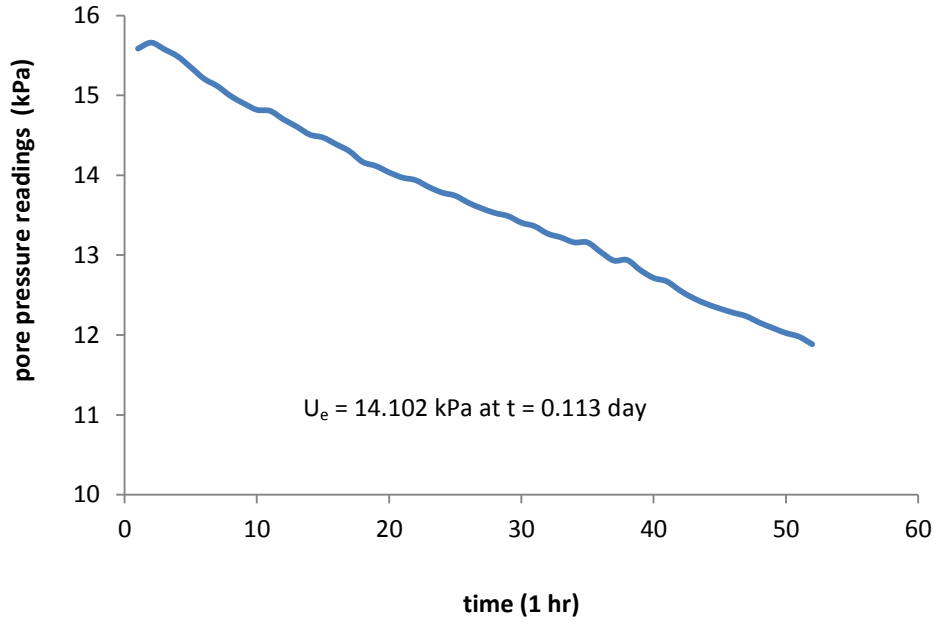

FIGURE E94 Pore pressure of frozen/thawed sample two at the beginning with one-way drainage (50 kPa)

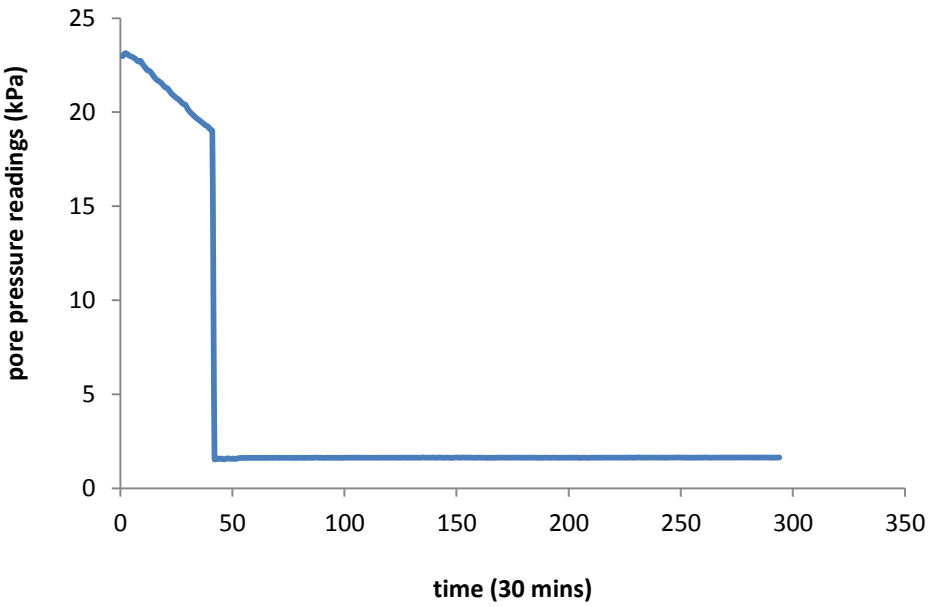

FIGURE E95 Pore pressure of frozen/thawed sample two after switching into double drainage (100 kPa)

APPENDIX F Comparisons between Different MFT

TABLE 1 Some information regarding different MFT

	PL (%)	LL (%)	Bitumen (%)	Additive
Syncrude (Sorta & Sego 2010)	26	53	4.5	NaOH
Suncor (Proskin 1998& Torghabeh 2012)	22	48	0.3-9.9	NaOH
Albian	27	54	1.29	Calcite

NOTE: Additive standards for additives added in the bitumen extraction process.

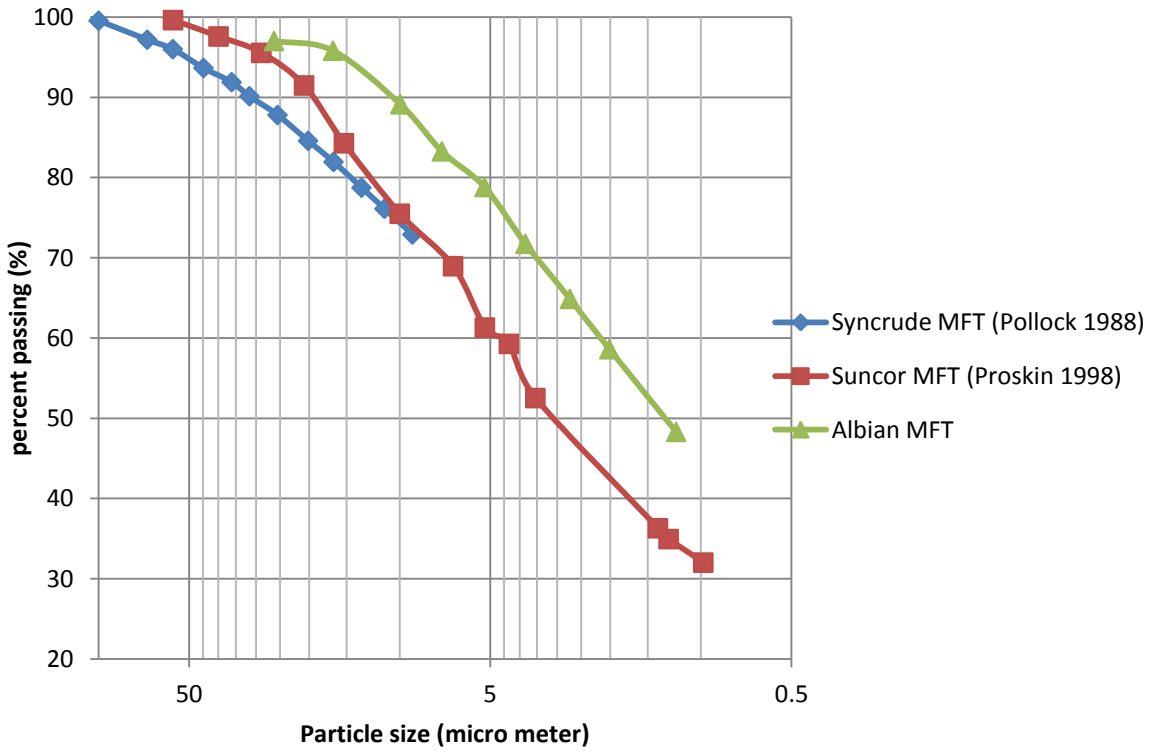

FIGURE 1 Particle size distribution of different MFT (solid content = 30%)

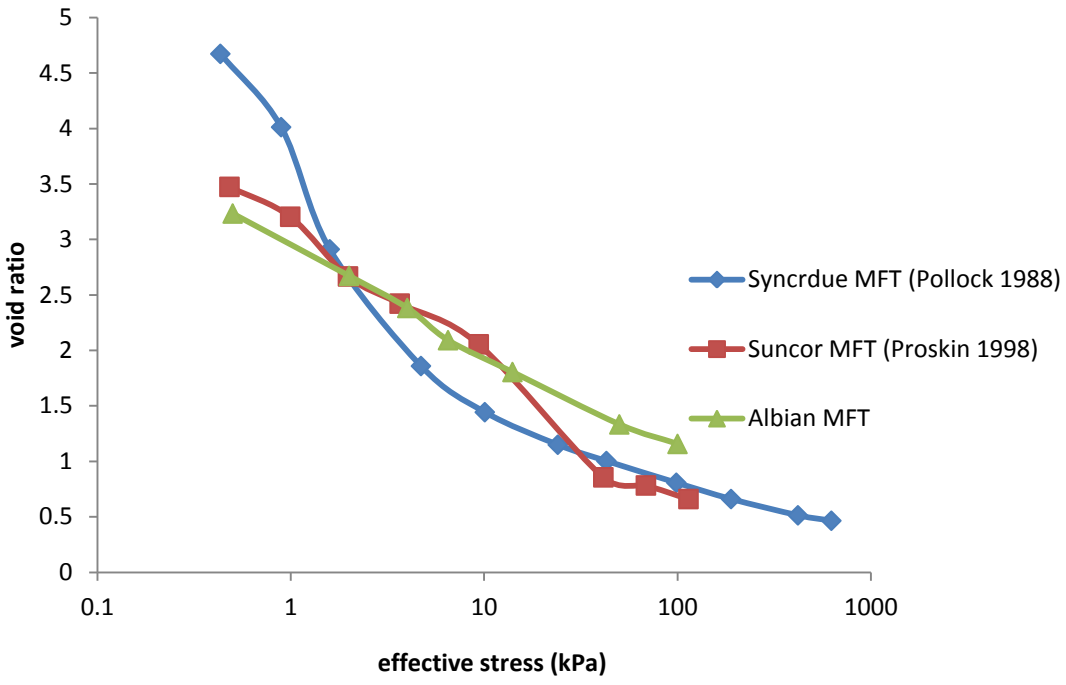

FIGURE 2 Compressibility behaviours of different MFT (initial solid content = 30%)

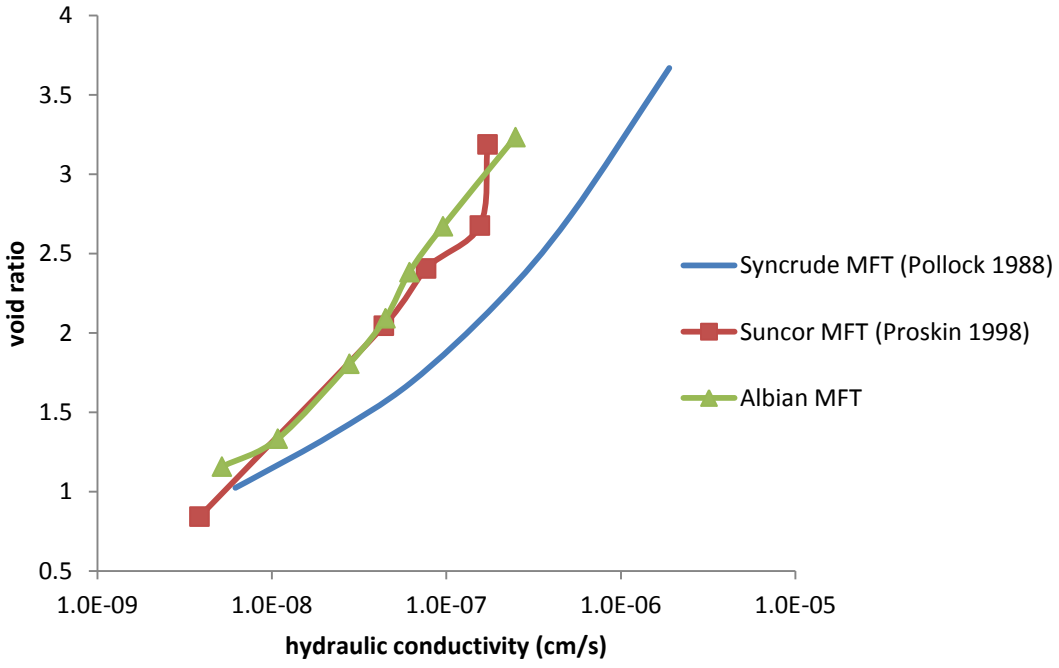

FIGURE 3 Permeability behaviours of different MFT (initial solid content = 30%)

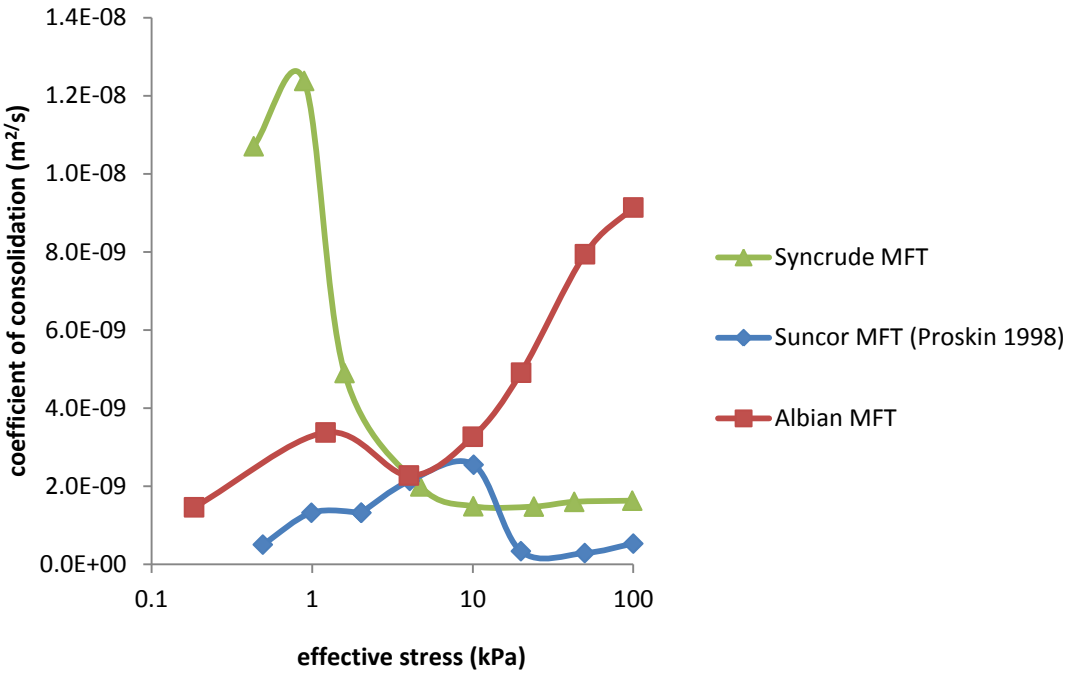

FIGURE 4 Coefficient of Consolidation of different MFT

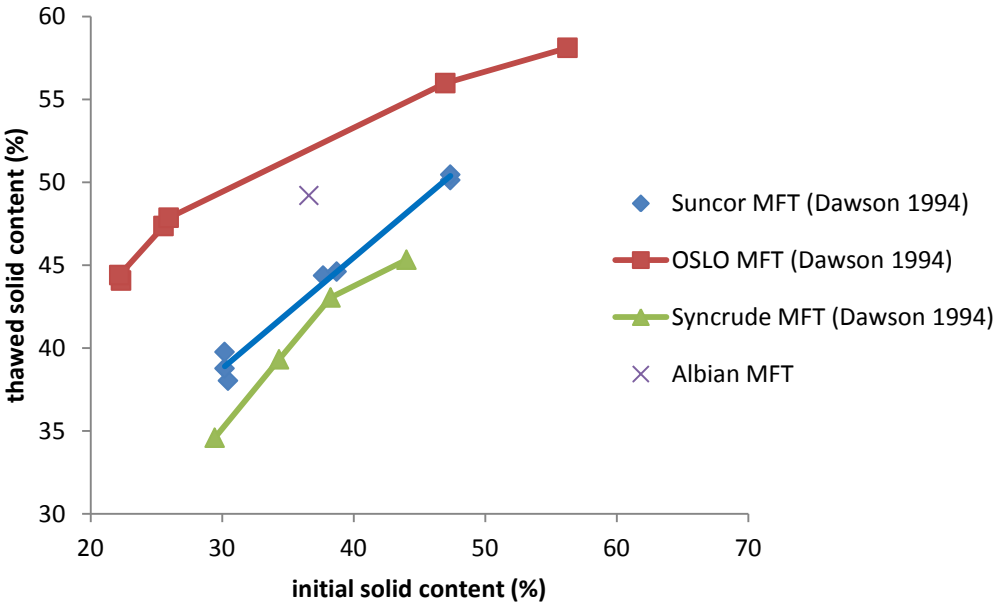

FIGURE 5 Solids content change upon freeze-thaw

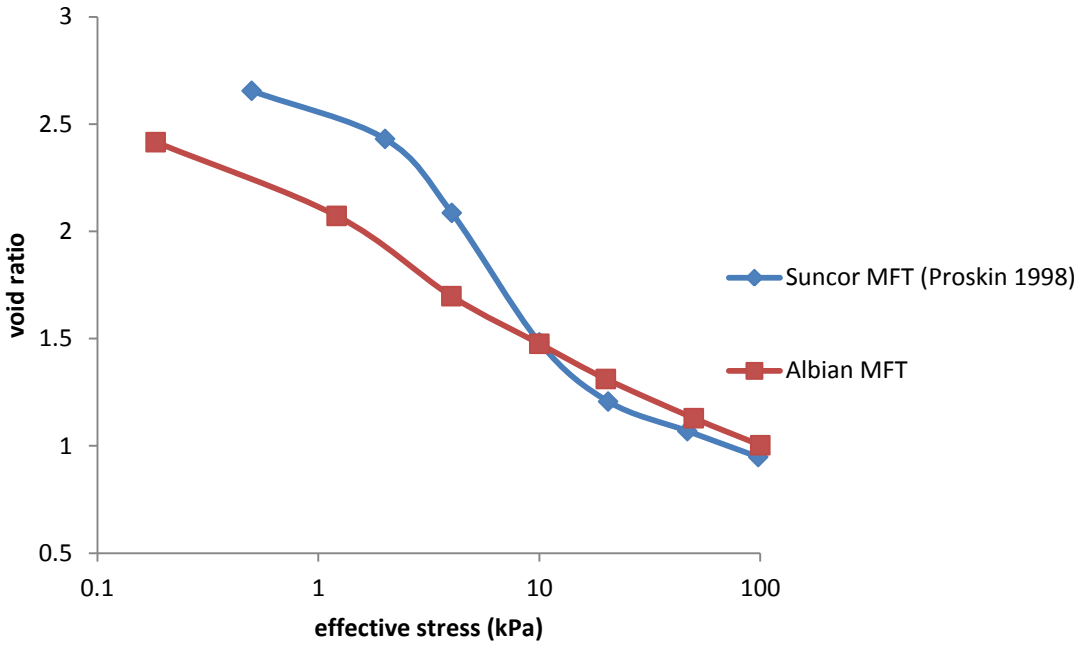

FIGURE 6 Thawed Compressibility behaviours of different MFT

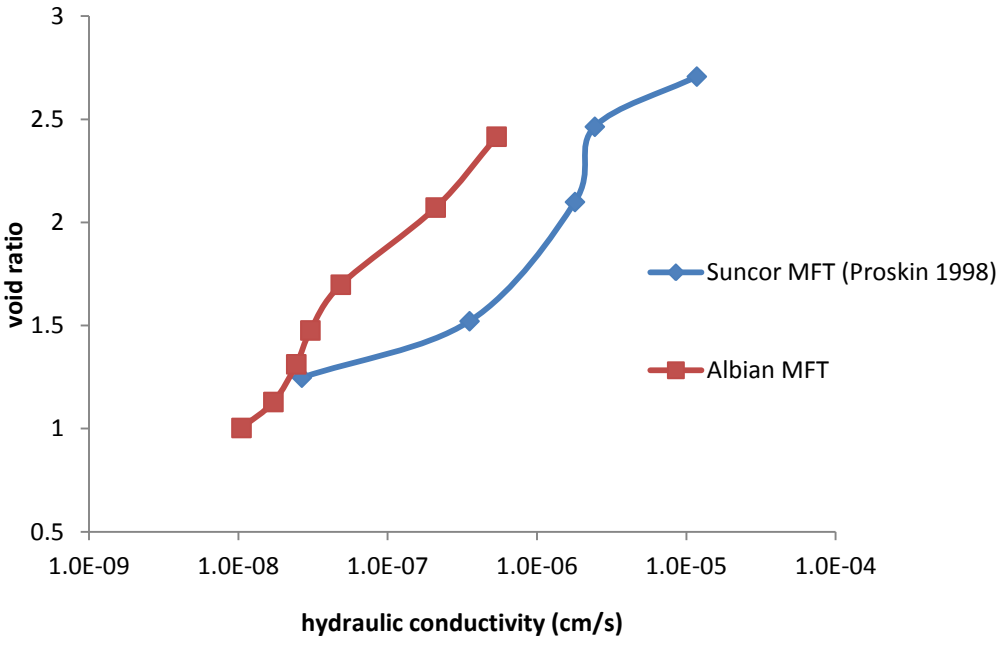

FIGURE 7 Thawed permeability behaviours of different MFT

APPENDIX G Clarification of Some Concerns

Why the excess pore pressure at the bottom of the MFT specimen increases from zero instead of jumping to the pore pressure with the magnitude of load increment upon loading? Why the increasing rate decreases with time? Why is the peak excess pore pressure smaller than the magnitude of load increment? And why the excess pore pressure change back to zero instantly after switching into double drainage?

MFT is a soft plastic quasi-stable material. Its card-house fabric experience progressive failure starting from top and propagating to bottom upon loading. When the load is added on specimen, the soil structure "tries" to carry to load and prevent excess pore pressure from generating. Meanwhile, the upper part of MFT responds to the load: pore water escapes to eliminate excess pore pressure and soil structure collapses to give birth to excess pore pressure. Therefore, the excess pore pressure starts to increase from zero upon loading.

The soil structure becomes stiffer along with collapsing and it attributes to the reduction in pore pressure increasing rate and peak value of excess pore pressure.

The pore pressure transducer measure the pore pressure at the bottom of sample. When the system switches into double drainage, the pore pressure at the bottom responds instantly and the pore pressure is the static pressure.

Does upwards seepage force induce significant heave during permeability tests?

No. Although the effective stress along the specimen profile is reduced by seepage force, negligible rebound takes place. At early load steps, deformation during consolidation is plastic, that is, the slope of rebound curve is very flat. Besides, creep rate is large at high void ratio. It offsets the rebound. At higher load steps, the seepage force is very small comparing to the effective stress in

the specimen. The deformation data recorded by LVDT also indicates no rebound occurs during permeability tests.

Why does MFT with different initial void ratio have particular compression curves?

Suthaker (1995) argued that the process of aging yields different micro-structure and it accounts for the variation in compressibility of as-received MFT. In the author's opinion, the effect of aging disappears by thoroughly remoulding during specimen preparation. The MFT from different depth differs in solids content and composition. The composition of specimen (size distribution curve, bitumen content and pore water chemistry) actually determines the compression behaviors.

A little trace of MFT may be squeezed through the gap between the porous stone and side wall upon applying 0.5 kPa. The MFT particles finally settle down on top of porous stone. Will it affect the permeability of MFT? How to account for the squeezed MFT in determining the relationship between void ratio and deformation?

The squeezed/settled MFT is in a very loose, saturated, quasi-stable state. It is theoretically similar as thin MFT and has card-house fabric. Particles of the squeezed MFT stay on top of porous stone. The permeability of MFT beneath the porous stone is several orders larger than that on top of porous stone. Thus, the squeezed MFT does not affect the permeability of MFT.

Collect the squeezed MFT at the end of the whole test and measure its dry weight. The sample height at the end of consolidation under 0.5 kPa can be back-calculated by virtue of deformation data and final sample height. The sample height before squeezing is also known. The solids content of the

squeezed sample can be assumed as the average solids content before applying 0.5 kPa. The squeezed sample height can be estimated. According to the deformation data, the actual deformation at 0.5 kPa (excluding the squeezing) can be determined. Finally, back-calculate the sample height before self-weight consolidation by excluding the squeezed part.

Why seepage force causes effective stress difference within slurry sample in seepage test?

Velocity head is negligible in low permeability sample.

No seepage flow:

Effective stress: $\sigma'_{0s} = 0$, $\sigma'_{1s} = \gamma' h_3$, $\sigma'_{2s} = \gamma'(h_2 + h_3)$.

With seepage flow:

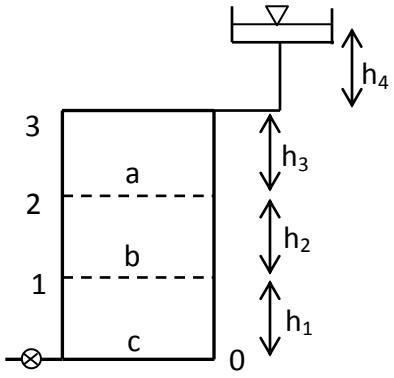

Total head at point 0: $h_{t0} = (h_1 + h_2 + h_3) + h_4$

Total head at point 1: $h_{t1} = (h_1 + h_2) + h_{p1}$

Total head at point 2: $h_{t2} = h_1 + h_{p2}$

Head loss in section a: $h_{t0} - h_{t1} = C_1$

Pressure head at point 1: $h_{p1} = h_3 + h_4 - C_1$

Head loss in section a and b: $h_{t0} - h_{t2} = C_2$

Pressure head at point 2: $h_{p2} = h_2 + h_3 + h_4 - C_2$

Total stress at point 0: $\sigma_{t0} = \gamma_w h_4$, effective stress at point 0: $\sigma'_0 = 0$;

Total stress at point 1: $\sigma_{t1} = \gamma_w h_4 + \gamma_{sat} h_3$, effective stress at point 1: $\sigma_1' = \gamma' h_3 + \gamma_w C_1$;

Similarly, effective stress at point 2: $\sigma_2' = \gamma'(h_2 + h_3) + \gamma_w C_2$;

Effective stress difference:

Point 0: $\Delta\sigma_0' = 0$; Point 1: $\Delta\sigma_1' = \gamma_w C_1$; Point 2: $\Delta\sigma_2' = \gamma_w C_2$.

If seepage gradient j=constant,

Point 0: $\Delta\sigma_0' = 0$; Point 1: $\Delta\sigma_1' = \gamma_w h_3 j$; Point 2: $\Delta\sigma_2' = \gamma_w (h_2 + h_3) j$.

What is the effective stress at different point in sample during permeability tests?

Similarly, effective stress combined with seepage force:

Point 0: $\sigma_0' = \gamma'(h_1 + h_2 + h_3) - \gamma_w h_4$

Point 1: $\sigma_1' = \gamma'(h_2 + h_3) - \gamma_w (h_4 - C_1)$

Point 2: $\sigma_2' = \gamma' h_3 - \gamma_w (h_4 - C_2)$

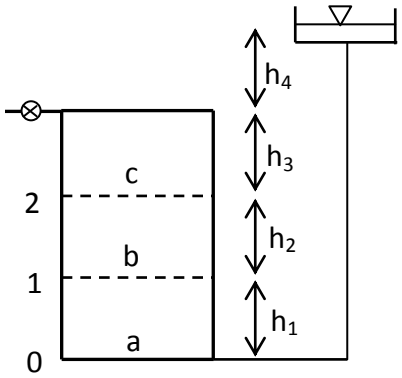

Assume seepage gradient j=constant, h_1=h_2=h_3.

In order to keep effective stress larger than zero,

At point 0, 1, 2: $\gamma' L \geq \gamma_w h_4$, where, L is the length of sample.

Therefore, the sample fails at each point simultaneously if the seepage force reaches the critical value.